Soft-glass microstructured optical fibres for nonlinear applications.

Wen Qi Zhang

Thesis submitted for the degree of

Doctor of Philosophy

in

Physics

at

The University of Adelaide

(Faculty of Chemistry and Physics)

Department of Sciences

March 4, 2012

Contents

Abstract

The objective of this thesis is to explore the potentials of using soft-glass (non-silica) based microstructured optical fibres (MOFs) for nonlinear optical applications. The high linear and nonlinear refractive indices of soft glasses and the ability to tailor the dispersion properties of MOFs have made them an ideal platform for developing nonlinear optical applications. Soft glasses also provide the possibilities of developing waveguides with mid-infrared transmission capability. In addition, the advances in fabricating MOFs with sub-wavelength structures and high refractive index contrast mean that nonlinear processes in these fibres can no longer accurately explored using conventional theories (namely scalar theories). A full vectorial theory is thus required, and this thesis drives forward some applications of recently developed generalised nonlinear theory. In this work, the author studies soft-glass MOFs from two aspects. The first aspect is to develop soft-glass MOFs for new frequency light generation using the scalar theories. The second aspect is to explore new nonlinear phenomena in sub-wavelength scale high-index-contrast waveguides, which includes soft-glass MOFs, using a full vectorial theory. The goal of studying these two aspects is develop a general theory that can explain and accurately predict all nonlinear effects in all types of waveguides.

Progress towards two novel nonlinear light sources is described, namely a femtosecond near-transform-limited tunable light source based on a fibre optical parametric oscillator (FOPO) and a broadband highly coherent supercontinuum (SC) source in the mid-infrared. The advantages of soft-glass MOFs have never previously been employed to enhance the performance of FOPOs. Also the bandwidth

and coherence of SC sources have never been optimised simultaneously, utilising the advantages of soft-glass MOFs. In this work, a genetic algorithm based fibre design approach is developed and applied to design and optimise fibres for these devices. The extrusion technique is used to fabricate fibre preforms. Simulations and experiments are performed to demonstrate SC generation and new frequency light generation in the final fibre.

The Kerr nonlinearity and nonlinear polarisation interactions are studied in a full vectorial framework. A continuous self-phase-modulation method was used to measure the Kerr nonlinearity of soft-glass MOFs, which confirmed the validity of the full vectorial theory. After that, new polarisation behaviours including polarisation self-switching were discovered and studied.

The outcomes of the works demonstrate the efficiency of using soft-glass MOFs for nonlinear applications. As described in Part I, for the FOPO, only a few millimetres of fibres were used to achieve near transform limited output with high conversion efficiency across a large frequency separation. For the supercontinuum source, a broadband continuum spectral output that was only limited by the transmission window of the glass and highly coherent was obtained. The supercontinuum experiments indicated the fabricated fibres had behaved as expected with the consideration of fabrication distortion.

As described in Part II, the work on the nonlinear effects with the full vectorial theory indicates that the Kerr nonlinearities of soft-glass MOFs can be significantly larger than they were previous predicted. New nonlinear polarisation behaviours including polarisation self-switching can take place in soft-glass MOFs with milliwatt level of power which indicates significant differences in the nonlinear processes that involved in FOPO and SC light sources should be observed with soft-glass MOFs.

Combining the full vectorial theory with FOPOs, supercontinuum sources and other nonlinear applications will lead to a better understanding the physics of the nonlinear processes behind these applications as well as further increase the efficiency of using soft-glass MOFs for these nonlinear applications and discover new

applications.

Declarations

I, Wen Qi Zhang certify that this work contains no material which has been accepted for the award of any other degree or diploma in any university or other tertiary institution and, to the best of my knowledge and belief, contains no material previously published or written by another person, except where due reference has been made in the text.

I give consent to this copy of my thesis when deposited in the University Library, being made available for loan and photocopying, subject to the provisions of the Copyright Act 1968.

The author acknowledges that copyright of published works contained within this thesis (as listed in "List of Publications") resides with the copyright holder(s) of those works. I also give permission for the digital version of my thesis to be made available on the web, via the University's digital research repository, the Library catalogue and also through web search engines, unless permission has been granted by the University to restrict access for a period of time.

SIGNED: ..... DATE: .....

List of Publications

JOURNAL:

1. Wen Qi Zhang, H. Ebendorff-Heidepriem, Tanya M. Monro, and Shahraam Afshar V., "Fabrication and supercontinuum generation in dispersion flattened bismuth microstructured optical fiber," Opt. Express **19**, 21135–21144 (2011)

2. Wen Qi Zhang, Max A. Lohe, Tanya M. Monro, and Shahraam Afshar V., "Nonlinear polarization bistability in optical nanowires," Opt. Lett. **36**, 588-590 (2011)

3. Wen Qi Zhang, Jay E. Sharping, Richard T. White, Tanya M. Monro, and Shahraam Afshar V., "Design and optimization of fiber optical parametric oscillators for femtosecond pulse generation," Opt. Express **18**, 17294–17305 (2010)

4. Shahraam Afshar V., Wen Qi Zhang, H. Ebendorff-Heidepriem, and Tanya M. Monro, "Small core optical waveguides are more nonlinear than expected: experimental confirmation," Opt. Lett. **34**, 3577–3579 (2009)

5. Wen Qi Zhang, Shahraam Afshar V., and Tanya M. Monro, "A genetic algorithm based approach to fiber design for high coherence and large bandwidth supercontinuum generation," Opt. Express **17**, 19311–19327 (2009)

6. Wen Qi Zhang, Shahraam Afshar V., H. Ebendorff-Heidepriem, and Tanya M. Monro, "Record nonlinearity in optical fibre," Electron. Lett., **44**, 1453–1455 (2008)

CONFERENCE:

1. Wen Qi Zhang, Max A. Lohe, Tanya M. Monro, Shahraam Afshar V.,"Nonlinear polarization self-flipping and optical switching," in International Quantum Electronics Conference/Conference on Lasers and Electro-Optics Pacific Rim, OSA Technical Digest (CD) (Optical Society of America, 2011), pp.152–154

2. Jay E. Sharping, Wen Qi Zhang, and Shahraam Afshar V., "Modeling of Ultrafast Fiber Optical Parametric Oscillators," in Frontiers in Optics, OSA Technical Digest (CD) (Optical Society of America, 2010), paper FTuJ5

3. Wen Qi Zhang, Richard T. White, H. Ebendorff-Heidepriem, Tanya M. Monro and Shahraam Afshar V., "Supercontinuum generation in dispersion-tailored bismuth microstructured optical fibre," in Proceedings of the 19th Australian Institute of Physics Congress incorporating the 35th Australian Conference on Optical Fibre Technology, 2010, pp. 1-4.

4. Wen Qi Zhang, Tanya M. Monro, Shahraam Afshar V., "Nonlinear Birefringence in Sub-Wavelength Optical Waveguides," in ANIC/BGPP/NP/Sensors/SPPCom/PV /SOLED on CD-ROM (Optical Society of America, Washington, DC, 2010), paper NME55

5. Shahraam Afshar V., Wen Qi Zhang, Tanya M. Monro, "Structurally-based nonlinear birefringence in waveguides with subwavelength structures and high index materials," in Proceedings of the Australasian Conference on Optics, Lasers and Spectroscopy and Australian Conference on Optical Fibre Technology in association

with the International Workshop on Dissipative Solitons, 2009, pp. 374–375.

6. Shahraam Afshar V., Wen Qi Zhang, H. Ebendorff-Heidepriem, Kamran Eshraghian, Tanya M. Monro, "New frontiers in nano-scale highly nonlinear photonic circuits for System on System (SoS) Integration" Proceedings of the International SoC Design Conference (ISOCC) 2009: pp.1–4

7. Shahraam Afshar V., Wen Qi Zhang, and Tanya M. Monro, "Experimental Confirmation of a Generalized Definition of the Effective Nonlinear Coefficient in Emerging Waveguides with Subwavelength Structures," in Conference on Lasers and Electro-Optics/International Quantum Electronics Conference, OSA Technical Digest (CD) (Optical Society of America, 2009), paper CThBB6

8. Richard T. White, Wen Qi Zhang, Shahraam Afshar V. and Tanya M. Monro, "Mid-IR Sources Based on Four-Wave Mixing in Microstructured Optical Fibres," in Proceedings of the Australasian Conference on Optics, Lasers and Spectroscopy and Australian Conference on Optical Fibre Technology in association with the International Workshop on Dissipative Solitons, 2009, pp.489–490.

9. Wen Qi Zhang, Jay E. Sharping, Richard T. White, Tanya M. Monro and Shahraam Afshar V., "Towards Microstructured-Fibre-Based Optical Parametric Oscillators for Ultra-Short-Pulse Sources in the Near-Infrared," in Proceedings of the Australasian Conference on Optics, Lasers and Spectroscopy and Australian Conference on Optical Fibre Technology in association with the International Workshop on Dissipative Solitons, 2009, pp.501-502.

10. Wen Qi Zhang, Shahraam Afshar V. and Tanya M. Monro, "Optimizing the Bandwidth and Coherence of Supercontinuum in Soft Glass Microstructured Fibers," in Conference on Lasers and Electro-Optics/Quantum Electronics and Laser Science

Conference and Photonic Applications Systems Technologies, OSA Technical Digest (CD) (Optical Society of America, 2008), paper CMDD5

POSTDEADLINE:

1. Wen Qi Zhang, "New Regimes of Polarization Bistability in Linear Birefringent Waveguides and Optical Logic Gates," in ANIC/BGPP/NP/Sensors/SPPCom/PV /SOLED on CD-ROM (Optical Society of America, Washington, DC, 2010), Post-deadline paper NThD4

Acknowledgements

It has been a long journey since I started my PhD in the autumn of 2006. Besides a great professional gain, this time has been for me an amazing life experience. Looking back, I had the honour of working with many great people, and I would like to thank to some of them who make this thesis possible.

My deepest gratitude goes to my supervisors, Prof. Tanya M. Monro, Dr. Shahraam Afshar Vahid and Dr. Heike Ebendorff-Heidepriem who guided my research steps from the very beginning. Without their continuous commitments this thesis would have never come to this point. Thank you all for your continuous challenge, efficient feedback, and your patience. Tanya's vision in science and her acute intuitive insights into problems are definitely the most important source of inspiration during my learning process. I would also like to thank you for your willingness to help me in my further career. I would like to thank Shahraam for guiding me into both theoretical and experimental works. His new theoretical model is one important base of part of the work in this thesis. From Shahraam, I learn the way of insight into research questions, and that become one of the most important achievements of this PhD. Heike and her supervision on fibre fabrication guided me tiding over all the difficulties I faced during all fibre fabrication processes. I'm also grateful to my supervisors, through whose involvement the quality of my thesis has increased.

I am also grateful to Prof. Jay E. Sharping for his advice and help on the study of microstructured fibre optical parametric oscillators. Jay is a pioneer in this area. With his help, I could quickly become familiar with this area of study and achieve

results in a most efficient way.

I am also grateful to Dr. Max A. Lohe, whose expertise in mathematics helped on explaining the new physical phenomena discovered in Shahraam's new theory, which troubled Shahraam and me for more than one year. Without his involvement, the journey to achievement of results in this thesis would be greatly prolonged.

I would also like to acknowledge Dr. Richard T. White and Dr. Tak W. Kee for their support in the experimental work.

I would also like to thank to Mr. Roger Moore for helping performing the fibre drawing of all the fibres fabricated in my PhD.

Last but not the least; I would like to express my deepest gratitude to my parents and grandparents for their love and support. And a special thanks to my girlfriend, Chloe, for her words of encouragement in my difficult moments.

Chapter 1

Motivation

Fibre optic communication has become an essential part of the modern society. When fibre nonlinearity is firstly introduced in undergraduate courses, it is as a negative side effect of optical fibres that causes signal degradation in telecommunication. However, there are two sides to everything. Fibre nonlinearity has become an indispensable property of optical fibres that led to the development of modern optical communication systems and more [1]. Many applications for optical communications such as optical wavelength conversion, optical switching, all-optical sampling, optical signal regeneration and optical data processing are all based on fibre nonlinearity [2]. Apart from fibre optical communication, nonlinearity of optical fibres and other forms of optical waveguides opens up new horizons in other areas. Fibre nonlinear applications such as optical computing [3] and optical quantum computing [4] bring the computing technology beyond the capability of conventional computers. Meanwhile, other applications based on fibre nonlinearity such as lasers, amplifiers, quantum noise squeezing and quantum entanglement [2] also helps to understand both fundamental physics and sciences in other areas.

The magnitude of the nonlinear effects that occur in an optical fibre are determined by the combined contribution of fibre nonlinearity and dispersion. Fibre nonlinearity is usually associated with pulse peak power and propagating length (fibre length). With conventional step-index fibres such as SMF-28, the fibre non-

linearity is rather low. To use these fibres for nonlinear optical applications, either high power or long fibre length are required. However, for ideal devices, low power consumption and high compactness are preferred. To achieve these features, highly nonlinear fibres are needed. Fibre dispersion is another crucial property of nonlinear processes, such as Self-Phase Modulation (SPM), Cross-Phase Modulation (XPM), Four-Wave Mixing (FWM) and soliton-related dynamics, property. It determines how much nonlinear interaction can take place between different wavelength components of light. A fine dispersion control is as important as high nonlinearity.

The discovery of microstructured optical fibres (MOFs) has not only increased fibre nonlinearity extensively but also provided extra degrees of freedom of tailoring fibre dispersion. For these high-index-core low-index-cladding MOFs, they guide light using total internal refraction the same way as conventional fibres. However, MOFs can have higher index contrast in core and cladding than conventional fibres but still have single-mode operation. The high index contrasts of MOFs enable them to guide light more tightly than conventional fibres. As a result, MOFs can have smaller effective mode area than conventional fibres which lead to higher fibre nonlinearity in MOFs. The holey structure of MOFs also provides the control of dispersion by allowing the guided light partially leak into the cladding structure.

Non-silica glasses (soft-glasses) as a class of new material for optical fibre have attracted great attention in the past years due to their high nonlinearity and mid-infrared light transmission capability. Using soft glasses for MOFs allow a further increase of fibre nonlinearity. Most soft glasses have linear and nonlinear refractive indices higher than silica glass. Both of them are advantages for achieving high fibre nonlinearity. High linear refractive index allows the waveguides to guide light more tightly which result in smaller effective mode area and thus higher nonlinearity. High nonlinear refractive index indicates high susceptibility of the material which leads to high base factor for fibre nonlinearity. The linear refractive index of soft glasses can be $2 \sim 3$ times higher than silica glass and the nonlinear refractive index of soft glasses can be $10 \sim 100$ times higher than that of silica glass.

Combining the characteristics with microstructured fibre designs and soft glasses, it is possible to achieve the most nonlinear fibre in existence. In addition, engineering the dispersion profile through tuning the microstructure of the fibre to accommodate specific nonlinear effects make soft glass MOFs the most attractive platform for developing fibre nonlinear applications. The use of soft glass also enables the possibility of developing these applications in the mid-infrared wavelength range to meet the needs of other science areas such as biology and chemistry.

The new opportunities brought by soft glass MOFs have not yet been fully explored. Such as the dispersion engineering for nonlinear applications are mainly limited at a level of control the zero dispersion wavelength of a fibre and the slope of the dispersion at this zero dispersion wavelength. Literature describing the effect of high-order dispersions is limited.

Accompanied with the new opportunities, new nonlinear phenomena and new knowledge gaps also come with soft glass MOFs. The complex fibre structure of MOFs usually involves two characteristics that conventional step-index fibre does not possess. They are high-index contrast and sub-wavelength scale (HS) features. These two characteristics are contradictory to the approximations made in the conventional theory which commonly used for studying and predicting the behaviours of the nonlinear processes in fibres and any other forms of optical waveguides. But the conventional theory is no longer adequate to be applied to novel MOFs, especially the ones with HS features.

The problems mentioned above have caught researchers' attention. During the past years, theories were developed to solve these problems. Interestingly, the new theories indicated that HS waveguides are in favour for nonlinear applications. Pioneer works have pointed out that the nonlinearity of these HS waveguides can be twice as large as the conventional theory predicts. Furthermore, new nonlinear behaviours are also predicted to be possible to take place in these waveguides.

In this thesis, two aspects of nonlinear applications with soft glass MOFs are studied. On one hand, the potential to employ soft glass MOFs for nonlinear ap-

plications as sources of generating new frequency light from near- to mid-infrared is explored through engineering the dispersion and nonlinear profiles of the fibres. On the other hand, nonlinear effects including Kerr nonlinearity and polarisation effects are studied using the new theories. The aim of this thesis is that, at the end, the new theory and the development of soft glass MOFs can merge together to form a powerful tool to benefit the future.

1.1 Thesis layout

This thesis is divided into two parts. In Part I, the potential of using soft glass MOFs as a platform for generating new frequency light for near- and mid-infrared are explored. A narrow band tunable fibre optical parametric oscillators (FOPOs) and a broadband supercontinuum source are studied based on the conventional models. Part I starts with an introduction of the conventional model and reviews of the development of current fibre optical parametric oscillators and SC sources in Chapter 2. In this part of the thesis, the fiber design and optimisation for both FOPOs and SC generation processes are performed using a design approach based on genetic algorithm which is introduced in Chapter 3. In the Chapter 4, GA was applied to design the fiber for FOPO for the first time. Simulations based on the conventional model were then performed with the dispersion and nonlinearity profiles of the designed fiber to evaluate the characteristics of FOPOs based on such fibres. In Chapter 5, the GA is used to design and optimise fiber for highly coherence broadband SC. Modifications are made to the design approach to adept the complexity of SC generation. To prove the feasibility of the designs, these designed fibers are fabricated, where corresponding descriptions and discussions are given in the Chapter 6. A certain degree of fabrication distortion is usually unavoidable. Before conducting the experiments with fabricated fiber, modelling and simulations of FOPO and SC generation based on the fabricated fibers are described in Chapter 7. Finally, in Chapter 8, the experimental results are shown and compared to the

simulated ones. Chapter 9 summarises the work in Part I.

In Part II, a new nonlinear theory is used to study the Kerr nonlinearity of HS waveguides and the nonlinear interactions between polarisation modes in these waveguides. This part starts with a review of the theory of a full vectorial nonlinear pulse propagation (VNPP) model in Chapter 10. It is followed by the study of the Kerr nonlinearity in the VNPP model in Chapter 11, the focus is on the experimental confirmation of the prediction of the VNPP model. In Chapter 12, the VNPP model is developed to focus on the nonlinear interactions between different polarisation modes and study novel polarisation behaviours in HS waveguides finishing by proposing a few potential applications. In Chapter 13, the work in Part II is summarised.

The thesis is concluded in Chapter 14 with the discussions on potential future work.

Part I

New frequency light generation in in soft-glass microstructured optical fibres

Chapter 2

Background of Part I

2.1 The scalar nonlinear pulse propagation model

When light is propagating in any dielectric media, the refractive indices of the media change with the intensity of the light. This is a result of the interaction between bound electrons and the electric field of the light. The polarisation $\mathbf{P}$ induced by the electric dipoles of a dielectric medium is nonlinear related to the electric field. It can be expressed as [5]

$$\mathbf{P} = \epsilon_0 \left(\chi^{(1)} \cdot \mathbf{E} + \chi^{(2)} : \mathbf{EE} + \chi^{(3)} \vdots \mathbf{EEE} + \cdots \right), \tag{2.1.1}$$

where ϵ_0 is the vacuum permittivity, $\mathbf{E}$ is the electric field of the light and $\chi^{(j)}$ is jth order susceptibility tensor. The $\chi^{(1)} \cdot \mathbf{E}$ term corresponds to linear index of the media and is responsible for linear process. The term $\chi^{(2)} : \mathbf{EE}$ is responsible for nonlinear effects such as second-harmonic generation. However, in isotropic media like glasses (i.e. SiO_2), the inversion symmetry of the molecule leads to zero for $\chi^{(2)}$, as a result $\chi^{(3)}$ becomes the lowest order and dominant term responsible for nonlinear effects.

The propagation of the light can be described by wave equation [5]

$$\nabla \times \nabla \times \mathbf{E} = -\frac{1}{c^2} \frac{\partial^2 \mathbf{E}}{\partial t^2} - \mu_0 \frac{\partial^2 \mathbf{P}}{\partial t^2}. \tag{2.1.2}$$

To solve this wave equation, we first assume ϵ is independent of the spatial coordinates and therefore

$$\nabla \cdot \mathbf{D} \equiv \nabla \cdot \epsilon \mathbf{E} = \epsilon \nabla \cdot \mathbf{E} = 0. \tag{2.1.3}$$

With Eq. 2.1.3, we can write $\nabla \times \nabla \times \mathbf{E}$ as

$$\nabla \times \nabla \times \mathbf{E} \equiv \nabla(\nabla \cdot \mathbf{E}) - \nabla^2 \mathbf{E} = -\nabla^2 \mathbf{E}. \tag{2.1.4}$$

If we rewrite equation Eq. 2.1.1 as

$$\mathbf{P} = \mathbf{P}_{\mathrm{L}} + \mathbf{P}_{\mathrm{NL}}, \tag{2.1.5}$$

where $\mathbf{P}_{\mathrm{L}}$ is responsible for the linear term $\chi^{(1)}$, and $\mathbf{P}_{\mathrm{NL}}$ is responsible for the nonlinear term $\chi^{(3)}$. Following wave equation can be obtained,

$$\nabla^2 \mathbf{E} - \frac{1}{c^2}\frac{\partial^2 \mathbf{E}}{\partial t^2} = \mu_0 \frac{\partial^2 \mathbf{P}_{\mathrm{L}}}{\partial t^2} + \mu_0 \frac{\partial^2 \mathbf{P}_{\mathrm{NL}}}{\partial t^2}. \tag{2.1.6}$$

The electric field $\mathbf{E}$ and induced polarisation $\mathbf{P}_{\mathrm{L}}$ and $\mathbf{P}_{\mathrm{NL}}$ can be written in the following forms [5],

$$\begin{aligned} \mathbf{E}(\mathbf{r},t) =& \frac{1}{2}\hat{x}[E(\mathbf{r},t)\exp(-i\omega_0 t) + c.c.], \\ \mathbf{P}_{\mathrm{L}}(\mathbf{r},t) =& \frac{1}{2}\hat{x}[P_{\mathrm{L}}(\mathbf{r},t)\exp(-i\omega_0 t) + c.c.], \\ \mathbf{P}_{\mathrm{NL}}(\mathbf{r},t) =& \frac{1}{2}\hat{x}[P_{\mathrm{NL}}(\mathbf{r},t)\exp(-i\omega_0 t) + c.c.], \end{aligned} \tag{2.1.7}$$

in which

$$\begin{aligned} P_{\mathrm{L}}(\mathbf{r},t) =& \frac{\epsilon_0}{2\pi}\int_{-\infty}^{\infty} \tilde{\chi}^{(1)}\tilde{E}(\mathbf{r},\omega-\omega_0)\exp[-i(\omega-\omega_0)t]d\omega, \\ P_{\mathrm{NL}} =& \epsilon_0 \frac{3}{4}\chi^{(3)}|E(\mathbf{r},t)|^2 E(\mathbf{r},t), \end{aligned}$$

where "$\sim$" denotes the element is in Fourier domain.

The Fourier transform of the electric field $\tilde{E}(\mathbf{r},\omega-\omega_0)$ can be found to satisfy the following Helmholtz equation after substituting Eqs. 2.1.7 into Eq. 2.1.6,

$$\nabla^2 \tilde{E} + \frac{\epsilon(\omega)\omega^2}{c^2}\tilde{E} = 0, \tag{2.1.8}$$

where c is the speed of light and

$$\tilde{\epsilon}(\omega) = 1 + \tilde{\chi}^{(1)}(\omega) + \frac{3}{4}\tilde{\chi}^{(3)}|\tilde{E}(\mathbf{r},\omega)|^2 \tag{2.1.9}$$

Equation 2.1.8 can be solved by using Eq. 2.1.10 [5],

$$\tilde{E}(\mathbf{r},\omega-\omega_0) = F(x,y)\tilde{A}(z,\omega-\omega_0)exp(i\beta_0 z), \tag{2.1.10}$$

in which, $F(x,y)$ is the modal distribution, $\tilde{A}(z,\omega)$ is the amplitude of the field, and it is a slowly varying function of z, β_0 is the propagation constant corresponding to central frequency ω_0. Using the weak guidance approximation, which assumes that the index contrast in a waveguide is small and therefore the field is weakly guided (implies the electric fields of the guided modes are transverse), one can separate the modal distribution and amplitude so that they can be evaluated and studied separately. With Eq.2.1.10, Eq.2.1.6 leads to following separated equations

$$\frac{\partial^2 F}{\partial x^2} + \frac{\partial^2 F}{\partial y^2} + \left[\epsilon(\omega)k_0^2 - \tilde{\beta}^2\right]F = 0, \tag{2.1.11}$$

$$2i\beta_0\frac{\partial \tilde{A}}{\partial z} + (\tilde{\beta}^2 - \beta_0^2)\tilde{A} = 0. \tag{2.1.12}$$

in which $\dfrac{\partial^2 \tilde{A}}{\partial z^2}$ is neglected since $\tilde{A}$ is a slowly varying function.

The dielectric constant ϵ (Eq. 2.1.9) can be rewritten as

$$\epsilon = n^2 \approx (n_0 + n_2|E| + \frac{i\tilde{\alpha}c}{\omega})^2, \tag{2.1.13}$$

where n_0 is the linear refractive index (the index at low input power), $n_2 = \frac{3}{8n_0}\mathrm{Re}(\chi^{(3)})$ is the nonlinear-index coefficient and α_0 is the absorption coefficient. In Eq.2.1.13, the real part of the refractive index is approximated to the term of n_2 and imaginary part of refractive index is approximated to the first order since $\alpha_2 = \frac{3\omega_0}{4n_0c}\mathrm{Im}(\chi^{(3)})$, also called as the two-photon absorption coefficient, is small for silica fibres [5] and can be ignored.

Using the first-order perturbation theory [6] and applying a Taylor series expansion to $\tilde{\beta}$ which is solved from Eq. 2.1.11, one can derive a nonlinear Schrödinger

equation Eq. 2.1.14 from Eq. 2.1.12 [5].

$$\frac{\partial A}{\partial z} + \sum_{n=1}^{\infty} \frac{(i)^{n-1}}{n!} \beta_n \frac{\partial^n}{\partial t^n} A + \frac{\alpha}{2} A = i\gamma |A|^2 A, \tag{2.1.14}$$

where

$$\gamma = \frac{n_2 \omega_0}{c A_{\text{eff}}} \tag{2.1.15}$$

is the effective nonlinear coefficient (also referred as nonlinearity in this thesis) and A_{eff} is the effective mode area defined as

$$A_{\text{eff}} = \frac{\left(\iint_{-\infty}^{\infty} |F(x,y)|^2 dxdy \right)^2}{\iint_{-\infty}^{\infty} |F(x,y)|^4 dxdy}. \tag{2.1.16}$$

The nonlinear Schrödinger equation 2.1.14 can be further generalised when high-order nonlinear effects such as stimulated Raman scattering are included. A general nonlinear Schrödinger equation can be obtained [5]

$$\frac{\partial A(z,t)}{\partial z} + \frac{\alpha}{2} A(z,t) - \sum_{n \geqslant 2} \frac{i^{n+1}}{n!} \beta_n \frac{\partial^n A(z,t)}{\partial T^n} = i\gamma (1 + i\tau_{shock} \frac{\partial}{\partial T}) \left(A(z,t) \int_{-\infty}^{\infty} R(T') \times |A(z, T - T')|^2 \, dT' \right), \tag{2.1.17}$$

where $R(t)$ is the nonlinear response function (see details in Appendix A.1), τ_{shock} is the optical shock time which is defined as [7, 8]

$$\tau_{shock} = \frac{1}{\omega_0} - \frac{1}{n_{eff}(\omega_0)} \frac{\partial n_{eff}(\omega)}{\partial \omega}|_{\omega_0} - \frac{1}{A_{eff}(\omega_0)} \frac{\partial A_{eff}(\omega)}{\partial \omega}|_{\omega_0} \tag{2.1.18}$$

in which n_{eff} is the effective refractive index of the propagating modes and it is calculated based on $\beta(\omega)$ using Eq. 2.1.11.

The works in Part I of this thesis uses this scalar pulse propagation model and the models built based on it.

2.2 Applications of fibre nonlinear effects for new frequency light generation

Nonlinear effects in optical fibres can be applied to construct devices such as optical wavelength convertors, optical signal regenerators, lasers, amplifiers, optical switches

and optical pulse compressors [2]. The majority of the nonlinear applications are related to the generations of new frequency light. Four-wave mixing (FWM) process and supercontinuum (SC) generation are the two typical nonlinear processes that have been widely used for generating new frequency light. In this section, works on FWM based fibre parametric oscillators (FOPOs) and SC generation are reviewed.

FWM process is a type of parametric nonlinear process based on the third-order nonlinear susceptibility of the glass. It can be used for optical signal processing, including signal amplification, wavelength conversion (such as optical parametric amplifiers and oscillators), signal regeneration, time division multiplexing, all-optical sampling, etc [9]. It can also be of interest for quantum communications [2, 10] due to the tight phase relations between pump, signal and idler pulses.

SC generation, in contrast to the FWM process, is a process that involves many nonlinear processes, including self-phase modulation (SPM), cross-phase modulation (XPM), FWM, stimulated Raman scattering (SRS) and optical soliton generation. But like FWM, SC generation is also of interest for many applications such as Light Detection and Ranging (LIDAR) [11], optical coherence tomography (OCT) [12], absorption spectroscopy [13] and coherent anti-Stokes Raman scattering (CARS) [14–16]. Some characteristics of SC sources, including octave wavelength span and high coherence, are of special interest for certain applications such as a frequency comb generation [17, 18]. These characteristics become essential for improving current applications and developing new applications as well.

Both FWM and SC generation can be used to construct devices to generate new frequencies efficiently. However, for the most of the time, FWM process is used for constructing tunable light sources and SC generation is used for constructing broadband light sources.

FWM and SC generation applications based on conventional high nonlinearity fibers and silica microstructured fibers have been well studied. However, the use of silica glass limits the further development of these nonlinear applications due to the low nonlinearity and the lack of mid-infrared (mid-IR) transmission of silica glass.

In this work, new frequency light generation sources for mid-IR, more specifically, FWM-based fiber optical parametric oscillators (FOPOs) and SC generation in mid-IR are studied based on non-silica glass microstructured fibers. But before the details of this work are revealed, relevant literature on both FOPOs and SC generation are reviewed.

2.3 Fiber optical parametric oscillators

FOPOs, especially those based on microstructured optical fibers (MOFs), are attractive sources of tunable, coherent radiation. FOPOs are more compact and cost less than crystal-based OPO systems and, unlike most lasers, FOPOs are capable of generating coherent light with broad continuous wavelength tunability. The use of optical fiber ensures the beam quality of the output light and microstructure provides significant control of dispersion for four-wave mixing (FWM) phase matching across wide wavelength ranges.

FOPOs utilise FWM processes in the fibre. FWM process originates from the nonlinear response of electrons of the fibre material interacting with the electromagnetic field propagating inside it. This nonlinear interaction provides gain to the electromagnetic field at certain wavelengths depending on wavelength of field the dispersion of the fibre. This gain is called parametric gain. FWM is a third-order nonlinear process. It involves four optical waves (or three waves if two of the four waves are degenerated, see details in Chapter 4). FWM has been studied since the first low loss fiber came into existence. FWM processes are polarisation dependent, which means full vector theory of nonlinear pulse propagation is needed to be used. However, by considering four linearly co-polarised waves in a non-birefringent fibre or polarised along one of the principle axes of a birefringent fibre, it is possible to study FWM in scalar forms (i.e. Eqs. 4.1.1∼4.1.4).

FWM processes are mainly determined by the parametric gain of a fibre, which includes two major properties of the fibre, nonlinearity and dispersion. To design or

optimise a FOPO is equivalent to design or optimise the nonlinearity and dispersion profiles of the fibre used in the FOPO.

2.3.1 Conventional fibre optical parametric amplifiers and oscillators

Using parametric gain in fibres, fibre optical parametric amplifiers (FOPAs) and oscillators (FOPOs) can be constructed. Comparing to other fibre amplifiers (such as erbium doped fibre amplifier) and fibre lasers, the operational wavelengths of FOPAs and FOPOs are not limited by the material that is used to make the fibre, which is a difficulty for the development of other fibre amplifiers and lasers, since they usually rely on the doped ions in the fibre.

The early works of FOPAs and FOPOs can be traced back to early 1970s and 1980s [19, 20]. Since then, studies have been performed for many wavelengths and power levels using approaches such as applying external stress [21], utilising Raman gain [22], birefringent fibers [21, 22], MI [23] and multiple pumps [24, 25].

The first FOPA was demonstrated in a 9 cm silica core SiO_2-B_20_3 cladding fibre pumped with 532 nm Nd:YAG laser [19]. Phase matching was achieved between fundamental and high-order modes: Pump, signal (626 nm) were LP_{01} modes, and idler (463 nm) was LP_{02} mode. This very first FOPA demonstrated only a gain of -40 dB in the idler wavelength. Although the small gain could not prove the practical use of a FOPA, but it showed the possibility of obtaining the gain and generating new frequencies via third-order nonlinearity. A few years later, a FOPA was constructed with 30 m of single mode fiber pumped with a Q-switched pulse laser at 1.3 μm [26]. The pump wavelength of this FOPA was longer than the zero dispersion of the fibre (1.22$\sim$1.27 μm [27]). Phase matching was provided via MI. Therefore, the wavelength shift was small (around 20nm). However, it was capable of generating a significant gain maximised at 46.6 dB with 70 W pulsed pump and 0.62 mW CW seed. Phase matching is the key for achieving high gain.

With step-index fibre, the freedom of tailoring the dispersion profile is limited. But, FWM is a polarisation dependent process. Phase matching can also be achieved through different polarisation modes of a birefringent fibre. One advantage of using birefringent fibre is that the birefringence can be altered through applying stress onto the birefringent fiber. The phase matching condition can be adjusted through applying stress onto the fibre without necessarily changing the fibre designs [21].

The works listed above were all based on silica step-index fibers pump with visible and telecommunication-band sources. The nonlinearity of silica step-index fibers is around 1∼10/W/km (1550 nm). To achieve a high gain, it usually requires long length of fiber or high pump power. For example, to achieve 30 dB gain with 1 m of SMF-28 fibre, a theoretical value of 6.9 kW peak pump power is needed. To increase the efficiency of FOPAs, Raman gain of the fiber had also been utilised. One important work in this area showed that by applying stress on a birefringent fiber and tuning the phase matched frequency to the Raman shift frequency, the FOPA can gain benefits from both FWM and Raman effects [22].

The study of MI-based FOPA started in the 1990s. It was discovered that broad-band parametric gain can be obtained through pumping the fiber in its anomalous dispersion region or very close to the zero dispersion wavelength [28]. Early works demonstrated 40 nm tunability in a 100 m long fiber [23]. In this case, the fibre was pumped with 7 kW peak power 20 ns square pulses at wavelengths slightly longer ($0.55 \sim 0.8$ nm) than the zero dispersion wavelength 1539.3 nm of the fibre. It was also found that through tuning the pump wavelength, the shape of the gain band can also be tailored. Another work demonstrated a 40 nm band with 28 dB gain in a 720 m long fiber pumped with only 600 mW peak power pulses [29]. In this work, a highly nonlinear dispersion-shifted fibre with the zero dispersion wavelength at 1534 nm was used and the fibre was pumped at 1534.6 nm.

Study shows that using dual-wavelength pumping, broad gain bandwidth can be obtained for FOPA [25]. With two pumps, more degrees of freedom are added to the phase matching condition and gain value of FWM processes. Furthermore,

besides the non-degenerated MI process, dual wavelength FWM also includes phase conjugation and Bragg scattering processes [25]. In theory, it is possible to obtain a broadband gain that covers the whole wavelength range between the pumps with proper configurations of these two pumps with respect to dispersion, i.e. equally separated around the zero dispersion wavelength. Two pumps provide extra flexibility of tuning the FOPA not only in wavelength tunable range but also in the polarisation of the modes. One example is the work done in 2004, in which the FOPA was capable of covering entire C-band with mW level pump power in a 1 km long fiber [30]. With two pumps, polarisation independent FOPAs were also studied due to their applications in telecommunication [24, 31, 32].

A FOPO is a simple application of parametric amplification. Similar to fiber lasers, in FOPOs, fibers are used as a gain medium inside cavities. The first FOPO was demonstrated soon after the demonstration of the first working FOPA [20]. It consisted of a 1.4 m long graded index multimode fiber. This FOPO was pumped with a 1064 nm pulsed laser. The peak power of the pump pulse was below 100 kW. This FOPO showed output peaks at 4 wavelengths including 520, 628, 792 and 1620 nm with total conversion efficiency around 25%. A few years later, a group in Sweden also demonstrated a FOPO pumped with 100 ps 1.2 kHz 1∼10 kW peak power pulses at 1064 nm and generated signal and idler at 991 and 1149 nm.

MI based FOPOs were also demonstrated using a ring cavity [33]. In this work, the pump pulse was 13 ps long at 1525∼1550 nm with 100 MHz repetition rate and 39∼45 W average power. Outputs with a maximum of 44 nm wavelength shift were observed. The material dispersion of silica glass limits MI based FOPOs to wavelengths larger than 1.3 μm since positive β_2 was needed. However, by taking advantage of birefringent fibres, MI based FOPOs in the visible region were also demonstrated [34, 35]. The principle of these works is similar to the birefringent OPA [21, 22]. The phase matching was achieved between slow and fast axis modes, which was more like a dual pumped scheme. The wavelength shifts in these works were small compared to non-birefringent MI FOPOs. The maximum wavelength

shift was 14 nm achieved through 3 cascaded processes [34].

The broad bandwidth of MI processes inspired the development of broadband tunable FOPOs. The very first tunable FOPOs was demonstrated in 1999 at 1.5 μm wavelength region with a tunable range of 40 nm [36]. Through theoretical studies [28], it was observed that flat dispersion can enhance the bandwidth of MI. FOPOs with dispersion engineered fibres have also been investigated. A work in 2003 demonstrated a FOPO with a dispersion flattened fibre generated outputs extend about 350 nm around 1550 nm [37]. The dispersion flattened fibre used in this work had an anomalous dispersion region approximately from 1511 to 1648 nm, and its β_2 and β_3 at 1550 nm were -0.53 ps^2/km and 0.013 ps^3/km, respectively. This work showed the importance of dispersion engineering for developing highly efficient FWM related applications, which become one important aspect of the work in this thesis.

CW FOPOs did not came into existence until 2002 due to the low nonlinearity of the fibres available at that time, which were predominately made from silica glass. The first CW FOPO work involved two fibres, a 100 m long highly nonlinear silica fiber, which had a nonlinear coefficient of 17/W/km, with internal fiber Bragg grating (FBG) written in two ends and a 1km long highly nonlinear fiber with external FBGs connected to the two ends [38]. The 1 km version produced 30% internal conversion efficiency at idler wavelength 1566 nm (100 mW output) when pumped with 700 mW source at 1563. The 100 m version did not produce a very high conversion efficiency due to its short length, but it showed a tunable range extending over 80 nm. The success of this work could be attributed to the high nonlinearity of the fibers used. However, the nonlinearity of step-index silica fibers are limited which indicates the needs of developing MOFs with non-silica glass for FOPO applications.

Besides generation of new frequencies, optically bistable behaviours were discovered in a FOPO [39]. Bistability is a rather common characteristic of nonlinear feedback systems. It refers to a nonlinear steady-state where two stables outputs

correspond to one input. The output state of a bistable system depends on the history of the system, in this case, the previous output from the FOPO. Later studies revealed the relation between MI and the bistable behaviour and was confirmed experimentally [40]. Bistable behaviour in FOPO can be used as an optical flip-flop which is an important discovery for the development of all-optical computing.

Studies of FWM parametric processes in silica step-index fiber revealed the usefulness of the parametric gain in fiber. It can be utilised to construct not only amplifiers but also wavelength convertors, parametric lasers as well as optical flip-flops utilising the bistability. FWM parametric processes can occur in both normal and anomalous dispersion regions, where in the normal dispersion region, significant frequency separation can be achieved between parametric sidebands and pump, in the anomalous dispersion region, broad gain bandwidth can be achieved with degenerated pump configuration. However, due to the limitation of dispersion profile and low nonlinearity of silica step-index fiber, high pump power or long fiber length are usually required, and the maximum frequency shift and the wavelength tunability of the FOPO are limited.

2.3.2 Microstructured optical fibres and FOPAs/FOPOs

Dispersion and nonlinearity of the fibre are both important parameters for the development of FOPAs and FOPOs. Microstructured optical fibres (MOFs) have opened a new era for the FWM parametric application development.

The first MOF-band FOPA was demonstrated in 2001. A 6.1 m long microstructured fibre was pumped with two 150-fs 12 W maximum peak power pulses with 3∼5 nm separation in the anomalous dispersion regime of the fibre [41]. Signal and idler were observed with more than 13 dB gain. To achieve similar results using standard dispersion shifted fiber at the 1550nm wavelength region, 225 m of fibre would be needed. In another work, a MOF taper was used and a wavelength conversion with 730 nm wavelength shift and 10% conversion efficiency was achieved

in only 1.4 cm [42]. Using MOFs, wide tunability can also be achieved. In 2004, a FOPA with 450 nm tunability has been demonstrated through tuning a 60 W peak power 20 ps pump pulses over 10 nm [43].

CW FOPAs have also been demonstrated in MOFs. In one work, a CW FOPA was demonstrated using a 20 m long MOF with two zero dispersion wavelengths at 755 nm and 1235 nm respectively [44]. This work showed the extensive tunability of MOFs based FOPA. Phase-matching was obtained from 500 to 1500 nm over 15 nm pump wavelength tuning range with 100 mW level of pump power.

From these works, the significance of the parametric improvements with MOFs are obvious. The high nonlinearity and the flexibility of dispersion control of MOFs reduces the necessary fibre length by at least an order of magnitude. Meanwhile, the tunability of the MOF-based FOPAs was increased by at least an order of magnitude. Furthermore, CW FOPAs which were difficult to implement in conventional fibre also came into existence with the use of MOFs. The benefits of using MOFs in FOPO are therefore undoubtable.

The world's first MOF based FOPO was constructed based on a 2.1 m long MOF [45]. It was pumped close to its zero dispersion wavelength (ZDW) at 751.8 with 630 fs FWHM pulses. In this FOPO, a 40 nm wavelength tunable range and μW-level outputs were obtained with pump peak power less than 100 W. Another MOF-based FOPO demonstration was pumped in the normal dispersion regime of a birefringent MOF [46]. With only 1 m of fiber, two sets of sidebands of the two orthogonal modes were observed simultaneously.

The combination of high nonlinearity and high dispersion control enables the possibility to construct FOPOs that are compact. Deng, et al. demonstrated a broadly tunable femtosecond FOPO using 65 cm of MOF [47]. In this work, the pump source was a train of 1.3 ps pulses with repetition rate of 36.6 MHz and average power of 260 mW. The FOPO outputs were 460 fs near transform limited pulses with average power more than 400 μm and could be tuned over 200 nm through tuning the pump wavelength across 16 nm. A more recent work demonstrated similar

results with only 3 cm of fibre and tens of mW (∼1 kW peak) pump power [48]. MOF based CW FOPO has also been demonstrated. In one example, 100 m of MOF were used in an all-fibre FOPO configuration operating around 1550 nm [49]. The MOF has a nonlinearity of 16 $W^{-1}km^{-1}$, which is not particularly high, but this FOPO system can produce a 30-dB extinction ratio output signal which has a linewidth of 10-pm and carries 38% of the total output power.

The work outlined above indicates that the advantage of MOFs enabled significant enhancements in the properties of FOPAs and FOPOs. The required fiber length and pump power were reduced for at least one order of magnitude and the frequency shift and wavelength tunability were greatly increased. Until recently, the development of silica MOF FOPA and FOPO had reached a plateau due to transmission and nonlinearity limitation of the silica glass. Soft-glass exhibits broader transmission windows than silica [50] as well as both higher linear and nonlinear refractive indices [51]. Using soft-glass as the base material for MOFs can increase both the transmission window of the fiber and the efficiency of nonlinear effects. One aim of this thesis is to use soft-glass as the base material to design MOFs for FOPOs.

From the literature, it can be found that most works on the design and optimisation for FOPO have focused on controlling the ZDW and the slope of dispersion at the ZDW [52]. The standard approach is to assume that the dispersion of the optical fiber is described by a Taylor-series of the propagation constant, $\beta(\omega)$ (refer to Chapter 4 for details). One can then model the FOPO using a set of coupled wave equations such as Eqs. 4.1.1∼4.1.4. The adaptive range of this combination of approaches is limited for three main reasons. Firstly, a truncated the Taylor series is inadequate in describing the actual dispersion when the frequency shifts between the pump and the signal/idler are large. For large frequency shifts, the importance of higher-order terms of $\beta(\omega)$ increases significantly, and each term must be incorporated into any optimisation procedure. Secondly, the coupled wave equations, which usually only consider the fields at pump, signal and idler wavelengths, are not suited

to simulating complex nonlinear processes with dynamic frequency shifts or large spectral broadening. Thirdly, cascaded FWM cannot be modelled using only four equations, number of equations increases as cascaded effects increases. Furthermore, it is difficult to include Raman scattering into the coupled wave equations, especially when simulating short pulses where the convolution of the Raman response function and the field should not be simplified. To address these points, a different approach is used in Chapter 4.

The review above shows the works of using nonlinear effects in fibres to generate narrow band but tunable light sources. From the next section, nonlinear processes used for generating broadband light sources are reviewed.

2.4 Coherent supercontinuum generation

Supercontinuum (SC) generation is a process of spectral broadening of a high-intensity pulse that occurs as a result of a cascade of nonlinear processes. It was initially observed in bulk glasses [53, 54]. SC generation in fibre occurs as a result of a cascade of nonlinear processes, which could involve self-phase modulation (SPM), cross-phase modulation (XPM), four-wave mixing (FWM), stimulated Raman scattering (SRS), soliton fission, dispersive wave generation [5, 55]. Depending on the pump pulse duration, line width, wavelength, powers, chirp and noise to fibre dispersion and nonlinearity profiles, the nonlinear processes involved in SC generation vary.

Unlike FWM process, it is difficult to write an explicit expression for the gain of a SC generation. However, the process of SC generation can be simulated numerically using a general nonlinear Schrödinger equation Eq. 2.1.17. For cases that the waveguide is symmetric or only one polarisation mode of the waveguide is considered, the scalar form of GNLSE can be used.

2.4.1 SC generation in step-index fibers

The first SC generation in optical fiber was demonstrated in Bell Laboratory in 1974 [56]. SC spectra of approximately 200 nm bandwidth was observed in 19.5 m of silica fibre when pumped with 20-kW 10-ns long 15-nm spectral wide pulses. The total output power was approximately 1 kW and the major nonlinear processes caused this broadening was attributed to SPM and stimulated Raman scattering (SRS).

SPM and SRS dominate the SC generation of normal dispersion pumping. When a fibre is pumped in the anomalous dispersion regime, solitonal dynamics become significant. Fiber soliton related studies started as early as 1973 [57]. Since then, both theoretical and experimental work on solitons include fundamental [57, 58] and high-order solitons [59–61], soliton stabilities and fissions [62–72] were carried out over 20 years. Depending on the dispersion and nonlinearity profile of the fiber and the wavelength, the duration, shape, chirp and power of the pump pulse, the exact soliton phenomena involved in a SC generation differ. However, soliton fission has been identified as one of the most important nonlinear processes in SC generations pumped in the anomalous dispersion regime. Soliton fission [65] describes a process of a pulse or a high-order soliton breaks down into many small lower order solitons. Studies show that this process is particularly sensitive to the noise inside the pulse [70–72] as well as other nonlinear effects such as Raman effects [73, 74] and two-photon absorption [75].

Developing multi-wavelength sources for wavelength-division-multiplexing networks was the original driving force of developing SC sources in step-index fiber at telecommunication bands. A 170 nm wide SC spectrum around 1.3 μm was demonstrated in 450 m of fiber and was employed to support more than 100 wavelength channels with 10 ps pulses separated by 1.9 nm [76]. The pump source in this experiment was a CW mode locked Nd:YLF laser with output of 7.6 ps 100 W peak power pulses at 1.314 μm. Another work by Morioka demonstrated similar SC effects

around 1550 nm region with 3 km of dispersion shifted fiber when pumped with 1.7 W peak power 3.3 ps pulses [77]. In both works, the pump wavelengths were close to ZDWs of the fibers and obtained fairly symmetric broadening, which indicates that the spectral broadening could be originated from MI. The requirements of the wavelength span in these works are not demanding. However, low noise is required in the SC output, which translates into the stability of the SC generation. The studies on MI and soliton dynamics, especially soliton fission processes, indicated that soliton fission processes were unstable and very sensitive to the noise inside the pump pulses [78–80]. This has opened a new area of study to investigate the stability of SC generation which is also known as the pulse to pulse coherence.

2.4.2 SC generation in silica MOFs

The advent of MOFs led to a significant boost in the development of SC generation based sources. MOFs can support high nonlinearity as well as tailoring the dispersion of the fibre to a level that cannot be achieved in conventional step-index dispersion-shifted fibres, such as changing the slope of dispersion and shifting the ZDW wavelength of a silica fiber below 1.28 μm [81–86]. With higher nonlinearity, a similar degree of nonlinear phase ($\gamma P_0 L$) can be achieved in a shorter propagation length. This not only means shorter fibres are required but also indicates that dispersion has less effects on pulse propagation. The temporal overlap of different wavelength components of a broadband pulse is also a deterministic condition to produce nonlinear interactions. Less dispersion effects during pulse propagation indicate longer nonlinear interaction length. Furthermore, certain nonlinear processes such as FWM, require phase matching between different wavelength components, and nonlinear processes such as FWM are important components of SC generation. Being able to enhance nonlinearity as well as tailoring the dispersion made MOFs the best platform for supporting the most efficient SC generation in fibers.

One outstanding work showed a SC generation with bandwidth spanning nearly

two octaves from 400 to 1600 nm in 75 cm of MOF [87]. The MOF was pumped at 770 nm around its ZDW with 100 fs nanojoule pulses. SC generation with longer pulse (sub-nano second) is also easier to realise with MOFs. Another example demonstrated the generation of SC from 460 to 750 nm in 1.8 m of fiber using 0.8 ns 300 nJ pulses pumped at 532 nm [88]. In this example, SC generation was assisted by FWM parametric and Raman processes. Later, similar work also showed a SC generation with wavelength span over an octave with 60 ps pulses [89].

The development of SC in MOFs allowed octave span SC spectra widely accessible for different applications. For this reason, MOF-based SC generation caught significant attention in the early 2000s. Many theoretical/numerical models and experimental work were developed to interpret the broadening mechanism in MOFs [90–99]. Through these studies, the SC generation can be summarised into following categories: (a) short (femto-second and sub 10 pico-second) and long (10s of pico-seond to CW) pulses and (b) normal and near zero/anomalous dispersion pumping. The dominant nonlinear processes are summarised in Table.2.4.1. Similar categorisation can be performed for conventional fibres too.

Table 2.4.1: Summary of the dominant nonlinear processes of SC generations

	Short pulses	Long pulses	Notes
Normal dispersion pumping	SPM	FWM and Raman	With short pulses, FWM and Raman effects also presents. Raman effects includes spontaneous and stimulated Raman effects
Near zero/anomalous dispersion pumping	SPM and soliton	MI and soliton	soliton effects includes soliton fission and soliton Raman shifting

The fast development of SC generation has also led to the development of many applications that are based on SC spectra. Apart from the applications mentioned early as broadband sources for WDM [76, 77], SC sources can also be used for frequency metrology [17, 18, 100], optical spectroscopy [11, 13, 14, 16] and optical imaging [12, 15], etc. The development of applications also extended into the mid-IR wavelength region which is beyond the transmission capability of silica glass. The

practical needs of mid-IR SC sources started the research of non-silica MOFs based SC generation.

2.4.3 SC generation in soft glass MOFs

The broad transmission windows and high nonlinear refractive indices of soft glasses make them the ideal materials for SC generation. Using soft-glass MOFs for SC generation not only shortens the usage of fiber and lowers requirement pump power but also extends the SC spectral span and operational wavelength regions.

SC generation in soft glass MOFs was demonstrated soon after the SC generation in silica MOFs was demonstrated. A spectral span from 350 to 2200 nm was obtained in 75 cm of fiber made of SF6 glass using 100 fs 375 pJ pulses pumped at 1550 nm [101]. Taking advantage of the high nonlinearity of soft glasses, a more than 1.5 times broader spectrum was generated using less than half of the pulse energy comparing to the first silica MOFs SC generation [87]. One year later, another octave-span SC generation was demonstrated using only 200 pJ energy pulse in a MOF made of the same glass [102]. In 2005, a lead silicate SF57 glass based MOF with the highest nonlinearity of the time was fabricated with a nonlinear coefficient of 1860 $W^{-1}km^{-1}$ at 1550 nm [103]. A 600 nm span was obtained with 200 fs 81 pJ pulses. In the same work, an octave span was also demonstrated in a variation of the high nonlinearity fiber with dispersion optimised for 1.06 μm pumping using 130 pJ pulses. Until 2009, the pump pulse had been reduced to 20 pJ for octave-spanning SC generation [104].

Spectral span of SC generation in soft glass MOFs was also been broadened extensively. More than a 2 octave span from 350 to 2200 nm was easily achieved in soft glass MOFs [101]. Using chalcogenide glass based MOFs, SC generation in mid-IR was successfully generation from 2 to 3.6 μm in 1 m of fiber pumped with 100 fs 100 pJ pulses [105]. Further study of SC generation soft glass base MOFs reveal the possibility of generating a SC span from UV (350 nm) to mid-IR (3 μm) in

only 6 mm of fiber [106]. Same year, a SC expands from 800 nm to 4.5 μm was also demonstrated in a few meteors of ZBLAN fiber [107]. A breakthrough was made in 2008, the broadest continuum spectrum at the time span over 4000 nm bandwidth extends from 789 to 4870 nm was measured at 20 dBm below the peak spectral power in only 8 mm of tellurite MOF [108]. And this record was once again broken in 2009. A SC spectrum from UV to 6.28 μm was generated in 2 cm of ZBLAN fiber [109]. This continuum nearly covered the whole transmission spectrum of that ZBLAN glass and become the broadest continuum ever being produced.

Table 2.4.2 summarises the development of SC generation in soft-glass MOFs. The table is divided into three parts. The first part is a list of some significant work with silica MOFs. The second part shows the decrease of pump pulse energy with the developing of SC in MOFs. The last part shows the increase of spectral span with the developing of SC in MOFs. The development shown in the table proved the effectiveness of using soft glass MOFs for SC generation. The required pump power and fibre length were continuously decreased and the bandwidth of the SC was broadened extensively. However, in the previous works, the potentials of using MOFs for SC generation were not fully explored. These potentials can be optimising both dispersion and nonlinearity for large bandwidth and low pump power or, what this work is about to do, optimising dispersion and nonlinearity for large bandwidth and high coherence of the SC spectrum. In the next section, the concept coherence of SC generation is introduced and related works are reviewed.

2.4.4 The coherence of SC outputs

The study of the stability of SC generation can be related to the early work on the soliton stability. The concept of the coherence degradation of SC output was first proposed and studied in 1998 [78]. Coherence is a measure of the correlation properties between two SC pulses. It represents the ability of two SC pulses to interfere hence it can be measured using interferometers [110–113]. The coherence

Table 2.4.2: Development of supercontinuum generation in soft-glass MOFs

Glass	Spectral Range (nm)	L_{Fibre}	λ_{Pump} (nm)	Pulse duration	Pulse Energy	Year	Ref.
Silica	400∼1600	75 cm	770	100 fs	800 pJ	2000	[87]
Silica	460∼750	1.8 m	532	0.8 ns	300 nJ	2001	[88]
Silica	400∼1000	10 m	647	60 ns	40 μJ	2001	[89]
SF57	350∼2200	75 cm	1500	100 fs	375 pJ	2002	[101]
SF6	400∼1750+	30 cm	1560	60 fs	200 pJ	2003	[102]
SF57	600∼1500	50 cm	1060	200 fs	130 pJ	2005	[103]
SF6	600∼1450	4 cm	1060	60 fs	20 pJ	2009	[104]
Chalcogenide	2000∼3600	1 m	2500	100 fs	100 pJ	2005	[105]
SF6	350∼3000	6 mm	1550	110 fs	875 pJ	2006	[106]
ZBLAN	800∼4500	7 m	1553	2 ns	8 μJ	2006	[107]
Tellurite	789∼4870	8 mm	1550	100 fs	1.9 nJ	2008	[108]
ZBLAN	200∼6280+	2 cm	1450	180 fs	36 nJ	2000	[109]

of SC generation also indicates the stability of the SC generation, in another word, the reproducibility of the SC spectrum from pulse to pulse.

Many SC based applications depend on the coherence, especially in frequency metrology where it stabilises optical frequency combs [17, 114–116].

It has been noted that the cause of SC coherence degradation is related to high-order solitons [78] and MI [79]. More specifically, the coherence degradation is reflection of the temporal and spectral differences from pulse to pulse due to these nonlinear effects. Further study showed the coherence degradation in SC is due to both elements and was particularly sensitive to pulse power, during, noise, pump wavelength with respect to ZDW [55, 117–119].

By avoiding soliton-related effects, especially those associated with high-order solitons, and MI, it is possible to obtain high coherent SC. Previous work had demonstrated this [80, 120–122]. However, to obtain high coherence, it is necessary to trade off bandwidth since the main broadening mechanism needs to rely mainly on SPM. In Ref.[80], the coherent bandwidth was about 200 nm. In Ref.[120], this coherent bandwidth was extended to 500 nm. And in 2007, octave-spanning highly coherent SC was generated from 1.0 to 2.2 μm [121] when nearly 4 μm span SC been already existed for a year [107].

From the literature, it seems that simultaneous achievement of broad bandwidth and high coherence in SC generations are rather challenging. It is because many dominant nonlinear processes that lead to broad bandwidth are the main sources of coherence degradation. However, it is still possible to generate broadband coherent SC if the dispersion and nonlinearity profiles of the fibres are carefully designed in a way such that the broadening effects from coherent nonlinear processes are enhanced, and the broadening effects from incoherent nonlinear processes are suppressed. The work in Ref. [121] is an example, but in this work, a piece of conventional fibre was used.

We believe it is possible to further improve the coherence of SC generation if a piece of soft-glass MOF is used. As a part of the aims of this thesis, we will explore different fibre structure and seek out an optimised MOF design using soft-glass to achieve broadband coherent SC generations.

2.5 Summary

In this chapter, we briefly introduced some background theory and reviewed relative literature about the fibre-based optical parametric amplifiers, oscillators and previous work on SC generation in optical fibres. From the literature review, we summarised that by combining soft glass and microstructured fibre design, it is possible to further develop FOPO and SC sources, which include the development of a narrow band tunable light source, a soft-glass MOF based FOPO that operates across a broad spectral span (pumped at telecomm-band 1560 nm and outputs at 880 nm) and a broadband light source, a soft-glass MOF that is capable of generating broadband highly coherent SC pulses.

A review of the parametric amplification process in silica step-index fibers has identified that the key of controlling parametric process in fiber is the ability to tailoring the fibre's dispersion and nonlinearity profiles, especially β_2 and γ values at the pump wavelengths are the most important features. Combining MOFs with

FOPAs and FOPOs greatly extends operational wavelength range and efficiency. However, to date, the impact of this approach has been limited by the transmission window and nonlinearity of silica glass.

Dispersion and nonlinearity profiles of a fiber are also crucial to SC generation. Early studies on SC generation in fiber revealed many dispersion-sensitive nonlinear processes in SC generation. Soliton-related dynamics are such nonlinear processes. They were dominate nonlinear processes of SC generation in the anomalous dispersion and were tightly related to the dispersion properties of the fiber. Many theories were established and formed the bases of future SC related research. In the majority of the works, the importance of fiber ZDWs to SC generation stood out and became the focus and target of the development SC generation in silica MOFs. SC generation in the anomalous dispersion yells MI and soliton fission which are rather sensitive to the noise in the input pulses and causes coherence degradation in the SC output. From literature, to obtain high coherence, the bandwidth of SC was compromised. However, whether and how it is possible to have both SC coherence and bandwidth optimised in MOFs has not been studied.

Soft glass as materials with broader transmission windows and higher nonlinear refractive indices than silica, became more and more important to nonlinear applications. Previous FOPO work was based solely on the use of optical fibers made from silica glass [46, 47, 52, 123–127]. The great improvement of using soft glass MOFs for SC generation highlights the potential of this new platform for future development of nonlinear applications, particularly in the mid-IR spectral region. Using soft glasses for FOPO can enhance conversion efficiency as well as extend the operation wavelength range such as to mid-IR.

Previous studies of SC generation, especially those related to soft glass MOFs, have demonstrated extensive continuum bandwidth. However, the coherence of the SC was not optimised. To achieve high coherence, the SC bandwidth are greatly reduced.

In this work, soft-glass MOFs are designed and optimised for two nonlinear

applications as light sources. One is a FOPO believed to be the first design based on soft-glass that generates 880 nm femtosecond pulses by pumping at telecomm-band 1560 nm as a viable alternative source for the 880 nm femtosecond Ti:sapphire laser. The other is a soft-glass SC source that generation broad and highly coherent supercontinuum.

To achieve the target of this part of the thesis, fibres design and optimisation is required. In this thesis, a genetic algorithm (GA) based fibre design approach is used to overcome the complexity of the nonlinear processes in FOPO and SC generation. The detailed reasons for using GA for fibre design of FOPO and SC generation are introduced in Chapter 4 and 5 respectively. However, the GA itself is not restricted to any specific applications. Therefore, in the next chapter, Chapter 3, GA and how to apply GA for fibre design are introduced first. After that fibre designs for a FOPO and SC generation are shown in Chapter 4 and 5 respectively followed by the fabrication of the designed fibre in Chapter 6 and numerical simulations based on the fabricated fibre structure in Chapter 7.

Chapter 3

Fibre design and genetic algorithms

3.1 Background

In order to construct the target FOPO and SC source, fibres are needed to be designed such that they enhance specific nonlinear processes Although, for FOPO and SC applications, the required nonlinear processes are different, the purposes of their fibre design are still in common. That is the design of fibres with specific dispersion (propagation constant) and nonlinearity profiles. The differences between the two applications are the requirements of different dispersion and nonlinearity profiles, which are introduced separately in Chapter 4 and 5. Here, in this chapter, an efficient and universal fibre designed approach, an approach of using a genetic algorithm for fibre design, is introduced and discussed.

Depending on the complexity of the structure, there could be many parameters of the fibre structure needed to be tuned to achieve required properties. Meanwhile, the conditions for achieving the targets (such as the dispersion and nonlinearity profiles of a fibre) may conflict with each other. For example, to achieve high nonlinearity, usually tight confinement (small core size and large index contrast between core

and cladding) is required. On the contrary, to achieve low and flat dispersion, relative loose confinement is preferred (large core size and small index contrast). For designing a fibre that satisfies both nonlinearity and dispersion properties, a balance must be found, where an optimisation algorithm is needed.

A conventional approach of designing a fibre with certain properties usually follows the following procedures. Firstly, a fibre structure is chosen, which either been selected based on experience or through trial-and-error. Secondly, the structure is parameterised such that fibre properties can be controlled through the structural parameters. Finally, ranges of structural parameter values are tested until the fibre properties match with the targets which depend on the specific application. This design approach works efficiently when the number of tuning parameters is small with respect to the time required for calculation of the fibre properties. Since the total calculation time increases exponentially with the increase of tuning parameters, this design approach is unsuitable for complex problems. However, if a feedback mechanism can be provided in the design procedure that allows the designer to adjust itself to the current situation of fibre properties, it is possible to increase the design efficiency of complex structures. This kind of design approach requires a control algorithm that is running on top of the conventional design approach and provide a supervision of the search of parameters in the design procedure. A genetic algorithm (GA) can be applied to serve as such a mechanism.

3.1.1 Chapter outline

In this chapter, a range of optimisation approaches is reviewed. Based on the reviewed contents, it is justified that a natural optimisation algorithm is needed for the fibre design in this work. Then, natural optimisation algorithms are introduced and the discussion is focused on genetic algorithms. Details of applying GA on MOF design are follow at the end.

3.2 Traditional Optimisation Algorithm

There are many algorithms that can be used to optimise systems, among which traditional "minimum-seeking" algorithms, such as exhaustive search method, analytical optimisation, downhill simplex method [128] and line minimisation method [129] are all well known and widely used optimisation methods that can be applied to fibre design. In this section of the chapter, these optimisation algorithms are reviewed to find out the pros and cons of them.

Exhaustive search methods are the most simple methods to implement but also the most time consuming methods. When applying this type of methods for designing fibre structure, they usually work for most of the situations where there are only few free parameters. However, when the number of free parameter increases, the times required in the calculation increases exponentially. Therefore, when there many free parameters in the fibre structure (such as 6 for our fibre), exhaustive search methods become less efficient and too time-consuming to be used in practice.

Analytical optimisation methods depend on whether the object that needs to be optimised can be expressed in an analytical form. This type of method is most efficient since they find the optimised solutions analytically. There are also a range of methods similar to analytical optimisation methods, which include the minimax theorem [130], linear programming [131], etc. These methods are fast and accurate. However, for fibre design, since no analytical expressions can be given, this type of methods cannot be employed.

Downhill simplex method, line minimisation method and methods developed based on these methods are fast converging and robust. But the solutions of these methods are likely to be converged at local minima. A local minimum is a localised minimum value of a function within a small parameter region (These methods were initial designed to find minimum values. However, the maximum values can also be found using these methods). A local minimum may be the minimum value of the whole parameter space, i.e. it may also be a global minimum, but most of the time,

it is not. To prevent the algorithms giving localised solutions, one normally needs to run the algorithms many times with different initial values. At the end, these methods may not be efficient for complicated problems. And it may require a lot of man power to analyse the solution to determine if it is a global solution and reset proper initial values for the algorithms.

There are also advanced methods that have been developed by combining different methods together to improve the efficiency of designing fibres. For example, a method combining a large scale exhaustive search and an analytical method has been developed [132]. This method samples the whole structural parameter space and interpolates the samples to map out the derivatives of a dispersion profile with respect to each free parameter of the structure. Once the derivatives are found, analytical methods are applied to reconstruct fibre structure with specific dispersion properties. However, a few assumptions were made for this method such as the dispersion of a fibre is a summation of the material dispersion of the fibre material and waveguide dispersion of the fibre structure ($D_{tot} = D_{mat} + D_{gw}$). Also, the efficiency of this method still greatly depends on the complexity of the structure. And the generality of this method has not been proven in practice yet.

The optimisation methods mentioned above have their own advantages, but in the context of designing fibre structures for specific fibre dispersion and nonlinearity profiles, these methods are unsuitable. Later in this chapter and in Chapter 4,5 we discover that the structure needed to be optimised (Fig. 4.2.2) has six free parameters. The linear and nonlinear properties of the target fibre are interlinked through these structural parameters. Furthermore, the optimised structures for FOPO and SC generation are not unique. These features of the fibre design work in this thesis made the traditional optimisation algorithms inefficient.

In the following sections, we describe optimisation procedures inspired by natural phenomena called natural optimisation algorithms and show that these optimisation algorithms can be used efficiently for the fibre design work.

3.3 Natural Optimisation Algorithm

In nature, there are many processes such as biological evolution that can be considered as optimisation processes. Throughout the history, people have tried to mimic these mechanisms to help us solve complex problems. A range of optimisation algorithms were developed including genetic algorithms [133], simulated annealing algorithms [134], particle swarm optimisation algorithms [135], ant colony optimisation algorithms [136], evolutionary algorithms [137], etc. Among them, genetic algorithms are one type of the most developed and widely used natural optimisation algorithms. We choose GAs as the optimisation algorithm for fibre design because its robustness and it has been used for fibre design before [138] so that it usefulness for this work is guaranteed.

A genetic algorithm simulates the natural selection process and optimises systems from a statistical point of view. It evolves a group of test samples gradually towards optimised regions as well as creates new search points to diverge the searching path. This characteristic of the natural optimisation algorithm greatly reduces the chances of converging to localised solutions and enhance the probability of reaching global solutions.

A typical optimisation process with GA can be described as following and illustrated as in Fig. 3.3.1. The optimisation starts with a collection of test samples (i.e. a collection of different fibre structures), referred as a population, and a fitness function. Each sample is referred as an individual which is generated randomly within a preset parameter space. Each individual consists one or more parameters (such as the fibre core diameter in the context of fibre design) where each parameter is referred to as a gene. Every individuals in the population are evaluated using the fitness function which results in a value that quantitatively describes and ranks the properties of each individual. In this way, the fitness values of the individuals reflect how well the individuals are optimised. Once all the individuals are evaluated, a procedure called “mating” will take place, which normally includes three

steps: "pairing", "crossover" and "mutation" [139]. The main purpose of the "mating" process is to exchange genes among the individuals to generate new individuals called "offspring". The offspring will contain the genes from their parents but also differ from them so that they will have different status of optimisation. The detail process of "mating" (in particular, the gene inherited by each of the offspring) determines if and how the new generation will evolve. After the "mating" process, offspring form the new generation are evaluated by the fitness function again. If the fitness values of the new generation reach or exceed a preset target, then the optimisation finishes, otherwise the new generation will go through the same processes again until the target is reached.

The three steps in the "mating" process are the core component of a GA that mimics the nature. In the "pairing" step, two individuals from the collection are selected to form a couple. To avoid any individuals dominating the evolution process and cause the optimisation to fall into localised solutions, or the good genes being lost accidentally, rules are set such that individuals cannot be paired with themselves but can be paired multiple times. The chances that any two individuals will be paired depend on the fitness values of these individuals. If we consider high fitness values to be good solutions, we can arrange for two individuals with high fitness values to have higher probabilities of mating. In this way, good genes will gradually merge together and produce an individual that might reach the optimisation conditions.

In the "crossover" step, the genes of two paired individuals merge together and form new genes of offspring. There are different ways to crossover genes. One way is to partially exchange the gene codes (red) as shown in Table 3.3.1. A section of gene codes from one parent is replaced by the counterpart of the gene from another parent. Depending on how the gene codes are arranged, the section of gene codes that is used for "crossover" may not be necessary contain meaningful information, i.e. a few bits of a complete byte of data, but GAs can still optimise our problem which shows the robustness of the algorithms.

Another way to "crossover" the genes is to exchange genic information numeri-

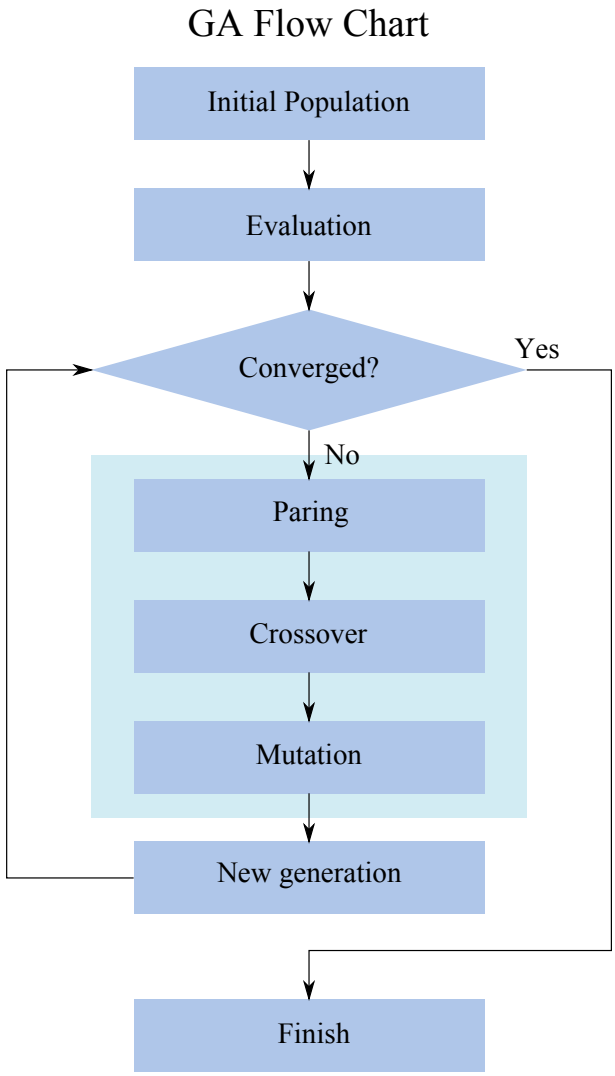

Figure 3.3.1: Initial fibre structure with all elements parameterised.

Table 3.3.1: Crossover example: partial exchange of gene codes

	Parents							Offspring						
Gene codes	a	b	c	d	e	f	g	a	b	c	**k**	**l**	f	g
	h	i	j	k	l	m	n	h	i	j	**d**	**e**	m	n

cally. Different portions of numerical value are taken from parents to form offspring as shown in Eq. 3.3.1 where G_{pn}, n = 1,2 represent the gene codes two parents and G_{on}, n=1,2 represent the offspring. The second method is normally used when the gene codes cannot be simply exchanged through the first method. For example, when the gene codes are represented in the form of floating-point numbers in a computer, the data in memory is not stored in a way how it is naturally presented [140]. Change of any bit may result in a significant and undesirable change in its numerical value.

$$\begin{aligned} G_{o1} &= \alpha \times G_{p1} + (1-\alpha) \times G_{p2} \\ G_{o2} &= (1-\alpha) \times G_{p1} + \alpha \times G_{p2} \end{aligned} \tag{3.3.1}$$

Apart from the "crossover" step, GA also simulates "mutations" of the genes that occur in nature. "Mutations" introduce sudden changes in the gene codes that cause certain individuals to jump away from the trace of the convergence of the whole collection, which increases the opportunities for finding the global solution.

The choice of a fitness function does not need to reflect the physical process of that is to be optimised. However, certain considerations have to be taken to ensure that the GA can solve the problem. As an example, imagine an arbitrary two-dimensional system such as Eq. 3.3.2 (Fig. 3.3.2). In this system, $x, y \in R$ are two free parameters. One wants to find out what combination of x, y that correspond to the maximum output of this system. The exact expression of this system (Eq. 3.3.2) is presumed to be unknown. This is equivalent to the situation that the analytic expression of a certain nonlinear process is unknown. However, there are two features identified as A and B of the system can be measured, although the exact expressions of A, B are also unknown. In the case of fibre design, A and B can be the fibre dispersion (D) and the inverse of nonlinearity ($\frac{1}{\gamma}$), respectively. If it is known that by minimising A and B, the system can give the maximum output, then the fitness function for this problem can be defined using Eq. 3.3.4 or Eq. 3.3.5. However, in this example, Eq. 3.3.4 is a better choice because Eq. 3.3.5 tends to be

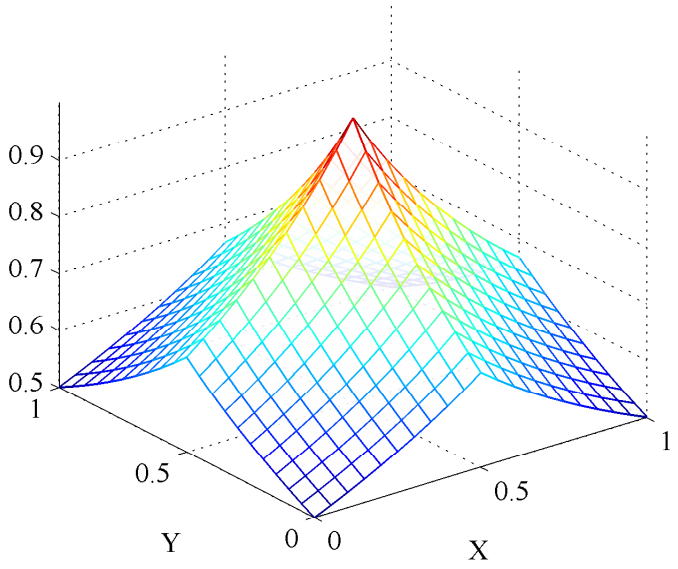

Figure 3.3.2: An example the fitness function.

dominant by the smaller component among A and B which will cause difficulty for GA to converge on both of them.

$$F = \frac{1}{1 + |0.5 - x| + |0.5 - y|} \tag{3.3.2}$$

$$A = 0.5 - x \qquad B = 0.5 - y \tag{3.3.3}$$

$$F' = \frac{1}{|A| + |B|} \tag{3.3.4}$$

$$F'' = \frac{1}{|A|} + \frac{1}{|B|} \tag{3.3.5}$$

For this particular example, the convergence of the population is shown in Fig. 3.3.3. Each circle in Fig. 3.3.3 represents an individual. The colour and size of the circles indicate the fitness value. Big and red circles represent large fitness values, and small and blue circles represent small fitness values. As the number of

generations increases, one can see that the population converges to the centre of the plot ($x = 0.5$, $y = 0.5$), and the fitness values increases steadily.

In the case of fibre design and optimisation, the fitness function will of course differ from this example. However, if the definition of the fitness function is suitable for the problem, similar convergence behaviour should be observed.

In the next section, the method of applying a GA to fibre design is showed.

3.4 Genetic Algorithm and Optical Fibre Structure Design

In the context of optimising optical fibre structures for particular nonlinearity and dispersion profiles, an initial fully parameterised structural topology of fibre is required for populating the initial generation. Each gene of an individual in the population corresponds to a structural parameter in the fibre cross-section. In this work, the fibres are design for nonlinear applications (FWM and SC generation), which closely related to the nonlinearity and dispersion profiles of the fibre, i.e. the dispersion and nonlinearity profiles of fibres determine the behaviour of the nonlinear processes in these fibres. Therefore, the fitness function of the GA includes a combination of nonlinearity and dispersion properties of the fibre.

The initial design of the structure is inspired by suspended nano-wires (also called wagon-wheel fibres shown in Fig. 3.4.1 top-left) and fibres structured to contain rings of air holes (referred as holey structure, shown in Fig. 3.4.1 top-right). The suspended nano-wires, due to their small core sizes and high core-clad index contrasts, are capable of provide high confinement (and low confinement loss) to the light propagating inside them, which lead to small effective mode area and high intensity. By varying the core size of these suspended nano-wires, a critical size can be found for a wavelength at which the mode area of the light is minimised for the nano-wire structures and therefore, achieve the highest peak intensity as well as the

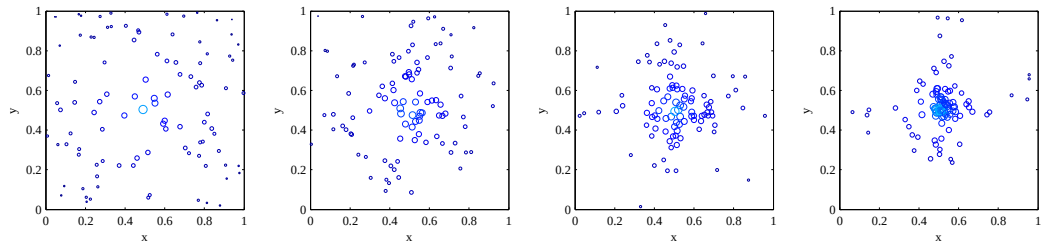

(a) Generation 1 (b) Generation 2 (c) Generation 3 (d) Generation 4

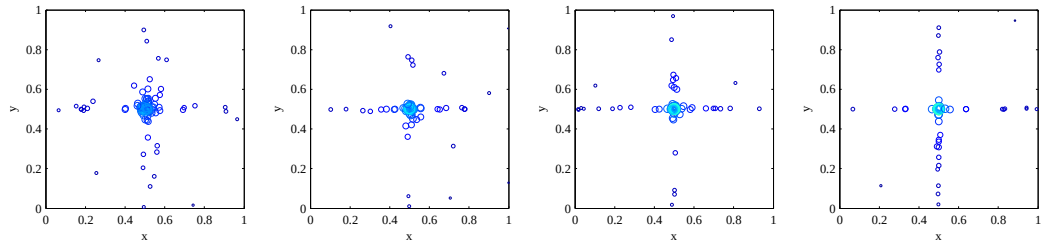

(e) Generation 5 (f) Generation 6 (g) Generation 7 (h) Generation 8

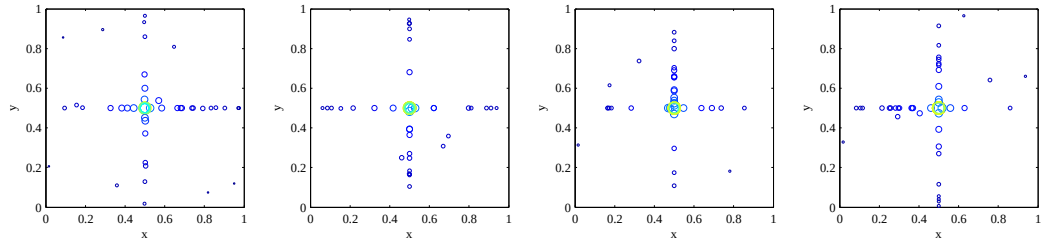

(i) Generation 9 (j) Generation 10 (k) Generation 11 (l) Generation 12

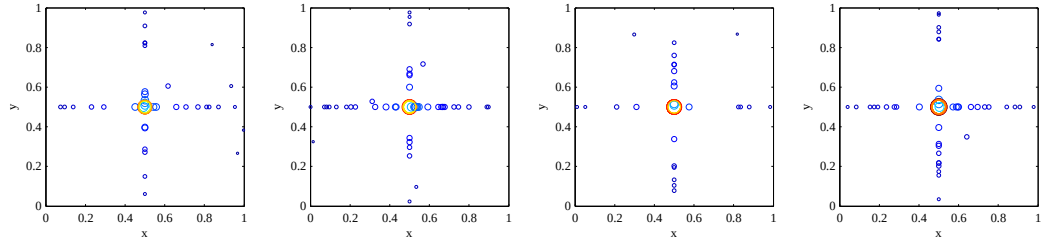

(m) Generation 13 (n) Generation 14 (o) Generation 15 (p) Generation 16

Figure 3.3.3: An example shows the convergence of the population under the influence of the fitness function Eq. 3.3.2.

highest nonlinearity.

The holey structure, on the other hand, enables the dispersion properties of the fibre to be tailored. The holey structure allows mode field to extend into the gaps between the air holes. The amount of the field that extends into the gaps depends on the wavelength of the field and is closely related to the effective refractive index of that mode. This is the origin of the dispersion tailoring ability of holey structured fibres. Previous reports already demonstrated the capability of tailoring dispersion in holey structure [141]. Here in this work, the two classes of structure are merged together to form the initial structure for GA (Fig. 3.4.1 bottom) to allow the high nonlinearity of a suspended core fibre to be combined with the holey structure's capacities for dispersion tailoring.

The structure in the bottom of Fig. 3.4.1 is defined by a set of parameters R1, R2, R3, R4, R5, r1, r2, r3, L1 and L2. Depending on the values chosen for these parameters, this structure can vary from a suspended nano-wire structure (when the core region (R3) is small) to hexagonal lattice structure (when inner six holes are at a similar size and sit at the middle of the core region). In order to increase the efficiency of this GA calculation, only R1, R3, R4, r1, r2 and L1 are set as free parameters. The remaining parameters are set as functions of the free parameters: $R2 = R1$, $R5 = (11/12 \times R4 + 1/12 \times R3 + 1/2 \times L1)/cos(\pi/6)$, $r3 = 1/2 \times (L1 + L2)$ and $L2 = 0.1 \times R3$.

The reason why only 6 free parameters are chosen is due to the consideration of the computational time. Each free parameter is a degree of freedom. To let GA converge to a solution in all degrees of freedom, a large population is required, which determines the convergence of the optimisation process. A general rule that can be applied to any GA is that the more degrees of freedom in the system, the larger size of population is the required. Although, the exact size of population also closely related to the details of the system one want to optimise, it is always the best to choose free parameters only where they are necessary. In this work, after a few tests, we choose a population of 1000 to cooperate with 6 free parameters.

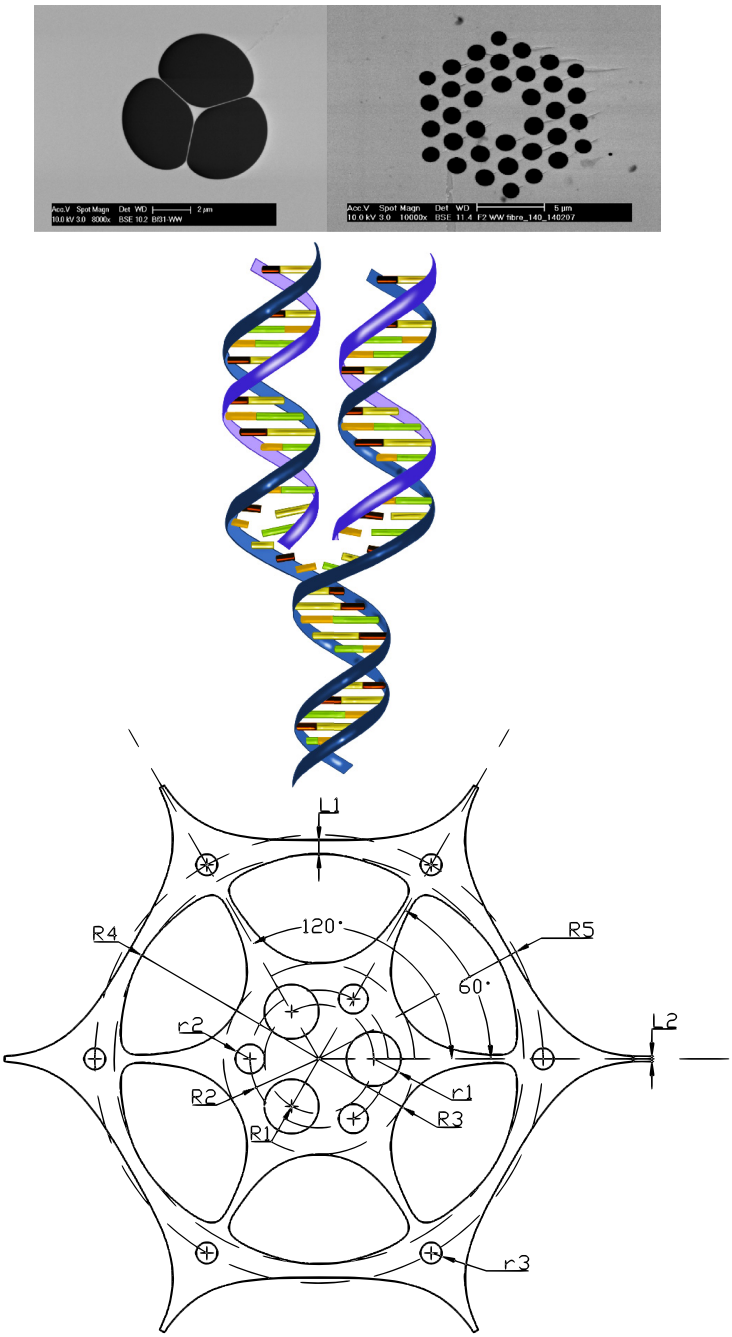

Figure 3.4.1: A genetic algorithm is used to combine the optical properties of two different types of fibres

Table 3.4.1: Example of the fitness list for the "mating" process

Individual	Fitness	Re-scaled fitness	Region
1	100.0	0.1	0.1
2	200.0	0.2	0.3
3	300.0	0.3	0.6
4	400.0	0.4	1.0

The evaluation of a population requires a series of complicated calculations. To obtain dispersion and nonlinearity profiles, one needs to first solve the eigenmodes of the fibre for a range of wavelengths. An commercial solver, COMSOL Multiphysics, is used to accomplish this task. Once the eigenmodes are found, effective refractive indices and mode fields are obtained for calculating the dispersion and nonlinearity of the fibres. A fitness function is going to be defined using the dispersion and nonlinearity data. The detailed form of the fitness function depends on specific situations.

To pair the individuals for "mating", a list is constructed which consists all the fitness values of the population. This list of fitness is then normalised such that the sum of the fitness values is equal to 1 (see Table 3.4.1). In this way, each re-scaled fitness in the list corresponding to a percentage between 0 and 100% and occupies a specific "region" in the list. When "pairing" individuals, pairs of random numbers between 0 and 1 are generated. Each random number corresponds to a "region" in the list that belongs to an individual. For example, if the random number is 0.5, it will corresponding a region $(0.3, 0.6]$ which corresponding to Individual 3. In this way, the corresponding individual is chosen for "pairing". If the same individuals were chosen, one of them will be discarded and a new random number will be generated until two different individuals are chosen for "pairing".

After "pairing" the whole collection, the genes of the individuals in each pair are

crossed over. Equation 3.3.1 is used with parameter α randomly generated between 0 and 1. During this process, an additional random modification ("mutation") is made. This random modification occurs once every 5 times (a rate of 20%) for each individual. When the "mutation" occurs, only one gene is altered, and the changed is completely random. A "mutation" rate of 20% is chosen after a few tests. The "mutation" rate should be low enough that the convergence of population is not sensitive to it. Otherwise, too high "mutation" rate could result in failures of convergence. However, the existence of mutation is important that it provides a chance to extend GA's search region as well as avoid failure of convergence due to localised minima.

With a carefully defined of the fitness function, convergence should be observed as the number of generation increases. Occasionally a GA may fail to converge. When this occurs, one needs to examine the fitness function and the parameter space. A number of selections may be needed before a good fitness function can be identified. As mentioned earlier, GAs optimise the collection statistically, which means there may be a range of fibre structures satisfy the target requirements. By studying this range of structures, one may obtain information such as structural sensitivity related to fibre dispersion and nonlinearity, hence understand the fabrication challenges (see Chapter 5 for details). This is another advantage of using GA for fibre design.

The details of designing fibre for FOPO and SC generation are presented in Chapter 4 and 5, respectively. In Chapter 4, a GA is applied directly to optimise the efficiency of the parametric process. In Chapter 5, the GA technique introduced in this chapter is combined with a simplified model to exclude the time-consuming pulse propagation model out of the GA loop. Both work show great effectiveness of GA in fibre design work.

Each evaluation in GA takes approximately 20 minutes which including solving the dispersion and nonlinearity values for a fibre structure at three wavelengths (see details in Chapter 4&5). Assuming the population size is 1000 and it will take 10 generations before results can converge. The total amount of time required will be

approximately 20 weeks. To shorten the modelling period, we must apply a parallel computational implementation to the GA. A GA program was written in C/C++ which provides a convenient environment for interfacing with other programs, in this case COMSOL Multiphysics and MATLAB. This GA program distributes evaluation tasks across multiple CPU cores and computers. This allows the calculations to finish in a small time frame.

3.5 Summary

In this chapter, an introduction to a GA has been given, which is used to design fibres in Chapter 4 and 5. A brief review of conventional optimisation algorithms including "minimum-seeking", exhaustive search, analytical optimisation, downhill simplex and line minimisation methods are not the most efficient methods to be applied to fibre design in this work. On the contrary, GAs as a type of natural optimisation algorithm has the ability of handle complicated problem such as fibre structure design easily. A general introduction of GAs provided the background of how GAs work and how it can be implemented for fibre design. At the end of this chapter, we pointed out that a distributed GA program is needed for this work to reduce the research time circle to a reasonable level.

In Chapter 4 and 5, when GAs are applied to design fibres for FOPO and SC generation, the details on the definition of fitness functions and outputs of GA are given correspondingly.

Chapter 4

Four-Wave Mixing

In Chapter 3, a fibre design approach that employs a genetic algorithm (GA) is introduced. But before a GA can be applied to design fibres for FOPOs. A fitness function is needed to be defined. To do so, background theory of the core nonlinear process of any FOPOs, the FWM nonlinear process, is introduced.

4.1 Background

FWM process can be described using coupled wave equations [5]. In the scalar form, four coupled equations representing the four waves. Equations 4.1.1∼4.1.4 are one example [5].

$$\frac{dA_1}{dz} = i\left[\left(\gamma(\omega_1)\left|A_1\right|^2 + 2\sum_{k\neq 1}\gamma_k(\omega_1)\left|A_k\right|^2\right)A_1 + 2\gamma_c(\omega_1)A_2^* A_3 A_4 e^{i\Delta kz}\right], \quad (4.1.1)$$

$$\frac{dA_2}{dz} = i\left[\left(\gamma(\omega_2)\left|A_2\right|^2 + 2\sum_{k\neq 2}\gamma_k(\omega_2)\left|A_k\right|^2\right)A_2 + 2\gamma_c(\omega_2)A_1^* A_3 A_4 e^{i\Delta kz}\right], \quad (4.1.2)$$

$$\frac{dA_3}{dz} = i\left[\left(\gamma(\omega_3)\left|A_3\right|^2 + 2\sum_{k\neq 3}\gamma_k(\omega_3)\left|A_k\right|^2\right)A_3 + 2\gamma_c(\omega_3)A_4^* A_1 A_2 e^{-i\Delta kz}\right], \quad (4.1.3)$$

$$\frac{dA_4}{dz} = i\left[\left(\gamma(\omega_4)\left|A_4\right|^2 + 2\sum_{k\neq 4}\gamma_k(\omega_4)\left|A_k\right|^2\right)A_4 + 2\gamma_c(\omega_4)A_3^* A_1 A_2 e^{-i\Delta kz}\right]. \quad (4.1.4)$$

where, A_k, $k = 1, 2, 3, 4$ are the amplitudes of the four waves, γ's are the nonlinear coefficients and $\Delta k = \beta^{(3)} + \beta^{(4)} - \beta^{(1)} - \beta^{(2)}$ is the phase-mismatch of the four waves and βs are the propagation constants.

When the following approximations are applied, one can reduce the equations and obtain a gain expression for the signal and idler waves ($\omega^{(3)}$ and $\omega^{(4)}$, assuming $\omega^{(1)}$ and $\omega^{(2)}$ are pump waves). The approximations are 1) the spacial overlap of the electric fields of the four waves are the same which leads to $\gamma(\omega) = \gamma_k(\omega) = \gamma_c(\omega)$, 2) the differences in nonlinear coefficients at different frequencies are small which leads to $\gamma(\omega) = \gamma$ where γ is the average nonlinear coefficient of the four $\gamma(\omega)$ and, 3) pump waves are not depleted during the process. With these approximations, one can obtain the parametric gain for the signal and idler waves as

$$g = \sqrt{\left[2\gamma \left(P_1 P_2\right)^{\frac{1}{2}}\right]^2 - \left(\kappa/2\right)^2}, \tag{4.1.5}$$

$$\kappa = \Delta k + 2\gamma \left(P_1 + P_2\right) = \beta^{(3)} + \beta^{(4)} - \beta^{(1)} - \beta^{(2)} + 2\gamma \left(P_1 + P_2\right). \tag{4.1.6}$$

where $P_k = |A_k|^2$, $k = 1, 2$ are the power of the two pumps.

In the cases where the two pumps have the same frequency $P_1 = P_2 = 1/2P_0$. The FWM process is called degenerate FWM also referred as scalar parametric modulation instability (MI) [142]. Since MI was only observed and studied in the anomalous dispersion regime until 2003 [46], MI is more commonly referred as degenerate FWM pumped in the anomalous dispersion regime.

The degenerate FWM parametric gain can be written as

$$g = \sqrt{\left(\gamma P_0\right)^2 - \left(\kappa/2\right)^2}, \tag{4.1.7}$$

$$\kappa = \beta_s + \beta_i - 2\beta_p + 2\gamma P_0. \tag{4.1.8}$$

where $\beta_{s,i,p}$ are the propagation constants at the signal, idler and pump frequencies respectively. The maximum parametric gain exists when $\kappa = 0$. Therefore, in the rest of the work, κ is referred to as the FWM phase-mismatch and $\kappa = 0$ as the FWM phase-match condition.

The parametric gain and the phase-mismatch within the parametric gain imply two conditions of the wavelengths of the four waves. Firstly, the frequency of the four waves must follow the law of energy conservation. One or more photons annihilate and generate new photons at other frequencies but their total energy kept the same. Secondly, the wave vectors (or propagation constants) of the four waves are confined within a limited wavelength range that is determined by the peak power of pumps, fibre nonlinearity and dispersion profiles. This wavelength range is referred as parametric bandwidth. When the law of energy conservation is applied, Δk is determined by the dispersion property of the fibres.

From equations above, it can be concluded that FWM processes are mainly determined by the parametric gain. To design fibres for FWM-based nonlinear applications is usually equivalent to design the parametric gain profile, where in the parametric gain, phase matching and fibre nonlinearity are the two main characteristics that determine the wavelengths of the four waves and the maximum value of the gain, respectively.

4.1.1 Parametric bandwidth and frequency shift

For designing fibres for FOPOs or any other FWM-related applications, knowing the peak frequency and width of the parametric gain is an essential guideline. The peak frequency of the FWM gain can be defined at the frequency of the maximum gain by setting $\kappa(\Omega) = 0$, where $\Omega = \omega - \omega_0$ is the frequency shift with respect to the central frequency ω_0 of the pump pulse, and $\Omega_s = -\Omega_i = \Omega$. Taking βs to the fourth order, one can rewrite κ as

$$\kappa = \beta_2\Omega^2 + \frac{\beta_4}{12}\Omega^4 + 2\gamma P_0. \tag{4.1.9}$$

The solutions of $\kappa(\Omega^2) = 0$ are,

$$\Omega^2 = -\frac{6}{\beta_4}\left(\beta_2 \pm \sqrt{\beta_2^2 - \frac{2}{3}\gamma P_0\beta_4}\right). \tag{4.1.10}$$

Depends on the exact value of β_2 and β_4, Ω^2 can be divided into regimes:

$$\Omega^2 = \begin{cases} \frac{6}{|\beta_4|}\left(\sqrt{\beta_2^2 + \frac{2}{3}\gamma P_0 |\beta_4|} + |\beta_2|\right), & \beta_4 < 0, \beta_2 > 0, \\ 2\sqrt{\frac{6\gamma P_0}{|\beta_4|}}, & \beta_4 < 0, \beta_2 = 0, \\ \frac{6}{|\beta_4|}\left(\sqrt{\beta_2^2 + \frac{2}{3}\gamma P_0 |\beta_4|} - |\beta_2|\right), & \beta_4 < 0, \beta_2 < 0, \\ \frac{6}{|\beta_4|}\left(|\beta_2| \pm \sqrt{\beta_2^2 - \frac{2}{3}\gamma P_0 |\beta_4|}\right), & \beta_4 > 0, \beta_2 < 0\ . \end{cases} \tag{4.1.11}$$

As one can see, the frequency shifts of the sidebands are bigger in the normal dispersion regime ($\beta_2 > 0$) than in the anomalous regime($\beta_2 < 0$). In addition, if $\beta_4 > 0$ in the anomalous dispersion regime, multiple pairs of sidebands are possible to appear. If one expand Ω into Taylor series and only keep the terms to the zero order of β_4, simple approximate solutions of Ω can be obtained:

$$\Omega \approx \begin{cases} \pm\sqrt{\frac{2\gamma P_0}{|\beta_2|} + 12\left|\frac{\beta_2}{\beta_4}\right|}, & \beta_4 < 0, \beta_2 > 0, \\ \pm\sqrt{2}\sqrt[4]{\frac{6\gamma P_0}{|\beta_4|}}, & \beta_4 < 0, \beta_2 = 0, \\ \pm\sqrt{\frac{2\gamma P_0}{|\beta_2|}}, & \beta_4 < 0, \beta_2 < 0, \\ \pm\sqrt{\frac{2\gamma P_0}{|\beta_2|}}, & \beta_4 > 0, \beta_2 < 0 \text{ and } \beta_2^2 > |\beta_4|\gamma P_0, \\ \pm\sqrt{12\left|\frac{\beta_2}{\beta_4}\right| - \frac{2\gamma P_0}{|\beta_2|}}, & \beta_4 > 0, \beta_2 < 0 \text{ and } \beta_2^2 > |\beta_4|\gamma P_0. \end{cases} \tag{4.1.12}$$

The last equation in Eq. 4.1.12 corresponds to a second pair of sidebands that appear when β_2^2 is much larger than $|\beta_4|\gamma P_0$, which, however, have not been seen in practice [5]. If we ignore this case, the frequency shift of FWM sidebands can be summarised as following. In the normal dispersion regime, the FWM frequency shift is approximately $\sqrt{\frac{2\gamma P_0}{|\beta_2|} + 12\left|\frac{\beta_2}{\beta_4}\right|}$, which is mainly determined by β_2 and β_4 and usually large compared to that pumped in the anomalous dispersion regime. In the anomalous dispersion regime, the frequency shift is approximately $\sqrt{\frac{2\gamma P_0}{|\beta_2|}}$,

which is mainly determined by pump power P_0 and β_2 and usually small compared to that pumped in the normal dispersion regime (see examples in Chapter 4).

The bandwidth of the parametric gain can be approximated by setting $g^2(\Omega) = 0$ and calculate the width between its roots $|\Omega_1 - \Omega_2|$ with Ω_1, Ω_2 as a pair of roots of $g(\Omega) = 0$. If one also take β coefficients to the fourth order, the following solutions can be found. Firstly, for Ω^2, one can have,

$$\Omega^2 = \begin{cases} -\frac{6}{\beta_4}\left(\beta_2 \pm \sqrt{\beta_2^2 - \gamma P_0 \beta_4}\right), \\ -\frac{6}{\beta_4}\left(\beta_2 \pm \sqrt{\beta_2^2 - \frac{1}{3}\gamma P_0 \beta_4}\right). \end{cases} \tag{4.1.13}$$

This equation can also be divided into following regimes.

$$\Omega^2 \approx \begin{cases} \frac{6}{|\beta_4|}\left(|\beta_2| + \sqrt{\beta_2^2 + a\,|\beta_4|\,\gamma P_0}\right), & \beta_4 < 0, \beta_2 > 0, \\ 6\sqrt{a\frac{\gamma P_0}{|\beta_4|}}, & \beta_4 < 0, \beta_2 = 0, \\ -\frac{6}{|\beta_4|}\left(|\beta_2| - \sqrt{\beta_2^2 + a\,|\beta_4|\,\gamma P_0}\right), & \beta_4 < 0, \beta_2 < 0, \\ \frac{6}{|\beta_4|}\left(|\beta_2| \pm \sqrt{\beta_2^2 - a\,|\beta_4|\,\gamma P_0}\right), & \beta_4 > 0, \beta_2 < 0, \end{cases} \quad a = 1 \text{ or } \frac{1}{3}. \tag{4.1.14}$$

If one expand Ω and only keep the terms to the zero order of β_4, then one can have

$$\Omega = \begin{cases} \pm\sqrt{\frac{\gamma P_0}{a\,|\beta_2|} + 12\left|\frac{\beta_2}{\beta_4}\right|}, & \beta_4 < 0, \beta_2 > 0, \\ \pm\sqrt{6}\sqrt[4]{a\frac{\gamma P_0}{|\beta_4|}}, & \beta_4 < 0, \beta_2 = 0, \\ \pm\sqrt{\frac{\gamma P_0}{a\,|\beta_2|}}, & \beta_4 < 0, \beta_2 < 0, \\ \pm\sqrt{\frac{\gamma P_0}{a\,|\beta_2|}}, & \beta_4 > 0, \beta_2 < 0 \text{ and } \beta_2^2 > |\beta_4|\,\gamma P_0, \\ \pm\sqrt{12\left|\frac{\beta_2}{\beta_4}\right| - \frac{\gamma P_0}{a\,|\beta_2|}}, & \beta_4 > 0, \beta_2 < 0 \text{ and } \beta_2^2 > |\beta_4|\,\gamma P_0. \end{cases} \quad a = 1 \text{ or } \frac{1}{3}. \tag{4.1.15}$$

Each solution in Eq. 4.1.15 corresponds to a pair sidebands peaked at frequencies according to Eq. 4.1.12 and the bandwidth can be calculated using $|\Omega_1 - \Omega_2|$. Finally, the FWM parametric bandwidth is given as

$$W = \begin{cases} \dfrac{\gamma P_0}{2\left|\beta_2\right|}\sqrt{\left|\dfrac{\beta_4}{3\beta_2}\right|}, & \beta_4 < 0, \beta_2 > 0, \\ \sqrt{2}\left(\sqrt[4]{3}-1\right)\sqrt[4]{3\dfrac{\gamma P_0}{\left|\beta_4\right|}}, & \beta_4 < 0, \beta_2 = 0, \\ \left(\sqrt{3}-1\right)\sqrt{\dfrac{\gamma P_0}{\left|\beta_2\right|}}, & \beta_4 < 0, \beta_2 < 0, \\ \left(\sqrt{3}-1\right)\sqrt{\dfrac{\gamma P_0}{\left|\beta_2\right|}}, & \beta_4 > 0, \beta_2 < 0 \text{ and } \beta_2^2 > \left|\beta_4\right|\gamma P_0, \\ \dfrac{\gamma P_0}{2\left|\beta_2\right|}\sqrt{\left|\dfrac{\beta_4}{3\beta_2}\right|}, & \beta_4 > 0, \beta_2 < 0 \text{ and } \beta_2^2 > \left|\beta_4\right|\gamma P_0. \end{cases} \tag{4.1.16}$$

It is clear that the smaller β_2 the broader bandwidth for all dispersion regimes. In addition to that, in the normal dispersion regime, bandwidth reduces faster with the increase of β_2 than in the anomalous dispersion regime and this results in an overall view of narrower bandwidth in the normal dispersion regime than in the anomalous dispersion regime. An example can be found in Fig. 4.2.8. In previous reports, similar work on fibre parametric gain peak and bandwidth were also studied [23, 46, 142, 143], but the work here combines the bandwidth and the peak frequency of the gain in both the normal and anomalous dispersion regimes together.

Based on the theory introduced here and the introduction of fibre design using GAs in Chapter 3, a soft-glass MOF based FOPO pumped by telecomm-band 1560 nm sources and outputting 880 nm femtosecond pulsed is designed and studied in this chapter.

4.1.2 Chapter outline

In the rest of the chapter, the details of choosing a suitable fitness function for the GA model is discussed first. Then a review the GA results with be given with the study of the optical properties of the optimised structure. Using the dispersion and

nonlinear profiles of the optimised structure, a FOPO configuration is proposed and its behaviour is modelled using a pulse propagation method. The FOPO is studied by considering two key aspects, seed synchronisation and feedback power ratio, to find optimum parameters for highest FOPO output power and closest to transform limited pulses. Finally, the chapter is summarised and the results are discussed.

4.2 Fiber design and genetic algorithms

To design a MOF for a FOPO, one needs to consider a variety of things which can be categorised into two aspects.

The first thing need to be considered is the optical properties of the fibre. The theory described in Section 4.1 gives an insight of what fibre properties are needed to be controlled in order to design a fibre structure for the FOPO. In previous work, FOPO design mainly focused on the ZDW of the fibre and the slope of dispersion at the ZDW. It is reasonable to consider these two features because they are related to the gain peak frequency and gain bandwidth (see Section 4.1.1). However, to fully optimise a fibre for a FOPO, the considerations need to be taken at a more fundamental level. That is the light generated through any given FWM process is determined by

1. the phase-mismatch (κ), which determines the frequency of the new generated light,

2. the parametric gain (g) and interaction length, which determines the output power.

When designing a FOPO, the frequency of the newly generated light is usually considered as the first priority, which determines the required phase-mismatch κ for a given pump frequency. However, κ is a function of γ and pump power, which allows κ to be varied within a limited range. κ is also part of parametric gain. It appears that to optimise the emerge conversion of the FOPO, the two major free

parameters are the parametric gain and interaction length. However, in practice, these two parameters are not completely free. Fig 4.2.1 shows the relation between different properties of a fiber that related to the FWM process including nonlinearity ($\gamma(\omega)$), dispersion ($\beta(\omega)$), phase matching ($\kappa(\beta, \gamma)$), gain ($g(\kappa, \gamma)$) and walk-off between pump and signal pulses (related to $\beta_1(\omega)$), where the walk-off determines the interaction length. All of these properties are correlated to each other at some degree. Dispersion β has to be tuned to maximise g and minimise walk-off. β_1 is the first-order derivative of β. Gain g is a function of both κ and γ, and κ is a function of γ and β. Dispersion β and nonlinearity γ are linked through fibre structure. To reverse engineer the dispersion and nonlinearity profiles to satisfy any design target, such as maximising g and minimising walk-off for a given κ, is not straightforward.

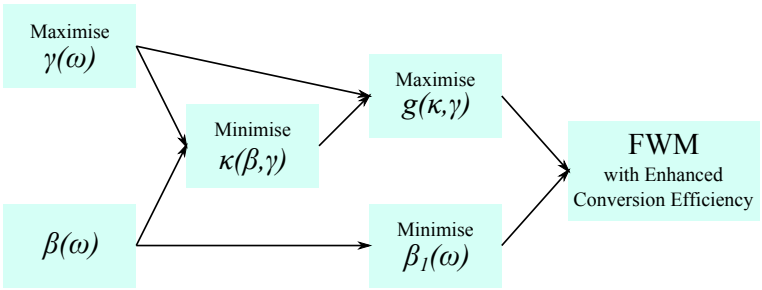

Figure 4.2.1: The relations between variables that are related to FWM process and how to enhance FWM process. γ nonlinearity, β dispersion, κ phase-matching condition, g parametric gain, β_1 related walk-off.

Secondly, it is crucial to design a structure that can be fabricated. One needs to consider the limitation of the smallest feature in fibre preform and the strength of preform so that it can be handled and draw into fiber. To link the fabrication limitations into the procedure of design fibre dispersion and nonlinearity profiles is also not straightforward.

To overcome the design difficulty and increase efficiency, a Genetic Algorithm (GA) based method is used in this work to optimise the design parameters of optical fibers. The details of GA and how it can be applied for fibre design is introduced in

Chapter 3

As discussed in Chapter 3, to design a FOPO using a GA, a suitable fitness function needed to be defined. To do so, the gain of the degenerate FWM 4.1.7 is considered first. Two features can be found that tightly related to any degenerate FWM process:

1. The maximum gain, which maximises when $\kappa = 0$ with $g_{\kappa_0} = \gamma P_0$.

2. The signal and idler wavelengths. According to energy conservation law, two pump photons convert into one signal and one idler photons with $2\omega_p = \omega_s + \omega_i$ where $\omega_{p,s,i}$ are the angular frequencies of the signal, idler and pump fields.

Maximising the conversion efficiency of a FOPO requires maximising the nonlinear interaction gL, where L is the interaction length. Long interaction length is one advantage of fiber based FOPO devices. However, not all the fiber length can contribute to the nonlinear interaction. This is due to both the fiber loss and walk-off between signal, idler and pump fields. The fiber confinement loss can be controlled through fibre design but the material loss is unchangeable, and thus walk-off is the most significant factor in the design that limits the useable fiber length. It is particularly important for short pulses such as femtosecond pulses. Thus the group velocities β_1^{-1} (where $\beta_1 = \partial\beta/\partial\omega$) of pump, signal and idler pulses also must be considered in the fitness as a walk-off factor (details are provided later in this section).

Since gL is needed to be maximised, the most straightforward way to define the fitness function is to use gL. However, with this definition, the fitness will be capped by $\gamma P_0 L$. This result can cause difficulties for GA to convergence when the fitness values are close to $\gamma P_0 L$. Therefore, instead of using gL directly, following fitness function F is chosen to maximise γ and minimise both κ and walk-off which is defined as $\Delta\beta_1 = \beta_{1,s} - \beta_{1,p}$. It is worth mentioning that this definition of fitness function is not unique. Other definitions may also perform same functionality.

$$F = \frac{\gamma}{|\kappa| \cdot |\Delta\beta_1|}. \tag{4.2.1}$$

From a practical perspective, the fitness function F can converge to extremely small values of $|\kappa|$ or $|\Delta\beta_1|$ since either of them will lead to extremely large fitness value. This means, using this fitness function directly, the GA can converge to $|\kappa| = 0$ only or $\Delta\beta_1 = 0$ only and neither of them is close to the most efficient FWM process. To avoid this undesirable behaviour, we set limits to both of them. As an example, if we target a FWM gain to be larger than 97% of the maximum achievable gain:

$$\sqrt{(\gamma P_0)^2 - (\kappa/2)^2} \geqslant 0.97\gamma P_0, \tag{4.2.2}$$

then

$$|\kappa| \leqslant 0.48\gamma P_0 \approx 0.5\gamma P_0. \tag{4.2.3}$$

Hence, we define κ' as

$$\kappa' = \begin{cases} \kappa, & |\kappa| > 0.5\gamma P_0 \\ \\ 0.5\gamma P_0, & |\kappa| \leqslant 0.5\gamma P_0 \end{cases} \tag{4.2.4}$$

and use it in the fitness function instead of κ. In this way, GA will only be active only when the gain is lower than 97% of the maximum achievable gain. If the gain is higher than 97%, the value of κ will have no effects on the optimisation process.

Similarly, a walk-off length can be defined as the length after which two pulses completely separate (assuming the pulse width is T_0 which corresponds to the width where intensity drops to $1/e^2$ and the pulses almost stop interacting) and the fiber length is preferred to be no more than a quarter of this length (25% of total walk-off, more than 75% of the power between signal and pump pulses are still overlapping). For example, for a fiber length of 3 mm (corresponding to approximately π nonlinear phase change in one of our test fibers, $\gamma \approx 0.2\ /W/m$ when pumping with pulses with 5-kW peak power), we have

$$L_{\text{walk-off}} = \frac{T_0}{|\Delta\beta_1|} \geqslant 4 \times 3 \times 10^{-3}\ \text{m} \tag{4.2.5}$$

and

$$|\Delta\beta_1| \leqslant \frac{T_0}{12 \times 10^{-3}} \approx (80\ \text{m}^{-1})T_0\ . \tag{4.2.6}$$

We define $\Delta\beta_1'$ as follows and use it in the fitness function instead of $\Delta\beta_1$:

$$\Delta\beta_1' = \begin{cases} \Delta\beta_1, & |\Delta\beta_1| > (80\ \mathrm{m}^{-1})T_0 \\ \\ 80T_0, & |\Delta\beta_1| \leqslant (80\ \mathrm{m}^{-1})T_0\ . \end{cases} \tag{4.2.7}$$

Similar to κ', when $\Delta\beta_1'$ is defined in this way, GA will only be active when walk-off is larger than 25% of the total amount, otherwise the value of $\Delta\beta_1'$ will have no effects on the optimisation process. The limits ($0.5\gamma P_0$ for $|\kappa|$ and $80T_0$ for $|\Delta\beta_1|$) chosen in this work are not optimised. However, practice in the next section proves that these limits have not been reached. Therefore, their values have insignificant effects on GA results. Further refinements of these boundaries can be considered for future work.

With these choices and definitions, one can set the target condition for our GA to

$$F_{\mathrm{target}} = \frac{\gamma}{0.5\gamma P_0 \cdot (80\ \mathrm{m}^{-1})T_0}\ . \tag{4.2.8}$$

In this paper, a hyperbolic secant pulsed pump source with FWHM = 832 fs (T_0 = 500 fs) and 5 kW peak power is used, which gives $F_{\mathrm{target}} \approx 1 \times 10^7$ m s^{-1} W^{-1}.

It is important to note that the propagation constant, $\beta(\omega)$, cannot be freely chosen. The bulk material properties are fixed for any given glass type, whereas one have some freedom to modify the waveguide contribution to $\beta(\omega)$ through the design of the waveguide. The goals for phase matching and walk-off may not always be achievable. The idea of setting these targets is to explore how closely they can be achieved via the use of flexible fiber designs and GA modelling techniques.

4.2.1 GA results

The GA started with 1000 randomly structures generated using a base structure shown in Fig. 4.2.2. These structures evaluated using a finite element method and the fitness values are calculated using Eq. 4.2.8. Fig. 4.2.3 shows the fitness of the population for each generation. The first plot (a) is the initial generation. The

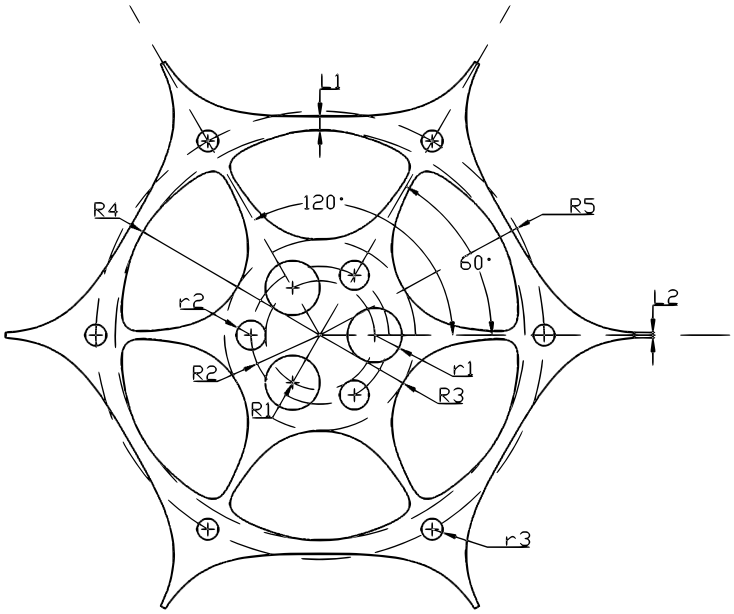

Figure 4.2.2: A genetic algorithm is used to combine the optical properties of two different types of fibers

plot is the projection of the population on the $R1/R3 : R3$ plane, and here, the population is in a 6-dimensional space. $R1$ is the radius from centre of the core to the centre of the holes on the inner ring. $R3$ is the radius from the centre of the core to the inner edge of the outer ring of holes.

As GA runs, the population continuously converges to a certain parameter region for each generation. This region can be clearly seen in Fig. 4.2.3f, $R3$ between $2 \sim 3$ μm, $R1/R3$ between $0.6 \sim 0.7$. High fitness values are concentrated near a curve, which indicates a relation between $R1$ and $R3$ that is corresponding to large fitness. Apparently, similar behaviours should also be noticed in other dimensions which are not shown here but the population converges to a region rather than a single point. This is expected due to the way we set the fitness function.

The GA modelling was manually stopped after six generations since the maximum fitness had saturated. The average fitness of the population in each generation increases stably as the generation evolves but the maximum fitness among each generation converges to 3.2×10^6 after just the second generation (shown in Fig. 4.2.4a).

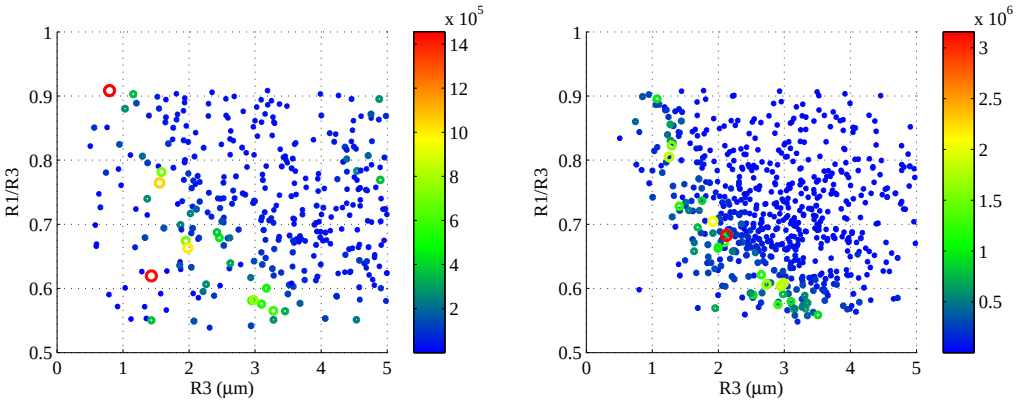

(a) Generation 1

(b) Generation 2

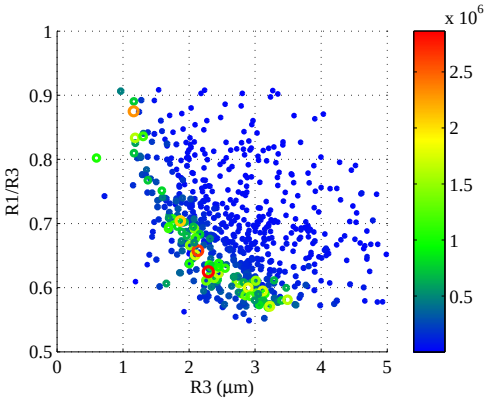

(c) Generation 3

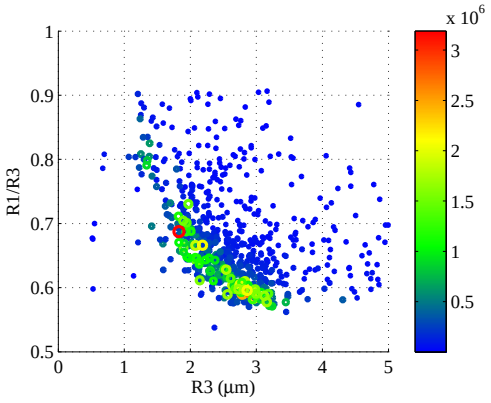

(d) Generation 4

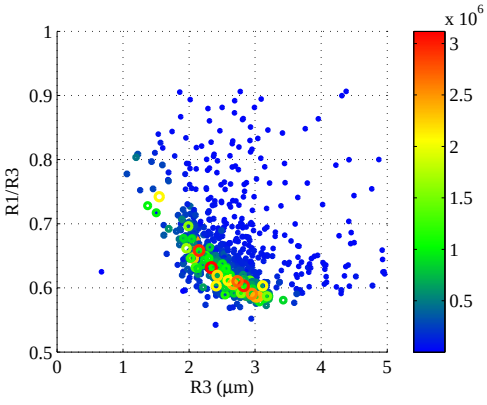

(e) Generation 5

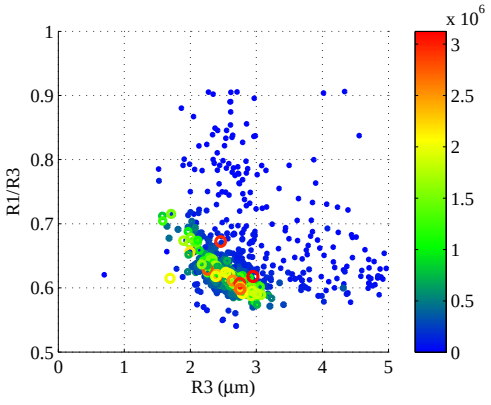

(f) Generation 6

Figure 4.2.3: The convergence of the population projected in the plane of R1/R3 ratio and R3. The size and colour of the circles represent the value of the fitness. Large circles corresponding to high fitness values.

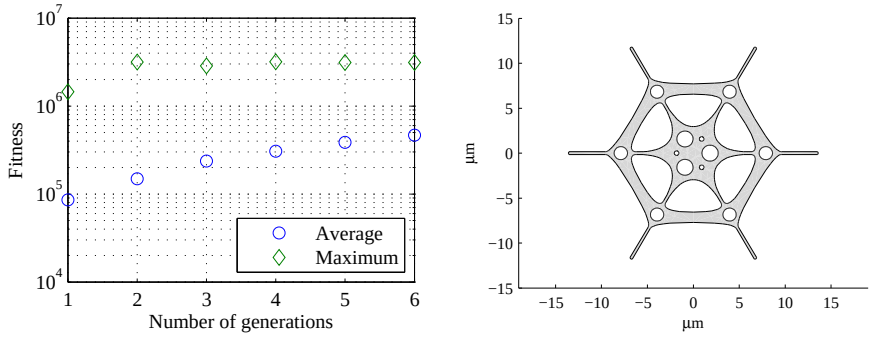

(a) (b)

Figure 4.2.4: (a) Convergence of the fitness values as a function of generation number. Circles are the average fitness of the whole population and diamonds are the maximum fitness of an individual within the population. (b) The optimised fiber geometry.

There are several possible reasons for this. Firstly, the bulk material dispersion of the glass limit the range of obtainable fitness parameters. Secondly, the size of the population is large, increasing the likelihood that the GA will yield structures with fitness values reach the limit. In other words, the use of successive generations may be more useful when smaller population sizes are used. Finally, there can be many localised maxima of fitness within the parameter space that prevents the population from reaching higher fitness structures.

The maximum fitness does not change significantly from the second generation, the structures corresponding to those fitness values are distinguishable as shown in Fig. 4.2.5. Similar structural variation can also be found in individual generations. For example, in the last generation, all the individuals with fitness within the 10% variations of the maximum fitness are shown in Fig. 4.2.6. For the same level of fitness, a variety of structures exist. However, the population did not reach the target fitness. This indicates a possibility that certain properties of the fibres, such as parametric gain and walk-off, compete with each other and limit further

optimisation of the conversion efficiency. A deeper insight explanation of the source of this competition is most likely the intrinsic dispersion of the material (Tellurite glass). Therefore, using a different glass for fibre can lead to a different optimisation result.

The GA gives a range of structures that promise to produce effectively high conversion efficiency. The structure with the highest fitness value in the last generation is shown in Fig. 4.2.4b. We name it as fibre "FG6". Its corresponding structural parameter values are: R1 = 1.82 μm, R3 = 2.95 μm, R4 = 6.56 μm, r1 = 0.885 μm, r2 = 0.253 μm and L1 = 1.15 μm.

By studying the statistics of the population, we can have a basic understanding of the sensitivity of the structure to the fitness and therefore know the required fabrication tolerances. To do so, we first use the most optimised structure parameters listed above as a reference. Then, the structures with parameters within a range, i.e. 20% of to the reference structure, are picked out from the last generation. Finally, the standard deviations of the fitness values of the picked structures are calculated. The 20% tolerance is chosen in order to get a reasonable number of structures. There are 7 structures picked from the last generation. The maximum relative differences of the six structural parameters of these 7 structures are ΔR1 = 16.1%, ΔR3 = 15.8%, ΔR4 = 10.1%, Δr1 = 19.3%, Δr2 = 16.7% and ΔL1 = 17.4%. The maximum change in the fitness values of the 7 structures is 96%. According to this data, using the minimum change in the structural parameter, it can be estimated that by changing the structural parameters by 10%, the fitness of the structure can drop to 4% of the optimised one. The results indicate that the fabrication tolerance of this design is particularly small.

However, we also discovered the structural parameters of high fitness structures also varies significantly. We examined several fiber designs from the last GA generation whose fitness values are larger than 90% of the maximum fitness (shown in Fig. 4.2.6). For these structures the standard deviations of the six structural parameters are: σR1 = 4.4%, σR3 = 8.4%, σR4 = 8.5%, σr1 = 27.3%, σr2 = 11.2% and

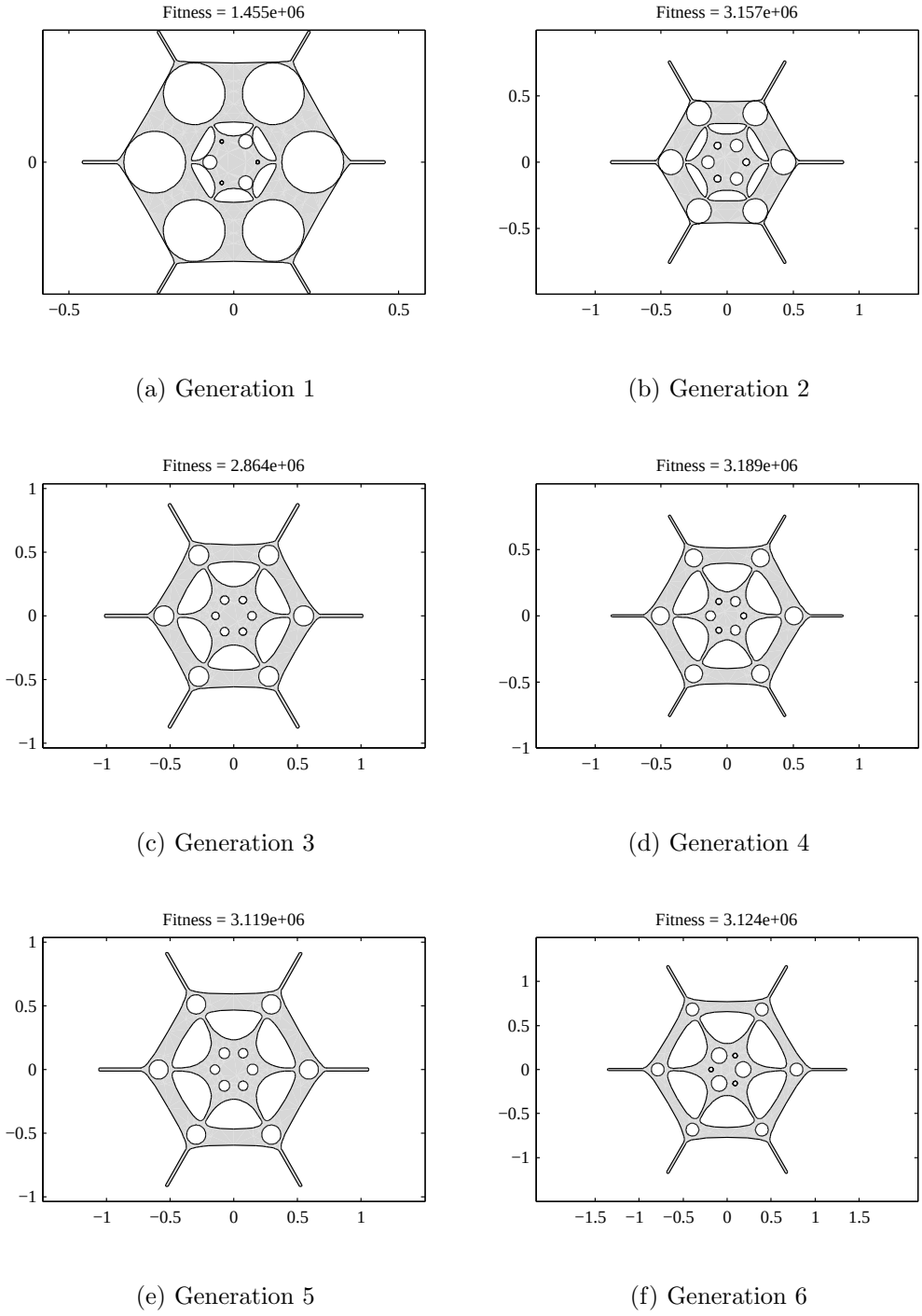

(a) Generation 1

(b) Generation 2

(c) Generation 3

(d) Generation 4

(e) Generation 5

(f) Generation 6

Figure 4.2.5: The fiber geometries have the highest fitness values in each generation

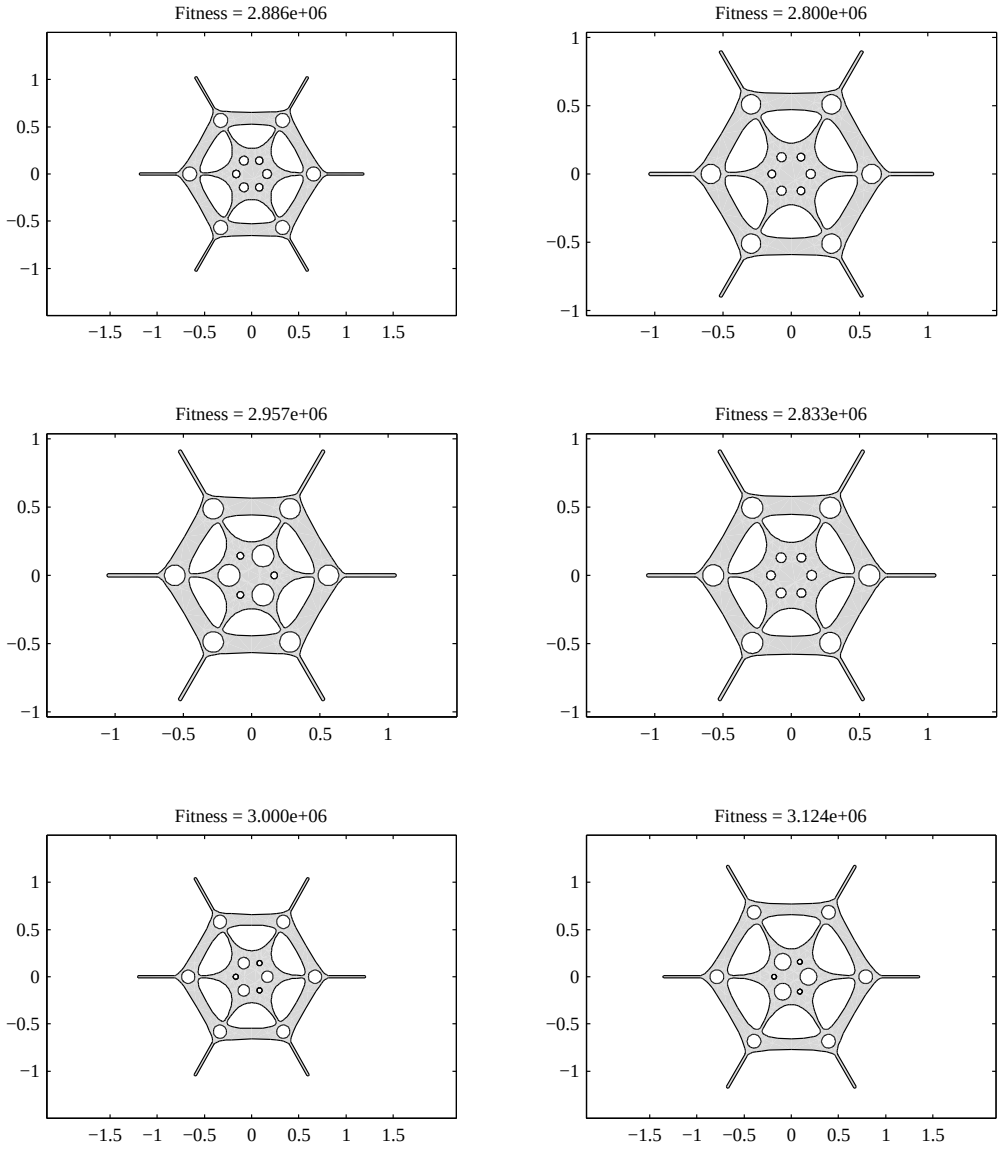

Figure 4.2.6: Fiber geometries in last generation whose fitness values are larger than 90% of the maximum fitness in that generation

σL1 = 6.0%. Comparing these values to the relative differences discussed before, it can be concluded that there is more than one maximum fitness in the parameter space and there are multiple structures that can be used for the FOPO in this work.

The gain map of degenerate FWM is calculated for fibre FG6. A gain map is a map that shows the FWM gain at signal and idler wavelengths for a continuous range of pump wavelengths. The gain maps do not reflect the effects caused by walk-off. However, by comparing the gain maps to the β_1 of the fibre, one can have some insight on the operation of parametric amplification processes with this fibre structure.

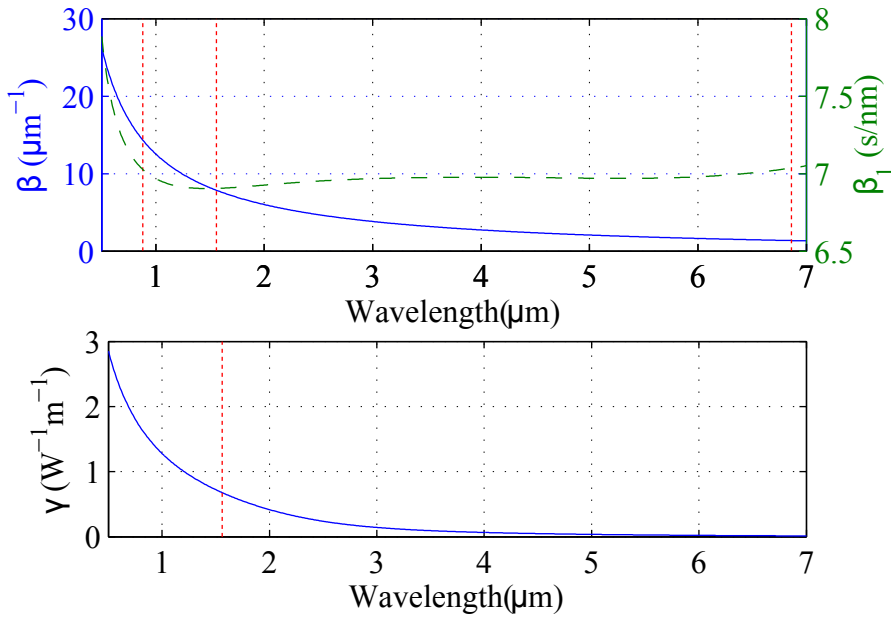

Figure 4.2.7: Propagation constant β, the inverse of group velocity β_1, nonlinear coefficient γ of fibre FG6 as functions of wavelength. The red dotted lines in top plot indicate the wavelengths of signal, pump and idler respectively from left to right. The red dotted line in bottom plot indicates the pump wavelength.

Figures 4.2.7 & 4.2.8 show the fiber properties (β, β_1 and γ) and FWM gain maps when the fiber is pumped with 1, 3, 5, 7 and 9 kW sources at 1560 nm.

The GA optimisation was performed using 5 kW peak power pulses. However, the FOPO should also work with other peak power levels except 1 kW which produces no gain at required wavelengths. It is also interesting that a broad gain bandwidth is obtained (Fig. 4.2.8) even though it is not considered explicitly in the fitness function.

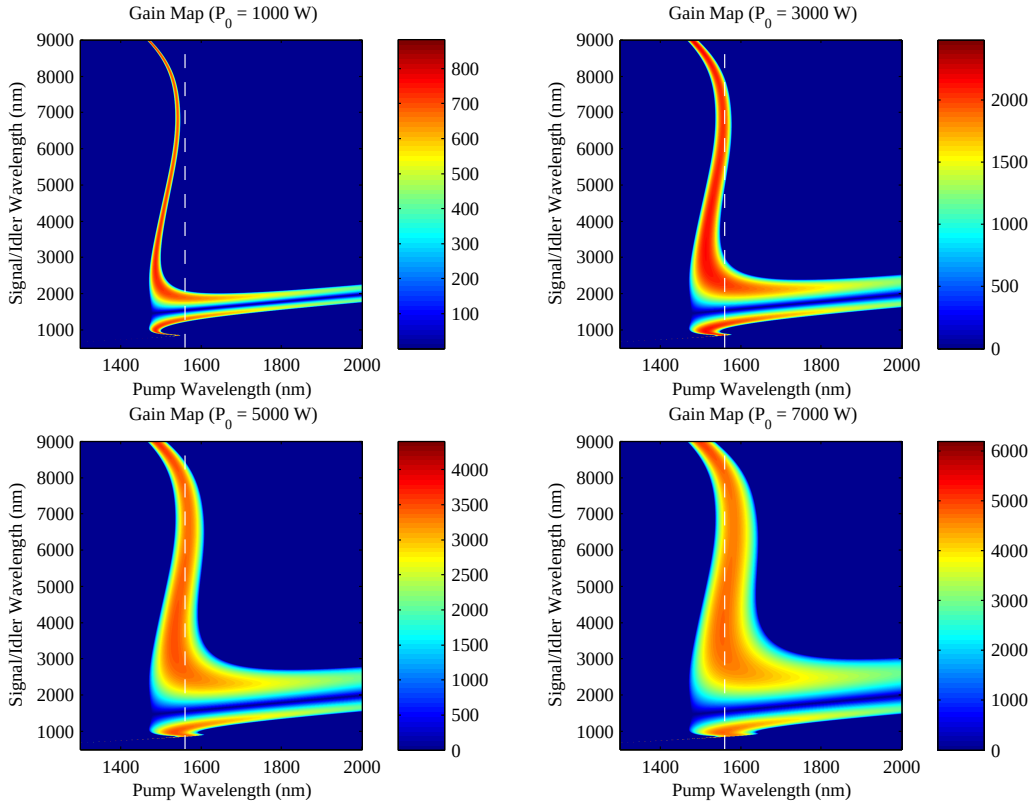

Figure 4.2.8: FWM gain maps of fibre FG6 pumped with 1, 3, 5 and 7-kW sources at 1560 nm.

These calculations indicate that a broad and relatively flat gain bandwidth can be obtained using a fibre designed by the GA. When the pump wavelength is not too far from (within the range where the waveguide dispersion can cancel the material dispersion) the ZDW of the material (ZDW $\approx 2.2\ \mu m$ for our glass) and the pump power is relatively high ($\approx$ 5 kW in this case), the GA tends to converge at the point where the ZDW is close to the pump wavelength. In this situation, phase matching is achieved mainly through high-order dispersion. In our specific case, one

observes an s-shape in the gain maps is due to higher-order β terms beginning with β_6. This knowledge is obtained by calculating the gain map using the Taylor series expansion of β and gradually increasing the number of terms until the s-shape band is observed. If β_2 is positive, which is the situation here, one cannot achieve phase matching without negative-valued high-order terms. Furthermore, in order for 4^{th}, 6^{th}, and higher-order terms to be significant, one must reduce the magnitude of β_2, which, in turn, leads to a large bandwidth [5]. Note that, due to the symmetry of the FWM process, odd orders of β terms do not contribute to phase matching.

The ultra-broad bandwidth is an advantage for ultra-short pulse applications since short pulses have large spectral spans. However, not all the spectral width of the gain band is needed. To increase the parametric conversion efficiency, stimulated amplification at only the desired wavelengths are preferred, in this case, a band around 880 nm. One way to do this is to use a band pass filter. After the signal is amplified in each round trip, the filter narrows it prior to seeding the amplification in the next round trip. However, there are also drawbacks of using a filter. The filter brings additional loss to the FOPO cavity which reduces the energy conversion efficiency.

The designed fibre can only provide single pass amplification. To build an oscillator, this fibre needed to be placed inside a cavity. The configuration and the tuning of the cavity also provide significant contribution to the overall performance of the FOPO. In the next section, we discuss the configuration and the pulse power and quality (how close the pulses are to transform limited pulses) optimisation of a FOPO.

4.3 FOPO modelling

The modelling in this section is to mimic a FOPO with the configuration is shown in Fig. 4.3.1. A tunable stage with mirrors M1 and M2 is for cavity-pump synchronisation. The tunable band-pass filter (BPF) has a 20 nm bandwidth and a

Tukey-window shape [144] to minimise effects caused by the frequency response of the filter during the fast Fourier transform (FFT) processes of the pulse propagation model. The short-pass filter (SPF) at the output is used to filter the pump and transmit the signal at 880 nm. A beam splitter (BS) is used to combine an incoming pump pulse with the filtered signal and direct it towards the fiber. The fiber length is limited to 3 mm. The length is selected by considering the total loss and gain in the whole FOPO system and the spectral shape degradation of the pump due to self-phase modulation, which corresponds to a nonlinear phase change of $\sim \pi$. By doing so, the pulse quality of the FOPO output is expected to increase. The fiber is assumed to be lossless because of its short length.

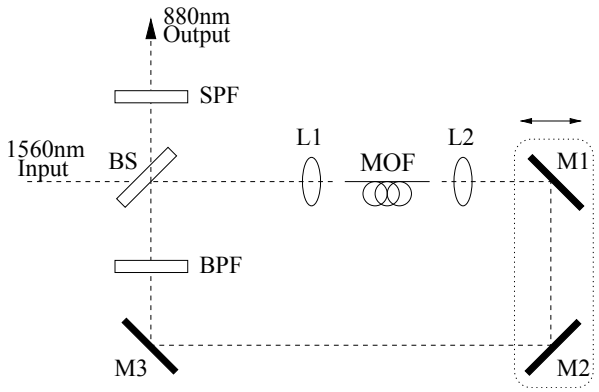

Figure 4.3.1: FOPO configuration. SPF: short-pass filter (to remove pump light). BPF: band-pass filter. BS: beam splitter. L1 & L2: lens. M1–3: mirrors. MOF: microstructured optical fibre.

The fibre design in this chapter is based on theory of small signal gain (see Section 4.1) which assumes the seed signals are small with respect to the pump pulses and the pump pulses do not deplete. However, in a FOPO, the seed signals grow significantly and can no longer be considered as small signals. Meanwhile, the pump depletion is also significant. The simulation of the FOPO can help us understand better the FOPO's oscillation processes and the interaction between signal and pump pulses.

In Chapter 2 Section 2.3.2, the drawbacks of previous FOPO simulation approach

are listed. They can be summarised as

1. Using a truncated the Taylor series is inadequate in describing the actual dispersion when the frequency shifts between the pump and the signal/idler are large.

2. The coupled wave equations 4.1.1∼4.1.4 are not suited to simulating complex nonlinear processes with dynamic frequency shifts or large spectral broadening.

3. Cascaded FWM cannot be modelled using only four equations, number of equations increases as cascaded effects increases.

4. It is difficult to include Raman effects into the coupled wave equations.

To address these points, in this work, an eigenvalue solver is used to obtain $\beta(\omega)$, and the GNSE Eq. 2.1.17 is used to model pulse propagation. This modelling approach can accurately describe FOPO performance and works equally well for small or large frequency shifts.

The simulation of this FOPO takes three steps. Firstly, we simulate pump pulse propagation through the fiber. Secondly, we filter the spectrum of the output and keep only the signal pulse to mimic the BPF. Finally, we combine the filtered output with a new pump pulse and let it propagate again through the fiber. We repeat step two and three for 100 times. A generalised nonlinear Schrödinger equation (GNSE) Eq. 2.1.17 is employed to simulation the pulse propagation instead of the coupled equations Eqs. 4.1.1∼4.1.4 for two reasons:

1. Femtosecond pulses are used which have broad line width and high peak power.

2. Other nonlinear processes apart from FWM should also be taken account into the simulations, such as Raman effects, XPM, cascaded FWM, pump and signal pulse broadening or SC generation.

To the best of our knowledge, this combination of modelling methods has not previously been used for simulating a FOPO.

The simulation is initialised by feeding a pump pulse with a quantum level of noise into the fiber leading to the generation of signal and idler spectral sidebands. The first pass forms the initial seed for feedback via the BPF. The filtered seed is combined synchronously with the next pump pulse and re-coupled into the fiber. The process is repeated for 100 round trips, by which the output is usually stabilised. To study the conditions leading to the generation of optimised output pulses, we explore the variations in the FOPO output pulses with different feedback ratios and time offsets between the signal and pump. The feedback ratio is the fraction of the output signal that is coupled back into the fiber after each pass.

4.3.1 Synchronisation

In real-time experiments, synchronisation can be achieved through tuning the optical path of the feed back loop and monitoring the output signal on an oscilloscope or spectral analyser. Tuning the optical path can cause changes not only in peak power but also in pulse shape. In order to study the physics behind this process, we perform simulations with different synchronisation conditions.

To simulate the synchronisation of the pulses, each pulse is placed inside a discrete temporal window. This window co-propagates with the pulse at velocity of $1/\beta_{1,p}$. Initially, considering only linear effects, the temporal offset with which the signal pulse needs to be set to re-synchronise with the pump pulse can be described as

$$T_{\text{offset}} = \frac{L}{v_{g,s}} - \frac{L}{v_{g,p}} = L\beta_{1,s} - L\beta_{1,p} = L\left(\beta_{1,s} - \beta_{1,p}\right) = L \cdot \Delta\beta_1. \tag{4.3.1}$$

This definition of offset time is equivalent to the walk-off time between pump and signal pulses. However, when nonlinear effects are involved, the walk-off time between pump and signal pulses can vary depending on the overlap between the two pulses during propagation. Fig. 4.3.2 show an example of walk-off within a single pass.

The blue dashed curves are pump pulses and the red solid curves are signal

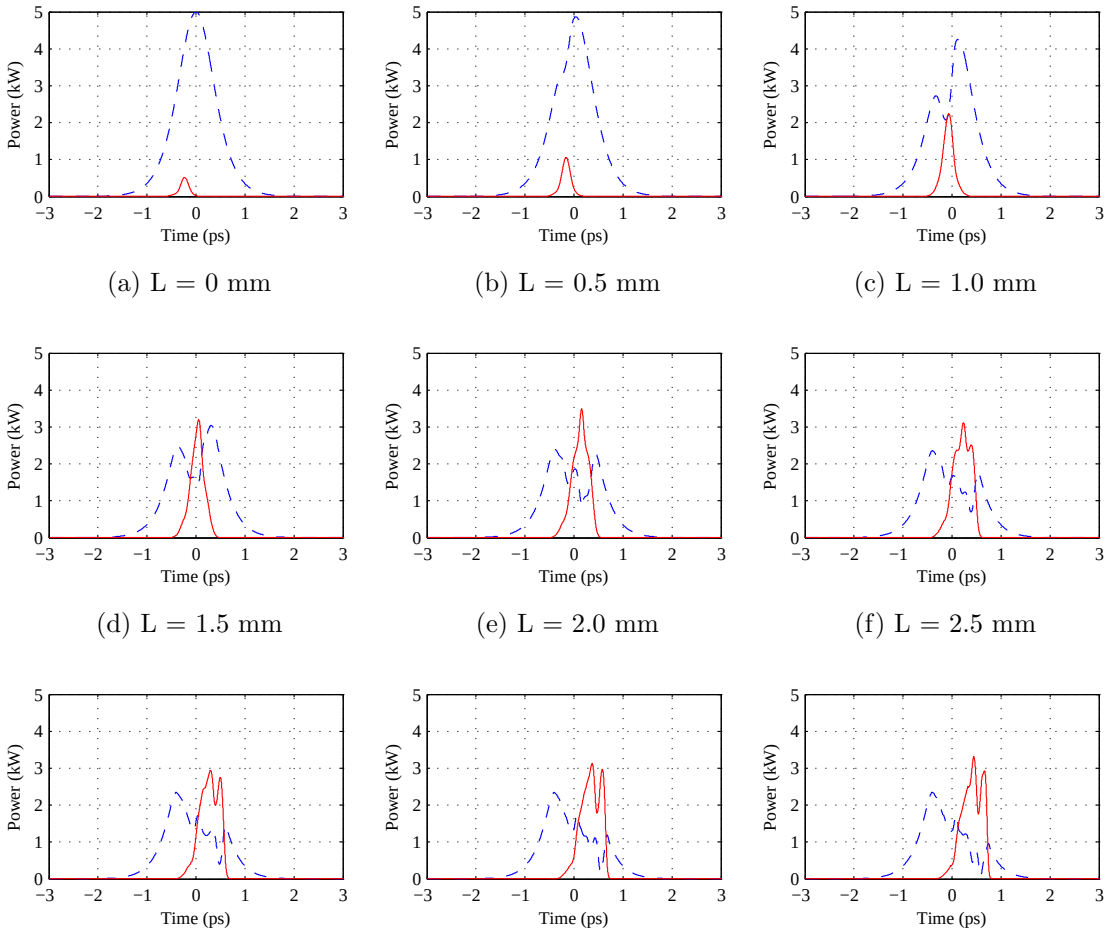

(a) L = 0 mm (b) L = 0.5 mm (c) L = 1.0 mm

(d) L = 1.5 mm (e) L = 2.0 mm (f) L = 2.5 mm

(g) L = 3.0 mm (h) L = 3.5 mm (i) L = 4.0 mm

Figure 4.3.2: Example of parametric amplification of a signal pulse within the fiber. Blue dashed curves: the pump pulses (1560 nm), Red solid curves: the signal pulses (880 nm).

pulses. The β_1's at the signal (880 nm) and the pump (1560 nm) wavelengths are approximately 7.027 ns/m and 6.905 ns/m respectively. According to Eq. (4.3.1), the offset time should approximately 0.49 ps at $L = 4$ mm (Fig. 4.3.3). But from the figure, the temporal offset is about 0.67 ps (measured using the highest peak of the signal pulse) due to nonlinear effects including self-steepening and Raman effects [5].

In the example Fig. 4.3.2, the seed pulse is 0.23 ps ahead of the pump pulse.

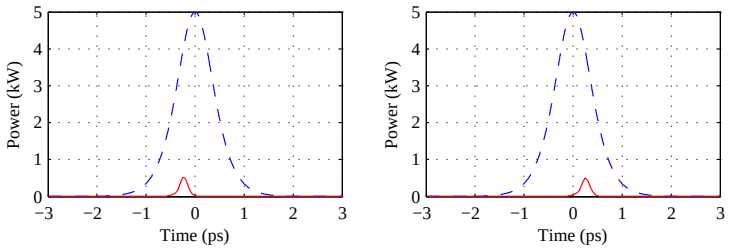

(a) L = 0 mm (b) L = 4.0 mm

Figure 4.3.3: Example of walk-off without the influence of any nonlinear effects, total walk-off 0.488 *ps* which matches T_{offset}. Blue dashed curves: the pump pulses (1560 nm), Red solid curves: the signal pulses (880 nm).

We used a 200 nm band pass filter to capture all the spectral contents of the signal pulse and we see multiple peaks appear in the signal pulses. To obtain output pulses that are close to Fourier transform limitation, a narrower bandwidth filter can be used such as 20 nm. In the following work, we use 20 nm band pass filter and tune its central wavelength around T_{offset} to study how this offset time can influence parametric processes.

Figs. 4.3.4 $\sim$ 4.3.7 show the development of the signal pulse (both temporal and spectral) as the round trip number increases for different offset time. In these simulations, 50% of the output power is coupled back into the fibre for each round trip. It is clear that an offset time around 560 $\sim$ 580 fs is the most efficient synchronisation position since the FOPO outputs reach maximum power most quickly (approximately 20 passes). The physical explanation is that with these offset time, the signal pulse overlaps with the highest power region of the pump pulse which result in the maximum nonlinear interaction between the two pulses. Therefore, the energy conversion between the two pulses is maximised through the nonlinear interaction, which can be reflected from the peak power of FOPO's output pulses.

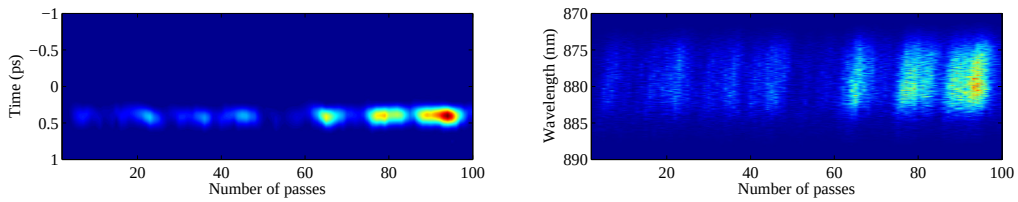

(a) Offset Time = 458 fs

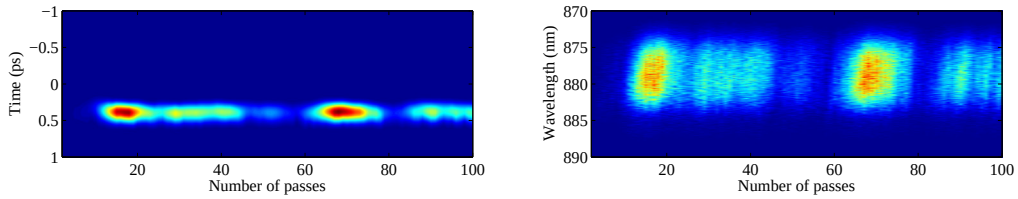

(b) Offset Time = 473 fs

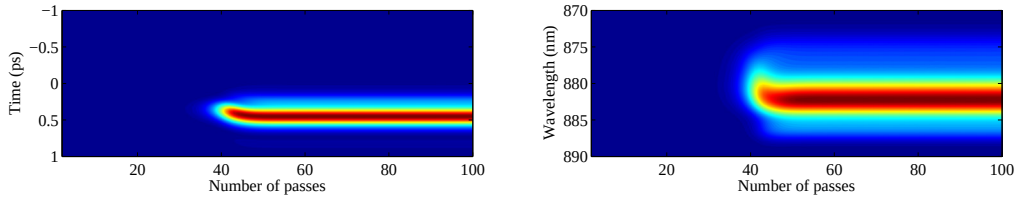

(c) Offset Time = 488 fs

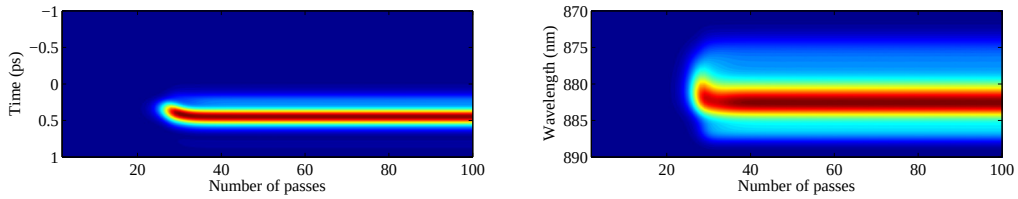

(d) Offset Time = 504 fs

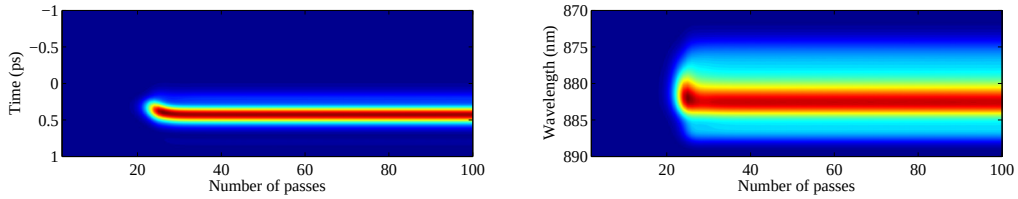

(e) Offset Time = 519 fs

Figure 4.3.4: The evolution of the temporal (left column) and spectral (right column) intensity profiles of signal pulses as a function of pass number at different offset time. Each figure is normalised to its maximum intensity.

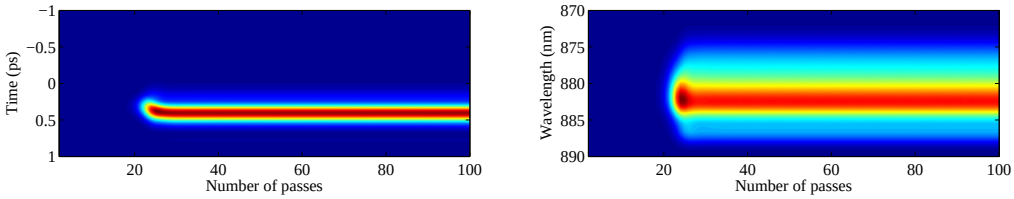

(a) Offset Time = 534 fs

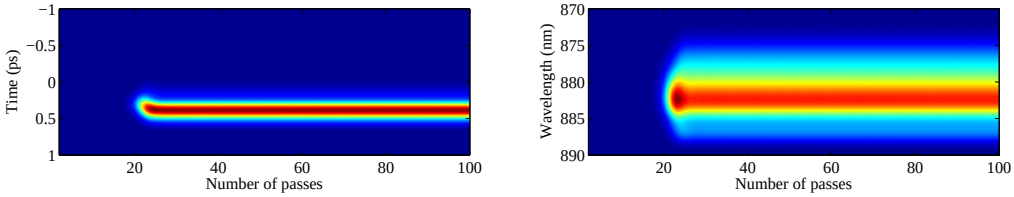

(b) Offset Time = 549 fs

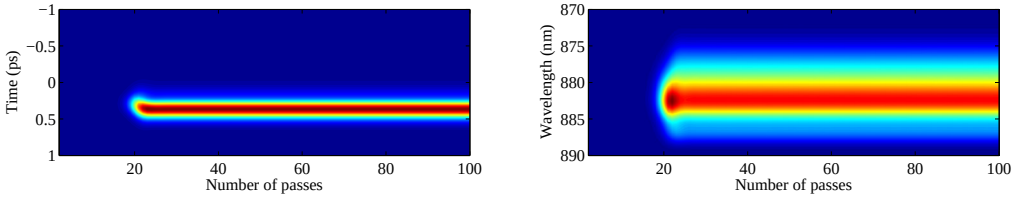

(c) Offset Time = 564 fs

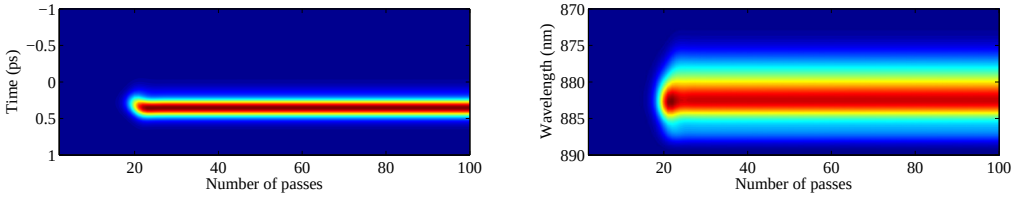

(d) Offset Time = 580 fs

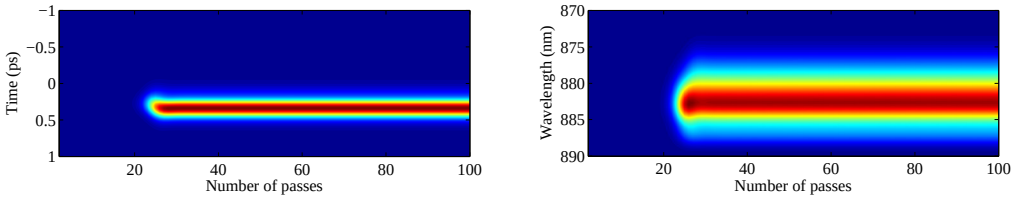

(e) Offset Time = 595 fs

Figure 4.3.5: Continuation of Fig 4.3.4.

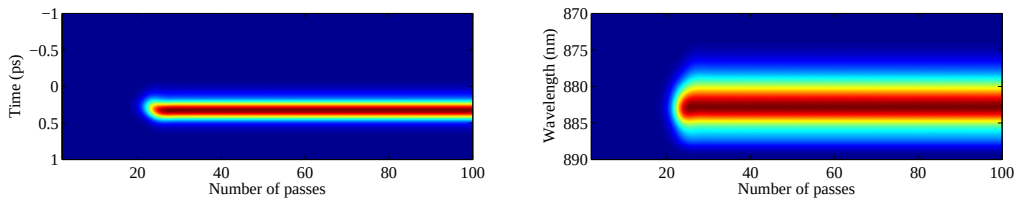

(a) Offset Time = 610 fs

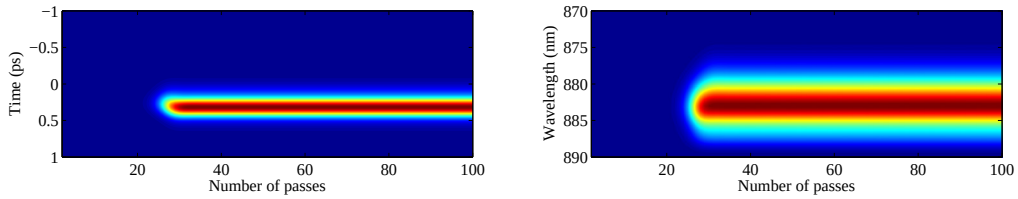

(b) Offset Time = 626 fs

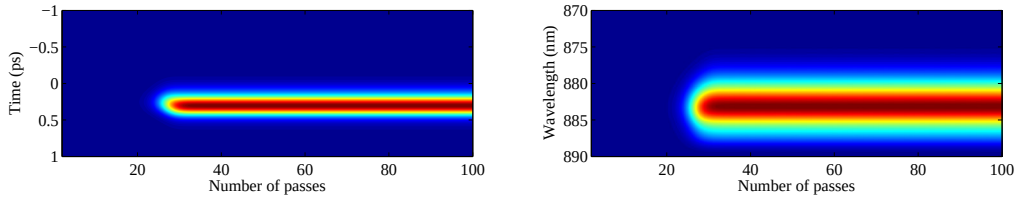

(c) Offset Time = 641 fs

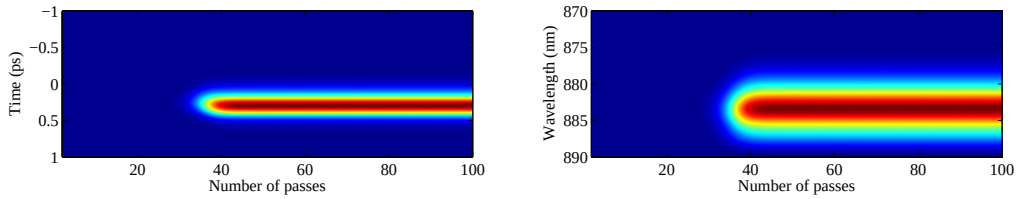

(d) Offset Time = 656 fs

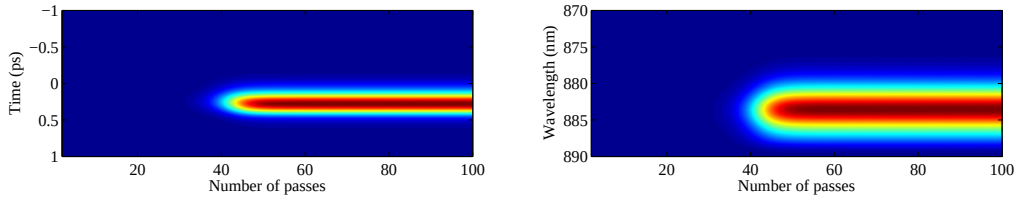

(e) Offset Time = 671 fs

Figure 4.3.6: Continuation of Fig 4.3.5.

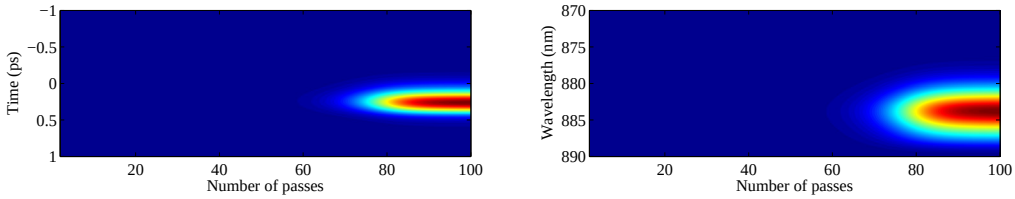

(a) Offset Time = 687 fs

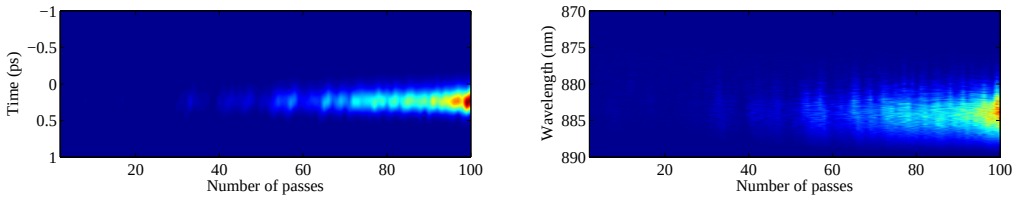

(b) Offset Time = 702 fs

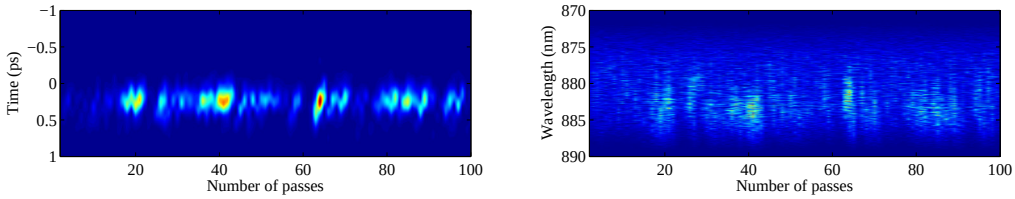

(c) Offset Time = 717 fs

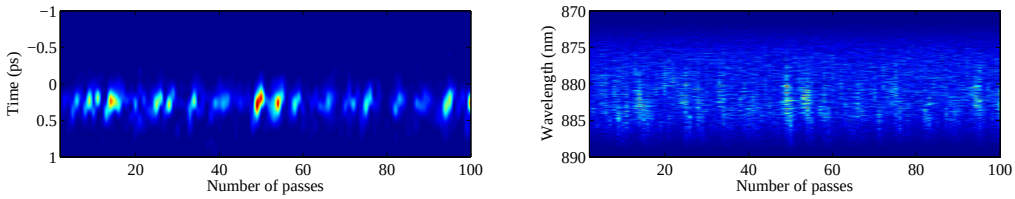

(d) Offset Time = 732 fs

Figure 4.3.7: Continuation of Fig 4.3.6.

The offset time also relates to the peak power of the output pulse of the FOPO and how close they are to transform limited pulses. Figure 4.3.8 shows the output pulse duration and time-bandwidth product (TBP) as a function of temporal offset corresponding to Fig. 4.3.4 $\sim$ 4.3.7. Figure 4.3.8a shows the peak power of the output pulses averaged over the last 20 passes of the simulation. The curve in the figure is asymmetric, reflecting the combined effects of frequency chirp, pump depletion and walk-off between pump and signal pulses. The pump pulses acquire

frequency chirp under their own SPM during which the signal pulses start to deplete the pumps at certain points while they walk across the pump pulses. As the offset time changes, the signal pulses overlap with different frequency components of the pump due to the frequency chirp and lead to deviations in the phase match condition. The output peak power reaches a maximum around 2.1 kW when the offset time is approximately 0.55 ps ahead of the pump pulse, which is consistent with the fact that signal pulses propagate slower than the pump pulses. Noticing that this offset time reflects the difference of the overall group velocity between pump and signal pulses. From the calculation at the beginning of this section, it is known that this group velocity delay consists of the contribution of both linear and nonlinear effects. The nonlinear part of the contribution has not been studied before can now be studied from this respective.

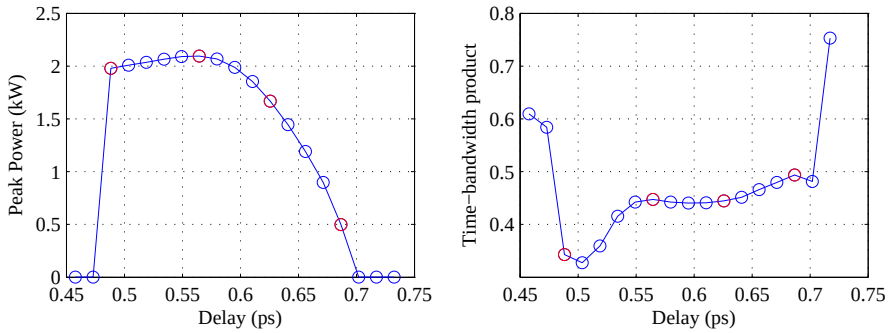

(a) (b)

Figure 4.3.8: Peak power (a) and time-bandwidth product (TBP) (b) of output pulses averaged over the last 20 passes as a function of offset time with a fixed feed-back ratio of 0.5

A TBP is used to qualitatively assess the quality of output pulses. For transform-limited Gaussian and hyperbolic secant pulses, TBPs are 0.44 and 0.315, respectively. However, it is important to keep in mind that the TBP is calculated using full width at half maxima (FWHM), and thus it neglects pedestals or other detailed features in the spectra that have power lower than half of the maximum. Fig. 4.3.8b

shows the TBP of the pulses corresponding to Fig. 4.3.8a also averaged over the last 20 passes. The dip in TBP at 0.5 ps is close to that of a transform limited secant pulse. However, in this particular case, the output pulses have large spectral pedestals below the half maximum points. Apart from the dip, the overall TBPs for different offset times are fairly constant at ∼0.45, which indicates the synchronisation does not significantly influence pulse quality over the range of oscillation from 0.48∼0.7 ps.

In general, it is found that if the group velocity of pump pulse is larger than the signal pulse, signal pulse should be put ahead of the pump pulse so that during propagation the pump pulse can catch up the signal pulse and provide its maximum power region to amplify the signal pulses. With this particular FOPO configuration, the best offset time is around 0.56 ps, which provides highest output peak power and relatively high pulse quality.

4.3.2 Feedback ratios

The power that is fed back into the fiber in each round trip also determines the output of the FOPO. For a FOPO that oscillates at the signal frequency and also outputs at the signal frequency (the configuration shown in Fig.4.3.1), the feedback power should be kept as low as possible in order to get the maximum output. Meanwhile, the feedback should also be kept high enough such that stimulated the parametric processes can take place and the power conversion is maximised. From what has been discussed so far, it is clear that an optimum feedback ratio should exist for each FOPO under each pump condition.

Figs. 4.3.9 ∼ 4.3.12 show the development of the signal pulse as the round trip number increases for different feedback ratios. The simulation results show an interesting behaviour of the development of the single pulses. The signal pulses emerge from noise with a slightly lower frequency for the first few passes compared with the steady state. This is because the phase-matching condition changes slightly once

the signal achieves enough power to begin to deplete the pump power. For feedback ratios below 0.35, it can be seen in Fig. 4.3.9 that the initial increase in signal pulse power is slow and unstable. For this particular FOPO, a feedback ratio of 0.3 is the threshold. When the feedback ratio larger than 0.3 the signal starts to build up stably. Once the feedback ratio exceeds 0.3 but below 0.8, as in Fig. 4.3.10 & 4.3.11, the signal power rises rapidly, overshooting the eventual steady-state value, and then converges to that steady-state value after a period of fluctuation. Further increases in the feedback ratio lead to the situation where the output power fluctuates regularly (feedback $\leqslant$ 0.95 Fig. 4.3.93 & 4.3.12) and then irregularly (feedback = 1.0 Fig. 4.3.12). This behaviour is due to pulse spectral broadening followed by BPF filtering. This broadening-filter loop leads to the oscillations of the output power. The high-feedback case in Fig. 4.3.12 also corresponds to the situation where the signal pulses behave like supercontinuum generation. Due to the complex nature of SC generation, the spectrum transmitted by the BPF is different for each pass.

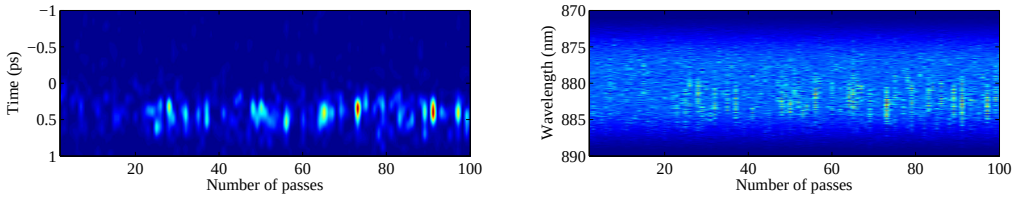

(a) Feedback ratio = 0.1

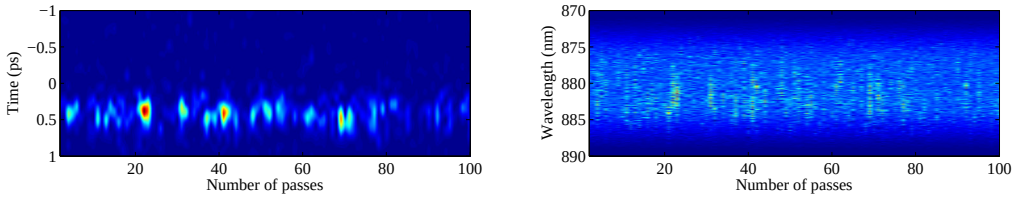

(b) Feedback ratio = 0.15

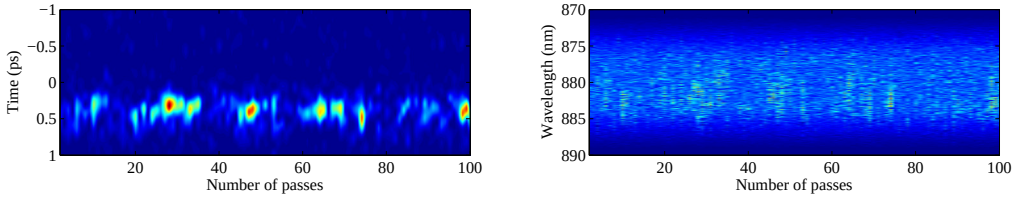

(c) Feedback ratio = 0.2

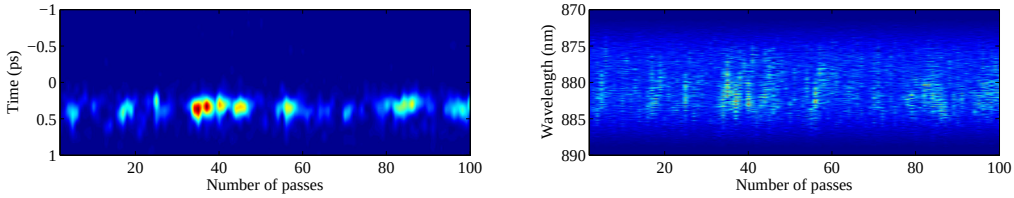

(d) Feedback ratio = 0.25

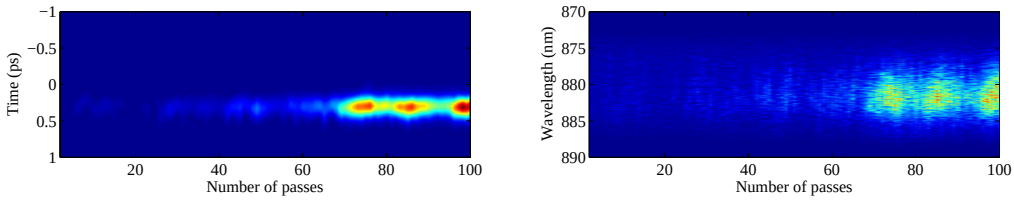

(e) Feedback ratio = 0.3

Figure 4.3.9: The evolution of the temporal (left column) and spectral (right column) intensity profiles of signal pulses as a function of pass number at different feedback ratio. Each figure is normalised to its maximum intensity.

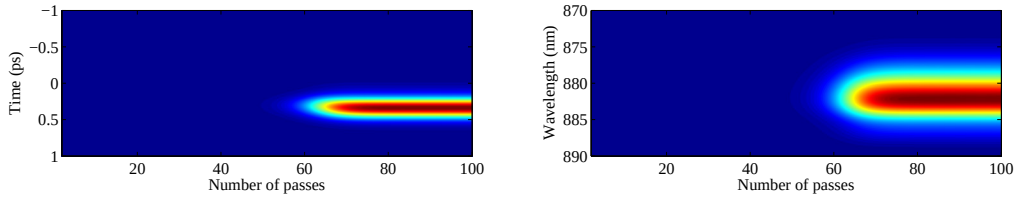

(a) Feedback ratio = 0.35

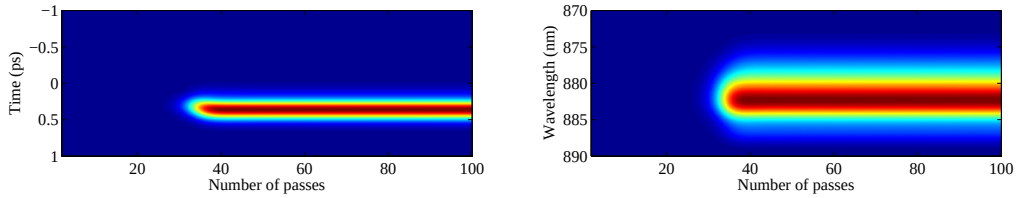

(b) Feedback ratio = 0.4

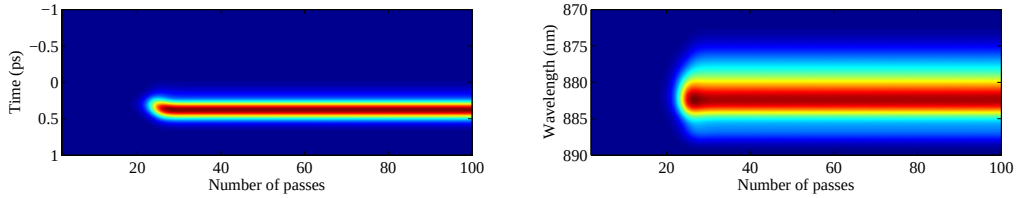

(c) Feedback ratio = 0.45

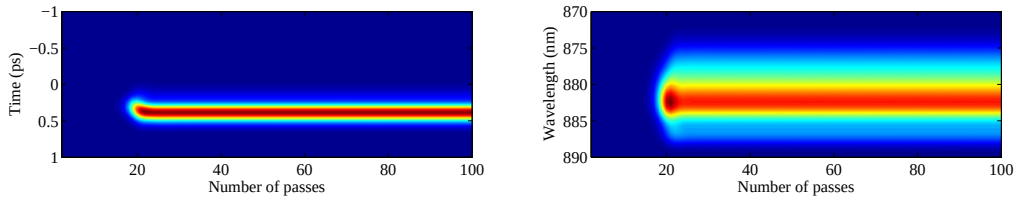

(d) Feedback ratio = 0.5

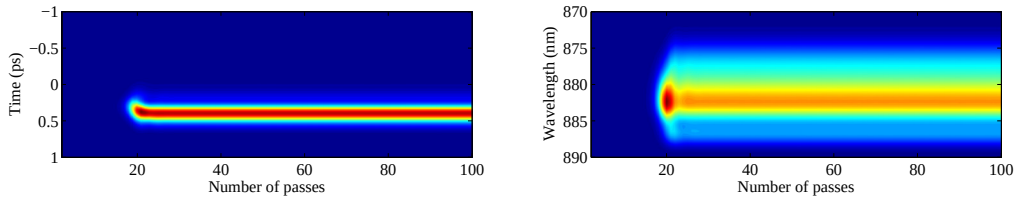

(e) Feedback ratio = 0.55

Figure 4.3.10: Continuation of Fig 4.3.9.

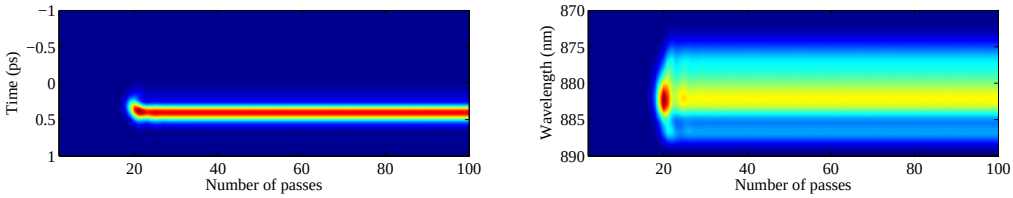

(a) Feedback ratio = 0.6

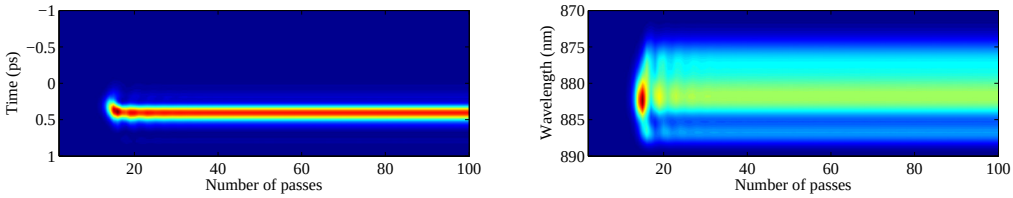

(b) Feedback ratio = 0.65

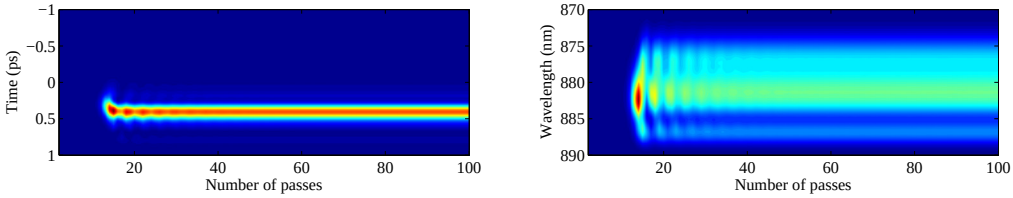

(c) Feedback ratio = 0.7

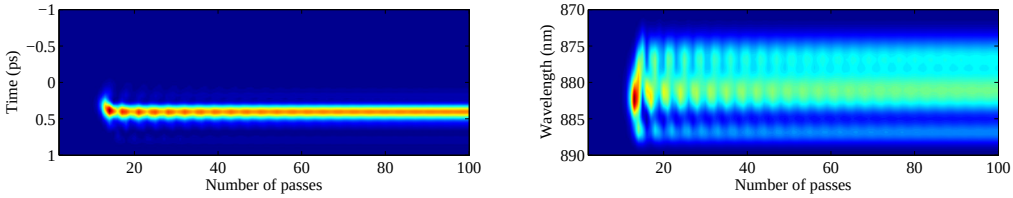

(d) Feedback ratio = 0.75

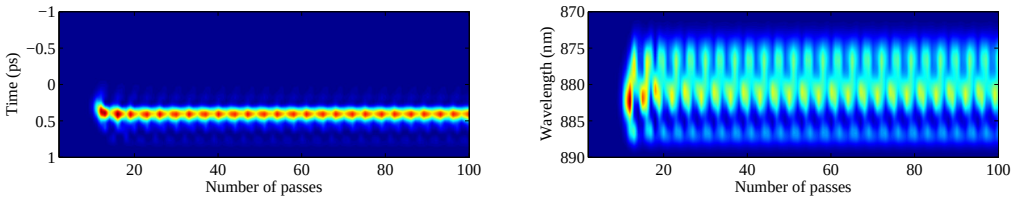

(e) Feedback ratio = 0.8

Figure 4.3.11: Continuation of Fig 4.3.10.

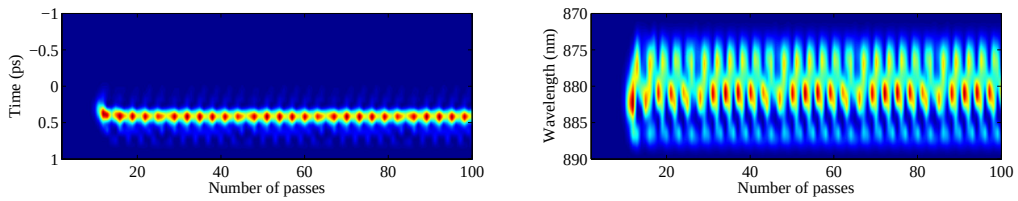

(a) Feedback ratio = 0.85

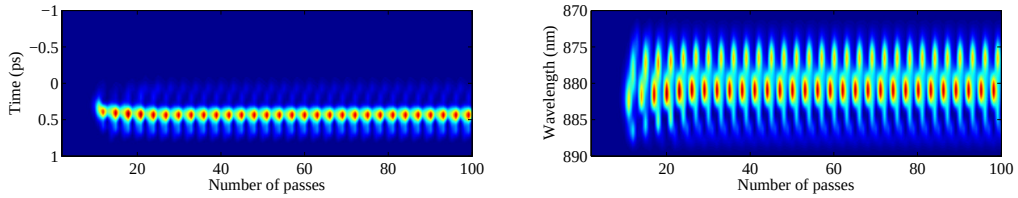

(b) Feedback ratio = 0.9

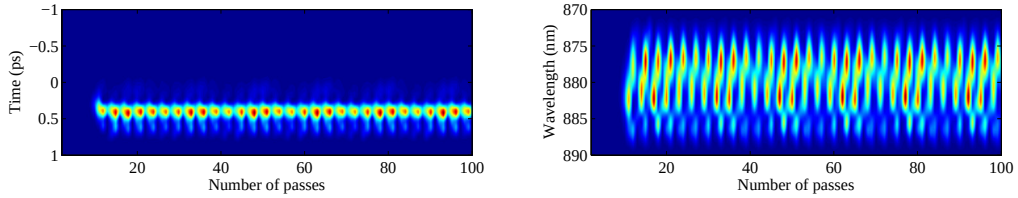

(c) Feedback ratio = 0.95

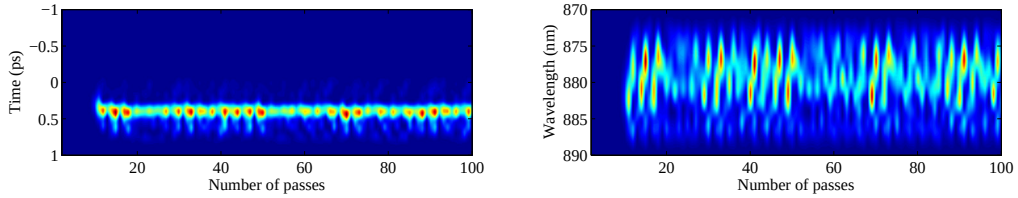

(d) Feedback ratio = 1.0

Figure 4.3.12: Continuation of Fig 4.3.11.

Figures 4.3.13a and 4.3.13b show the peak power and TBP for different feedback ratios with the temporal offset fixed to 0.55 ps. In Fig. 4.3.13a, one observes a threshold of the feedback ratio of 0.3, with the output peak power reaching a maximum at 0.5. For feedback ratios larger than 0.5, the peak power decreases slightly. This results from the temporal broadening of the signal pulse as the feedback ratio increases and the BPF filters more power beyond its pass band. For feedback ratios greater than 0.8, the average output peak power starts to change irregularly from

pass to pass. This effect will be discussed later in this section.

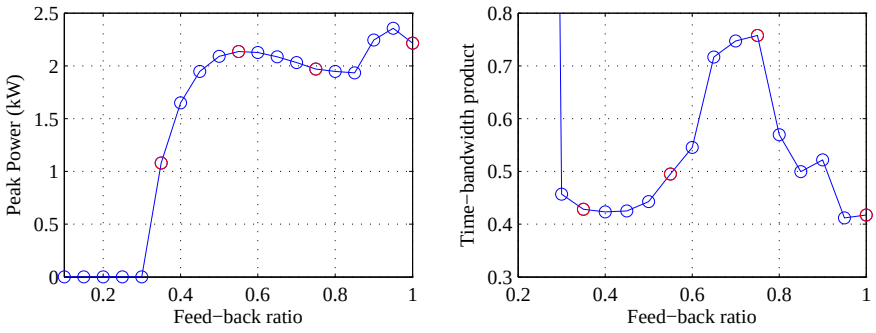

(a) (b)

Figure 4.3.13: Peak power (a) and TBP (b) of output pulses averaged over the last 20 passes as a function of feedback ratio and 0.55 ps offset.

The corresponding TBP curve is shown in Fig. 4.3.13b. As the feedback ratio increases, it can be seen that the TBP reaches a local minimum of 0.42 at a feedback ratio of 0.4. The TBP then increases to a maximum of 0.77 at a feedback ratio of 0.75. After reaching a maximum it also starts to behave irregularly due to SC generation.

It is clear from Fig. 4.3.9 $\sim$ 4.3.12 that for a stable FOPO system the feedback ratio should be kept at or below the threshold of generating SC (in this case 0.8). The unstable FOPO may have some potential use, such as a modelock mechanism, since the maximum peak power is much larger than the stable case. For our proposed system, the best choice of a feedback ratio which combines high output peak power (43% conversion efficiency) and small TBP ($\approx$ 0.43) is $\sim$0.5.

The proposed system is simulated incorporating the optimised synchronisation of 0.55 ps offset time, and the optimised feedback ratio of 0.5. The stable output pulse shape and spectrum of the fiber and the FOPO are shown in Fig. 4.3.14 and 4.3.15, respectively. The pulse is Gaussian on top of a small pedestal. The peak power exceeds 2 kW and the FWHM is $\sim$200 fs. The conversion efficiency of this FOPO is not the highest but it managed to output femtosecond nearly transform

limited pulses which is the first design of such a FOPO.

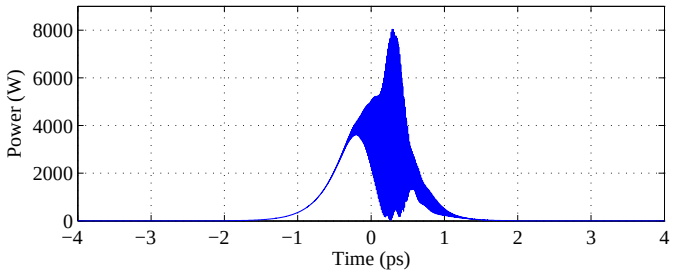

(a)

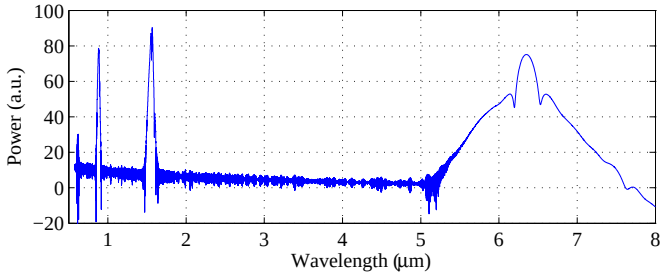

(b)

Figure 4.3.14: Pulse shape (a) and spectrum (b) of a globally optimised FOPO at the fiber output.

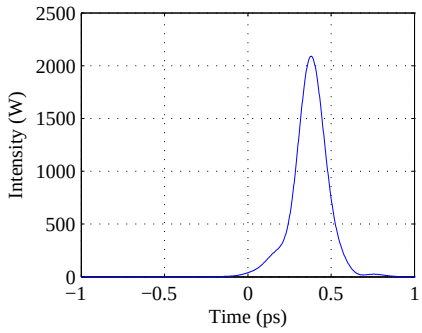

(a)

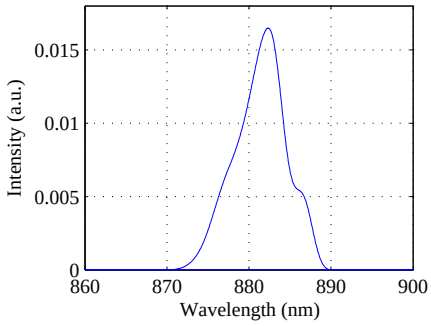

(b)

Figure 4.3.15: Output pulse shape (a) and spectrum (b) of a globally optimised FOPO

4.4 Summary

Here in this chapter, for the first time a GA is used to optimised a fiber structure for a particular nonlinear application: FOPO. Based on the understanding of how to apply GA to MOF design, the key physical properties of FOPO are analysed and a fitness function is defined according to design requirements. The output of the GA is surprising. Firstly, the highest fitness in each generation saturates at a lower level than the target. Secondly, high fitness individuals appeared as early as the second generation. Through analysis, it is found that the two points mentioned here are due to the nature of the problem. The large population size increases the chance to hit high fitness structure and the nature of the fiber material, material dispersion, limits GA to achieve higher fitness.

The difficulties encountered in fibre design stage do not influence the further study of FOPO. The highest fitness structure in the last generation is chosen and its nonlinearity and dispersion profiles are calculated. During the calculation, it is discovered that as a result of optimisation, an ultra-broad gain bandwidth (approximately 7 μm wide) is expected. The cause of this result is due to the need of a phase match across a large frequency span, which lead to the enhancement of the effects of high-order dispersion and the need of decreasing $beta_2$.

Using a pulse propagation model, a FOPO was numerically simulated. Synchronisation and feedback ratio as two important feature of a FOPO were then studied separately. Synchronisation studies revealed that algin seed and pump pulses peak to peak is not the best synchronisation condition. Due to walk-off effects, there exist a relative velocity between seed and pump pulses. The best scenario is to set the seed slightly ahead the pump pulse if the pump pulse propagates faster than the seed pulse and vice versa. In this way, as the walk-off happens, the seed can walk through the highest average intensity region of the pump pulse so that achieve the maximum gain. The feedback ratio study showed that to achieve best output, high peak power and good pulse quality, the feedback ratio cannot be too low or too high.

If the feedback ratio is too low, there is not enough peak power been generated. If the feedback ratio is too high, SC generation can take place and degrades the pulse quality.

After analysing the simulation data, it has been found that the best parameter for our FOPO, which allows the FOPO to provide approximately 43% peak power conversion with only relatively little pulse quality degradation (TBP ≈ 0.43). Such a system would be very attractive for many applications that require wavelength tunable femtosecond-pulses from the near- to mid-IR.

There are some limitations of the analysis. Firstly, the Sellmeier equation used here for tellurite glass may not be valid for the entire wavelength range because the experimental data used to generate the coefficients is ranging from 600 $\sim$ 1050 nm [145]. The ultra-broad bandwidth is calculated based on the Sellmeier equation, which implies that the actual bandwidth of a real fiber may not be as large as predicted. Secondly, the loss of the fiber is not included in the simulation, although the transmission losses through 3 mm of fiber will be small. Even for the idler wavelength (6.8 μm), which is beyond the edge of the transmission window for tellurite glass (normally 4–5 μm [145]), it is expected that the transmission losses after 3 mm of propagation is less than 10 dB. However, in practise, one should expect to see a difference in the generation of the signal and idler pulses. The purpose of this work is to combine GA with beam propagation simulation to design a FOPO. To achieve a fully optimised FOPO, a few iterations of design and fabrication will be required. Once fabricated, these fibers will allow one to gather more information about the fiber's absorption spectrum, Raman spectrum and nonlinear response as a function of wavelength to refined the predictions. Note that simply due to the Fresnel reflection, the maximum coupling efficiency is around 89%. Other optics within the FOPO system, such as mirrors beam splitters and filters, contribute additional losses such that not all the feedback ratios are accessible. The analysis in this work is relevant for bulk cavities which exhibit high losses as well as all fiber configurations which can greatly reduce intra-cavity losses.

In this chapter, a relative narrow band light source is designed and analysed. In the next chapter, a similar fibre designed approach is applied to design a MOF for a broadband supercontinuum light source.

Chapter 5

Supercontinuum Generation

5.1 Background

In literature, a number of methods have been used to tailor the SC spectrum, such as shifting the zero dispersion wavelength (ZDW) [146], flattening dispersion slope [147], tuning pulse chirp [148], modification of the pulse shape [149] and connecting multiple piece of fibres with different dispersion [150]. All of these methods can tune the generated SC. However, because of the lack of degrees of freedom (free parameters), their usefulness in the design of SC generation is usually limited, and in general, large parameter space searches are required. For example, shifting the ZDW with respect to the pump wavelength can vary the SC output dramatically. However by doing this, higher order dispersion and nonlinearity also change, which also influences the generated SC.

A more advanced dispersion design method was using in Ref.[147]. This method was based on a mathematical model that assumes the total fibre dispersion is the linear summation of material dispersion and waveguide dispersion ($D_{total} \approx D_{material} + D_{waveguide}$) [132, 151, 152]. This method is quite efficient after the necessary parameter spaces are mapped out. However, the pre-calculation could take very long time depending on the number of free parameters of the structure which

does not necessarily be efficient. Also, this method does not include nonlinearity optimisation and the assumption of simple addition of D's is inaccurate.

In the previous chapter, a GA was used to optimise a fibre structure for a specific nonlinear parametric process. With the initial structure provided, the GA has been proven efficient for tailoring dispersion profile of a fibre. With this experience, a GA is used to design a fibre for SC generation with large bandwidth and high coherence. However, different to the work in Chapter 4, the evaluation of SC generation is more computational intensive. Modifications to the GA fibre design approach are needed. To understand this, a brief explanation is provided.

One way to study and evaluate SC generation is to simulate them numerically. Accurate predictions of SC generation can be made using general forms of nonlinear Schrödinger equations Eq. 2.1.17.

$$\frac{\partial A(z,t)}{\partial z} + \frac{\alpha}{2}A(z,t) - \sum_{n\geqslant 2}\frac{i^{n+1}}{n!}\beta_n\frac{\partial^n A(z,t)}{\partial T^n} = i\gamma(1+i\tau_{shock}\frac{\partial}{\partial T})\left(A(z,t)\int_{-\infty}^{\infty}R(T')\times|A(z,T-T')|^2\,dT'\right). \quad (2.1.17)$$

The bandwidth of a SC can be calculated using the output of the numerically simulation. However the coherence of a SC spectrum cannot be obtained through a single-step evaluation. As described in Section 2.4.4, the coherence of a SC represents the ability for two SC generated pulses to interfere. It can be defined as the cross-correlation of two fields

$$\left|g_{12}^{(1)}(\lambda,t_1-t_2)\right| = \left|\frac{\langle E_1^*(\lambda,t_1)E_2(\lambda,t_2)\rangle}{\sqrt{<|E_1(\lambda,t_1)|^2><|E_2(\lambda,t_2)|^2>}}\right|, \quad (5.1.1)$$

where E_1 and E_2 are the electric fields, λ is the wavelength, t_1 and t_2 are the time. Now consider E_1 and E_2 are the fields from two independent SC generation and the difference in the optical path between the two field is zero, so $t_1 = t_2$, then $g_{12}^{(1)}$ is the mutual coherence of the two electric fields. During SC generation, random noise in the pump pulse triggers random jitters in both time and phase of the pulses

which can result in significant differences in the output pulses. When this happens, coherence $g_{12}^{(1)}$ will decrease. Thus, this definition of coherence reflects the stability of SC generation and it can be experimentally measured in a modified Young's two sources experiment [110].

Sometimes, for convenience, a concept of average coherence,

$$< |g_{12}^{(1)}| >= \int |g_{12}^{(1)}(\lambda, 0)||E(\lambda)|^2 d\lambda / \int |E(\lambda)|^2 d\lambda, \tag{5.1.2}$$

is also used to describe the overall coherence of a pulse across the spectrum [55].

The coherence of SC generation is a statistical concept. To calculate the coherence of SC generation, random noise is introduced into the input pulses. Using Eq. 5.1.1 in Chapter 2, the coherence is calculated from pairs of pulses. To perform a reasonable average on the calculated coherence, 10 pairs of pulses are needed which lead to 20 pulse propagation simulations [55].

The way that SC coherence is calculated is very time consuming. Each propagation simulation takes approximately 20 minutes on a 2.66 GHz quad-core computer with 800 MHz DDR2 memory. Assuming there are 1000 structures and GA needs 10 iterations to get the required result, then by calculating the coherence itself will take approximately 7.6 years and this does not include the time to calculate the nonlinearity and dispersion profiles of the fibres. It is thus not feasible to apply a GA to this fibre design job with pulse propagation simulations included as a whole, which is referred as a "Full Genetic Algorithm Approach" (dashed blue arrows) in Fig. 5.1.1.

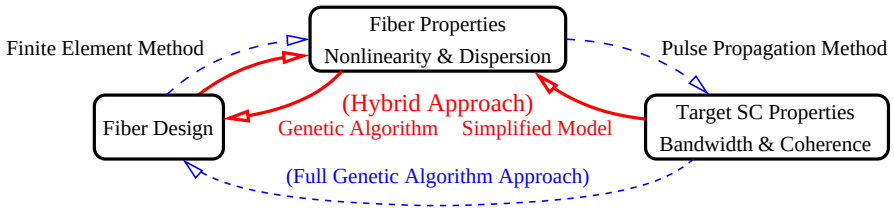

Figure 5.1.1: Schematics of full and hybrid GA approach. Dashed blue arrows form the full GA loop, solid red lines form the hybrid GA loop.

One approach to avoid doing pulse propagation simulation within the GA is to use a "Hybrid Approach". As the red solid arrows shown in Fig. 5.1.1, instead of using the full GA approach, this problem is solved with a two-step approach and apply GA only on one of the steps. The first step of the "Hybrid Approach" is to design an idealised dispersion and nonlinearity profiles that can result in SC generation with large bandwidth and high coherence that match the design requirements. This step can be achieved through a simplified model which uses abstracted dispersion and nonlinearity profiles to link the SC bandwidth and coherence to fibre dispersion and nonlinearity (see details in Section 5.2). In the second step, a GA is applied to optimise a fibre structure to let its dispersion and nonlinear profiles to approach the idealised dispersion and nonlinearity profiles constructed in the first step. Using the "Hybrid Approach", pulse propagation simulations are only invoked in the simplified model with which the total amounts of calculations are much less than in a "Full Genetic Algorithm Approach".

5.1.1 Chapter outline

In this chapter, the simplified model is firstly introduced and through the simplified model, a fitness function is defined for a GA model. Next, the GA model is used to optimised the structure. Nonlinearity and dispersion profiles are then calculated and inserted into the pulse propagation model to simulate the SC generation in the optimised structure. SC generation is simulated with a range of pumping wavelengths and the simulation outputs are then analysed and discuss. Finally, the SC generation in the optimised structure is compared to some other cases to find the keys to achieve both large bandwidth and high coherence in practice.

5.2 Simplified Models

SC generation can always be predicted numerically when all required initial conditions are provided. The main parameters that determine a SC generation are the

nonlinearity and dispersion profiles of the fibre as well as the parameters of the pulses themselves. Although the broadening process has random factors, noise, a basic understanding of the relations among fibre nonlinearity, dispersion, SC bandwidth and coherence still can be built up by exploring different combinations of nonlinearity and dispersion profiles. However, this exploration process is too complicated to be practical. That is why simplified models are required to explore the physics of combined linear and nonlinear processes involved in SC generation.

The simplified model will be used to provide guidelines for defining the fitness function for the GA. While the choice of a simplified model is not unique and it influences the accuracy of predicting the output SC in the final fibre. Because of this, it may require a few iterations before an appropriate simplified model can be decided for practical use. For example, nonlinearity and dispersion profiles are considered in terms of Taylor series, and take limited terms for the simplified model. The more terms are taken, the more accurate the model will be. Basically, this process trades accuracy and time for simplicity.

As a starting point, dispersion and nonlinearity are approximated to the first order, i.e. constant dispersion and nonlinearity are used. Noticing that although the group velocity dispersion D is constant, there still are high order $\beta's$ (such as $\beta_2 = -\frac{2\pi c}{\omega^2}D$, $\beta_3 = \frac{\pi c}{\omega^3}D$), which indicates high-order dispersion effects still exist in this simplified model. Therefore, this simplification of the model is more realistic than to consider β_2 as a constant for dispersion which removes all high-order dispersion related effects. Raman response function is included in the model since it is a key parameter for soliton-related dynamics. But this term is material related so that it is not a free parameter here. (Note that the model Raman response is determined by glass material and overlapping of the mode fields between pump, Stokes and anti-Stokes. However, the overlapping is considered as a constant in this work.) In this simplified model, the UV cutoff and IR cutoff are set at 0.4μm and 6μm respectively. The loss around the cutoffs is interpolated with exponential functions and the loss between these cutoffs is assumed to be zero. Loss is a linear effect

to the pulse propagating in the fibre. The loss profile is idealised in the simplified model since it is a linear effect. Further study of the loss on the SC bandwidth and coherence is given at the end of Section 5.4.3.

In the simplified model, SC spectra are simulated and bandwidth and coherence are calculated correspondingly for a range of constant dispersions and nonlinearities. Figs. 5.2.1 and 5.2.2 show the bandwidth (defined as the width at 20dB of the maximum point in the spectrum) and coherence variation of the SC generation of a 100 fs, 10 kW peak power pulse propagating along the fibre from 0 to 50 mm for values of D = -5 to 5 (ps/nm/km) and γ = 100 and 200 ($W^{-1}km^{-1}$). The basic trends of the spectral broadening and coherence degradation as shown in the figures can be summarised as follows:

1. The coherence decreases as either nonlinearity or dispersion increases, and it mainly happens in the anomalous dispersion regime,

2. The bandwidth increases as either nonlinearity or dispersion increases and it increases dramatically in the anomalous dispersion regime.

The explanations of the observation match previous report [55]. They can be concluded as

1. In the normal dispersion region, SPM dominated broadening maintains the coherence

2. In the anomalous dispersion region, MI and soliton fission are the main source of losing the coherence but they assist spectral broadening dramatically.

3. Large nonlinearity amplifies all nonlinear processes regardless of dispersion regimes.

It can be inferred from the results shown here that a broad bandwidth SC that is only limited by the transmission window of that fibre can readily be obtained

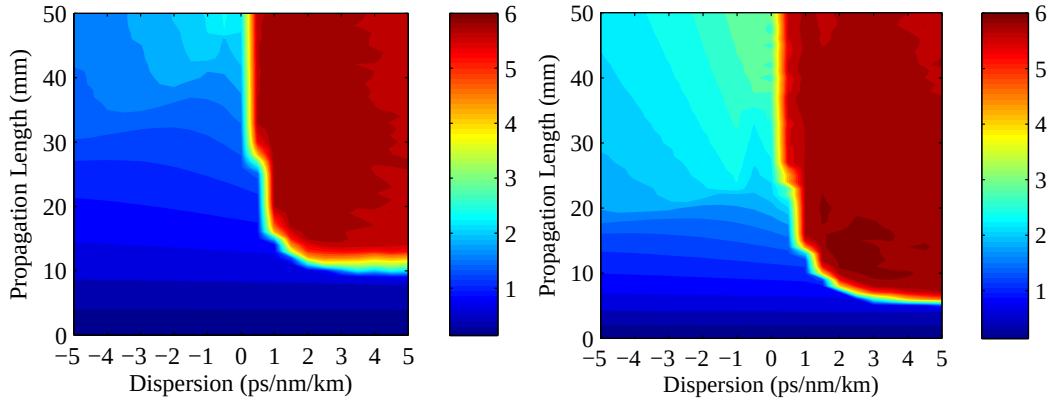

(a) $\gamma = 100W^{-1}km^{-1}$ (b) $\gamma = 200W^{-1}km^{-1}$

Figure 5.2.1: 20dB Bandwidth, in μm, of generated SC output with different constant dispersion D and nonlinearity γ at different propagation length.

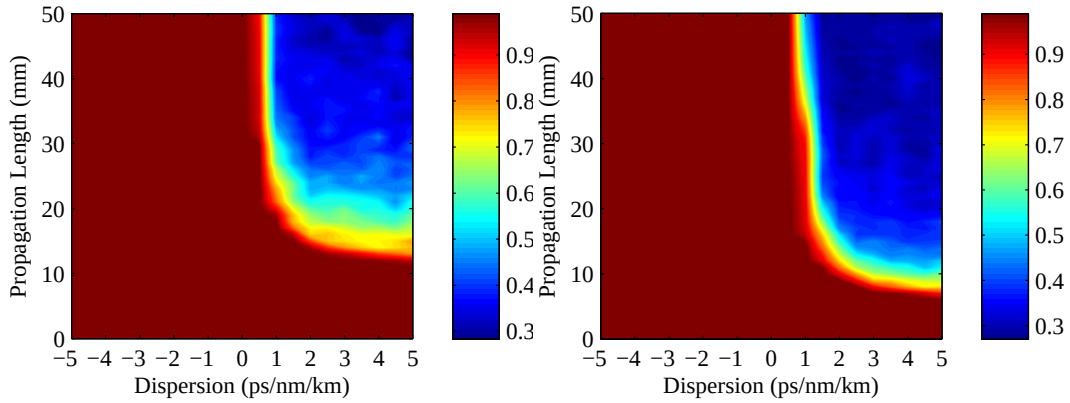

(a) $\gamma = 100W^{-1}km^{-1}$ (b) $\gamma = 200W^{-1}km^{-1}$

Figure 5.2.2: Coherence $< |g_{12}^{(1)}| >$ of the outputs of SC generation with different constant dispersion and nonlinearity at different propagation length. $< |g_{12}^{(1)}| > = 1$ is maximum value associated with perfect coherence

from SC generation based on fibres with the anomalous dispersion and large nonlinearity (Fig. 5.2.1). However, the coherence reduces dramatically in this regime. On the other hand, although the spectral broadening happens gradually in the normal dispersion regime (Fig. 5.2.2), a broad bandwidth can still be obtained with large nonlinearity and small absolute values of dispersion (for comparatively long

propagation lengths). Furthermore, no obvious coherence degradation is observed for small absolute values of dispersion. Therefore, for the purpose of designing a large bandwidth and highly coherent SC source, fibres with high nonlinearity and flat small absolute values of dispersion are preferred. It is worth mentioning that the conclusions obtained here are based on the definition of the simplified model. In reality, both nonlinearity and dispersion are wavelength dependent, and thus the broadening of pulses differs from the simplified model. However, this simplified model provides important information (at least to the first order) about the relation between SC bandwidth and coherence and fibre nonlinearity and dispersion, which forms the criterion for GA to design the fibre structure.

5.3 Fibre Structure Design with GA

5.3.1 The fitness function

With the information from the simplified model, the other half part of the "Hybrid GA" approach (Fig. 5.1.1), the GA optimisation, cab be carried on. As in Chapter 4, a the fitness function is needed to be defined for the problem. To do so one need to look at the conclusion of the simplified model; a low flat dispersion across a large wavelength range and as high as possible nonlinearity at the pump wavelength. A straightforward definition of the fitness function can be,

$$F = \gamma_{pump} \times (\sum_i |D_i|)^{-1} \tag{5.3.1}$$

where γ_{pump} is the nonlinearity at pump wavelength and D_i are the dispersion values at several wavelengths across the wavelength region for which one can strive for flat dispersion. The reason for taking the summation in Eq. 5.3.1 instead of integrating is to reduce the number of points used in the calculation to speed up the modelling. This fitness function is consistent with the results of our simplified model in Sec. 5.2 that large nonlinearity and small absolute values of dispersion are required for large

bandwidth highly coherent SC generation, since both large nonlinearity and small dispersion will result in large fitness. This is not the only definition for the fitness function that could be used. Other choices can also be used as long as the fibre structures converge as the fitness increases (or decreases).

There are some things to be concerned. In a real fibre, the material dispersion always exhibits large negative values at short wavelengths and large positive values at long wavelengths. The waveguide dispersion cannot cancel the material dispersion in those regimes unless the fibre structure is operating in the extreme sub-wavelength regime (when the core size is much smaller than the wavelength). In such cases, both material and waveguide dispersion are insensitive to the fibre structure. For fibres with relatively large core diameters, the cutoff wavelength of glass transmission is usually reached before the dispersion at that wavelength becomes insensitive to the structure. Therefore, in the dispersion profile of a non-sub wavelength fibre, there still are large negative and large positive values at short and long wavelengths respectively. Only in the middle region, where waveguide dispersion values can have similar magnitude of material dispersion, that the total dispersion can be effectively manipulated via the choice of the fibre structure.

In order to map out this region, a simple model is applied on a range of Tellurite suspended-core fibres (also referred as Wagon-Wheel (WW) fibres) with different core diameters. Fig. 5.3.1 shows the dispersion profiles of these fibres with the core diameter from 0.3 to 1.1 μm. The thick black curve in the figure shows the difference in between maximum and minimum dispersion values among these fibres. This curve indicates the dynamic range ($|D_{\min} - D_{\max}|$) that a waveguide can alter the dispersion with these core diameters. The thick black dashed curve in the figure represents the material dispersion of the glass. As mentioned earlier, the wavelength region of interest lays in the region where the dynamic range is larger than the value of material dispersion. It can be seen from the figure that the black solid curve becomes larger than the material dispersion for wavelengths longer than 750 nm. Therefore, 750 nm is the lower limit for dispersion control. On the long wavelength

side, material dispersion of Tellurite glass increases slowly with only 260 ps/km/nm at 6 μm which is well within the range of the dynamic range. Therefore, wavelengths longer than 750 nm are the wavelength range of interest of the fibre design work.

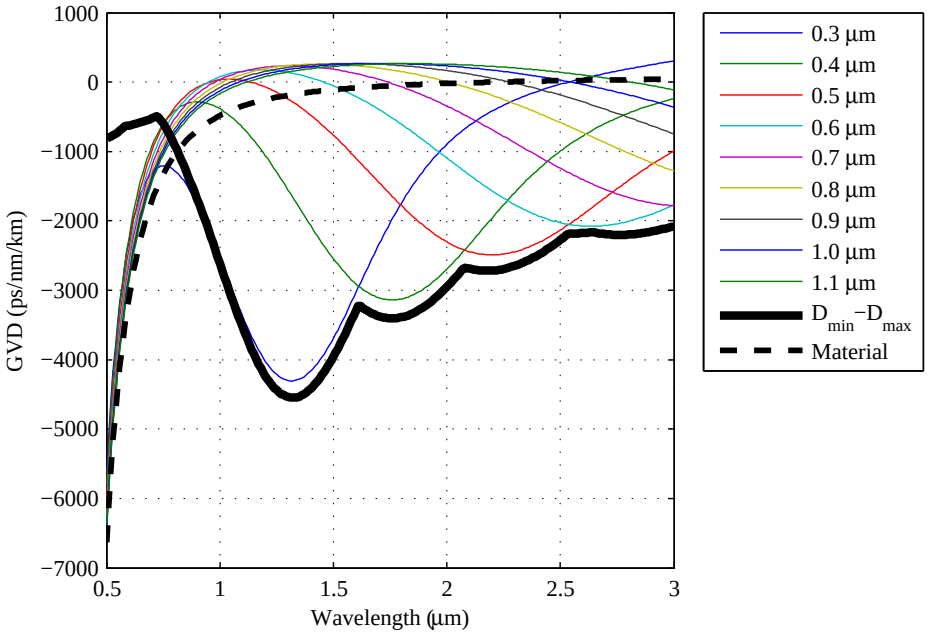

Figure 5.3.1: Dispersion profiles for a range of Tellurite WW fibres with different core diameters. Thick black line shows the max difference in D, which indicates how much fibre dispersion can be altered through waveguide effects. Thick black dashed line shows the material dispersion of Tellurite glass.

For simplicity and to make the numerical calculation viable, only three dispersion values at wavelengths λ = 2000 nm, 2500 nm and 3000 nm are used for the summation on the denominator of Eq. (5.3.1). To calculate the second derivative of effective refractive indices, at least three points around each wavelength are needed which results in 9 wavelengths to be solved for eigenvalues. Totally 1000 samples are used for the population. To avoid the explosion of the fitness value as the denominator approaches 0, limits are set to the dispersion values: the minimum values of $|D_i|$ is 1.

5.3.2 The results of GA

GA started with the same initial structure (Fig. 4.2.2) as used in Chapter 4. GA converged smoothly and after 6 iterations the output structures looked like Fig. 5.3.2. Fig. 5.3.2 shows the structures with highest fitness values which are larger than 90% of the maximum fitness. By comparing these structures, one can find that the cores of these structures are almost identical. The variations in the outer structure (the outer ring) indicate that the outer ring of glass is not sensitive to the dispersion and nonlinearity profiles in the wavelength region from 2 to 3 μm.

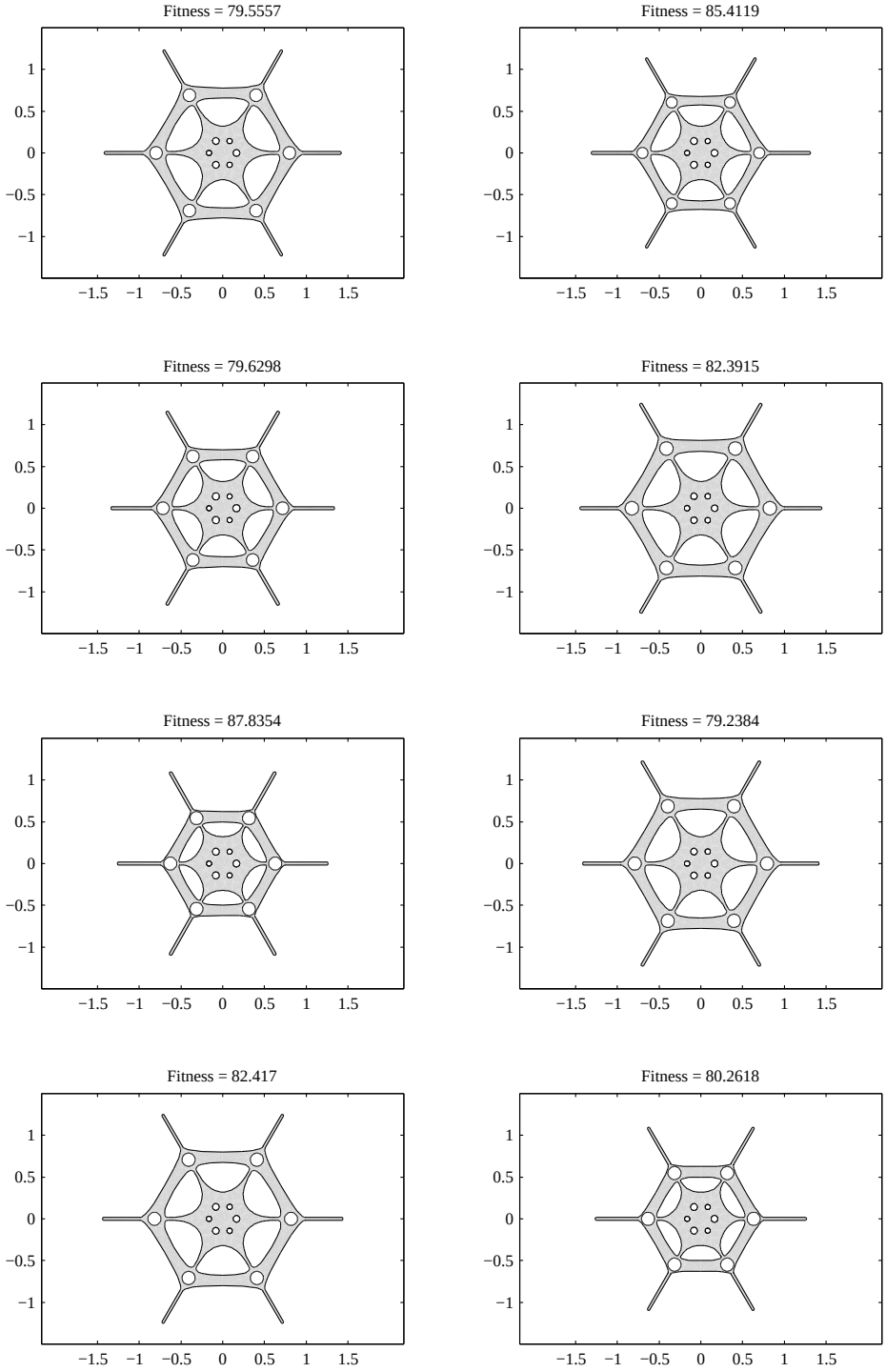

Figure 5.3.2: Fibre geometries in last generation whose fitness values are larger than 90% of the maximum fitness in that generation

Figs. 5.3.3a&b show the dispersion and nonlinearity profiles of the structures in Fig. 5.3.2. All of the dispersion profiles (Fig. 5.3.3a) show low flat region between $2 \sim 3$ μm shown in Fig. 5.3.3b. Within this wavelength region, the maximum dispersion value is 2.5 $ps/nm/km$ and the minimum is -2 $ps/nm/km$, the range of nonlinearity at 2 μm is from $161 \sim 193$ $(W^{-1}km^{-1})$ and the nonlinearities decrease as wavelength increases due to the increase of mode areas.

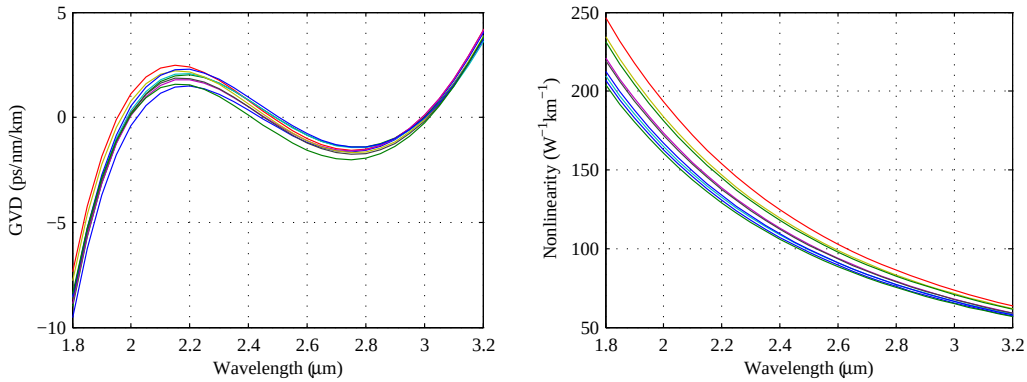

(a) (b)

Figure 5.3.3: The optimised structures with fitness values larger than 90% of the maximum fitness of the whole population (a) Dispersion (b) Nonlinearity.

The fitness values of these structures are larger than 90% of the maximum fitness of the whole population are plotted in Fig. 5.3.4. Within 10% variation in fitness values, a maximum variation of 1.5 $ps/nm/km$ in dispersion and 33 $W^{-1}km^{-1}$ in nonlinearity at 2 μm can be found.

The variations of each parameter of the structures are listed in Table 5.3.1. There are only 9 structures that have fitness values within the 10% variation of the maximum fitness. To obtain more representative results, we also did the calculation with samples whose fitness is larger than 75% of the maximum.

The relative errors $Err_{90\%}$ and $Err_{75\%}$ in Table 5.3.1 show the relative change of each structural parameter within the subset, which indicates the relative importance of each parameter to the fitness. From this table, it can be noticed that the position

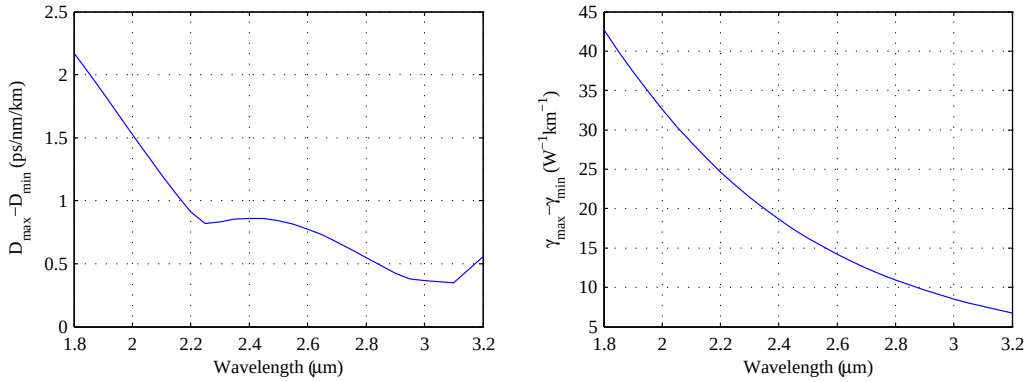

(a) (b)

Figure 5.3.4: The relative difference in nonlinearity and dispersion profiles among the optimised structures shows in Fig.5.3.2 (a) Dispersion (b) Nonlinearity.

Table 5.3.1: Statistics of the structure parameters

	$Avg_{90\%}^{(\mu m)}$	$Std_{90\%}^{(nm)}$	$Err_{90\%}^{(\%)}$	$Avg_{75\%}^{(\mu m)}$	$Std_{75\%}^{(nm)}$	$Err_{75\%}^{(\%)}$
R1	1.64	7.42	0.45	1.64	8.03	0.49
r1	0.40	11.6	2.88	0.40	10.1	2.49
r2	0.32	8.91	2.81	0.32	8.14	2.57
R3	3.20	9.46	0.30	3.20	8.50	0.26
R4	6.14	782	12.7	6.24	654	10.48
L1	1.20	83.9	6.97	1.17	176	15.02

of the six holes in the central region (R1) and the amount of glass around these holes (R3) are particularly critical (smallest relative error $Err_{90\%}^{(\%)}$ and $Err_{75\%}^{(\%)}$). The size of the centra six holes are also important parameters. The standard deviations of r1 and r2 are smaller than the difference between them, which means r1 and r2 need to be different in order to have fine control of dispersion and there are at least two localised solutions around the average radius of these two since the symmetry of the fibre geometry shows they are exchangeable. The influence of the outer ring (R4)

and its thickness (L1) is clearly less. These results shows that, in fabrication, more attention needs to be paid to the central structure rather than outer parts, which is unsurprising. Later in Chapter 6, when the fabrication of the fibre is considered, the designed structure is simplified. The outer-most ring of glass is removed in the fibre preform. According to the study shown here, the modification in the preform should have limited influence to the dispersion and nonlinearity profiles of the fibre.

5.4 SC Generation

As discussed in Section 5.3, unlike the ideal constant dispersion cases, any practical fibres always have a large negative (normal) and positive (anomalous) dispersion for short and long wavelengths respectively. The fibre nonlinearity is also wavelength dependent. Nonlinearity decreases as wavelength increases as results of the decrease of nonlinear refractive index and the increase of effective mode area. These wavelength dependencies make the choice of pumping wavelength critical for SC generation (in practice, one should choose the pumping wavelength before designing and optimising the fibre). To investigate this in detail, the optimised fibre structure developed in the previous section is used and predictions of SC generation with 10 kW peak power and 100 fs pump pulses are shown for pump wavelengths ranging from 1500 to 3500 nm.

5.4.1 Spectrograms

Fig. 5.4.1 shows the spectrograms of the SC output of a 5 cm fibre with different pump wavelengths from 1500 to 3500 nm with 100 nm interval. The spectrograms provide an intuitive view of the SC output in both temporal and spectral domain and the correlation between them. From the figure, one can see that 1) large bandwidth (beyond 4 μm) are easily achieved almost for all pumping wavelengths, 2) there are no significant walk-off between different wavelengths in the spectra (all spectral components are around the centre of the pulse, Time $t = 0$) and 3) soliton dynamics

especially soliton fission process are not dramatic (in the figure, the solitons are corresponding to the parts between $3 \sim 6\ \mu m$ which move away from $t = 0$ towards $t > 0$) and only happen for pumping wavelengths longer than $2.5\ \mu m$.

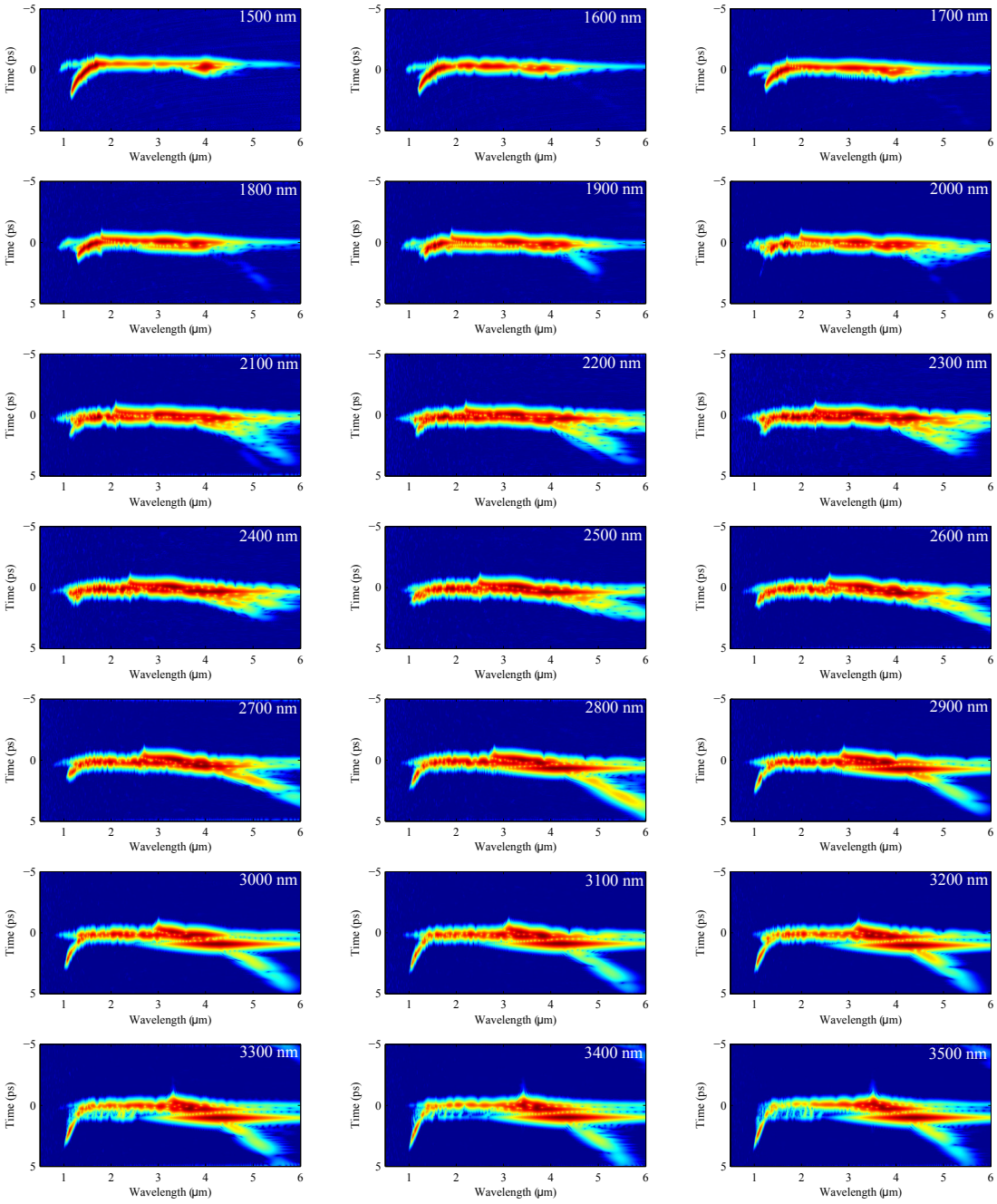

Figure 5.4.1: Spectrogram of SC generation in an optimised fibre.

5.4.2 Bandwidth and Coherence

Figure 5.4.2 shows the bandwidth and coherence of the pulses propagating along the fibre. Recall that the fibre design developed in previous section is optimised for SC generation in the spectral region of $2 \sim 3\mu m$ (region between the dashed lines). In this region, as indicated in Fig. 5.4.2, the bandwidth initially increases as pump wavelength increases. However, this is then followed by a decrease and an increase as the pump wavelength increases towards the end of the spectrum ($\sim 3\mu m$). On the contrary, the coherence first decreases and then increases as the pump wavelength increases.

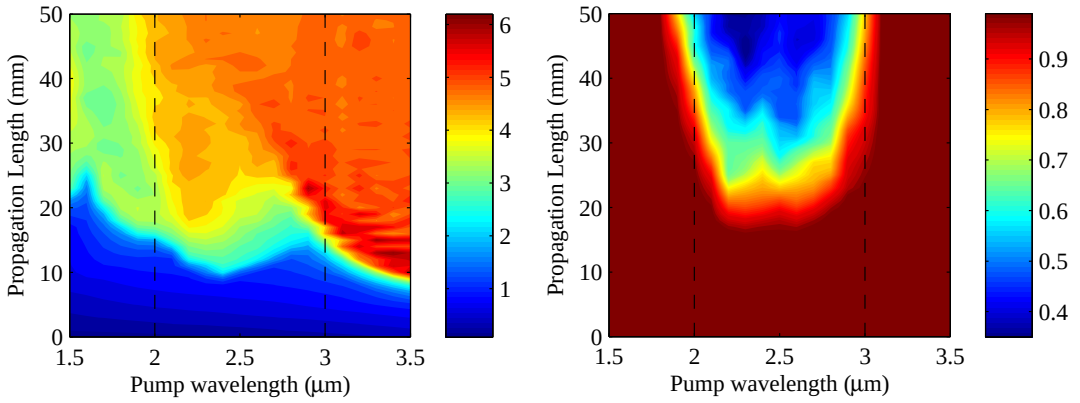

Figure 5.4.2: Simulated bandwidth (left) and coherence (right) of SC outputs with different pump wavelengths in the optimised fibre. Between the vertical dashed lines is the region of optimisation.

According to the results of the simplified model, large values of nonlinearity or dispersion result in large bandwidth and low coherence, small values of nonlinearity or dispersion result in small bandwidth and high coherence. The changes in the bandwidth and coherence in Fig. 5.4.2 are due to the increase of dispersion and decrease of nonlinearity at long wavelengths. For a certain propagation length, e.g. 20 mm, the pulse spectrum moves into the flat near-zero dispersion region when the pump wavelength moves from 2 to 2.2 μm, and then moves gradually into the anomalous dispersion region when the pump wavelength from 2.2 to 3 μm. However,

during this process, the nonlinearity drops more than a half as the pump wavelength increases from 2 to 3 μm. This is the reason why the bandwidth decreases for pump wavelengths around $2.5\mu m$ and the coherence increases slightly around the same region.

Figs. 5.4.3∼5.4.6 show the details of the evolution of the pulse intensity and coherence spectra at different pump wavelengths. From these figures, we can learn the cause of coherence degradation in these examples and understand SC generation to a more fundamental level.

When the pump wavelength is in the normal dispersion region and far from the first ZDW (1500 $\sim$ 1700 nm), it is known that the main broadening mechanism is through SPM as one can see in Fig. 5.4.3, which is a highly coherence process. The FWM process accompanied (from 25 $\sim$ 50 mm length at 4 μm in Fig. 5.4.3top) also becomes coherence since it is seeded by spectra generated through SPM. These are the main reasons highly coherent output is observed.

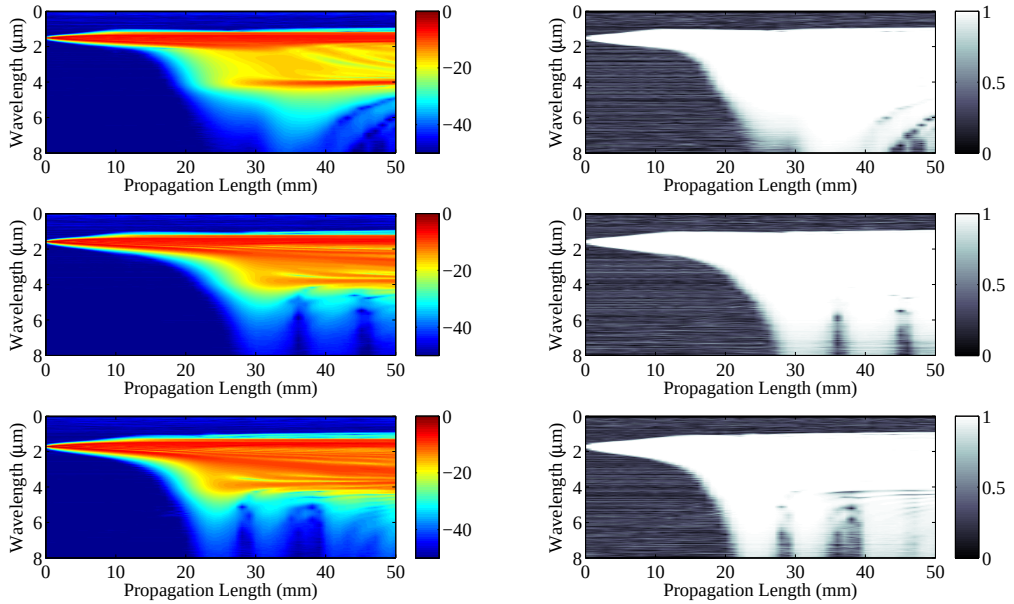

Figure 5.4.3: Normalised intensity (left) and coherence (right) spectrums of pulses propagating along the optimised fibre pump at 1.5, 1.6, 1.7 μm from top to bottom respectively.

As the pump wavelength moves towards the flat zero dispersion region, FWM/MI starts to kick in earlier and eventually the noise initialised parametric sidebands, which are not coherent, start to interfere with the SPM broadened spectrum. This can be seen in Fig. 5.4.4 $\sim$ 5.4.5.

Noticing the growth of the sideband around 4$\sim$6 μm from 5 cm length, once these sidebands merged into the central spectra, the coherence starts to decrease. However, these sidebands appear to be important for achieving large bandwidth.

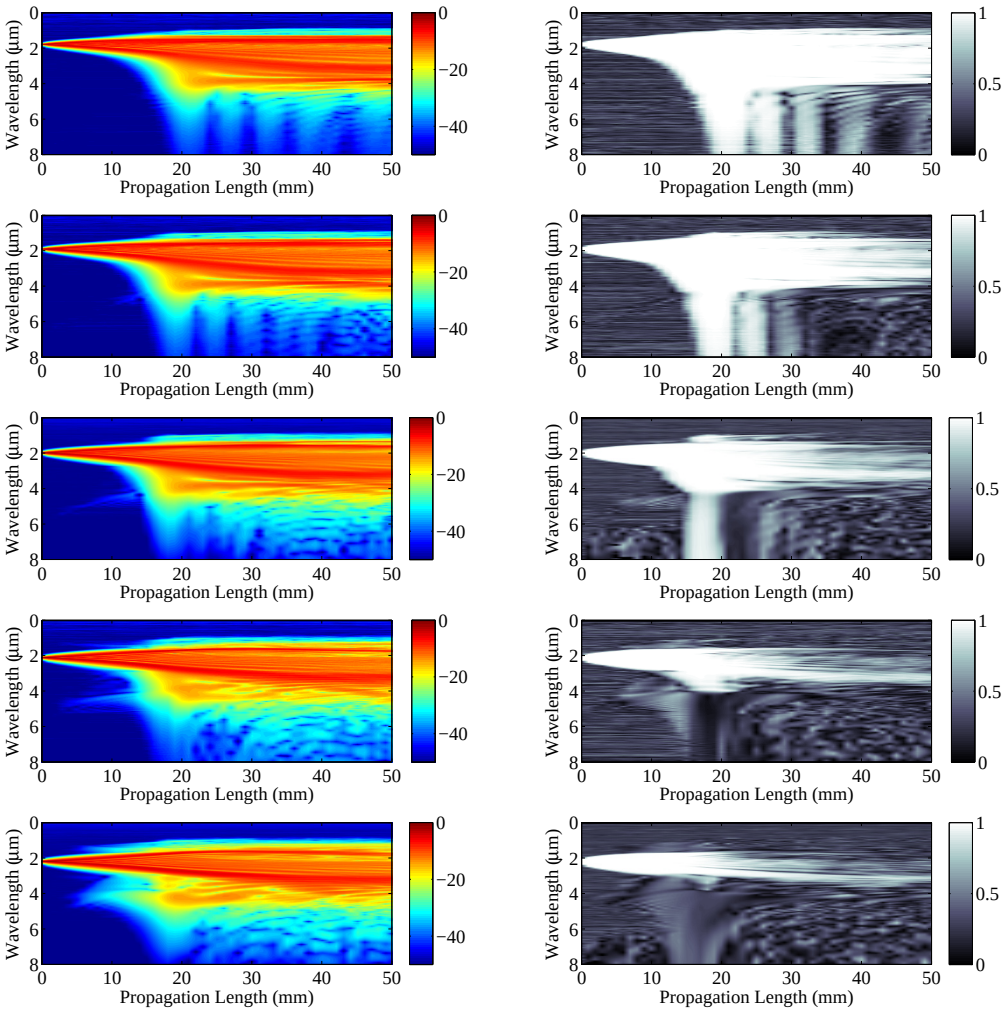

Figure 5.4.4: Normalised intensity (left) and coherence (right) spectrums of pulses propagating along the optimised fibre pump at 1.8, 1.9, 2.0, 2.1 and 2.2 μm from top to bottom respectively.

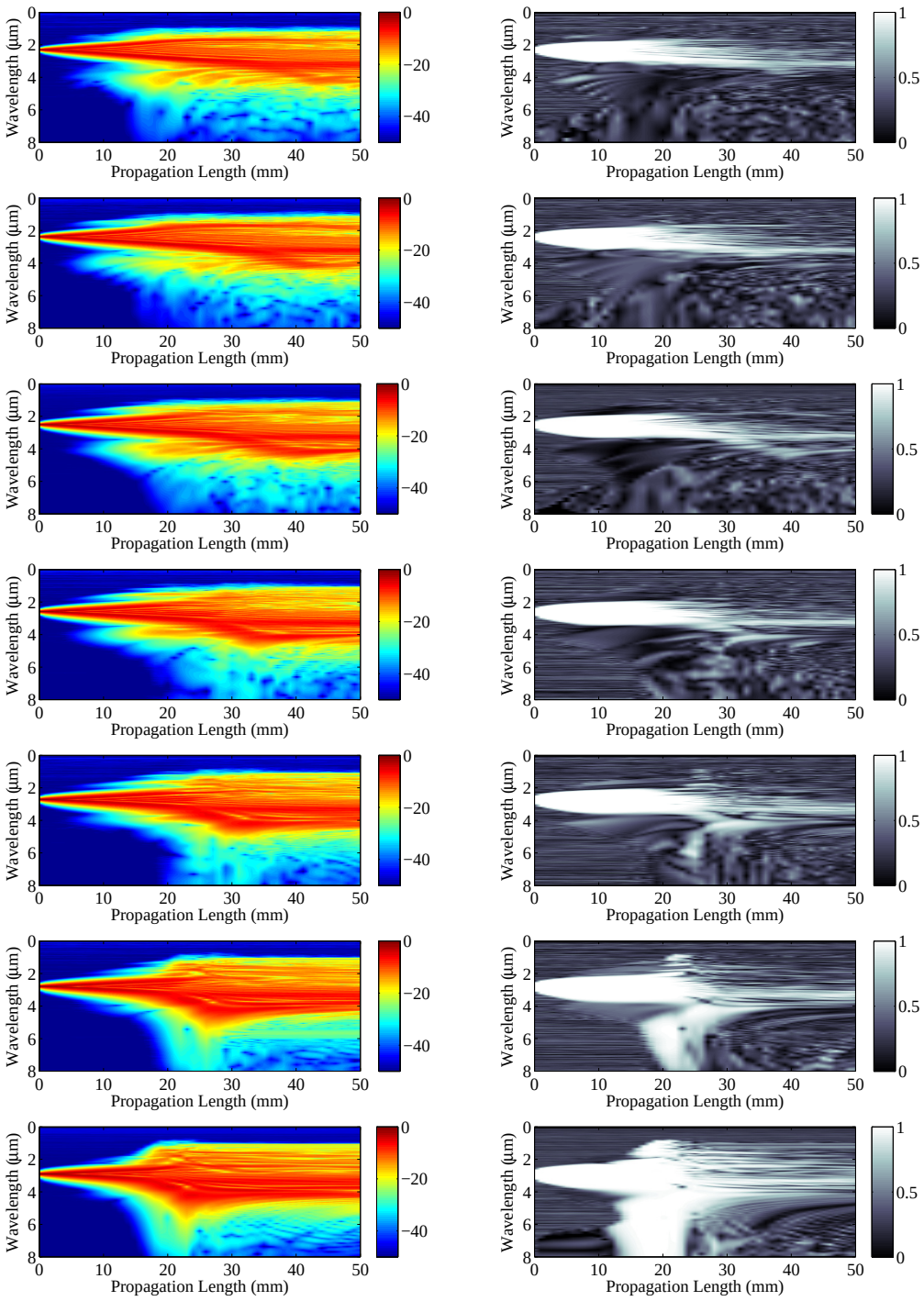

Figure 5.4.5: Normalised intensity (left) and coherence (right) spectrums of pulses propagating along the optimised fibre pump at 2.3, 2.4, 2.5, 2.6, 2.7, 2.8 and 2.9 μm from top to bottom respectively.

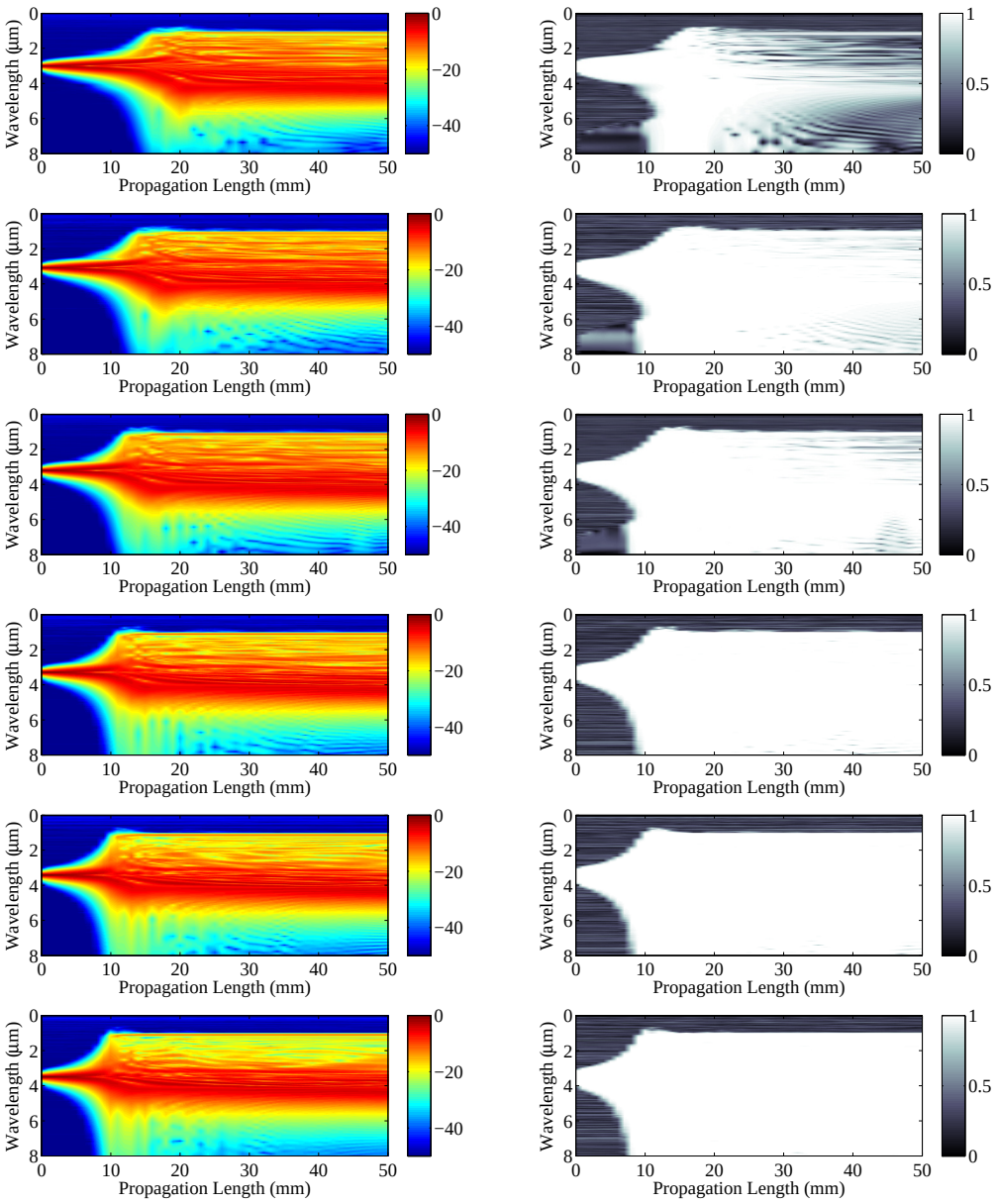

Figure 5.4.6: Normalised intensity (left) and coherence (right) spectrums of pulses propagating along the optimised fibre pump at 3.0, 3.1, 3.2, 3.3, 3.4 and 3.5 μm from top to bottom respectively.

Further shifting the pump wavelength into the anomalous dispersion region, the MI sidebands disappear again within the propagation length due to the decrease of nonlinearity. The soliton-related processes, for these cases, were not dramatic, which

result in high coherence as seen in Fig. 5.4.6. Noticing that, although the wavelength spans in these cases are larger than the ones pumped in the flat dispersion region ($2 \sim 3\ \mu m$), the frequency spans in these cases are not.

5.4.3 Comparison and Discussion

In order to show the improvement of bandwidth and coherence that can be achieved with the optimised structures, the SC outputs of the optimised fibres are compared with that of a $10\mu m$ diameter tellurite glass rod surrounded by air which also has zero dispersion around $2\mu m$. The dispersion (un-tailored) profile of the rod calculated using the same Sellmeier equation as we used for our new design, is shown in Fig. 5.4.7.

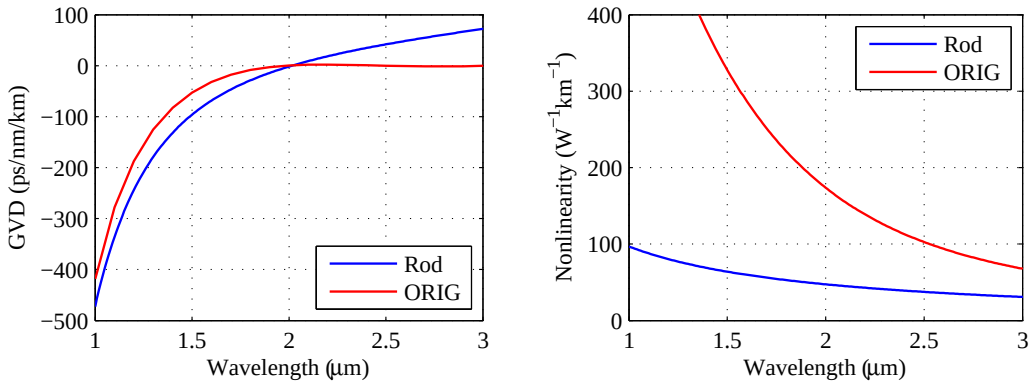

Figure 5.4.7: Dispersion and nonlinearity of a $10\mu m$ diameter Tellurite rod surrounded by air (Blue), and the optimised fibre (Red)

Fig. 5.4.8 and Fig. 5.4.9 shows the comparison of the SC bandwidth and coherence of three cases: a) the optimised structure, b) 10 μm rod and c) an artificial case of a 10 μm rod with the nonlinearity of the optimised structure. Fig. 5.4.8 is the evolution of the intensity and coherence spectra of SC generation along the propagation direction. The pump wavelength is 2 μm. Case b) does not display much spectral broadening although the coherence is high due to relatively low nonlinearity of the rod (47.3 $W^{-1}km^{-1}$ at 2 μm). Recall the optimisation of our design

is to achieve high coherence as well as large bandwidth. So case b) is not ideal. Case c) has a larger bandwidth than case b) due to higher nonlinearity. Comparing c) to a), the bandwidth of c) broadens at a shorter propagation length than a) but the final bandwidth of c) is not as large as a) and its coherence is also lower than the one of a). Fig. 5.4.9 shows the same conclusion in a different form. These comparisons show that the fibre structure optimised by the hybrid GA approach does have better SC performance in terms of both large bandwidth and high coherence than conventional fibre designs.

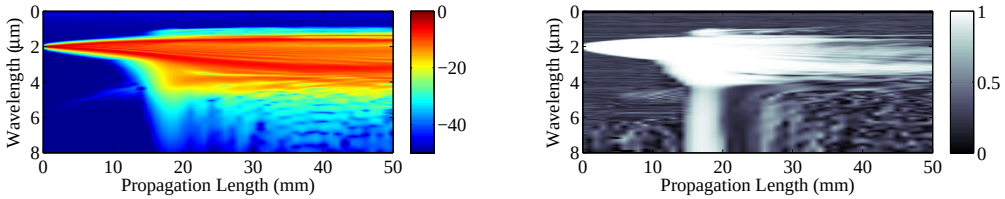

(a) Optimised structure

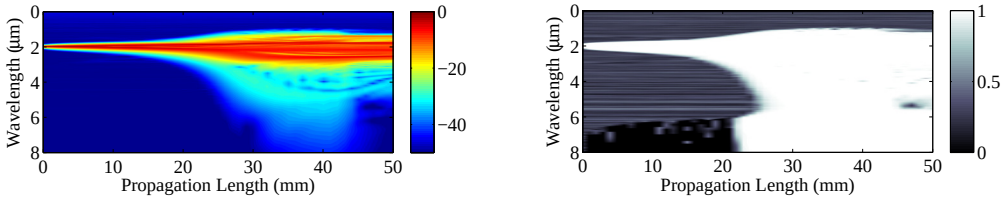

(b) 10 μm diameter rod

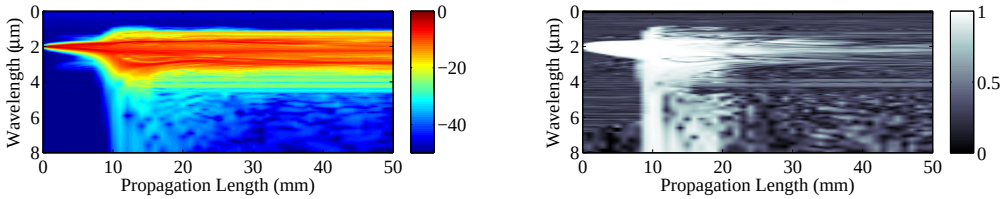

(c) 10 μm diameter rod with the nonlinearity profile of optimised structure

Figure 5.4.8: Intensity (left) and coherence (right) spectra of a pulse propagating along the fibre with different dispersions and nonlinearities. a) For dispersion and nonlinearity profiles of optimised structure, b) for dispersion and nonlinearity profiles of 10 μm diameter rod, shown in Fig. 5.4.7, c) for dispersion profile of 10 μm diameter rod with nonlinearity profile of the optimised structure.

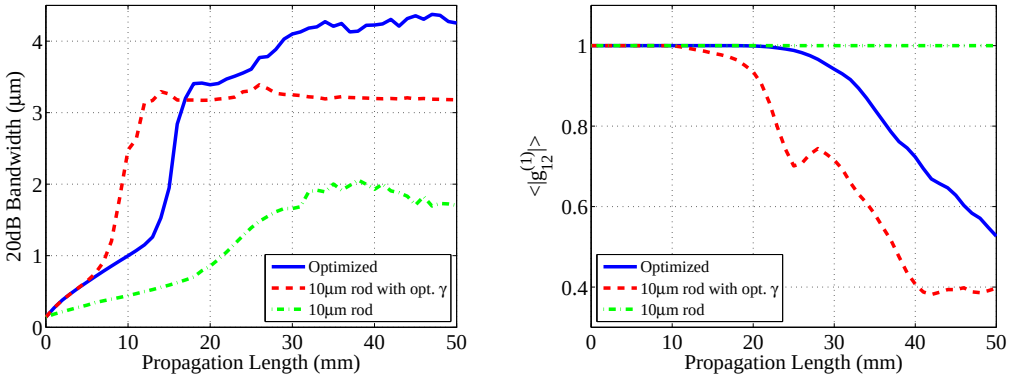

Figure 5.4.9: 20dB bandwidth (left) and coherence (right) of SCG with dispersion and nonlinearity profiles of optimised structure, 10 μm diameter rod and 10 μm diameter rod with nonlinearity profile of optimised structure.

From the results above, it can be concluded that the cause of coherence degradation is mainly due to the spontaneous (noise initialised) FWM/MI sidebands. If these nonlinearity processes can be suppressed then coherence can be maintained. The key to achieve this is to further tailor the anomalous dispersion tail from $3\mu m$.

To prove this point, the coherence of the SC with the dispersion profile of the optimised fibre is compared to the ones from a couple of artificial dispersion profiles as shown in Fig. 5.4.10. The dispersion profile MOD1 is modified based on profile ORIG where the flattened region is extended from $2 \sim 3\mu m$ to $2 \sim 4\mu m$. The dispersion profile MOD2 is obtained by inverting the tail of ORIG profile from the point when the derivative is zero. The third artificial dispersion profile MOD3 is also obtained by inverting the tail of MOD1 profile. Fig. 5.4.10b shows the behaviour of coherence as a function of propagation length for all the profiles. The behaviour of coherence in MOD1 is similar to ORIG, i.e., it decreases after a certain length of propagation, but the degradation happens at longer lengths compared to ORIG. In contrast, MOD2 and MOD3 do not show any obvious loss in coherence.

In practice, MOD2 and MOD3 dispersion profiles are very difficult to achieve due to the nature of material dispersion. However, MOD1 is practical. From these

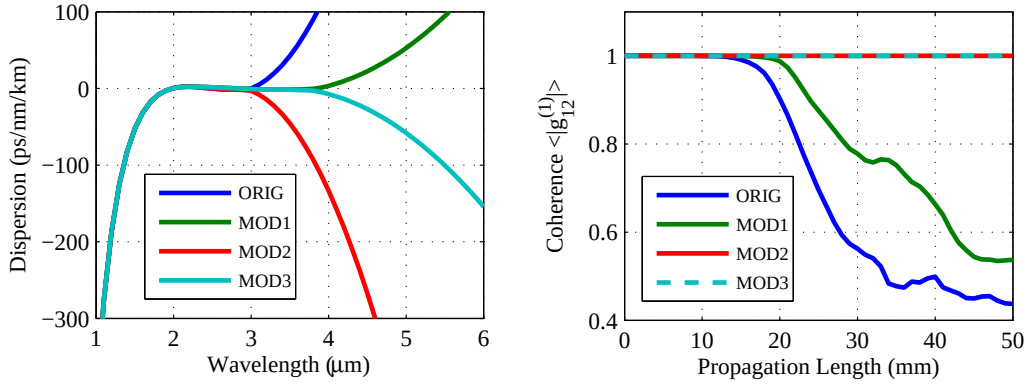

(a) (b)

Figure 5.4.10: Dispersion curves and corresponding coherence of the SC outputs. Curve ORIG is the original dispersion curve calculated from GA modelling, MOD1 to MOD3 are the artificial dispersion curves

results, it can be summarised that better SC coherence can be achieved in fibres with a wider flat region than the current design. The coherence of SC generation can also be improved by taking advantage of the fibre loss. A flat dispersion profile similar to ORIG with the anomalous dispersion region locates beyond the IR loss edge of the fibre can effectively suppress the effects of anomalous dispersion to the SC generation and therefore enhance the coherence of the SC.

Fig. 5.4.12a shows the SC intensity and coherence spectra with an artificial loss profile Fig. 5.4.11. The artificial loss has UV cutoff at 500 nm and IR cutoff at 3 μm right before the anomalous dispersion appears. Comparing to the same case without loss in Fig. 5.4.12b, the increase of coherence is significant. It worth mentioning that the fibre we fabricated for this work (see Chapter 6) has IR cutoff around 3 μm which is preferred for maintaining high coherence.

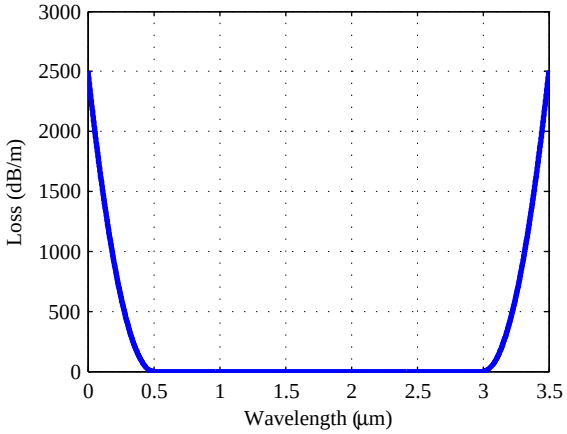

Figure 5.4.11: Artificial loss of the fibre.

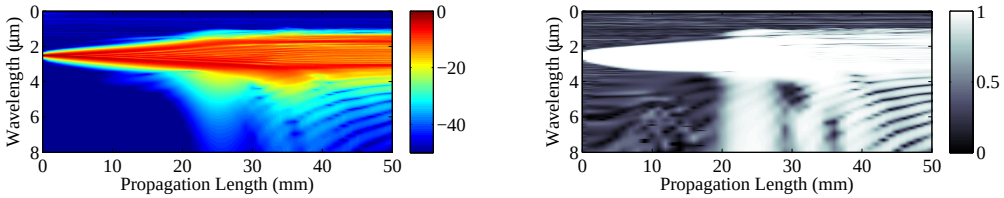

(a)

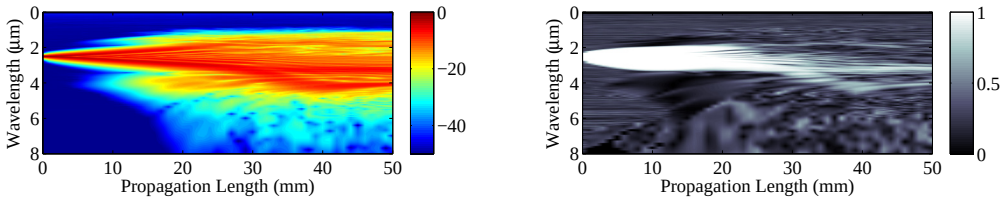

(b)

Figure 5.4.12: The comparison of the intensity (left) and coherence (right) spectra for fibre with artificial loss (a) and without (b).

5.5 Summary

Building on the previous chapter, the GA was developed for design and optimising fibres for a more complicated nonlinear process, SC generation, and target for SC generation with both large bandwidth and high coherence. Unlike the parametric process, the complex nature of SC generation cannot be characterised using simple

analytic expressions. An indirect approach has to be used to help define the fitness function. A simplified model is then developed.

The simplified model trades time and accuracy for simplified relations between fibre dispersion/nonlinearity and SC bandwidth/coherence. With approximating the nonlinearity and dispersion profiles to the first order, it can be summarised that to obtain SC with large bandwidth and high coherence, a fibre with near zero and flat dispersion across as large as possible wavelength range and as large as possible nonlinearity at the pumping wavelength is needed.

With the help of the simplified model, a fitness function was defined for the GA and by considering the material dispersion and our target, SC generation in mid-IR, the fitness function is chosen to flatten and zero the dispersion from $2 \sim 3\ \mu m$ and maximised the nonlinearity at $2\ \mu m$. The GA used 6 generations to produce the optimised structures and the statistic study shows nonlinearity and dispersion profiles corresponding to these structures are very sensitive to the structural parameters, which indicates special cares need to be taken in fibre fabrication.

The SC generation in the optimised structure shows interesting results. It can be summarised as following points: (1) For all pumping wavelengths from 1500 to 3500 nm, a minimum spectral span of $4\ \mu m$ can be obtained at 5 cm length of propagation. (2) No coherence degradations were observed for pumping wavelength below $2\ \mu m$ and beyond $3\ \mu m$. Within the region of interest, $2 \sim 3\ \mu m$, coherence degrades starting from 2 cm of propagation, however signs of coherence improvements are also observed. (3) Because of the small dispersion over a wide wavelength range, these is no significant walk-off across the whole pulse spectra been observed after the propagation.

To prove the coherence and bandwidth of the SC for the pumping wavelength between $2 \sim 3\ \mu m$, comparisons are made between the optimised SC to SC generation in non-optimised structures. The comparison results indicated that the GA balanced the bandwidth and coherence of the optimised structure and produced an overall better SC than a non-optimised structure.

From the simulation, it can be noticed the cause of coherence degradation is due to the incoherent noise initialised FWM/MI sideband interferes with the coherent pump pulse. And it is found that the key to improve coherence is to effectively remove the anomalous dispersion tail by design fibres so that the anomalous dispersion tail locates beyond the IR transmission edge. The numerical simulation with an artificial loss profile proves the concept and shows tremendous improvement of coherence for the case the pumping wavelength at 2.5 μm which used to have poor coherence at 5 cm propagation length. The IR edge of the artificial loss profile approximates the glasses we used for the fabrication. This promises possibility of producing fibres for SC with large bandwidth and high coherence in practice.

In the next chapter, the fabrication of the optimised fibre is presented.

Chapter 6

The fabrication of the designed fiber

6.1 Background

In Chapter 4 and 5, structures were designed for two nonlinear applications, a femtosecond OPO and a coherent SC source. The fabrication of a structured fibre with a specified design needs multiple trials which require a significant mount of resources and time. To accomplish our research within limited time and resources, we choose one structure among our designs for fabrication.

To determine which structure should be fabricated, we first review all the optimised structures of FOPO and SC generation applications. For the SC application, the structural variations between the optimised structures (Fig. 5.3.2 & Table 5.3.1) are relatively small compared to typical fabrication distortion, which indicates the margin of error for fabrication is small and there is no room in the structural parameters to compromise for the FOPO application. However, on the other hand, the FOPO application, the study shows that more than one structure can achieve the same outcome (Fig. 4.2.6) and it is difficult to distinguish which one is significantly better than the other. Furthermore, among the optimised structures for the FOPO

application (Fig. 4.2.6), there are structures similar to that of the SC application, which indicates the structure designed for SC application may also be used for the FOPO. Therefore, we decided to use the structure optimised for SC generation as the candidature for fabrication.

The statistical study in Chapter 5 Table 5.3.1 shows the averaged value of the structural parameters, we will use these parameters for the fabrication with two modifications. From the modelling, we realise that the outer-most-ring of glass in the design has relatively small effects to fibre's nonlinearity and dispersion profiles but its existence greatly increases the fabrication challenges. Hence, this ring of glass is removed from the design (see Fig.6.1.1). Apart from this ring, the holes of the inner-most ring have two sets of sizes. If we apply the typical 10% fabrication distortion onto the parameters, the difference in the size of the inner holes can be ignored. Therefore, we will use an average size for all six holes. Once the structural parameters are determined, R1 = 1.64, r1 = 0.36, r2 = 0.36, R3 = 3.20, R4 = 6.14 and L1 = 1.20 μm (refer to Chapter 5), the fabrication process can be proceeded.

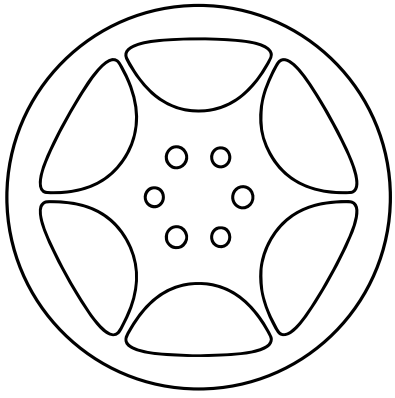

Figure 6.1.1: The modified structure for fabrication.

In this Chapter, all fibre drawing procedures were performed by colleague Mr. Roger Moore, other fabrication steps including die design and preform extrusion were preformed by myself.

6.2 Trial one

To fabricate structured fibre, a structured preform must be fabricated first. An extrusion fabrication method was used to fabricate the fibre preforms [153]. The extrusion fabrication method uses a die which resembles an engraved image of the preform structure. During the extrusion procedure, the heated and softened glass billet is extruded through this die. The glass will be divided and re-fuse inside the die. The key of design such die is to make the glass flow through the die smoothly and fully merge before exit. Also it is necessary to consider the inevitable distortion during the fibre pull where surface tension of the glass and gas pressure within the holes will play a significant role in modifying the preform structure. Ultimately, it will be necessary to reverse design a structure in the preform that when it is stretched it will match the desired structure in the fibre.

6.2.1 Die design: Version 1

The first die design consists of three parts, jacket (Die-Jacket), strut (Die-Strut) and core (Die-Core) parts. The reason of separating the die into three parts is for the convenience of the die fabrication. Fig. 6.2.1, 6.2.2 and 6.2.3 show the drawings of the Die-Jacket, Die-Strut and Die-Core respectively and Fig. 6.2.4 shows the computer illustrated effect pictures of die from different view angles.

In the die, the preform core was designed as a hexagon in shape. I predicted based on prior experience that when the preform is finally pulled into fibre, the six struts around it will pull the six corners of the hexagon away under the surface tension of the glass. Eventually, the edges of the hexagon will merge with the struts and form parabola-like curves.

The glass billet initially sits on top of the die. When it is extruded through the die, the main funnel in the core part provides smooth transition for the glass to flow into the 6 holes. The 6 holes align with the gaps of the six struts in Die-Strut. In Die-Strut, apart from the thin strut gaps, the horizontal funnels allow the glass to

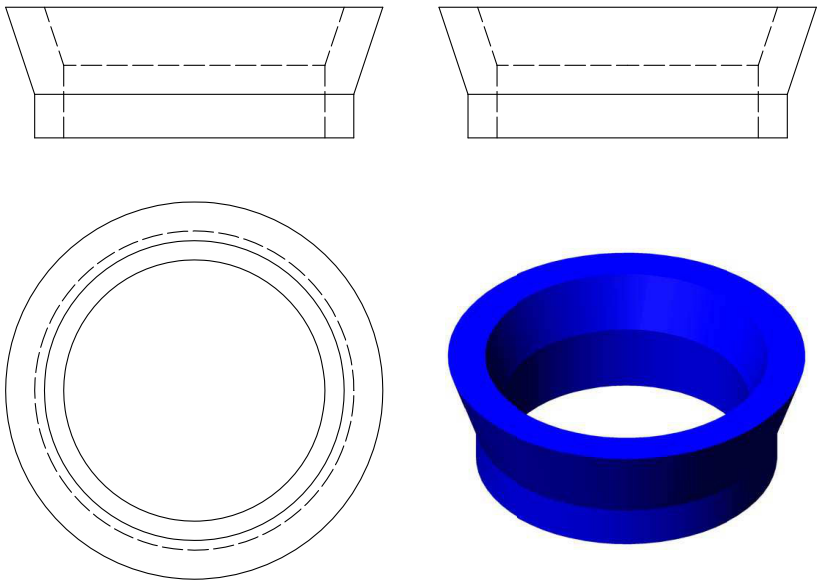

Figure 6.2.1: Drawing of the die jacket part (Version 1).

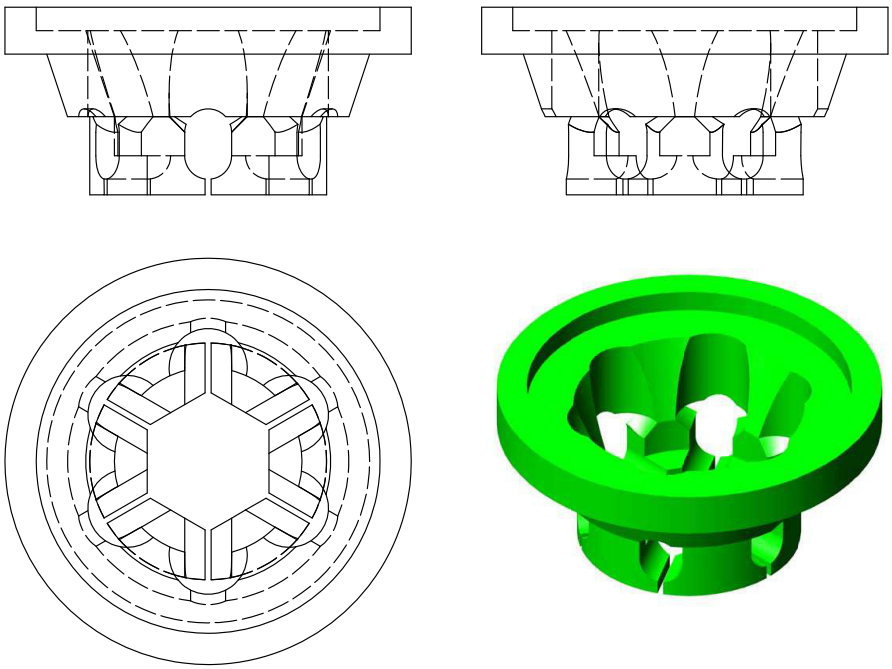

Figure 6.2.2: Drawing of the die struts part (Version 1).

flow towards both centre and outer side of this die part. The glass flow towards the centre to merge with the glass from Die-Core and form the inner six holes of

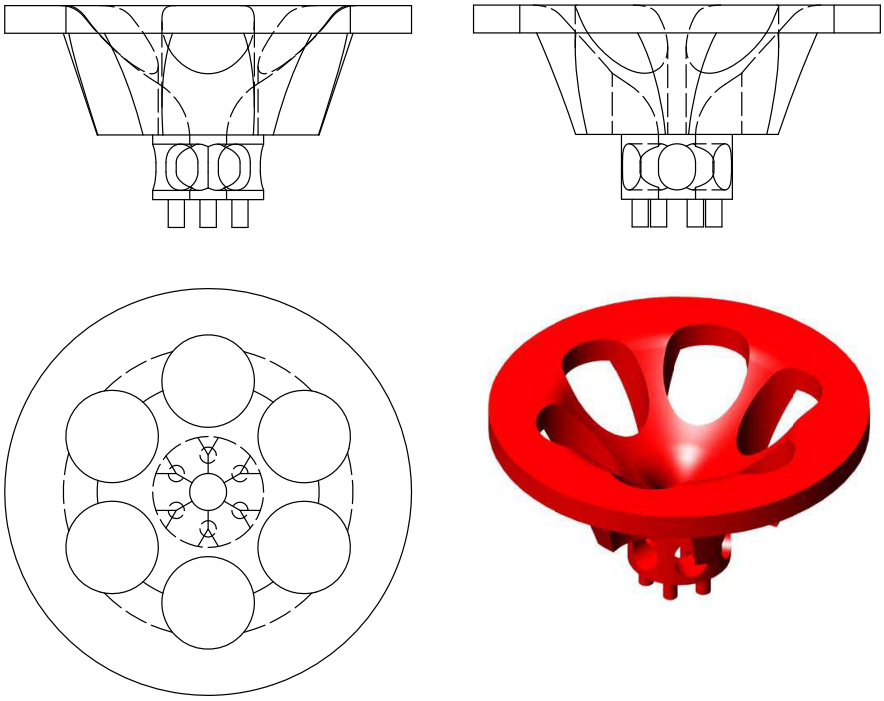

Figure 6.2.3: Drawing of the die core part (Version 1).

the preform, and the glass flow towards the outer side is confined by Die-Jacket and form the cladding.

The die was fabricated in stainless steel as shown in Fig. 6.2.5. Due to an error in the fabrication, the pins were rotated by 30 degrees compare to their original designed positions. Fortunately the die can be rotated to realign the pins but the six feeding holes will no longer be aligned with the struts. Apart from this, the rest parts of the die were produced as per the design specifications.

6.2.2 Preform fabrication: Tellurite glass billet with Die V1

To extrude a glass billet through a die, the glass billet needs to be heated close to its softening temperature [153], which is the temperature the glass starts to deform under its own gravity force, but not too soft so that its structure deforms significantly once it exits the die. The temperature used for extrusion depends not only on the

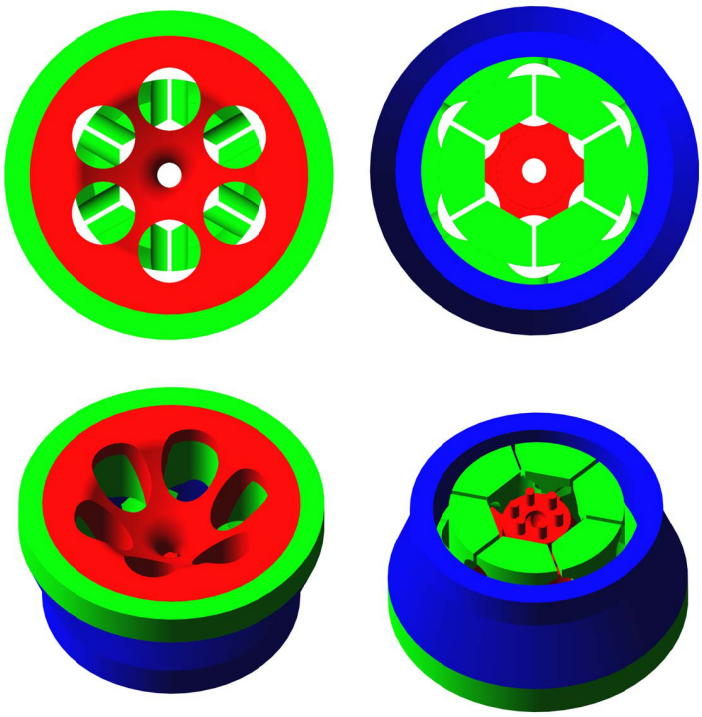

Figure 6.2.4: Effect pictures of the die with different view angles (Version 1).

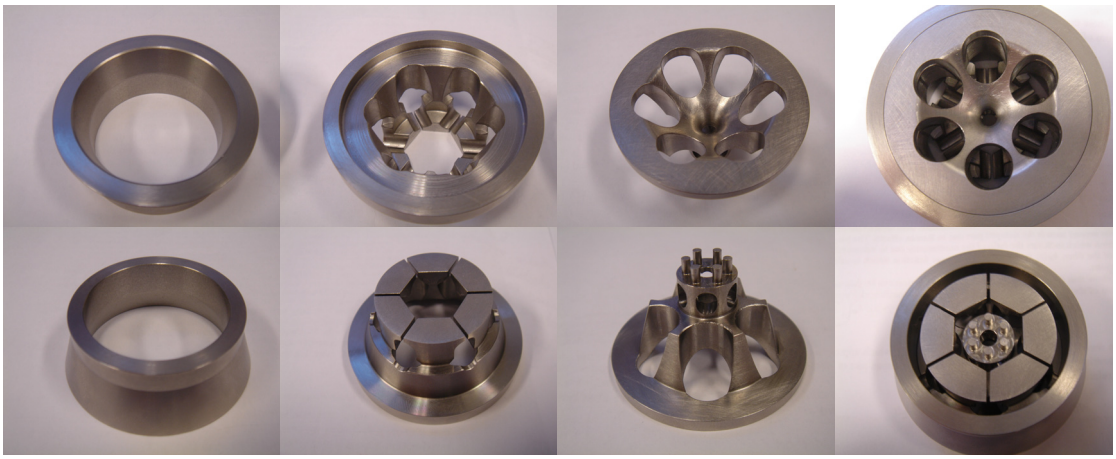

Figure 6.2.5: The fabricated stainless steel die parts separated and assembled (Version 1).

softening temperature of the glass but also the force required for extruding the glass through the die. Since this is the first attempt, only guess of the temperature can

be made based on the previous extrusions of the same glass with other dies. The glass used in this extrusion was a 50 mm diameter 25 mm tall tellurite billet. Based on previous experiences, 360 degrees Celsius was used for the extrusion.

The glass billet and the die were heated up together inside a resistance furnace in two steps. They were first heated up from room temperature to 345 ^oC with 10 $^oC/min$ ramp rate and then heated up to 365 ^oC with 1 $^oC/min$ ramp rate to avoid over heat due to the delay response in the temperature control system. Once the target temperature was reached, an automated extrusion procedure was performed with a constant extrusion speed 0.05 mm/min. The extrusion force was automatically increased to match up with the required speed.

The extruded preform is shown in Fig. 6.2.6. The preform was severely tapered and stretched under gravity as one can see in Fig. 6.2.6a. The preform is 114 cm in total and its diameter varies from 2.3 to 11 mm (also labelled in the Fig.6.2.6). Reference to the die drawing, the core part (Fig. 6.2.6b exited the die earlier than the rest of the preform indicates fast glass flow in the centre of the die. Fig. 6.2.6c is the break point that was connected to the main preform at Fig. 6.2.6d. The main preform contains the full structure to the very end (Fig. 6.2.6e).

The cross-section of the preform is shown in Fig. 6.2.7. The structure in the preform deformed due to the uneven flow of glass in the die and severe taper of the preform. However, as the first fabrication attempt, the cross-section of the preform shown remarkably good match with the design. This promising result proved that it is practical to fabricate the preform required for making this complex structured fibre.

To improve the fabrication for later work, the fabricated structure was compared to the ideal structure by overlaying the two on top of each other. From the figure, two important differences can be identified. 1) The struts in the preform is much thinner than the ideal one, 2) the inner six holes are stretched to elliptical shape towards the preform centre. The deformation may be reversed to a certain degree during the fibre drawing process through active control of drawing tension and the

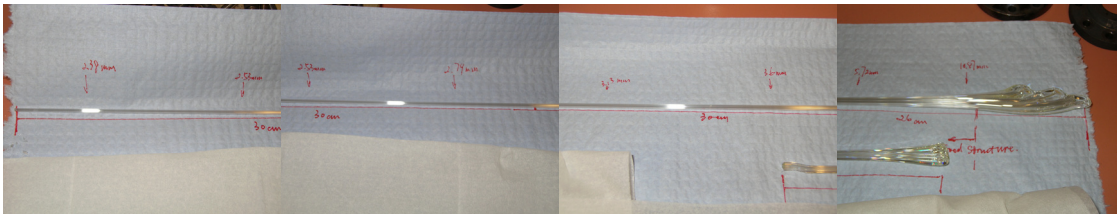

(a) Overview of the preform. The right hand side is end exited the die first. The preform diameter reduces quickly due to tapering effects.

(b) (c) (d) (e)

Figure 6.2.6: Tellurite preform fabricated die V1. (a) overview of the preform, severely tapered. The centner of the preform partially dropped out and broken off, put below the main preform. (b) The partially dropped out core part of the preform. (c) The broken point of the dropped out part. (d) The end of the main preform that firstly exited the die. The shape indicates the glass flew faster on one side than the other. (e) The end of the main preform connect to die after the extrusion.

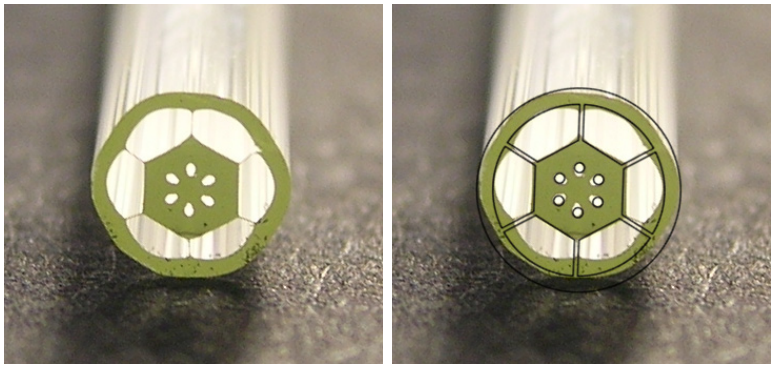

Figure 6.2.7: The cross section of the first tellurite preform with an overlay with the die structure on the right.

gas pressure inside the holes.

6.2.3 Fibre drawing: Tellurite preform

To pull the preform into fibres with a target core diameter (6.4 μm) and a reasonable outer diameter, i.e. 120 to 200 μm, so that the fibre is strong enough to be handled during experiments, the preform needs to be jacketed with a tube to increase the preform diameter. For the first extrusion trial, the outer diameter of the relative uniform part of the preform was around 4.5 mm. The core-to-outer-diameter ratio was approximately 47%. A core diameter of 6.4 μm and an outer diameter of 120 μm cannot be achieved in one jacketing step, which require a preform with an outer diameter of 350 mm. To achieve the target size, we need to jacket the preform with a 15 mm outer diameter and 4.5 mm hole tube twice, and then the preform can be pulled down to approximately 145 μm outer diameter, which lays well in the 120 to 200 μm region.

Unfortunately, the first jacketing process failed, the preform structure could not be preserved during the process. Fig. 6.2.8 shows some of the cross sections as the drawing progresses. It is clear that the fibre drawing parameters (temperature and speed) led to surface tension related collapse of fibre's internal structure.

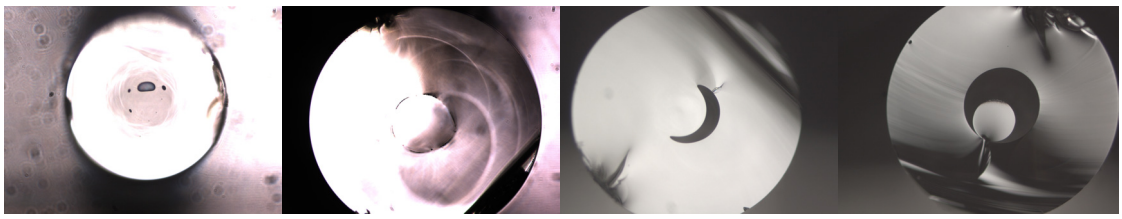

Figure 6.2.8: The cross sections of the jacketed preform along the drawing process from left to right.

To summarise this fabrication trial, the main courses of the failure are the imperfection of the preform and ignorance of the suitable drawing conditions for this preform. The struts of the preform are too thin to support the inter structure during fibre pulling process. And the size of the preform led to the requirement of two jacketing steps, which leads to complications in the fibre drawing processes. A

preform with an outer diameter of at least 10 mm is preferred for future trials. The glass flow in Die-Core needs to be balanced to reduce the structural distortion. One possible cause of the thin struts may be the false alignment of the 6 feeding holes due to the rotation of the pins and the unbalanced glass flow in the die.

6.3 Trial Two

Based on the experiences of trial one, Die-Core was redesigned to balance the glass flow. The aim of this modified die design is to reduce the structural distortion in the preform and increase the thickness of the struts.

6.3.1 Die design: Version 1.1

Different from the first design, this time multiple small feeding holes were used to supply the glass for the core structure of the preform. The sizes of the feeding holes are calculated such that the glass flow rate (volume per unit area) is the same in the core area.

Apart from the feeding mechanism, the base where the pins set from the old design was removed and replaced with longer pins so that there is more room for the glass to re-merge before it exits the die.

The new design of Die-Core is shown in Fig. 6.3.1. The original designs of Die-Strut and Die-Jacket are to be used.

6.3.2 Preform fabrication: Tellurite glass billet with Die V1.1

The extrusion procedure was similar to trial 1. A tellurite glass billet with almost the same volume was used. Considering the severe taper in trial 1, the extrusion temperature was reduced by 5 ^oC to 360 ^oC with the aim of reducing the tapering effects.

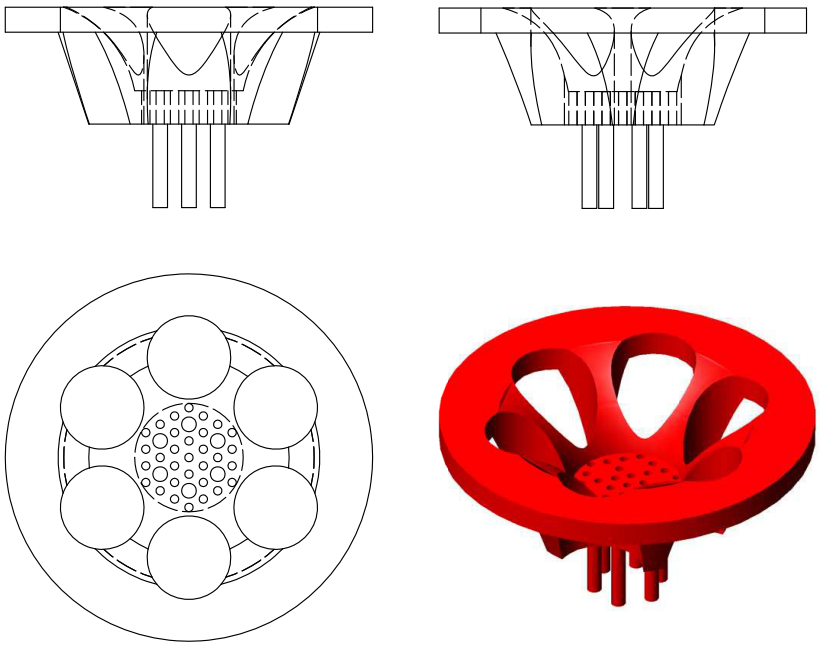

Figure 6.3.1: Drawing of the die core part (Version 1.1). The changes to the first version is the feeding holes in the centre area and prolonged pins

The fabricated preform was more than one metre long. Obviously, the tapering effects were still significant, which indicated the extrusion temperature was still too high. Due to the taper, the later part of the preform structure became thin and broken into pieces when it was out of the die. Different from trial 1, the taper was formed from the part of the preform that was close to the exit of the die. This part of the preform was left at a relative high-temperature environment comparing to the rest of the preform, and the taper was mainly caused by the gravity pull on the preform after the majority of the preform had exited the die.

Fig. 6.3.2a shows the remaining of the preform and Fig. 6.3.2b is the place that broken from the rest of the preform. The core part still extends about 4 cm out of the rest of the preform which indicates faster flow of the glass in this area. But tapering of this part was less than the first trial due to lower extrusion temperature.

The preform was cut to reveal the cross section (Figs. 6.3.2c&d). In the core

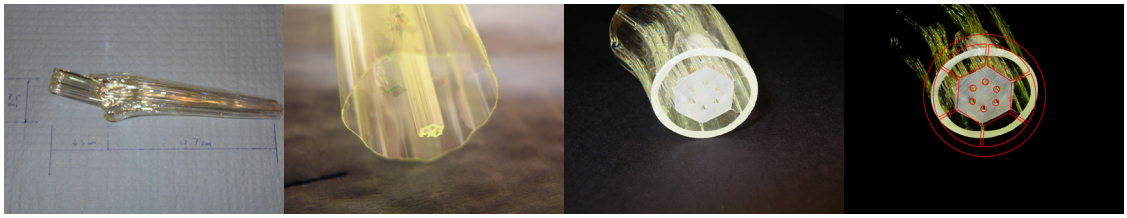

(a) (b) (c) (d)

Figure 6.3.2: The second tellurite preform. (a) the overview of the preform. (b) the broken point of the preform. It can be seen that the outer wall of the preform is extremely thin. (c) the cross section of the preform close to the starting end. (d) the cross section overlaid with the ideal die structure

area, the structure is closer to the ideal one than the first trial which indicates better glass flow balance in the new design. However, the struts are still too thin. The gaps for the struts in the die must be expanded.

The useful portion of the preform is too short to be made into fibre. The current die design left a significant amount of glass inside the die. Considering the volume of tellurite glass billets available, it is desirable to reduce this 'dead' volume within the die. For this reason, a new die design was considered. As a way of doing this effectively, a choice was made to use SF57 billets because the large volume (50 mm diameter $\times$ 60 mm tall) SF57 glass billets are available commercially. Thus, the next step was to make minor modifications to the current die and try again with a SF57 glass billet.

6.4 Trial Three

6.4.1 Die design: Version 1.2

The major problem of the die in trial two was the strut thickness which is too small. The modifications need to be made in the die are straight forward. Fig. 6.4.1 shows the drawing of the revised die. The only change is the strut gap width. It was

changed from 0.78 to 2 mm.

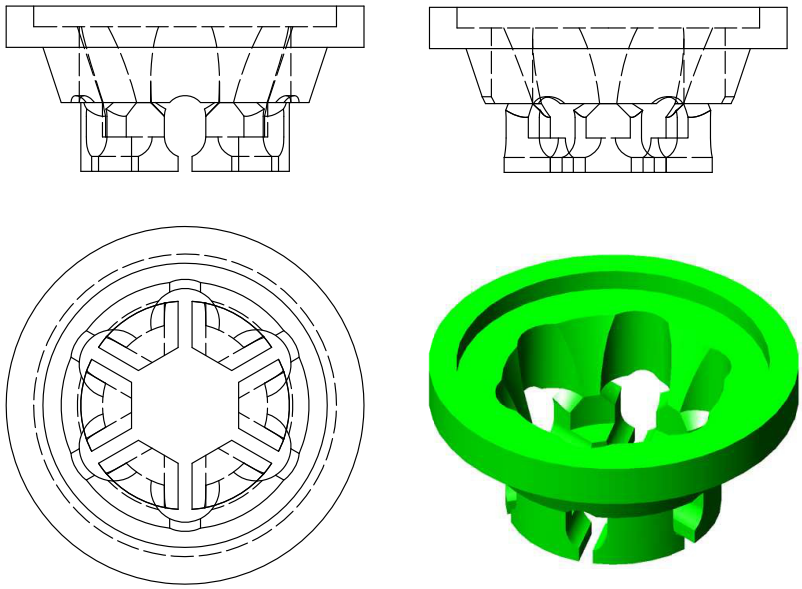

Figure 6.4.1: Drawing of the die struts part (Version 1.2).

6.4.2 Preform fabrication: SF57 glass billet with Die V1.2

A SF57 glass billet was used in this extrusion trial. The SF57 glass billets were supplied by Schott AG and had been used for other extrusions in my group before, which provides necessary information and experiences for extruding this glass with the new die.

The SF57 glass has higher softening temperature than the bismuth glass. For the extrusion, the glass was heated up together with the die in two steps. The first step is to 490 ^oC at 10 $^oC/min$ and then to 510 ^oC at 1 $^oC/min$. Once the final temperature was reached, the glass was extruded through the die at a constant speed of 0.05 mm/min.

The extruded preform is shown in Fig. 6.4.2. The overview of the preform shows significant improvement from the previous trials. The taper (Fig. 6.4.2a) was minor and did not hamper the next stage of the process, fibre drawing. The glass flow was

more balanced comparing to previous trials such that the glass from the full cross-section of the preform exited the die approximately the same time with the core part just slightly ahead (Fig. 6.4.2b). The break-off point of preform (Fig. 6.4.2c) directly connected to the die, which faithfully shows the reproduction of the structure as designed. However, due to thermal expansion, the extruded preform shrank somewhat when it cooled from 510 ^oC to room temperature. After the two ends of the preform were cut, the cross section was pictured and shown in Fig. 6.4.2d with the designed structure overlay on top of it.

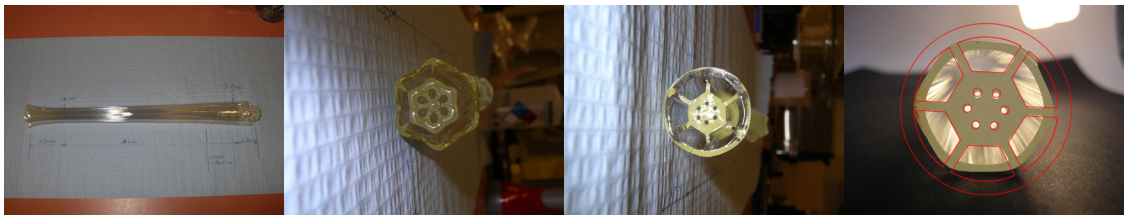

(a) (b) (c) (d)

Figure 6.4.2: The first SF57 preform. (a) the overview of the preform. (b) the view of the starting end of the preform. (c) the view of the finish end of the preform. (d) the cross section of the preform overlaid with the ideal die structure

The structure of the extruded preform was close to the design. The shortened struts could be caused by the thermal shrinking as explained. According to the statistical study in Chapter 5 Tab. 5.3.1, this distortion is not critical. The most important feature is the size of the core (R3) and the position of the inner holes (R1) regarding to the core. As one can see that the core was scaled and aligned to the ideal structure, the positions of the inner holes are almost right except the sizes are approximately 22% smaller. From previous experiences, the inside structure can be altered during the fibre pulling process through pressure control.

6.4.3 Preform caning and fibre drawing: SF57 preform

Unlike the one in trial 1, this preform can be made into 1 mm diameter canes to fit into 10 mm diameter jacket and then pulled into fibres with a required core diameter. The cane making (caning) process is similar to a fibre pull except for targeting a larger diameter.

Ideally, the cane will contain exactly the same structure as the preform. However, distortion is inevitable. The cross-section of the fabricated cane is shown in Fig. 6.4.3a. When comparing the cane structure to the ideal structure (Fig. 6.4.3b), one can find that the cane nearly preserved the structure in the preform except the inner holes. The size of the inner holes was further reduced to 46% of the original design. But apart from that, the majority of the structure was good.

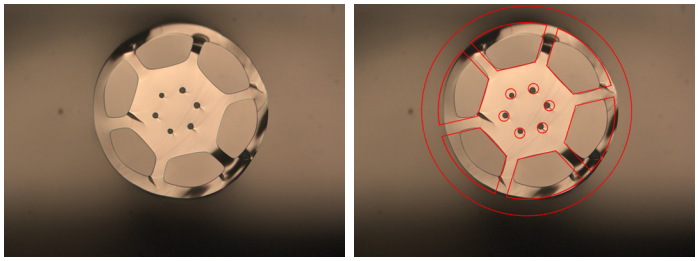

Figure 6.4.3: The cross section of the SF57 cane with an overlay with the ideal die structure on the right.

The inner holes of the cane are likely to expand during the fibre drawing process through either active pressure control or under self-pressurisation. Self-pressurisation approach was used in this trail. Once the cane was inserted into the jacket tube, the two ends of the cane were molten and sealed using flame so that pressure can build up through the air trapped in the holes. Using this pressure, the holes can be kept open during the drawing process. Meanwhile, vacuum was applied on the gap between the tube and the cane to help the two to merge together. These techniques are standard techniques for drawing microstructured fibre.

SEM images were taken for fabricated fibre. The structure of the fibre varies along the fibre. Fig. 6.4.4a is one example of the cross-section of the fibre with ideal

die structure (Fig. 6.4.4b) and ideal fibre structure (Fig. 6.4.4c) overlay on top of it.

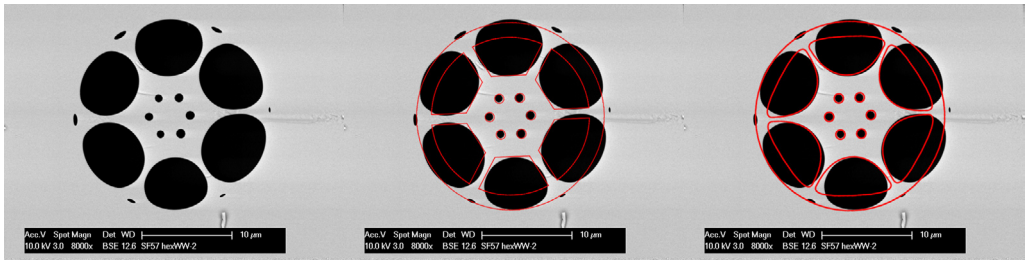

(a) (b) (c)

Figure 6.4.4: The SEM image of (a) the cross section of SF57 fibre. (b) the cross section overlay with the die structure. (c) the cross section overlay with the ideal fibre structure.

The actual fabricated structure in the fibre was closer to the target structure than both preform and cane. After the fibre drawing process, the inner holes were expanded close to the designed size, and the six struts were pulled and formed parabolic curves that nearly matched the curves of the outer ring of holes in the design.

There are also some distortions in the structure, such as the variations in the diameters of the inner holes (standard deviation: 6%) and the symmetry of the struts. These distortions also existed in the preform and cane. To eliminate these distortions, it is necessary to improve the quality of fibre preform and cane.

6.5 Trial Four

At the end of trial two, we discovered two problems with the die design. The first one is the strut thickness which has been solved in trial three with slight modifications to Die-Strut. However, the second problem remains. That is the waste of glasses due to internal volume of the die. With the available tellurite glass billet, which is around 25 $\sim$ 30 mm tall, the length of the preform can be fabricated is rather short. The fabricated Tellurite preform in Trial Two was less than 10 cm long and

the useful preform length was less than 5 cm. Even with 60 mm tall SF57 billet, the total preform length was 35 cm and the useful length is approximately 25 cm which can be used once for caning. Therefore, new die design is pursued.

6.5.1 Die design: Version 2

The prime directive of this new die design is to minimise the die's internal volume so that when an extrusion finishes only minimal glass remains inside the die. To do also, the original die design was abandoned. Instead, a thin plate with small holes was used to feed the glass through the die. Fig. 6.5.1 and 6.5.2 are the drawings for the new design.

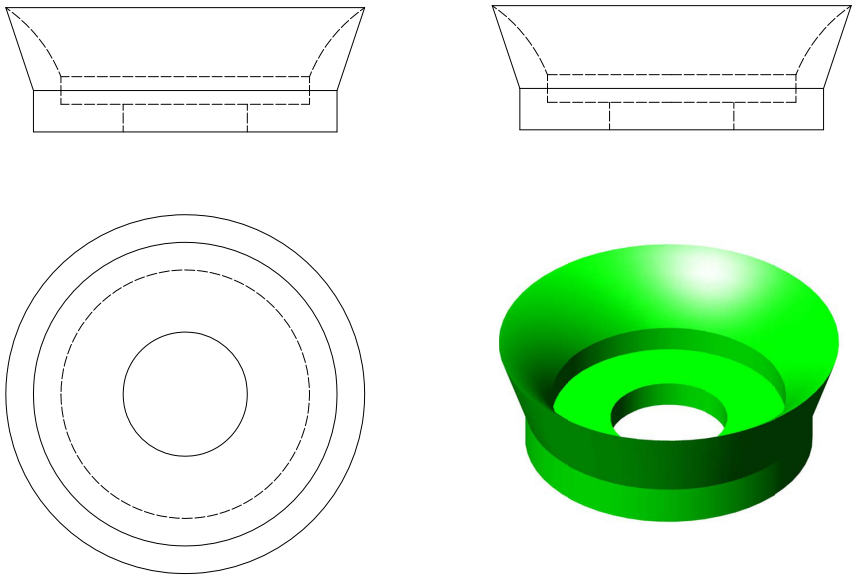

Figure 6.5.1: Drawing of the die jacket part (Version 2).

In this new die design, the preform diameter outer was also reduced from 36 to 18 mm, which will greatly increase the preform length. Furthermore, the preform outer wall thickness was increased, so that even if there will be severe tapering occurs, the preform will still be able to be handled unlike the case in trial 2.

The computer illustrated and fabricated die are shown in Fig. 6.5.3. The plates were drilled and cut from a single piece of metal except for the pins. The pins for

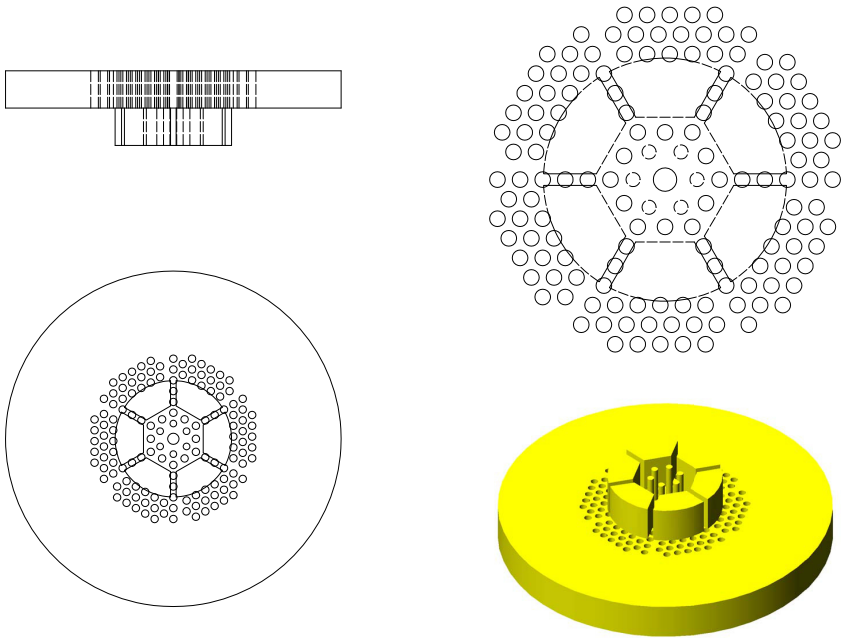

Figure 6.5.2: Drawing of the die plate part (Version 2).

the inner holes were fabricated separately and inserted into the plate afterwards for the convenience of fabrication.

6.5.2 Preform extrusion: SF57 glass billet with Die V2

Based on the success of SF57 glass billet extrusion in trial 3, we decided to use SF57 glass billet again with our new die.

The extrusion temperature was increased by 5 degree Celsius to compensate the increase in extrusion force due to the increase of friction related to the number of feeding holes. The glass was firstly heated up to 495 ^oC with 10 $^oC/min$ and then to 515 ^oC with 1 $^oC/min$. Surprisingly, the fabricated preform showed severe tapering (Fig. 6.5.4a) and changes in glass. After a few centimetres from the beginning of the preform, defects appear in the form of bubbles in the preform (Fig. 6.5.4b). From previous experience, these bubbles may relate to the crystallisation of the glass. The exact cause is still unclear at the moment, but this phenomenon appears often when the die consists many small feeding holes which usually require slightly higher

Figure 6.5.3: The computer illustrated effect picture (top) and fabricated (bottom) die version 2.

extrusion temperature too.

The extrusion process terminated prematurely due to excess of force limit (80 kN). Only approximately 1/3 of the glass was extruded through the die. The extruded preform length is 71 cm with taper.

Apart from the taper and bubbles, the preform structure is good. Comparing the preform cross section to the ideal structure, the outer wall of the preform (outer most ring of glass) is thicker than the design. It can be explained as the fast flow of glass in this area due to the big empty area presented caused less friction to the glass and the swell of glass when it exited the die.

The major defect in the core part of the preform is the inner ring of holes. The positions of the holes are close to the target dimensions, but the sizes are 40% smaller than the design. However, from our previous experience in trial 3, the sizes of holes are very likely to be restored during the fibre drawing process.

Unfortunately, after cut the preform end to reveal the cross-section the whole

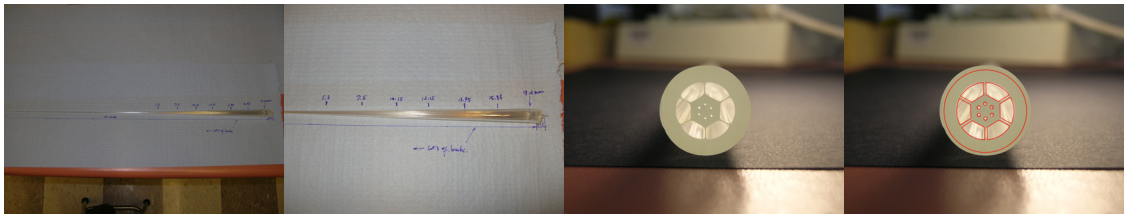

(a) (b) (c) (d)

Figure 6.5.4: The second SF57 preform fabrication die version 2. (a) the overview of the preform. (b) first half of the preform. The diameter at different position along the preform are labelled in the picture. The preform in the middle of the picture appears to be opaque due to bubbles in the glass. (c) the cross section of the preform. (d) the cross section overlaid with the ideal die structure.

preform is found to be covered with bubbles. Even the rest of the fabrication process proceeds seamlessly, the fibre will not be able to transmit light due to the extensive scattering caused by the bubbles. Therefore, this trial was terminated.

6.6 Trial Five

In the trial 4, extrusion temperature was increased by 1% which I did not expect to see such dramatic changes to the glass. However, the result indicates, either the 1% increase in the temperature or the die itself might have contributions to the final result. The new die design increased significantly more internal interfaces into the preform which could greatly increase the chances to form glass bubbles than the old designs.

Considering the lack of knowledge about the tellurite glass extrusion temperature for this die and risk another die (dies are for one-time use only), I decided to use a bismuth glass billet instead of tellurite. On one hand, the bismuth glass has very similar optical properties to tellurite glass. The main difference is the transmission window of the glass. The transmission window of the bismuth glass used in this work

extends to approximately 3 μm which is narrower than that of tellurite glass [50]. Other than that, the differences in the refractive index (1.98 for bismuth and 2.00 for tellurite at 1550 nm) and nonlinear refractive (index 5.9e-19 m^2/W for bismuth glass [154] and 5.5e-19 m^2/W tellurite glass (measured with Z-scan method [155])) are negligible. On the other hand, the thermal mechanical properties of bismuth glass are similar to SF57 glass than tellurite, and there is enough information from previous in-house extrusion experience for us to estimate an extrusion temperature.

6.6.1 Preform fabrication: Bismuth glass billet with Die V2

The bismuth glass billet (provided by Asahi Glass Co. LTD.) was 45 mm tall and 50 mm in diameter. The heating process was also performed in two stages. In the first stage, we heated the glass to 470 ^oC with 10 $^oC/min$ ramp rate. In the second stage, the temperature was increased to 490 ^oC with 1 $^oC/min$ ramp rate. Once the setting temperature was reached, the glass was extruded through the die at a constant speed of 0.036 mm/min.

The preform was tapered, though less severely than in previous trials. The extrusion went well until the preform became too long, and its tip touched the ground. After that, the preform was bent, distorted and broken as one can see in Fig. 6.6.1a (Left side). The straight part of the preform is more than 58 cm long.

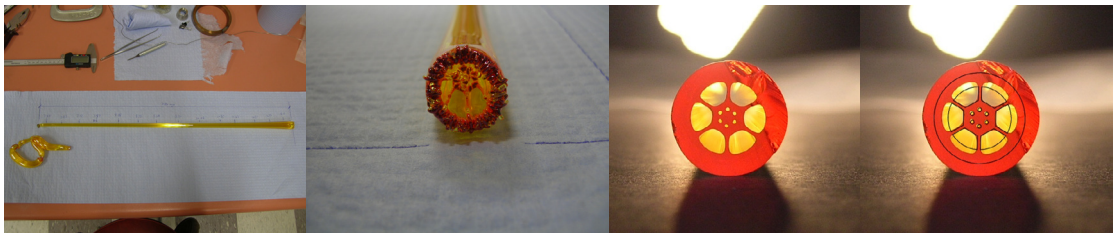

(a) (b) (c) (d)

Figure 6.6.1: Bismuth Preform. (a) the overview of the preform. (b) the view of the starting end of the preform. (c) the cross section of the preform. (d) the cross section overlaid with ideal die structure.

In this trial, the preform exited from the die nearly the same time with approximately 1 cm delay for the core (Fig. 6.6.1b). This indicates the flow of the glass is more balanced for bismuth than tellurite in trial 4.

Fig. 6.6.1c&d show the cross-section of the preform and an overlay with the ideal structure. From the picture, one can see that the sizes of inner holes of this preform are closer to (3% larger) the design than previous trials. However, the positions of this ring of holes are slightly offset by 4% with respect to the core diameter. The cause of this can be attributed to the uneven flow of glass inside the die, and the defect in the die since the pins were separately manufactured and manually installed into the plate, there is no guarantee the pins were absolutely straight. Nevertheless, the preform fabrication was a success.

6.6.2 Preform caning and fibre drawing: Bismuth preform

The preform in this trial is thick enough to be made into 1 mm diameter canes with a cross section shown in Fig. 6.6.2a. In the canes, the inner holes came smaller than in the preform and the design (Fig. 6.6.2b). One possible cause of this result could be the temperature during cane making process was too high or the tension of the pull was too low so that the holes started to close due to its own surface tension. From previous experiences, this defect can be compensated during the fibre drawing process.

Once the cane was available, it was inserted into another bismuth glass tube with 10 mm outer and 1 mm inner diameters, and drew them together into fibre. During this fibre drawing process, the two ends of the cane were flame sealed to establish self-pressurisation inside the cane to keep the holes open. Also a vacuum environment was applied on the cane and the tube to seal the gap between them.

The cross-section of the final fibre was shown in Fig. 6.6.3. Comparing to the die structure (Fig. 6.6.3b) and ideal fibre structure (Fig. 6.6.3c), the figure shows certain distortion, mainly in the inner hole positions which appear to be similar in

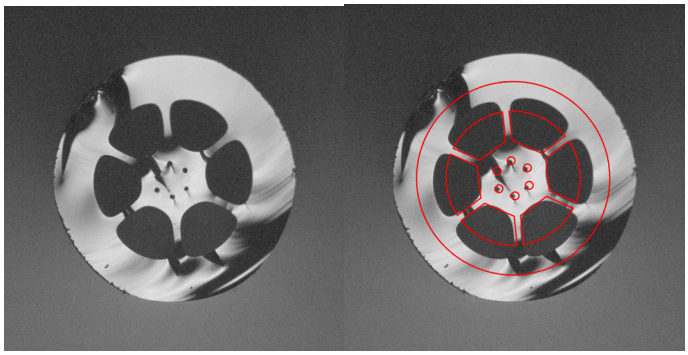

(a) (b)

Figure 6.6.2: The cross section of the bismuth cane (a) with an overlay with the ideal die structure (b).

the preform and the cane. Apart from that, the inner hole sizes are slightly larger than the design, and outer hole sizes are much bigger than the design, where the first one is crucial according to Chapter 5 Table 5.3.1 and the later one is not important and even better since they will provide better confinement.

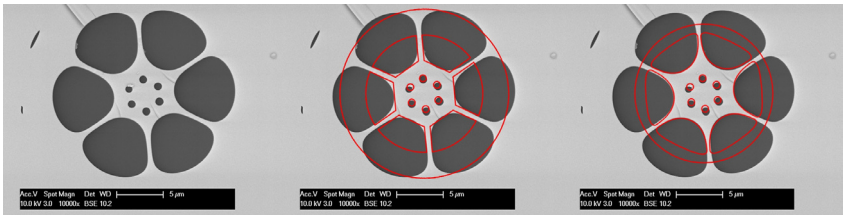

(a) (b) (c)

Figure 6.6.3: The cross section of the bismuth fibre (a). (b) overlaid with ideal die structure. (c) overlaid with ideal fibre structure.

6.7 Summary

In this chapter, the processes of fabricating the fibre designed in Chapter 5 were described and the evolution of the die design was showed.

The first die design focussed on resembling the design fibre structure and the easiness of the glass flow. The die consisted three parts. Large holes and gaps were used for reducing the friction between steel die and glass. The extrusion was done with a tellurite glass billet. Due to the lack of the knowledge of temperature needed for the extrusion, the fabricated preform suffered severe taper. Besides that, the glass flow speed in the core region appeared to be much faster so that the core came out of the die before the rest of the preform. Despite all the defects, the preform consists of useful structure. However, due to the severe taper, the preform could not be made into fibres with one jacketing step. Instead, we attempted to jacket the small end of the preform twice to reach the required core and outer diameters. Unfortunately, the attempt ended in failure. The structure was not survived after the first pulling process.

Modifications were made in the second die to reduce the flow rate in the core region. Instead of on big feeding hole, multiple small feeding holes were used this time. The second extrusion also used a tellurite billet. To reduce the tapering effect, the extrusion temperature was reduced by 5 degrees Celsius. The taper effect was reduced in the initial part of the preform, but the later part was still tapered under its own weight and broken due to its thinness. The core part of the preform still exited the die earlier than the rest of the preform but less in length. After cutting the preform to reveal the cross section, it is found that the struts in the preform was very thin, which indicated they might not be able to sustain the weight of the core for next fabrication processes as well as large friction force in these areas which caused the early exit of the core part of the preform.

In the next trial, expanded the strut width from 0.78 to 2 mm in the current die design and extruded a SF57 glass billet. I had much more experiences with SF57 glass than tellurite. And SF57 glass was a commercial product which had better stability. The extrusion with the SF57 glass was a success. Minor taper was observed in the preform and cross-section almost retained the die structure. the preform was successfully made into canes and drew into fibres. Only minor

distortion was observed in the final fibre. This result proved that the modified die design was successful and as long as the right temperature for extrusion could be found for tellurite glass, preforms with same quality can be produced.

The version 1 die design can successfully produce good SF57 preform but it has a large internal 'dead' volume which causes waste of glass. The SF57 billet glass was more than twice the volume of tellurite glass billet. The version 1 die cannot produce sufficient long preform with tellurite glass billet. For the reason, new die design was considered.

The version 2 die drew on experience from version 1 die. It consists only two parts with all the structural features assembled onto a thin plate with an output of half the diameter as version 1 die.

Following the success of SF57 glass fabrication, the new die design was tested with a SF57 glass billet first. But the trial was a failure. The preform not only greatly tapered but also shown bubbles inside it. The cause of this failure in unsure at the moment but it could be related only to the glass. Despite the defects mentioned here, the cross-section of the preform was quite close to the die structure.

Instead of risk the last die with tellurite glass billet, a bismuth glass billet is used instead. The bismuth glass has very similar optical properties to tellurite glass and similar thermal mechanical properties to SF57 glass. In general, the fabrication was a success. There was some distortion in the fabrication, especially the inner six holes, and the distortion was carried into the final fibre. However, the distortion was believed due to the pins in the die and can be fixed in the future.

Two fibres were successfully produced during these fabrication trials, SF57 and bismuth fibres. These fibres were the first microstructured fibres been intensional designed and fabricated with holes of significantly different sizes. In the next chapter, simulations based on the fabricated fibres are performed.

Chapter 7

Simulations of fabricated fibers

In Chapter 6, the transverse cross-sections of the fabricated fibers were compared with the initial design. Apart from the use of different types of glass, there also are significant distortions in the fabricated fiber structure. Changes in nonlinearity and dispersion profiles are therefore expected. The actual dispersion and nonlinearity profiles of the fabricated fibers will lead to different outputs. It is important to redo the simulations with actual dispersion and nonlinearity profiles to compare the outputs and understand the impact of the structural distortion on the nonlinear processes of interest here. The simulated result will help guiding the experimental work.

In this chapter, the FOPO and SC generation were simulated in the fiber fabricated in the previous chapter. First of all, the dispersion and nonlinearity profiles of both fabricated bismuth and SF57 HWW fibers were calculated base on their SEM images using a finite element method. Once these dispersion and nonlinearity profiles are obtained, simulations of FOPO and SC generation can be carried on by using the profiles, and results can be compared with the designed ones.

7.1 Dispersion and Nonlinearity Profiles

To calculate the nonlinearity and dispersion profiles of the real structure, an accurate measure of the fiber cross section needs to be taken. A scanning electron microscope (SEM) image of the fibre cross-section was taken. It is shown in Fig. 7.1.1a. The image was processed to remove the cracks and dirt on the fibre tip, and the contrast of the image was enhanced so that the boundaries of air holes could be easily detected by the modelling software (COMSOL Multiphysics). The processed imaged is shown in Fig. 7.1.1b. The imported geometry (Fig. 7.1.1c) was then scaled to its actual size by using the scale bar on the SEM image. The error accumulated in the import process is at order of 10 nm. This error includes the error from taking the SEM image, which is approximately 10 nm, and the error from plotting the contour of the fibre geometry edges in the SEM image.

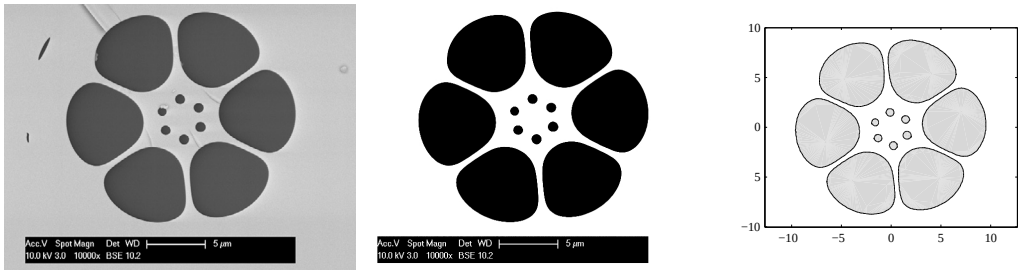

(a) (b) (c)

Figure 7.1.1: (a) SEM image of the fabricated fiber, (b) processed image, remove cracks and dirt, (b) structure imported into COMSOL.

Once the geometry is loaded into COMSOL, nonlinearity and dispersion profiles were calculated in the same way as they were done with the ideal structure.

7.1.1 Bismuth HWW fiber

Fig. 7.1.2 shows the dispersion (a) and nonlinearity (b) profiles of the actual fiber. Due to fabrication distortion, the fibre became birefringent, which is presented in the

form of the splitting of the dispersion and nonlinearity curves of the two polarisation modes. The distortion also caused other changes in dispersion and nonlinearity profiles. In the dispersion profile, the wavelength spread of the three ZDWs is wider than it was for the ideal fibre. They shifted from approximately 2, 2.5 and 3 μm to 1.7, 2.7 and 3.6 μm. Secondly, the maximum variation of the dispersion value between the first and third ZDWs increased from approximately 5 ps/nm/km to 23 ps/nm/km with 16 ps/nm/km for the maximum and -7 ps/nm/km for the minimum. The nonlinearity of the fibre increased approximately 40% for all wavelengths due to the increase of the inner hole diameters which reduces the effective mode area of the guided modes.

The fabricated fiber was also found to be multimode as well as the designed fibre. 49 core-guided modes were found in the modelling. Fig.7.1.3 shows the dispersion and nonlinearity of 2 fundamental, 6 first high order and 8 further higher order modes. As one can see, the dispersion and nonlinearity profiles of the high-order modes are a significantly different from that of the fundamental modes. The existence of the inner ring of holes causes significant difference in the confinement condition between fundamental and high-order modes. Fundamental mode is mainly confined inside the inner ring of holes where high-order modes distribute evenly across the core area. There is only one ZDW for each high-order mode at approximately 1.3 to 1.5 μm. The nonlinearity of the high-order modes are all lower than that of the fundamental mode because of the higher order of the mode, the larger the effective mode area.

7.1.2 SF57 HWW fiber

The material dispersion of SF57 glass is different from that of the bismuth and tellurite glass (Fig. 7.1.4). It is no surprise that the nonlinearity and dispersion profiles of the SF57 fibre are different from the design. Fig. 7.1.5 shows the dispersion and nonlinearity profiles of the SF57 fibre. The dispersion of the SF57 fibre increases

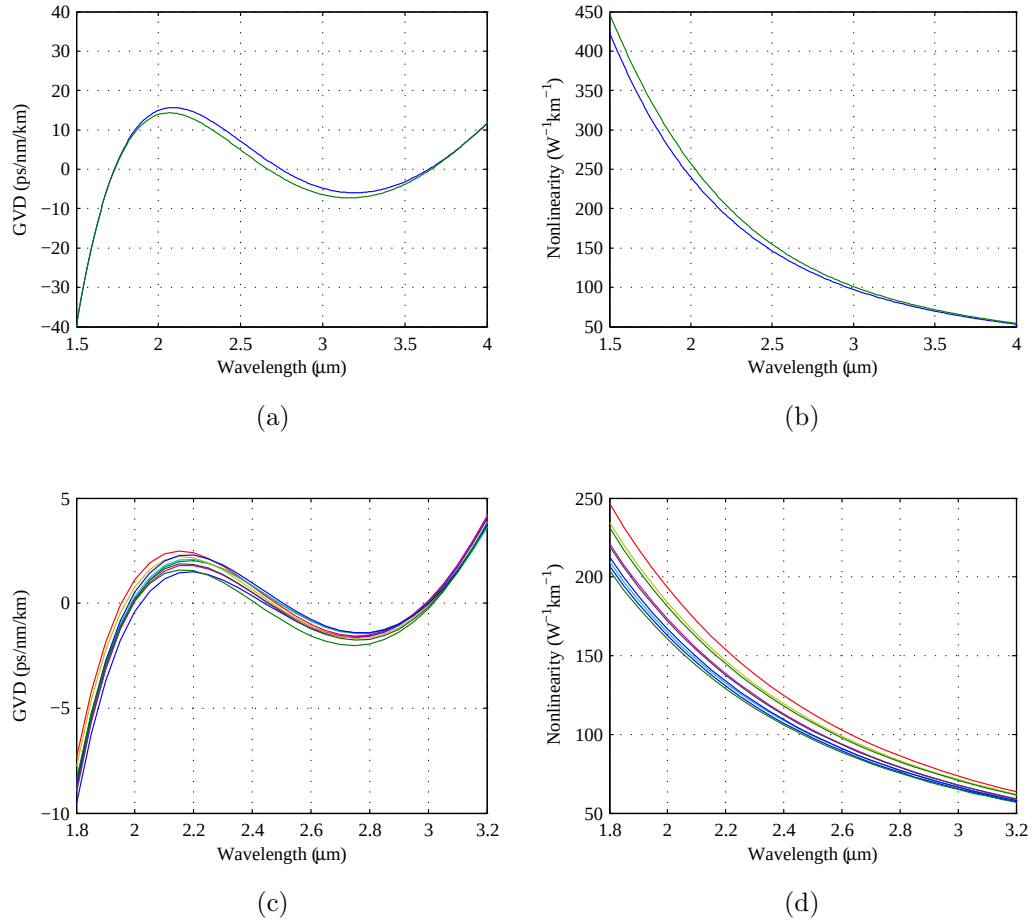

Figure 7.1.2: (a) Dispersion and (b) nonlinearity profiles of the fabricated Bismuth HWW fiber. (c) Dispersion and (d) nonlinearity profiles of the best 9 GA optimised structures in Chapter 5

monotonically with the increase of wavelength. There is only one ZDW at approximately 1.6 μm in the dispersion profile. The nonlinearity of the fiber is 60% lower than that of the bismuth fibers due to both lower linear and nonlinear refractive indices of SF57 glass ($n = 1.8$ and $n_2 = 4.1 \times 10^{-19} m^2/W$ at 1550 nm).

The changes in dispersion and nonlinearity profiles alter the behaviour of the parametric process and SC generation. In the following section, these nonlinear processes in the fabricated fibre are studied.

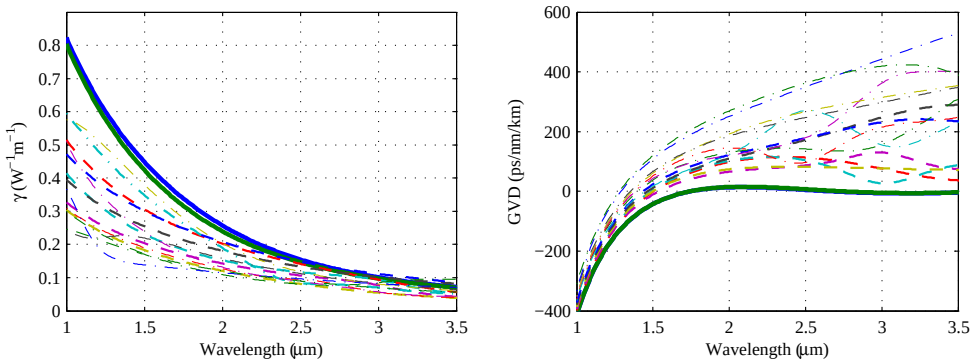

(a) (b)

Figure 7.1.3: Nonlinearity and dispersion profiles of the fiber modes. The thick sold lines correspond to fundamental modes, dashed lines correspond to the 6 first high order modes, dotted lines correspond to 8 further higher order modes

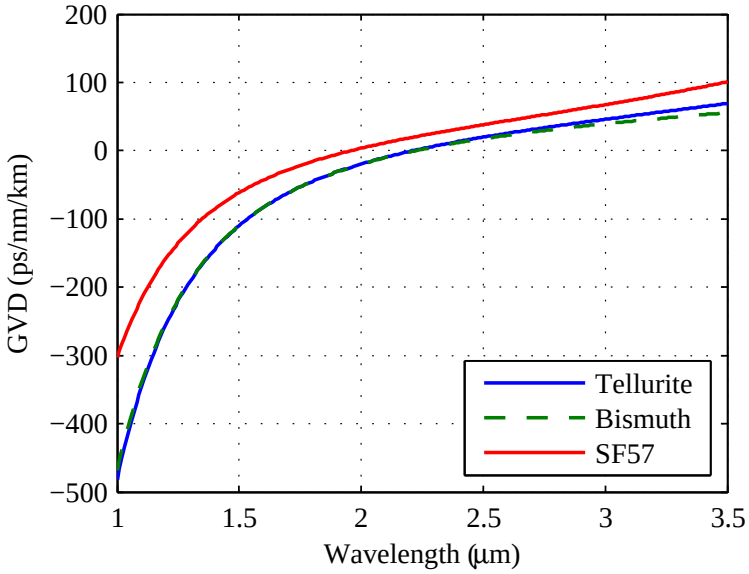

Figure 7.1.4: The material dispersion of SF57 (red solid line), Tellurite (blue solid line) and Bismuth (green dashed line) glass

7.2 Parametric Gain and FOPO

The target fibre that had been fabricated was designed for SC generation. Due to the similarity in the structures of the fibre designed for SC generation and FOPO, it

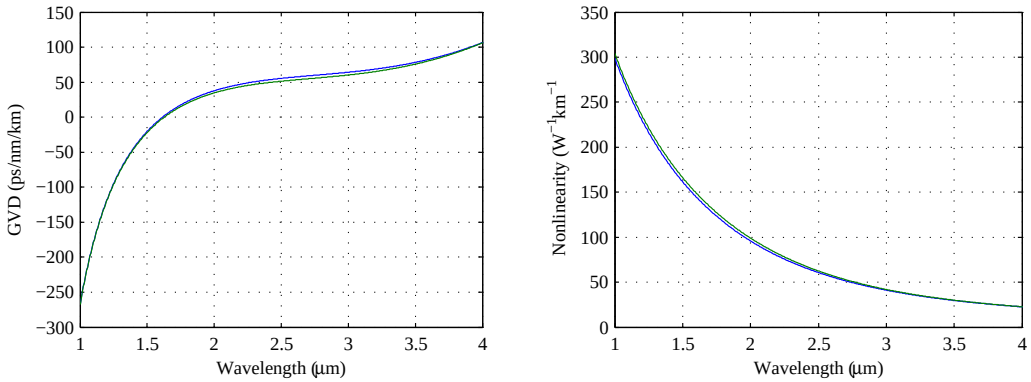

Figure 7.1.5: (a) Dispersion and (b) nonlinearity profiles of the fabricated SF57 HWW fiber.

is believed that the fabricated fibre can be used to confirm the behaviour of FOPOs.

7.2.1 FOPO with bismuth HWW fiber

Recall from Chapter 4, at a fixed power level, the parametric gain of a fibre is a function of nonlinearity at pump wavelength and the phase match between pump, signal and idler wavelengths. The parametric gain map of the fabricated bismuth fibre is shown in Fig. 7.2.1.

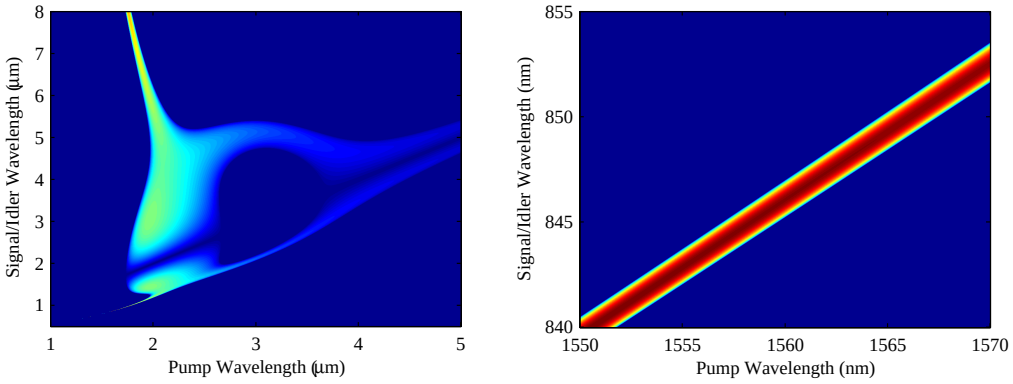

(a) (b)

Figure 7.2.1: (a) Parametric gain map of bismuth HWW fiber with 5 kW pump (b) zoom up the region around pump 1560 nm.

The most significant difference in the parametric gain of the fabricated fibre is that the bandwidth of the gain at the target wavelength (880 nm) is much narrower than the original design. The narrow bandwidth limits the tunability of the FOPO. According to the gain map (Fig. 7.2.1b), if the fiber is still to be pumped at 1560 nm with 5 kW peak power, the gain will exist around 840 nm. However, by increasing the pump wavelength, 880 nm output can still be obtained.

Having the gain map, simulations of the FOPO is performed. In this simulation, the pump wavelength was kept at 1560 nm and a 20nm band-pass filter was set at 840 nm. Based on the previous study in Chapter 4, this time we only look at cases where the feedback ratio is 0.5. The change in the dispersion also caused changes in the pump-signal walk-off time. A range of offset time were scanned through and the following outputs were obtained. Figs. 7.2.2 $\sim$ 7.2.5 show the evolution of the FOPO output as the pass number increases for a range of offset time from 534 to 824 fs. The main trend of the development of the signal pulses is very similar to the case discussed in Chapter 4 except that the spectral purity in this simulation is worse than the ideal case, which can be quantified through the time-bandwidth product (see Fig. 7.2.6). One possible cause of this phenomenon is the SPM of the pump which modulates the shape of the pump pulse and this modulate is transferred into the signal pulse through FWM.

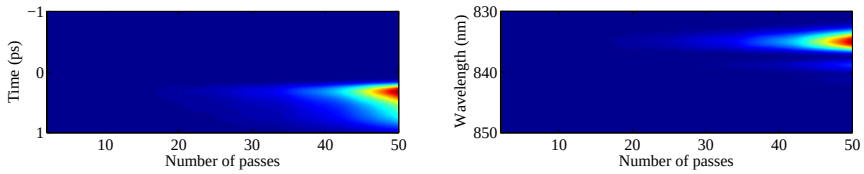

(a) Offset Time = 534 fs

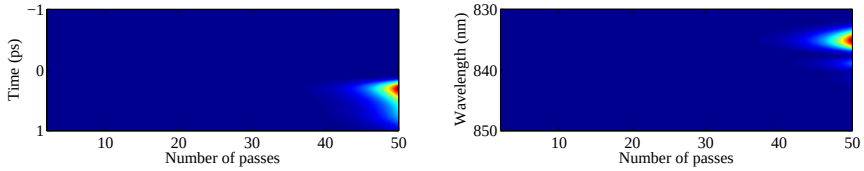

(b) Offset Time = 549 fs

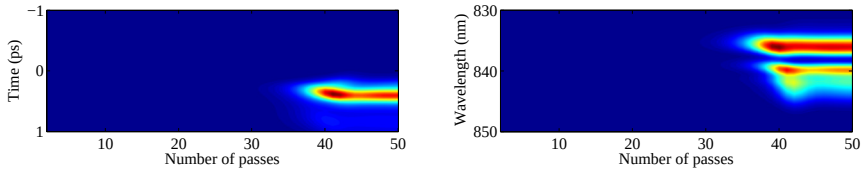

(c) Offset Time = 565 fs

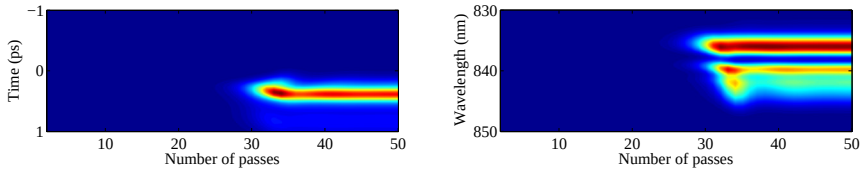

(d) Offset Time = 580 fs

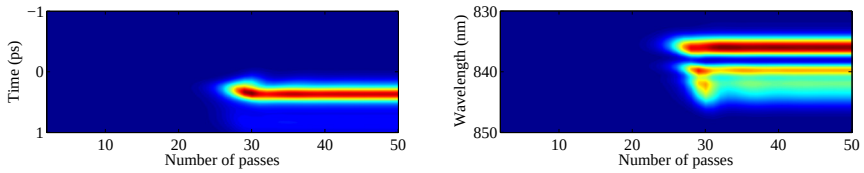

(e) Offset Time = 595 fs

Figure 7.2.2: The evolution of the temporal (left column) and spectral (right column) intensity profiles of signal pulses as a function of pass number with different offset time. Each figure is normalised to its maximum intensity.

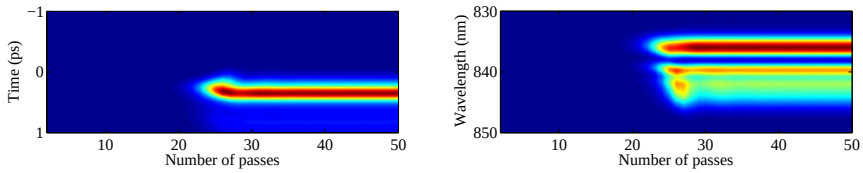

(a) Offset Time = 610 fs

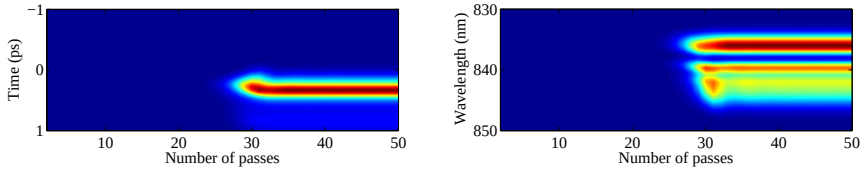

(b) Offset Time = 626 fs

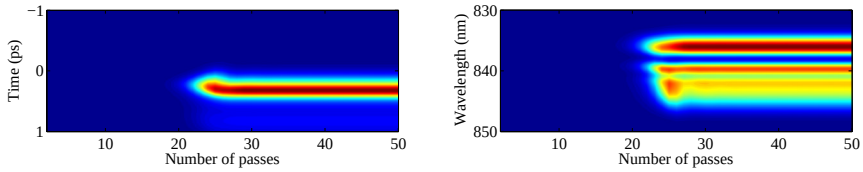

(c) Offset Time = 641 fs

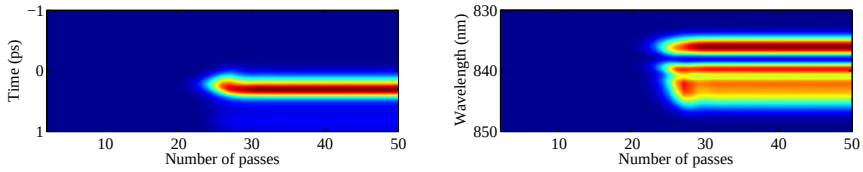

(d) Offset Time = 656 fs

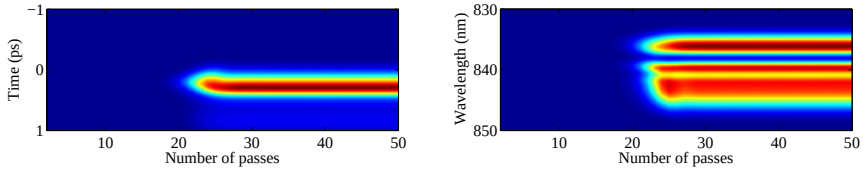

(e) Offset Time = 671 fs

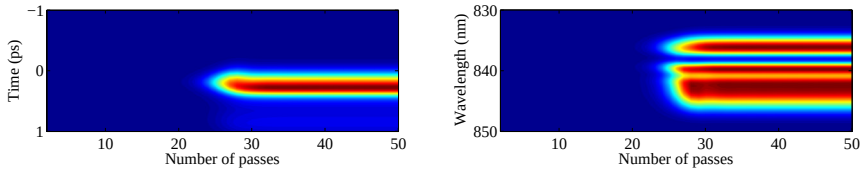

(f) Offset Time = 687 fs

Figure 7.2.3: Continuation of Fig 7.2.2.

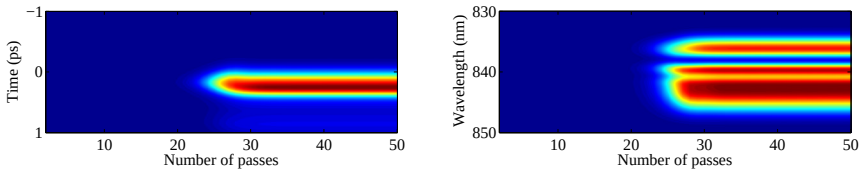

(a) Offset Time = 702 fs

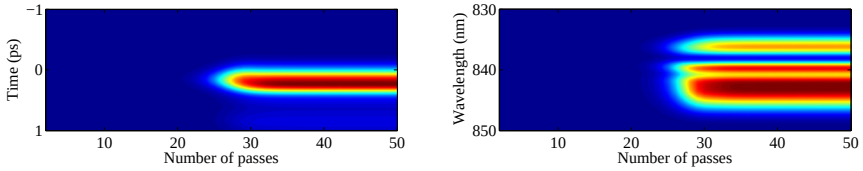

(b) Offset Time = 717 fs

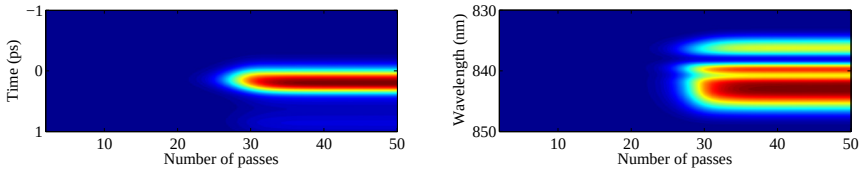

(c) Offset Time = 732 fs

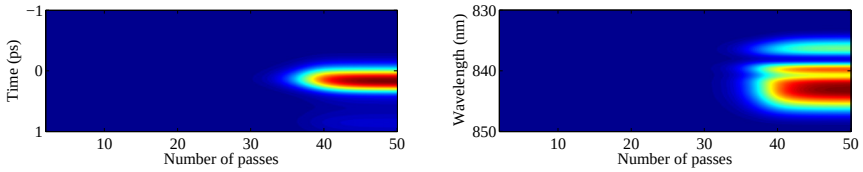

(d) Offset Time = 748 fs

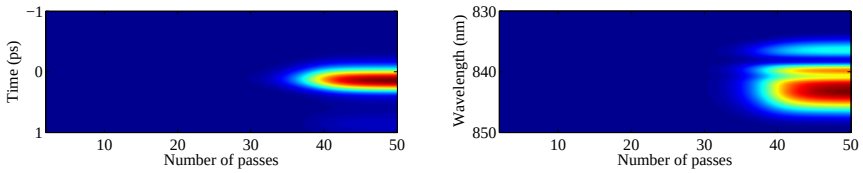

(e) Offset Time = 763 fs

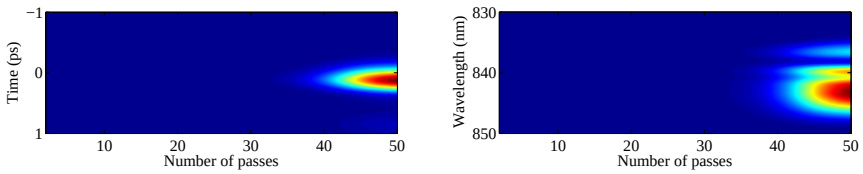

(f) Offset Time = 778 fs

Figure 7.2.4: Continuation of Fig 7.2.3.

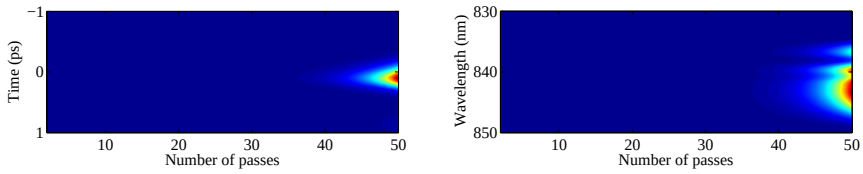

(a) Offset Time = 794 fs

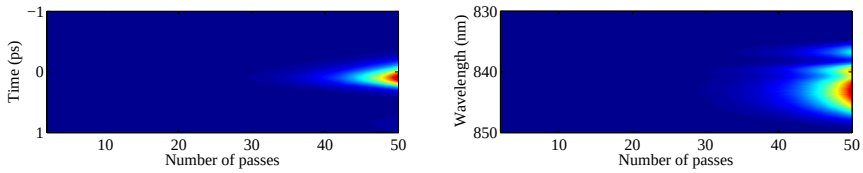

(b) Offset Time = 809 fs

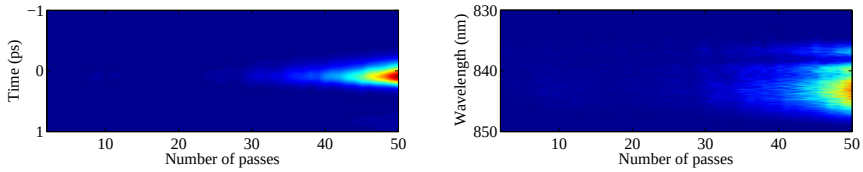

(c) Offset Time = 824 fs

Figure 7.2.5: Continuation of Fig 7.2.4.

The characteristics of the FOPO with the fabricated fibre can be summarised in terms of the peak powers and the time-bandwidth products of the signal pulses, which are plotted in Fig. 7.2.6. Through tuning the offset time between signal and pump pulses, a maximum output peak power of 1.8 kW and TBP of 0.8 can be obtained. Comparing this output to the designed one, one can find that with the fabricated bismuth fibre, the FOPO conversion efficiency is reduced by 15%, and the pulse quality is dropped from 0.5 to 0.8 (TBP). However, the overall peak power conversion with the fabricated fibre can still reach 36%.

7.2.2 Parametric gain of SF57 HWW fiber

The predicted parametric gain of the SF57 fibre with 5 kW pump is shown in Fig. 7.2.7a. Different to the bismuth fibre, the SF57 fibre does not have three ZDWs and its ZDW appears at approximately 1.6 μm. This ZDW is closer to the pump

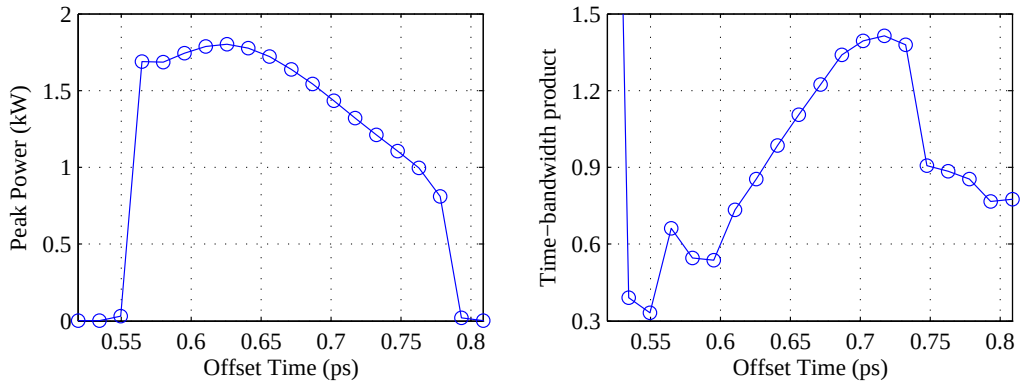

(a) (b)

Figure 7.2.6: Peak power (a) and TBP (b) of output pulses as a function of offset time with a fixed feed-back ratio of 0.5

wavelength 1560 nm which indicates that this fibre has a broader gain bandwidth than that of the bismuth fibre (see Eq.4.1.16 in Chapter 2). Furthermore, as one can see in Fig. 7.2.7b, the gain band at the pump wavelength 1560 nm is shifted 150 nm to 1030 nm, while for the bismuth fiber, the shift is only 40 nm. However, it is still possible to achieve 880 nm output if the pump wavelength is changed to 1475 nm. Another difference of comparing with the bismuth fiber is that the parametric gain of SF57 fiber at 880 nm is approximately 800 m^{-1} while for bismuth fiber is around 2000 m^{-1}, which matches their difference in nonlinearity.

7.3 SC generation

SC generation involves many nonlinear processes, including FWM process, which makes SC generation process more sensitive to the changes in the dispersion and nonlinearity profiles than FWM process. The fabricated fibres have shown differences in dispersion and nonlinearity to the ideal fibre due to the fabrication distortions. It is important to know how these fabrication distortions could influence our previous prediction of SC generation.

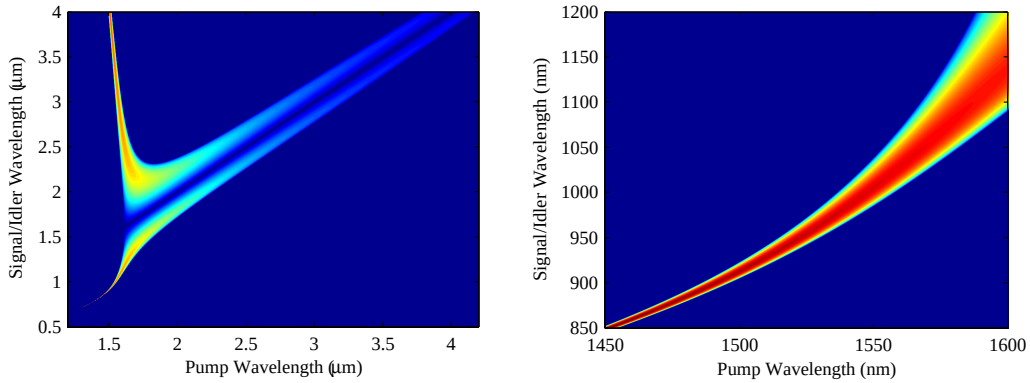

(a) (b)

Figure 7.2.7: (a) Parametric gain map of SF57 HWW fiber with 5 kW pump (b) zoom up the region around pump 1560 nm.

7.3.1 SC generation in Bismuth HWW fibers

The predicted SC generation of the fundamental mode of the fabricated bismuth fibre is shown for different pump wavelengths (Fig. 7.3.1). Similar to the optimised case, the SC generation in the fabricated fibre does not show significant soliton formation, and the spectral span of the continuum covers the whole transmission windows of the glass (assuming the transmission window is from 0.4 to 6 μm). Due to the flat dispersion design of the fibre, the spectrogram of the SC outputs are all similar for all pump wavelengths from 1200 to 4100 nm.

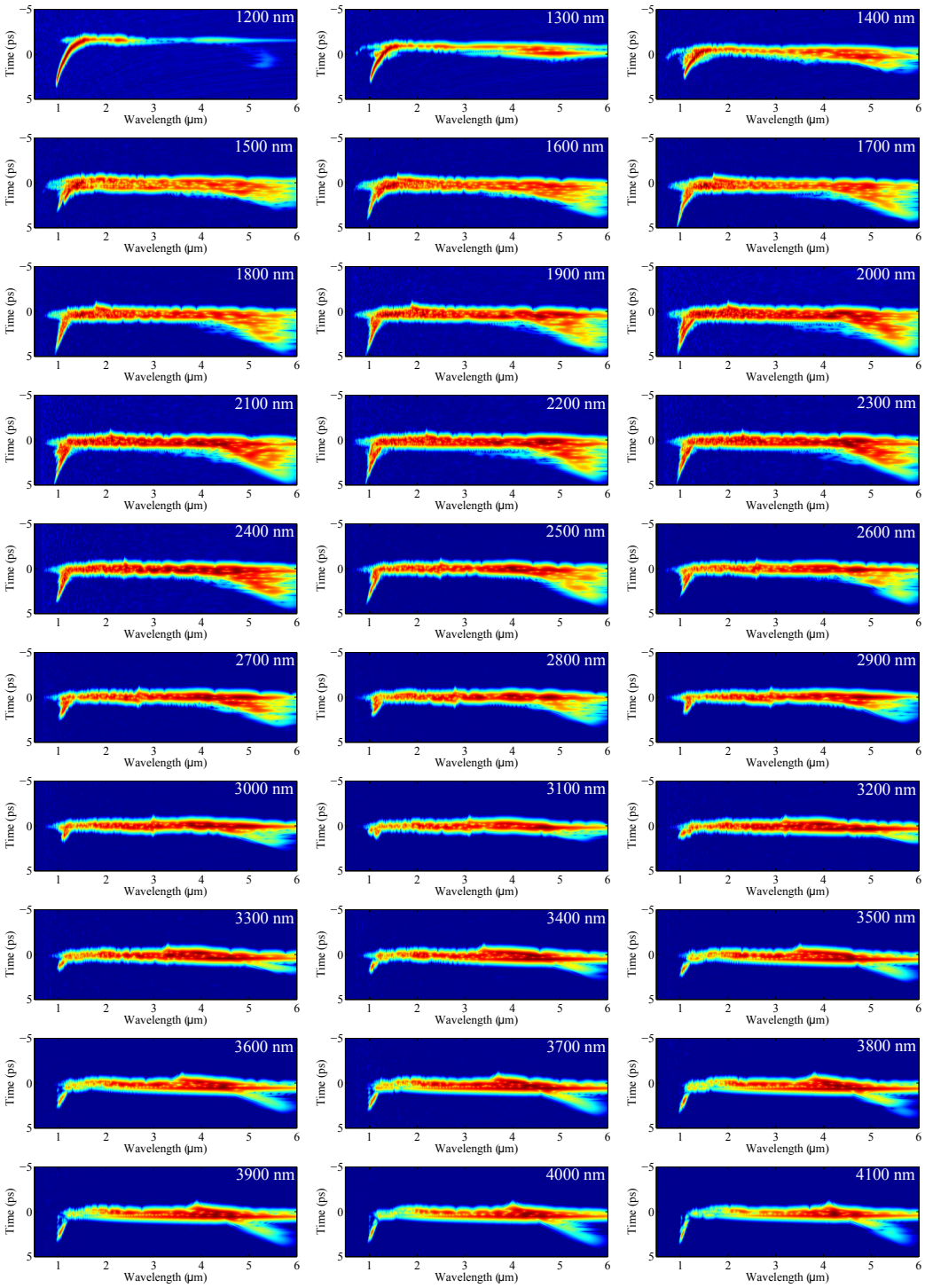

Figure 7.3.1: Predicted spectrogram of SC output of fabricated Bismuth HWW fibre. Pump wavelengths are labelled inside the plots

Fig. 7.3.2 shows the evolution of the bandwidth and coherence of the continuum as the pulse propagates for a range of pump wavelengths. Different to the SC generation in the optimised fibre, in this fiber, the maximum SC bandwidth happens when it is pumped around 2 μm at which the coherence decreases most quickly. Due to the anomalous dispersion at this pumping wavelength, spontaneous FWM/MI helps the fast increase of spectral span (refer to the parametric gain map in Fig. 7.2.1) but also lead to the fast decrease of coherence. According to our analysis in Chapter 5, spontaneous MI is the major causes of coherence degradations in this case.

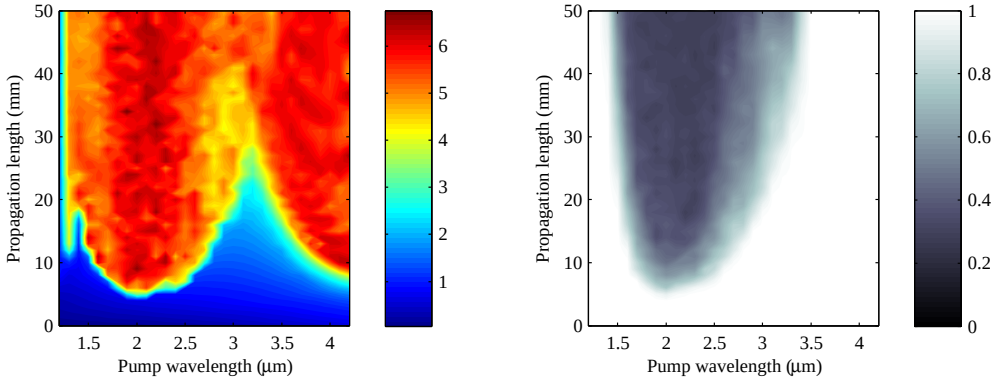

(a) (b)

Figure 7.3.2: Simulated bandwidth (left) and coherence (right) of SC outputs with different pump wavelengths in the fabricated bismuth fiber.

Fig. 7.3.3 and 7.3.4 show the evolution of the spectrum and coherence of a 2 μm pulse. Each row represents the pulse at a specific propagation distance from 0 with 2 mm interval. As one can see, the coherence of the pulse remains high before the sidebands rise. Those sidebands are MI sidebands which are incoherence as can be seen in the corresponding coherence plots (red arrows in Fig. 7.3.3). As the pulse broadens, the incoherent MI sidebands merge into the coherent central band and degrade its coherence.

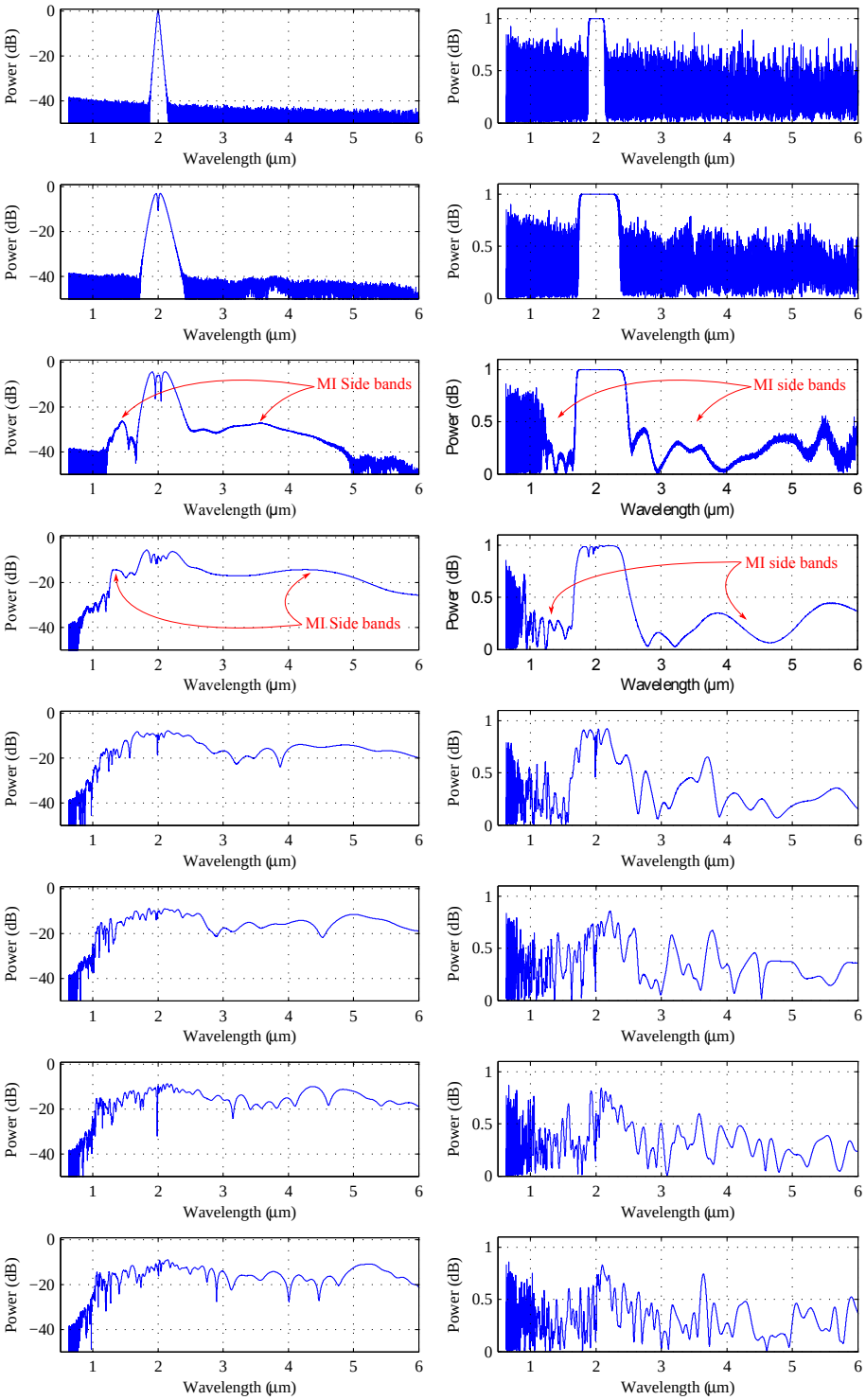

Figure 7.3.3: Simulated intensity (left) and coherence (right) spectra of pulse along the propagation from top to bottom with 2 mm intervals.

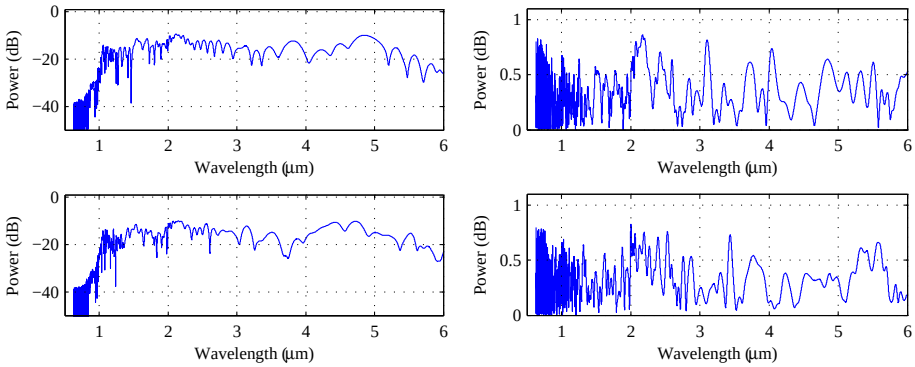

Figure 7.3.4: Continuation of Fig. 7.3.3.

Unlike the optimised case in Chapter 5, the anomalous dispersion between the first and second ZDWs is responsible for the degradation of the coherence of the continuum. This indicates that, to maintain the coherence of the continuum, the dispersion of the fibre has to be kept below 16 ps/nm/km to avoid MI.

Although, the fabricated fiber did not achieve the designed coherence qualification, its outputs at least have proven two important points of our model. Firstly, low and flat dispersion is a way to achieve broadband SC. Secondly, anomalous dispersion could lead to coherence degradation. The first point is preferred for applications that they only require large bandwidth, while the second point is more difficult to overcome. In the future studies, it will be useful to find out an approach to avoid MI when anomalous dispersion presents. Also, refining GA's fitness function to design fiber with no anomalous dispersion will be a way to achieve highly coherent SC generation.

Up to this stage, the simulations are for single mode propagation. However, as discussed in Section 7.1.1, the fabricated fibre is multimode. The multimode pulse propagation simulation is computational intensive and requires solving many of coupled nonlinear Schrödinger equations [156, 157]. Here, to facilitate comparison with experimental data later in this thesis, an alternative approach is considered in which two assumptions are made. Firstly, in experiments, the alignment of the laser beam and the fiber is optimised such that the majority of the light is coupled

into the fundamental mode along one of the principle axes. Therefore, the nonlinear pulse broadening is dominated by the fundamental mode. Secondly, nonlinear cross-talks between the modes are ignored, including cross-phase modulation and coherent coupling. With these assumptions, the total electric field at the fiber output is written as a superposition of the electric fields of all modes. The fraction of pulse power in each mode is then determined by the coupling between the input beam and that mode. The coupling efficiencies between an input beam, and the modes based on the mode field pattern calculated from COMSOL are calculated. The coupling efficiency can be described by Eq. (7.3.1) which is a simplified form derived based on Ref. [158]. Approximations that are implicit within this definition include the assumption that the modes are purely transverse and there is no coupling to radiation modes. The Fresnel reflection does not need to be considered here, since only the relative ratios of the coupling efficiencies of the modes are needed.

$$\eta_n = \frac{\left|\int E_{in} \cdot E_n^* da\right|^2}{\int |E_{in}|^2 |E_n|^2 da} \tag{7.3.1}$$

In Eq.7.3.1, η_n is the coupling efficiency of n-th mode, E_{in} is the electric field of the input beam and E_n is the electric field of n-th mode inside the fiber. Assuming the input field distribution is Gaussian, the coupling efficiencies from the input field to the different modes can be found for a range of input beam diameters (focal spot size in experiments) as shown in Fig. 7.3.5a.

These calculations indicate that the first 16 modes contain the majority ($\sim$94%) of energy of the launched beam (as shown in Fig. 7.3.5b). The pulse propagation for each of these modes were simulated independently with power determined by the coupling coefficients and for a range of input beam diameters. Following this, the electric fields of all the modes at the output of the fiber are superimposed. The superimposed electric fields interfere with each other, resulting in changes in the generated spectra.

Such simulations were carried out for a range of different pump wavelengths. The following wavelengths are chosen by considering the dispersion profile of the funda-

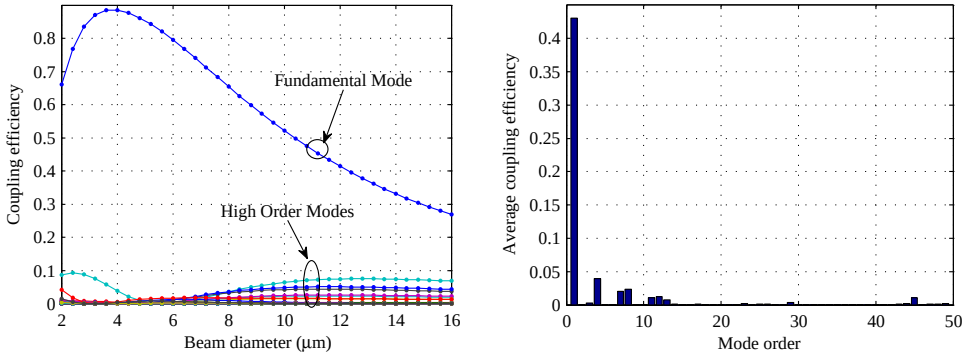

(a) (b)

Figure 7.3.5: (a) Coupling efficiencies for different modes vs. beam diameter of the incident Gaussian beam. (b) Average coupling efficiencies for a range of modes.

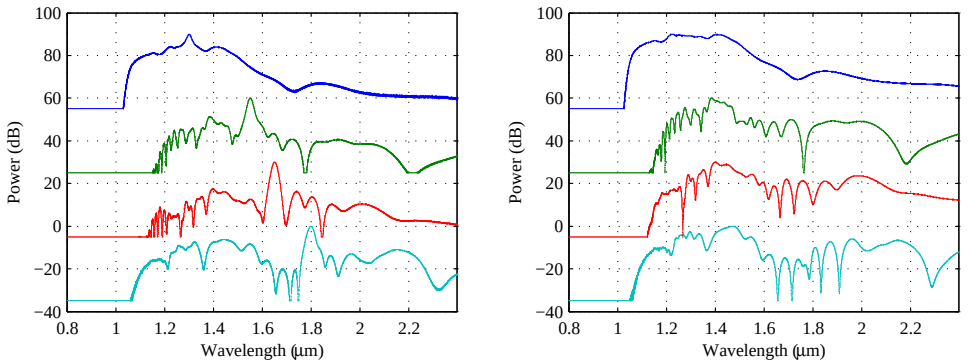

(a) (b)

Figure 7.3.6: Simulations of SC generation. Spectra are normalised to their peak level and offset vertically for easier viewing. (a) Spectra of multi-mode pulse propagation simulation pumped at 1300 (blue), 1550 (green), 1650 (red) and 1800 (cyan) nm with 100-fs 10-k peak power pulses, (b) SC spectra of the fundamental mode for the same range of pump wavelengths.

mental mode: a pump wavelength of 1300 nm is in the normal dispersion region, pump wavelengths of 1550 and 1650 nm are in the normal dispersion region but close to ZDW, and a pump wavelength of 1800 nm lies in the anomalous dispersion

region. The output of the pulse propagation model is shown in Fig. 7.3.6a.

The spectral broadening in these simulations is dominated by the fundamental mode as it contains most of the energy. Therefore, despite the multimodeness of the fiber, the single-mode-based design directives of this fiber are still valid. Fig. 7.3.6b shows the spectral output of the fundamental mode only. The most significant differences between multimode (Fig. 7.3.6a) and single-mode (Fig. 7.3.6b) simulations are the peaks around the pump wavelengths [the highest peaks at 1300 (blue), 1550 (green), 1650 (red) and 1800 (cyan) nm]. These peaks are contributions from high-order modes. Apart from that, the rest of the spectra are similar to the spectra generated by the fundamental mode alone.

7.3.2 SC generation in SF57 HWW fiber

The SC generation in the fabricated SF57 fibre was also modelled. As one can see from the spectrograms of the SC outputs with different pump wavelengths in Fig. 7.3.7, when the fibre is pumped far in the normal dispersion regime (pump wavelengths much shorter than 1600 nm, such as 1200∼1400 nm, refer to Fig. 7.1.5), the broadening is dominated by SPM. Therefore, the spectra broadening are limited. When the fibre is pumped close to the ZDW (1600 nm) and in the anomalous dispersion regime (pump wavelengths longer than 1600 nm), soliton formation and soliton fission take place. Depending on the nonlinearity and dispersion at the pump wavelength, the number of solitons that will split from the pump pulse is determined by the soliton order. In our SF57 HWW fiber, the soliton order is small ($\leqslant 3$), and decreases as pump wavelength increases. Correspondingly we see soliton formation and fission as pump wavelength increases while the number of soliton reduces from initially three to only one (from pump wavelength of 1900 to 4100 nm in Fig. 7.3.7). In this fiber, large bandwidth is obtained only when pumping around its ZDW.

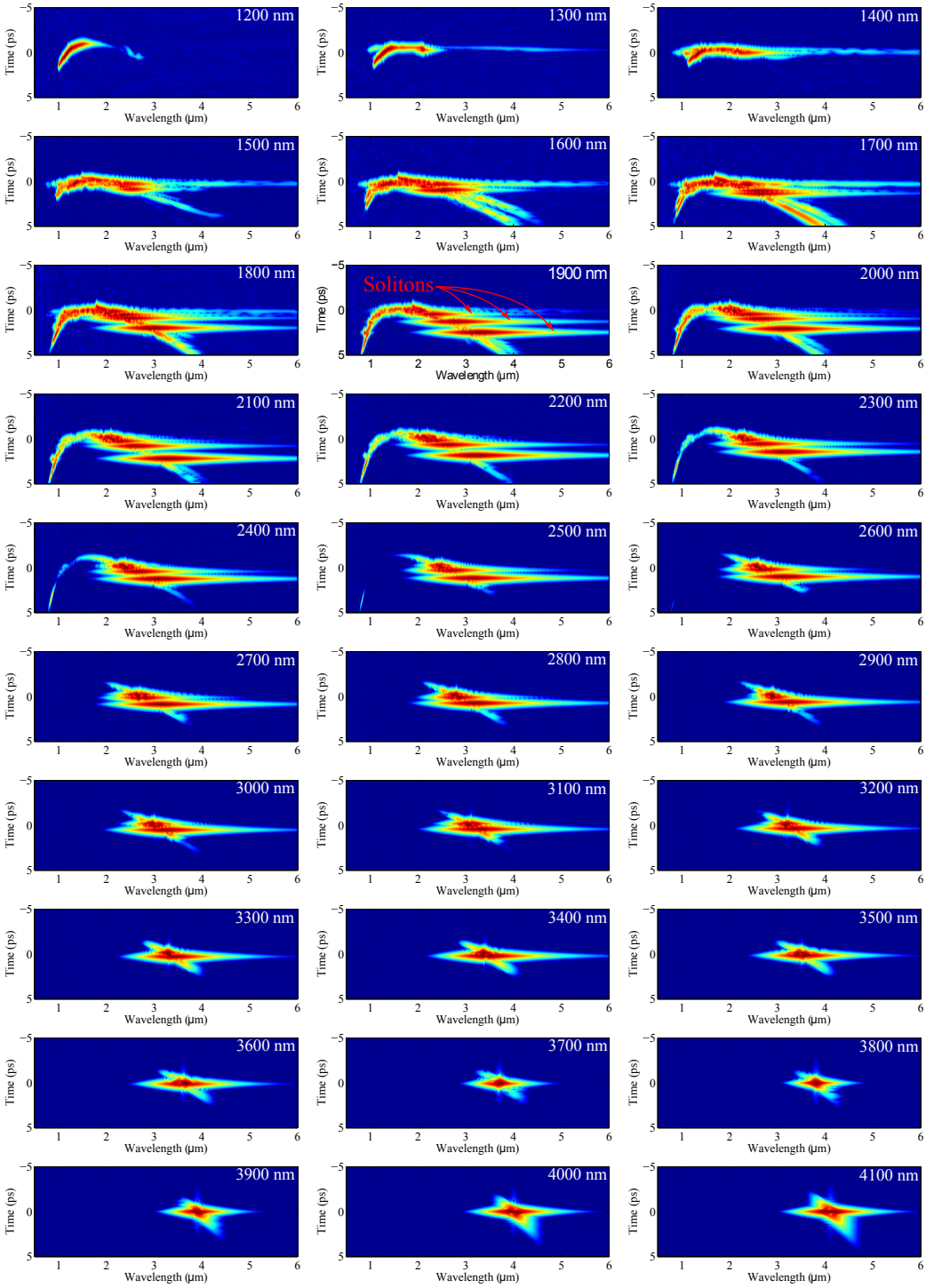

Figure 7.3.7: Predicted spectrogram of SC output of fabricated SF57 HWW fiber for different pump wavelengths.

Interestingly but not unexpectedly, the predicted coherence of the SC generation in this fiber is good except for the ones pumped around the ZDW. But this is mainly due to the low nonlinearity of the fibre and small spectral broadening of the SC in the high coherence pump wavelength region. Fig. 7.3.8 shows the overview of bandwidth and coherence of the SC generations along the propagation for different pumping wavelengths. Comparing to the bismuth fiber, the bismuth fibre provides broad spectra for a much larger pump region than the SF57 fibre.

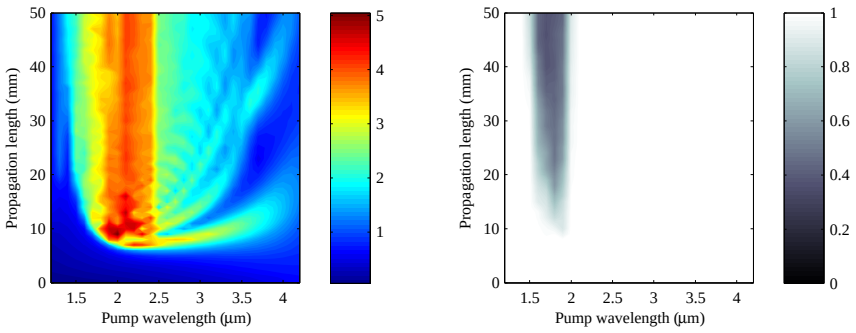

(a) (b)

Figure 7.3.8: Simulated bandwidth (left) and coherence (right) of SC outputs with different pump wavelengths in the fabricated SF57 fiber.

7.4 Summary

In this chapter, FOPOs and SC generation were simulated with the fabricated fibers. The fabrication distortions alter the dispersion and nonlinearity profiles of the fibres from what they were designed to be. The distortions result in the decrease of conversion efficiency and output pulse quality of the FOPO and the decrease of bandwidth or coherence of SC generation. However, through analysing the simulations result in those fabricated fibers, one can estimate what should be expected in the experiments as well as to understand the physical processes better. FEM calculations show the actual dispersion and nonlinearity profiles of the fabricated fibers.

The dispersion profile of the bismuth fiber still shows three ZDWs. The values of these ZDWs are changed from approximately 2, 2.5 and 3 μm to 1.7, 2.7 and 3.6 μm. The span of the low flat dispersion regime is therefore expanded by nearly 100%. However, the maximum difference of value in the dispersion curve within this wavelength region becomes bigger than the design. In mean time, the nonlinearity of the fabricated bismuth fiber is approximate 40% higher than the design in average for wavelengths from 1 to 4 μm. Dispersion and nonlinearity profiles of the SF57 fiber are much different to the design due to their difference in material. There is only one ZDW around 1.6 μm and the nonlinearities are around 40% lower than the design in average for all wavelengths.

In FOPO simulations, the changes in the dispersion profiles cause significant changes in the parametric gain. However, we found gain bands near the original design pump wavelength 1560 nm with both fibers. The gain band of bismuth fiber, at 1560 nm, is narrow but fairly close to, 40 nm shorter than, our designed target 880 nm. For the SF57 one, the bandwidth is relatively larger but the wavelength shift is bigger, 150 nm longer than 880 nm. For both, it is still possible to obtain 880 outputs with different pump wavelengths.

The bismuth fibre based FOPO was also simulated. The signal build-up behaviour is quite close to the one described in Chapter 4. But the walk-off between pump and signal pulses is bigger than the that of the design, which caused two side effects to the FOPO. Firstly, the increase in the best offset time (Fig. 7.2.6) which caused the decrease of maximum conversion efficiency. Secondly, the decrease of the TBP of the output pulses by a factor of 2 (Fig. 7.2.6).

In SC simulations, the results clearly show the superiority of the optimised fiber. In bismuth fiber, the small positive dispersion increase between the first and second ZDWs and causes a distinct increase in SC bandwidth and decrease in coherence. Different from the optimised fiber, the coherence degradation caused by this dispersion regime originated from MI and cannot be effectively removed through the loss profile of the fiber and therefore indicates it is crucial to keep low dispersion in the

flat dispersion regime for maintaining high coherence.

Simulation of SC generation in SF57 fiber shows clear soliton-related dynamics. Due to low nonlinearity of the fibre, the coherence of SF57 fibre remained high for most of the pump wavelengths away from the ZDW. However, the SC bandwidth in this case is smaller than that of the bismuth fibre. Similar large SC bandwidth was only achieved for pumping around the ZDW.

Based on the simulation results, it can be predicted that extensive pulse broadening can be easily observed in both Bismuth and SF57 fibres when they are pumped with femtosecond pulses. The outputs of the two fibres should be distinguishable from at least two aspects that indicate the characteristics of the fibre dispersion and nonlinear properties. Firstly, at same input power levels, spectral broadening in Bismuth fibre should be broader than in SF57 fibre regardless of pumping wavelength. Secondly, at the same pump wavelength, more high intensity solitons and their relayed dispersive waves should be observed in SF57 fibre than in Bismuth fibre when they are pumping in their anomalous dispersion regimes. Both of the two points indicate the benefits of optimised dispersion and nonlinearity profiles of the Bismuth fibre to the SC generation. Since the outputs of SC generation in these cases are equivalent to the single pass output of a FOPO, the benefits of optimised dispersion and nonlinearity profiles of the Bismuth fibre also apply to FOPO applications too.

In the next chapter, experiments of short pulse broadening are performed to demonstrate the SC generation in the fabricated fibres and prove the improvement of optimised design for SC generation and FOPO applications.

Chapter 8

Femtosecond pulse broadening experiments

8.1 Background

In the previous chapters, fibers with low and flat dispersion were designed and fabricated for generating highly coherent broadband SC and constructing high efficient near-IR femtosecond FOPOs. Calculations based on the SEM images of the fabricated fibres indicate that the fibre fabricated in Bismuth glass has a low flat dispersion profile with three ZDWs at 1.7, 2.7 and 3.6 μm and a variation of 15 $ps/nm/km$ around 0 across 1.7 to 3.6 μm. This nonlinearity of this fibre at 2 μm is predicted to be 175 $W^{-1}km^{-1}$. The calculations also indicate that dispersion profile of the fibre fabricated in SF57 glass is not as flat as that of the Bismuth fibre and there is only one ZDW at 1.6 μm. The nonlinearity of the SF57 fibre is also lower than the Bismuth fibre by 40% in average for wavelengths ranging from 1 to 4 μm. Simulations based the Bismuth and SF57 fibres indicate that although the coherence of SC generation in the optimised fibre (Bismuth) does not remain high due to the increased variation in dispersion, broad SC generation should be observed in both Bismuth and SF57 fibres. Simulations also indicate that through comparison and

analysing the outputs of SC generation in these fibres, significant differences in SC bandwidth and soliton-related nonlinear processes can be identified. The differences show the characteristics of the dispersion and nonlinearity of the two fibres.

In this chapter, short pulse broadening experiments are performed with both Bismuth and SF57 fibres to demonstrate the SC generation in these fibres and compare the experimental results to the simulations in Chapter 7 to help understanding the nonlinear processes and prove the advantages of the fibre design.

8.1.1 Chapter outline

In this chapter, the femtosecond laser source are firstly characterised to obtain information on pulse's spectral content, noise level and power stability. These information are used in Chapter 7 for simulating the pulse broadening in the actual fibre which provides insight into the nonlinear processes that occur as the pulses travel along the fibres. After characterising the laser source, pulse broadening in SMF28 fibre were first measured. The single modeness of SMF28 and well known dispersion and nonlinearity profiles enable us to check both the experimental setup and that the simulation program is working as expected.

During the experiments, the signal obtained from the photon detector was found to be weak. To overcome this, a signal processing step was added to extend the detection sensitivity. Spectral outputs of the bismuth and SF57 fibres were measured for a range of pumping wavelengths and power levels. The outputs of bismuth fibre were also compared to the numerical simulations from Chapter 7.

8.2 Characterisation of the pump laser source

A tunable femtosecond pump source is chosen for this work to provide the peak pulse intensity required for SC generation and to match the specification of fibre design. The femtosecond laser source includes a Millennia Prime pump laser, a Spectra Physics Tsunami ultrafast Ti:Sapphire laser, a Spitfire Pro XP Ultrafast

Ti:Sapphire amplifier and a TOPAS automated ultrafast OPA (see Fig.8.2.1). The Ti:Sapphire laser is pumped with 8 W 533 nm CW laser and outputs 800 nm 100 fs pulses at 80 MHz. The repetition rate is reduced to 8 MHz and about 400 mW power is sent to the amplifier. The amplifier amplifies the pulses to 1 W and at this time the repetition rate is reduced to 1 kHz. The output of the amplifier is then used to pump the OPA to provide mW-level tunable output from near- to mid-IR with the help of a linear polariser (Thorlabs LPNIR) to pick the signal or idler wavelengths.

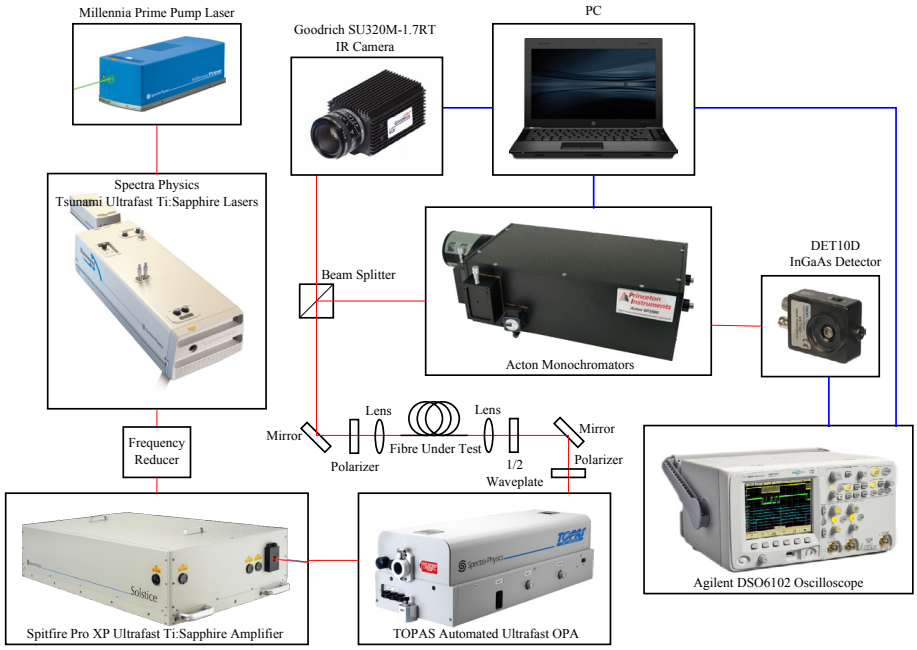

Figure 8.2.1: The illustration of experimental setup. Red lines: optical passes, blue lines: electrical connections

The OPA is seeded with a white light SC source generated from the same input source. The spectra of generated signal and idler pulses of the OPA is influenced by the seed. Knowing the stability and spectral content of the pump pulses is necessary to support the analysis of the nonlinear processes.

Figure 8.2.2 shows the spectra averaged over 1000 pulses at OPG output with different wavelengths. Those spectra were measured using a long-pass filter (to

remove the pump); a linear polariser (for separating signal and idler pulses whose polarisations are perpendicular to each other); a few neutral density (ND) filters (for limiting the pulse power); a broadband half-wave plate (for rotating polarisation) and two pairs of gold-coated mirrors. Nonlinear effects in these optical components are not obvious.

As it can be seen from the Fig. 8.2.2, the spectral content varies significantly with wavelength. As the wavelength becomes longer, the bandwidth of the output spectrum becomes broader. The spectral shape of the OPA outputs also varies with wavelength which could attribute to the change of alignment of the pump and seed beams inside the OPA crystal as it rotates to for different wavelengths.

The stabilities of the output power of the OPA at different wavelengths are also measured and shown in Fig. 8.2.3. The fluctuation in the power varies with wavelength over time. In Fig. 8.2.3(a)$\sim$(g), each red point in every plot is the measured power averaged over 1 minute, with 10 such measurements performed sequentially. The error bar represents the standard deviation of 1-minute measurements. The green and blue dots represent the minima and maxima power within each minute slot. Each plot shows two distinct types of power instability: a high speed pulse to pulse instability and a slow power drift.

The pulse to pulse instability, indicated by the standard deviation of each wavelength shown in Fig. 8.2.3(h), is most severe around 1600 nm. The slow power drifting over time, such as the power fluctuation in Fig. 8.2.3(a), could be caused by the temperature fluctuation of the nonlinear crystal in the OPA.

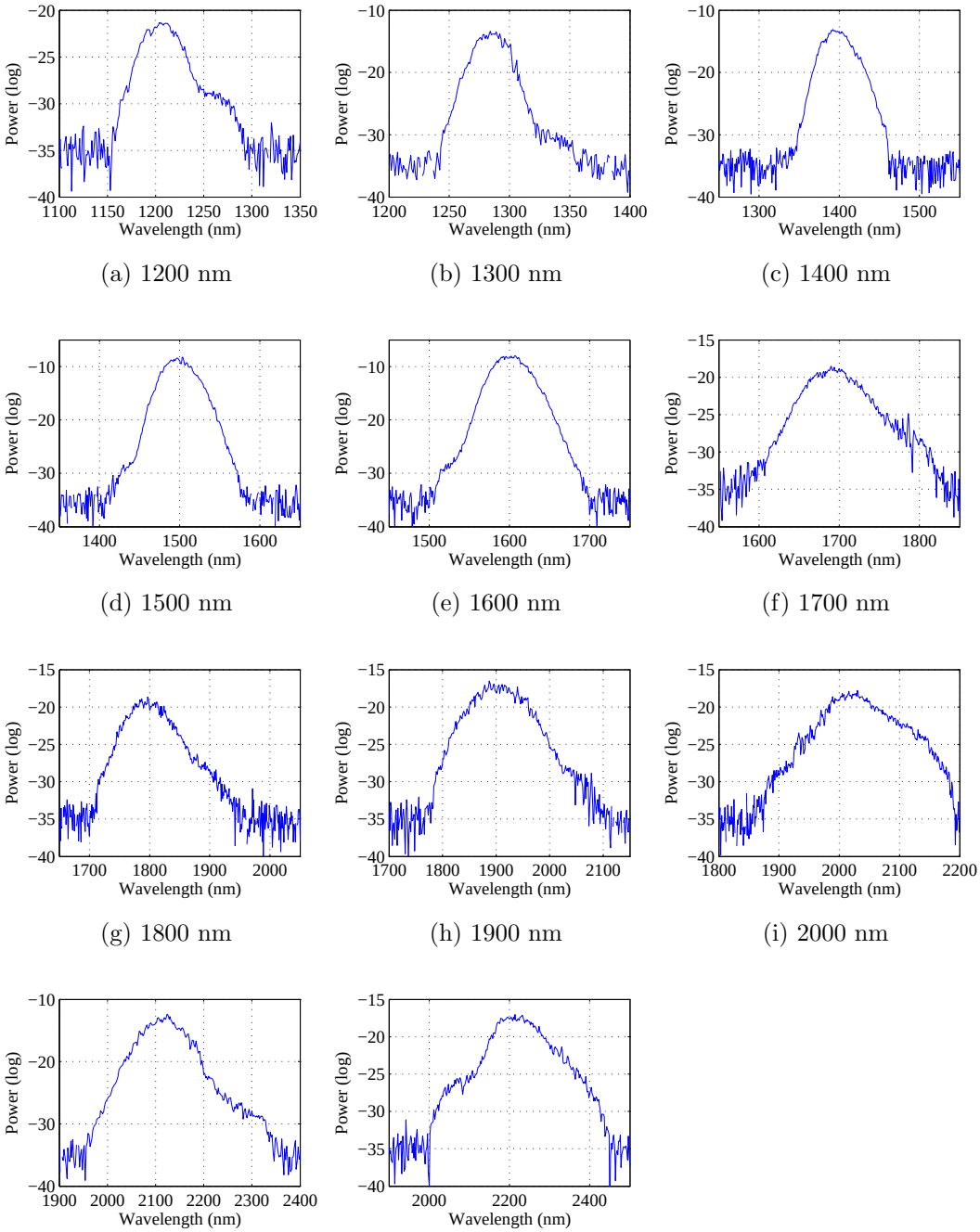

(a) 1200 nm (b) 1300 nm (c) 1400 nm

(d) 1500 nm (e) 1600 nm (f) 1700 nm

(g) 1800 nm (h) 1900 nm (i) 2000 nm

(j) 2100 nm (k) 2200 nm

Figure 8.2.2: Averaged spectra of the pump pulses from the TOPAS OPA at different wavelengths

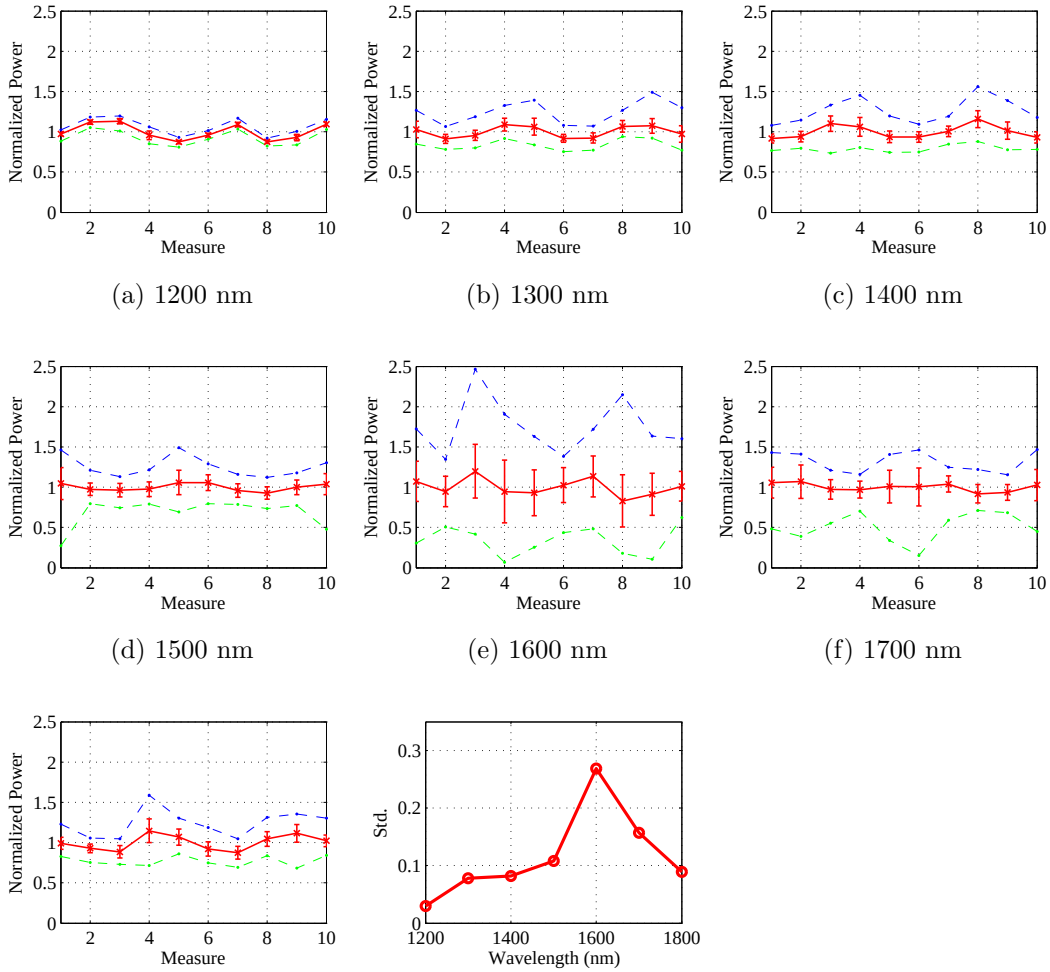

(a) 1200 nm (b) 1300 nm (c) 1400 nm

(d) 1500 nm (e) 1600 nm (f) 1700 nm

(g) 1800 nm (h)

Figure 8.2.3: Power fluctuation of the pump pulses at different wavelengths. Powers are normalised to the mean value. (a)∼(g): red: average, error bar: standard deviation, green: minimum, blue: maximum. (h): Variation of standard deviation with wavelength

The power fluctuation of the system limits the quality of experimental work, hence averages of 10,000 pulses are taken for each measurement in the experiments described here. With the knowledge of the pump source, nonlinear broadening experiments can be carefully carried out.

8.3 Spectral broadening in SMF-28

Before characterising the fiber designed and optimised in Chapter 5, pulse broadening in standard single-mode SMF-28 fiber was firstly explored to verify the experimental setup and the simulation programs. In the experimental setup (Fig. 8.2.1), the beam from the OPA was linearly polarised. After that a half wave plate (Thorlabs AHWP05M-1600) was used to tune the polarisation angle of the input beam. The beam was coupled in and out of the fibre using an aspheric lens (Thorlabs 352260-C). Three different pumping wavelengths were chosen to estimate the influence of the noise of the pump source on the generated SC. The three pump wavelengths selected are 1200 nm, 1300 nm and 1500 nm which are in normal, near zero (ZDW of SMF-28: 1310 nm) and anomalous dispersion regimes respectively for this fiber.

Figure 8.3.1 shows the experimental and simulation results of pulse broadening in a 1 metre long SMF-28 fiber pumped at 1200 nm, 1300 nm and 1500 nm. Observations made in these experimental match well with our simulation results. In the normal dispersion regime, SPM dominates the broadening. Smooth and narrow spectra can be observed as the pump power increases. For wavelengths near the ZDW, the broadened spectra are more noisy but wider and flatter than the ones in the normal dispersion regime. Once the pump wavelength moves into the anomalous dispersion regime, clear soliton dynamics are observed: two solitons are evident around 1650 nm and 1750 nm in the cases of pump power 5.2 and 8.2 μW, respectively. Simulations shown in right column of the plot matches with the experimental results. In the simulations, the pump pulses were ideal hyperbolic secant pulses with peak powers corresponding to the ones used in the experiments.

By comparing the experiments with simulations, one can find the best agreement was obtained in the normal dispersion regime. The influences of power fluctuation and spectral impurity are negligible when sufficient averaging are taken since the dominate nonlinear process in this dispersion regime is SPM which can be accurately

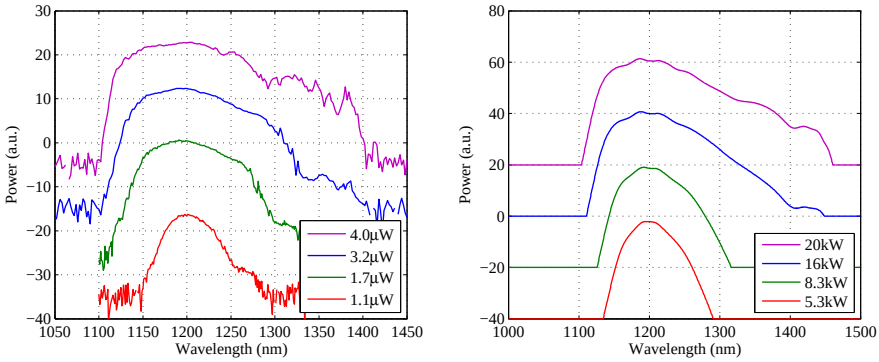

(a) 1200-nm Experiment

(b) 1200-nm Simulation

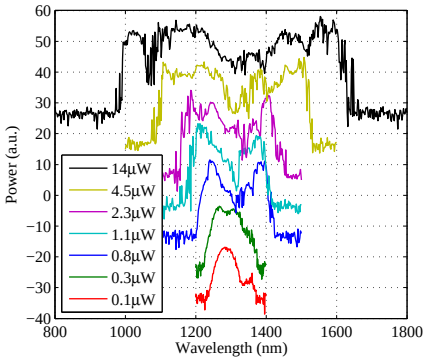

(c) 1300-nm Experiment

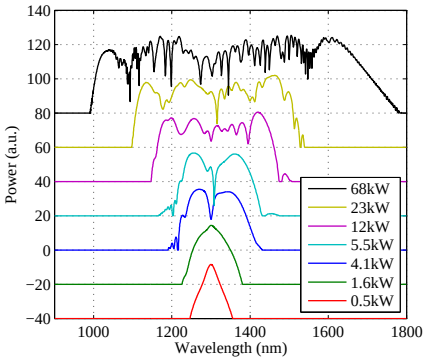

(d) 1300-nm Simulation

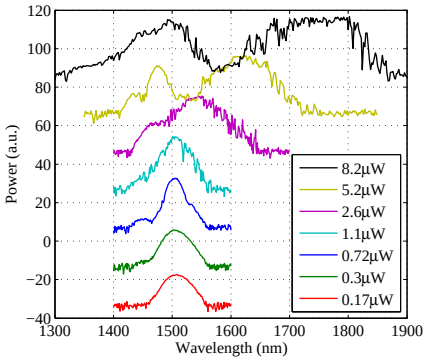

(e) 1500-nm Experiment

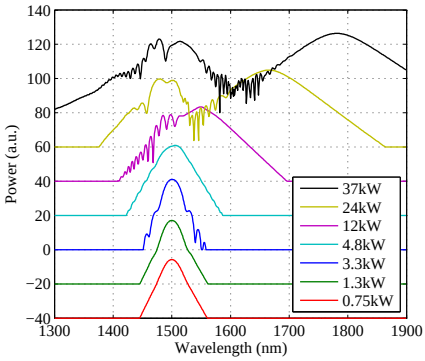

(f) 1500-nm Simulation

Figure 8.3.1: Comparison of experiments and simulations of spectral broadening in 1 metre of SMF-28 pumped at normal (1200 nm), zero (1300 nm) and anomalous (1500 nm) dispersion regions

predicted. As the pump wavelength move towards anomalous dispersion region, more complicated nonlinear processes such as modulation instability and soliton fission take place. These processes are sensitive to the noise in the input. Small fluctuation in the input can trigger significant changes in the output spectra. For the case of power level at 8.2 μW in Fig. 8.3.1(e), spectra averaged over 10,000 pulses is not enough to show a smooth spectrum of the soliton(s) between wavelengths 1600 to 1900 nm even the soliton order of this fiber is low (≈ 3, indicates 3 solitons will form during the fission process). Usually with low soliton orders, soliton fission processes are relatively stable. In addition to solitons, MI and XPM will also modulate the spectra randomly which could not be identified here.

Despite the source fluctuations, the agreement between simulations and experimental results confirms 1) the experimental setup can be used to measure the pulse spectrum. 2) The simulation tool can accurately predict nonlinear processes during pulse propagation.

8.4 Fibre alignment

The fibre designed in Chapter 5 is known to be multimode. The modal content of light in the fibre is sensitive to the way in which light is launched into the fibre. Variations in the modal content within the fibre can be expected to change the generated SC significantly since the modes differ significantly in their dispersion and effective nonlinearity (see Chapter 7 Fig. 7.1.3).

As a starting point, for simplicity, it is preferred to compare generated SC of fundamental mode only. Therefore, a careful fiber alignment was preformed to preferentially launch the pump power into the fundamental mode.

To do so, a IR camera (GOODRICH SU320M-1.7RT, wavelength ranging from 0.9 μm to 1.7 μm) is used to image the output of the fiber. Fig. 8.4.1a shows the mode profile of the output of 6 mm of SF57 fibre. The wavelength of the beam is 1550 nm. The bean is linearly polarised and its polarisation direction is aligned

to one of the principle axes of the fibre. The coupling is optimised by maximising the intensity of the peak in the centre of the fibre core. Fig. 8.4.1b is the mode profile of the same output after a linear polariser whose polarisation direction is perpendicular to that of the input beam. The fiber is polarisation maintaining according to our calculation based on SEM image (Fig. 6.4.4a) of the fibre as a result of the slight asymmetry within the structure. Therefore, one would expect that the fundamental mode should mostly be removed after the polariser. However, as one can see, Fig. 8.4.1b still shows a complex pattern, which indicates the possible excitation of other modes as predicted in Chapter 7. An M^2 measurement with the fabricated Bismuth fibre was performed in Appendix A.2, which experimentally confirm multimodeness of the fibre.

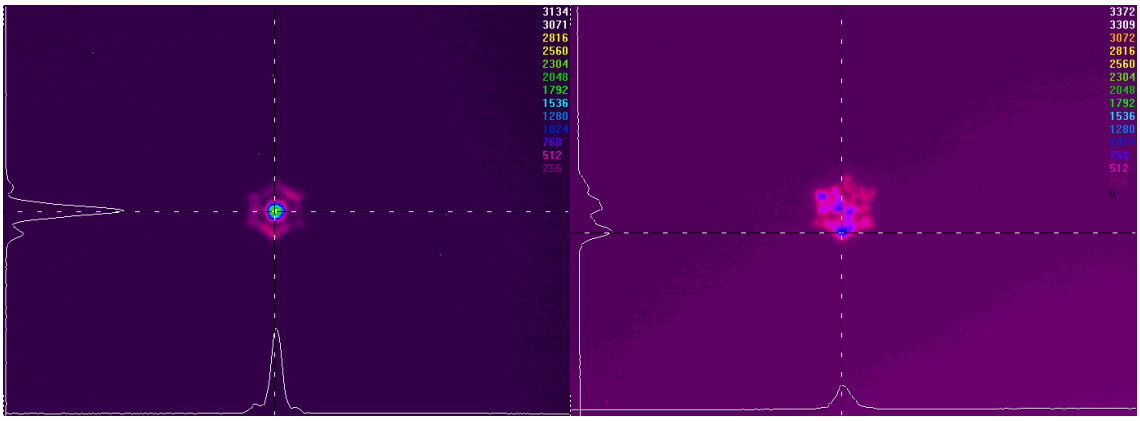

(a) (b)

Figure 8.4.1: (a) Output mode profile of the SF57 fibre aligned to one of the principle axes. (b) Same output filtered with a linear polariser with polarisation aligned perpendicular to that principle axis.

Since the response of the IR camera only extends to 1.7 μm, the alignment for pump wavelength longer than 1.7 μm cannot be done using it. An indirect approach was taken to bypass this difficulty: firstly, using a 1.7 μm beam to align the fibre and then increase the wavelength until the beam can barely be been on the camera. Now refine the alignment and increase the pump power to make the beam clearly

shown on the camera again. Repeat this process until the demanded wavelength is reached. As the pump power been gradually increased, SC was generated in the fibre and part of its spectrum extended into the operational wavelength range of the detector which allows one to observe the beam on the camera. However, this approach has its limitations. Although by optimising the detectable part of the spectrum, the alignment of the pump beam is also optimised in some sort. There is no guarantee that coupling is optimised for the fundamental mode; instead this process will optimise for the modal distribution that generates the best SC in the observable wavelength range.

8.5 Signal processing

The spectra in Section 8.3 were measured using a monochromator and a photon detector. The dynamic range of the detector (Thorlabs PDA10D 1.5 mV typical noise $\sim$ 10 V) limits the sensitivity of the measurement (maximum 38 dB). Meanwhile the femtosecond laser system provides 100 fs pulses with 1 kHz repetition rate. To obtain pulses with peak power in the range 1 $\sim$ 100 kW, the average power of the laser output needs to be in the range of 1 $\sim$ 10 μW which is difficult to measure using this detector. The detection dynamic range of the light from the monochromator is only approximately 20 dB for a 10 kW peak power pulse. Although the bandwidth of SC can be defined as the spectral width at 20 dB below the maximum, it is still better if the details below 20 dB of maximum power can be seen. It can help analysing the spectrum. To maximise the use of the dynamic range of the detector, a signal processing algorithm was developed.

As shown in Fig. 8.5.1, a PC is used to control both the monochromator and the oscilloscope. A script was developed to scan across the spectrum by setting the wavelength on the monochromator and reading data from the oscilloscope in turn. To ensure the maximum dynamic range of the detector and maximum resolution of oscilloscope are used, the script also automatically re-scaled the oscilloscope to

accommodate the pulse voltage. If the maximum and minimum readings from the oscilloscope exceed 90% or below 10% of the current scale, the current scan was discarded and a new one performed with a revised scale. In this manner, a voltage from a minimum of 0.1 mV to a maximum of 50 V on the oscilloscope can be read.

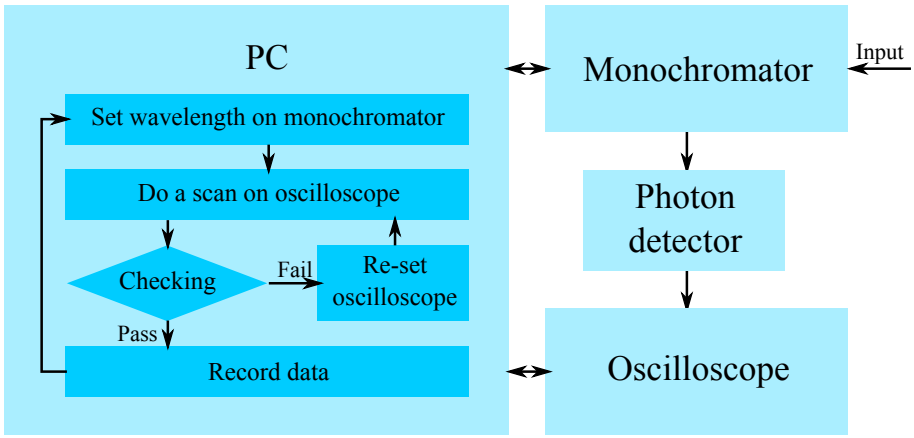

Figure 8.5.1: The flow chart of the automated signal detection system.

At first, individual pulses are measured in time and integrated to obtain the power for each wavelength. Fig. 8.5.2a shows an example of such measurements. Due to the noise in the detection system and the weak signal that reaches the detector, only approximately 20 dB below the maximum power of the signal can be detected. To improve this, a different approach can be taken.

The duty cycle of the laser is rather small (1 over 10 billion). If one takes a train of pulses such as the blue curve of Fig. 8.5.3(bottom plot), the pulses are simply spikes sitting on a noisy background. If a Fourier transform is applied to this pulse train, a spectrum like Fig. 8.5.3(top plot) can be obtained. In this plot, the spikes can be easily identified and separated from the background noise, where the signal is represented by the red dots. If everything except the red dots in Fig. 8.5.3(top plot) are filtered out and transformed back to the temporal domain, a clear signal of the pulses as the red curve shown in Fig. 8.5.3(bottom plot) can be obtained. If one integrates the pulse train after performing this transformation, spectrum can be obtained with much better signal to noise ratio. As a matter of fact, the detectable

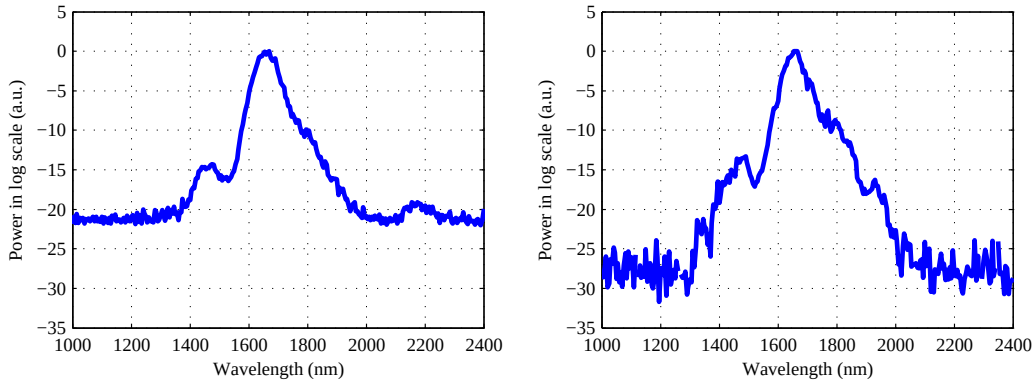

(a) (b)

Figure 8.5.2: Comparison of measured spectra. (a) Without data process. (b) With data process, the detection range increased by more than 5 dB.

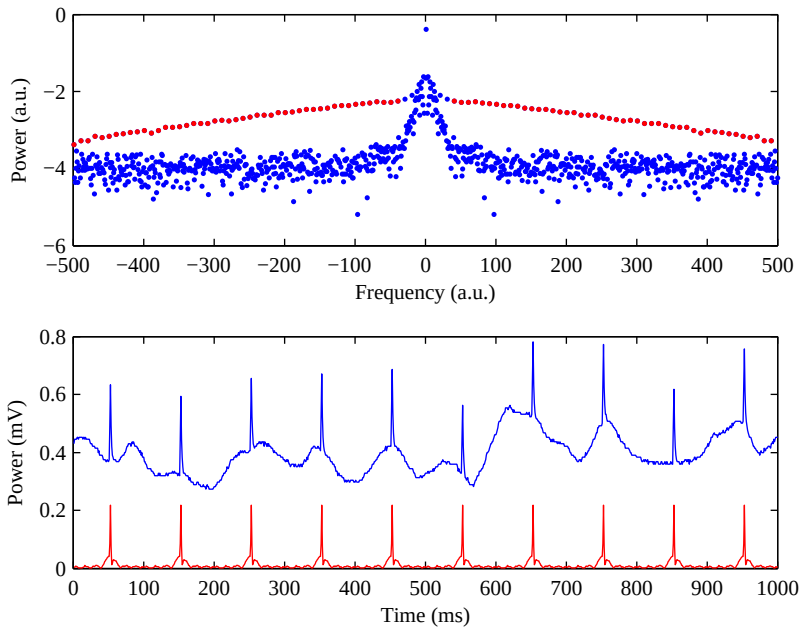

Figure 8.5.3: Signal process of the input pulse train. (top) The Fourier transform of the pulse train in the bottom plot. (bottom) The pulse trains before (blue) and after (red) filtering.

range is increased to approximately 30 dB.

8.6 Bismuth HWW fibre

The experiments were carried on in bismuth HWW fibres using only approximately 2 cm of the fibre. The reason of choosing this length is as following. From modelling, it is clear that the most significant pulse broadening is achieved in the initial few millimetres of the fibre (see Fig. 7.3.2). By comparing the spectra with simulations, one can identify and understand key features in the spectra. To do this, the fibre length chosen for the experiments should be short to limit uncertainties (including fabrication distortions, multimodeness, etc.) as much as possible but long enough to achieve a significant SC broadening. The simulations indicate that with 2 cm of fibre, one should see the initial stages of the SC as the power gradually increases as well as generated spectrum that covers the whole detection region as the pump power reaches higher levels.

8.6.1 Experimental Data

The broadened spectral outputs of the fibre for different input wavelengths are shown in Fig. 8.6.1&8.6.2. Each plot shows the spectral broadening from bottom to top as pump power increases. Using the dispersion plot in Fig.7.1.3 as a reference, one can estimate what nonlinear processes were taking place.

The main trend of spectral broadening of these measurements agree with the predictions. In the normal dispersion region and away from ZDW (1300 nm), the spectral broadening is dominated by SPM and develops smoothly. As pumping wavelength moves towards the first ZDW, part of the spectrum extends beyond the first ZDW during the broadening process. This part of the spectrum experiences different nonlinear phenomena. It can be seen from Fig. 8.6.1b that when the pulse spectrum extends into anomalous dispersion region, soliton-related dynamics begin to play a role in the features of the generated spectra. As a consequence, the red-

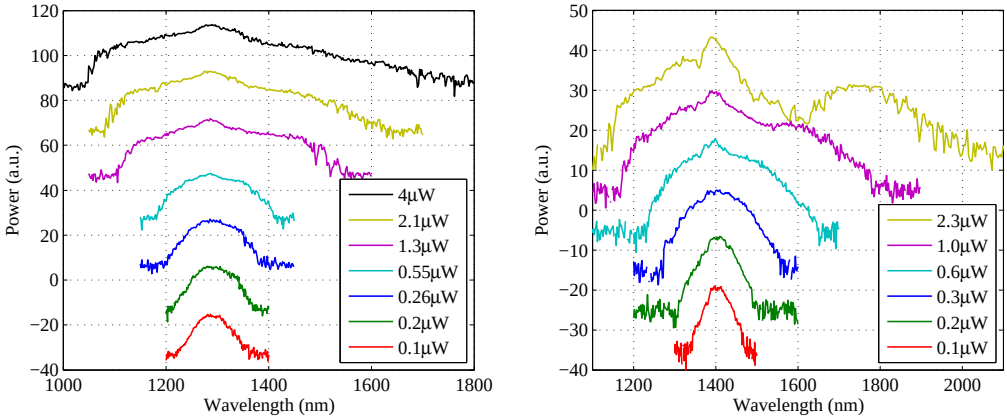

(a) 1300 nm (b) 1400 nm

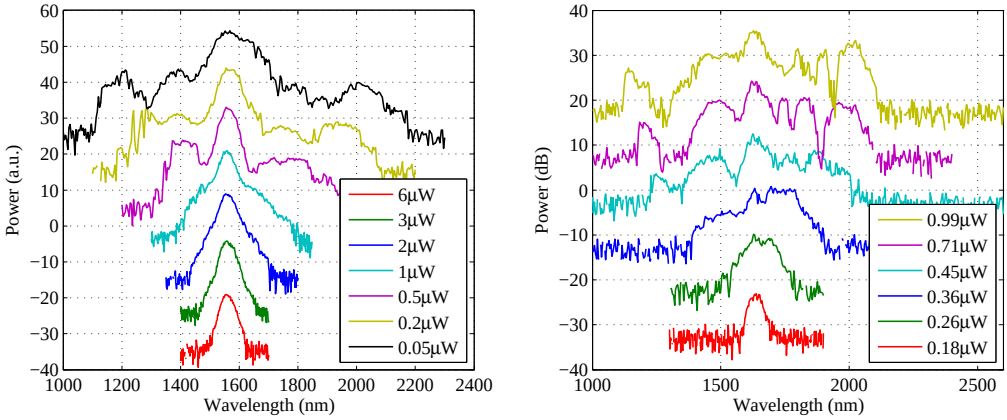

(c) 1550 nm (d) 1650 nm

Figure 8.6.1: Experiments of spectral broadening in 2 centimetre of Bi-HWW fiber pumped at different wavelengths (1300 to 1650 nm).

shifted solitons form the sidebands at 1.6 and 1.75 μm in the 1.0 and 2.3 μW curves respectively.

Moving the pumping wavelength further towards the first ZDW, the broadening mechanism becomes more complicated, with more features starting to appear in the spectra. The cause of this difference can be explained by considering two aspects. Firstly, FWM/MI is likely to take place when the fibre is pumped close to the ZDW. Secondly, during the spectral broadening, the pump pulse can extend

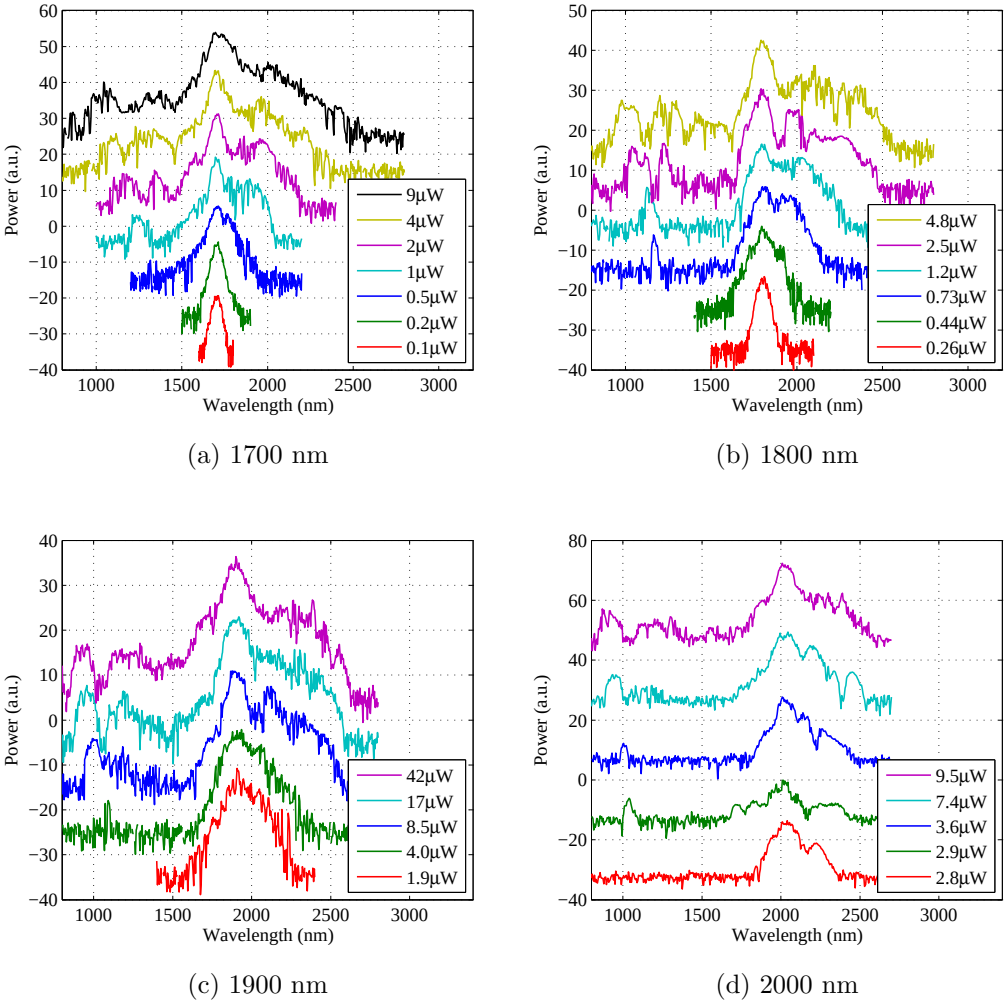

(a) 1700 nm

(b) 1800 nm

(c) 1900 nm

(d) 2000 nm

Figure 8.6.2: Experiments of spectral broadening in 2 centimetre of Bi-HWW fiber pumped at different wavelengths (1700 to 2000 nm).

into the anomalous dispersion region leading to soliton related nonlinear processes. Furthermore, small GVD around this wavelength region leads to reduced temporal walk-off in the pump pulses, and thus different wavelength components overlap in time, allowing them to interact with each other. In the plots, due to the fact that the bandwidth is limited by the detection range of the detector used in the experiments, only part of the spectrum is shown. However, later when one look at the simulations, it can be found that the spectral broadening around this wavelength

region is predicted to be extensive, extending beyond the range measured here. As the pump wavelength moves far into anomalous dispersion region, the bandwidth of the spectra keeps expanding under the influence of MI and soliton-related processes.

8.6.2 Comparison with simulated data

The parameters used in the multimode pulse propagation simulations performed in Chapter 7 were chosen to mimic the conditions found in this sets of experiments. Comparing these simulations to the experimental results helps extent our understanding of the broadening process under realistic environment and further helps refining the models and fibre design for future work.

Figure 8.6.3 shows a comparison of the simulation and experimental results. The following wavelengths are chosen by considering the dispersion profile of the fundamental mode: a pump wavelength of 1300 nm is in the normal dispersion region, pump wavelengths of 1550 and 1650 nm are in the normal dispersion region but close to ZDW, and a pump wavelength of 1800 nm lies in the anomalous dispersion region.

The spectra match better at shorter pump wavelengths than longer ones. This can be interpreted as being due to the anomalous dispersion at the long wavelength side, which causes more randomised nonlinear processes such as MI and soliton fission. At pump wavelength 1300 nm, the spectra are almost overlapped. The existence of normal dispersion ensures the SPM dominated broadening which can be accurately predicted when the input conditions are certain.

The pump wavelengths 1550 and 1650 nm are close to the ZDW of this fiber, and due to this property, the spectral features of SC pumped at these wavelengths are more sensitive to pumping wavelength than other normal dispersion pumped SC but still relatively stable to noise. This is the reason why spiky SC spectra are observed but there are still peaks can be identified.

The clear exception occurs for the pump wavelength 1800 nm. There are at

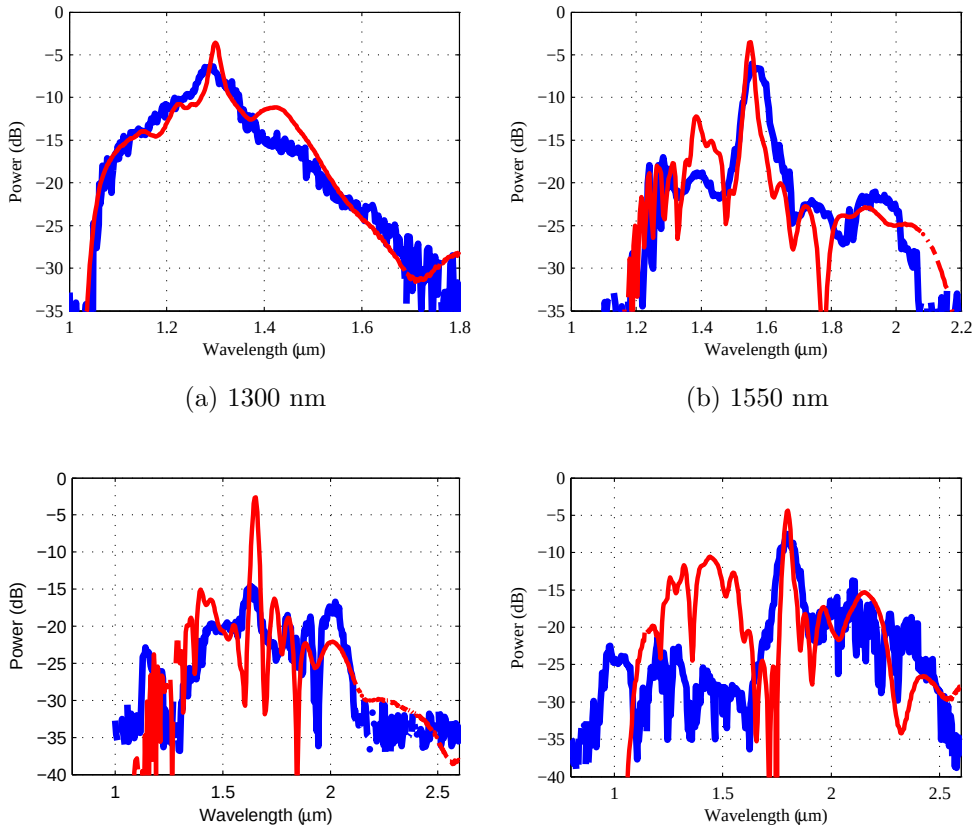

(a) 1300 nm

(b) 1550 nm

(c) 1650 nm

(d) 1800 nm

Figure 8.6.3: Measured spectra (thick blue curves) overlaid on the simulation results (thin red curves). Thick blue curves represent measured data and thin red curve represent simulation results

least two possible explanations for these results. Firstly, the anomalous dispersion allows MI and soliton-related dynamics to dominate the broadening process. These nonlinear effects are sensitive to the noise in the pump as well as other conditions that could not be fully anticipated in the simulation such as pulse chirp, modal interaction, polarisation interaction, Raman effects, etc. Secondly, the alignment of the beam. As described in Section 8.4, the alignment of the fibre to the laser beam is performed using an indirect approach. The light is likely to be coupled into the high order modes instead of fundamental one. For these reasons, the simulation

is deviated from the experimental results but in general, the experimental results match simulations well.

8.7 SF57 HWW fibre

The same fiber structure as in the Bismuth fiber was also fabricated in SF57 glass. This fibre is a test product during the fabrication progress. It is not designed to have special properties for SC generation. The SF57 glass has different material dispersion and nonlinear refractive index to Bismuth glass, which leads to different fibre dispersion and nonlinearity profiles (Fig. 7.1.5). But because it has different dispersion and nonlinearity profiles as the design, it can be used as a comparison to the Bismuth fibre. This fibre shows only one ZDW at approximately 1.6 μm and keeps increasing (reaches 50 $ps/km/nm$ at 2.3 μm), and lower value of nonlinearity (100 $W^{-1}km^{-1}$ at 2 μm) compared to the Bismuth fibre (250 $W^{-1}km^{-1}$ at 2 μm) whose first ZDW is at 1.7 μm and dispersion values keep low and flat until 3.6 μm with maximum value of 16 $ps/km/nm$ at 2.1 μm.

Experiments of SC generation in this fiber were done with three typical pump wavelengths. Each pump wavelength represents nonlinear broadening in a distinct dispersion region. The three wavelengths are 1300 (normal and far from ZDW), 1650 (close to ZDW) and 2000 (anomalous and far from ZDW) and their corresponding spectral outputs are shown in Fig. 8.7.1.

The SF57 fibre has nearly the same core size and structure as the Bismuth fibre except minor difference due to fabrication distortions. The differences between the SC generation in these two fibres can be considered as a result of different glass materials used for constructing these fibres. However, from a fundamental point of view, it is the difference in dispersion and nonlinearity profiles that caused these changes.

In general, the differences can be concluded in the following points. Firstly, at a similar power level, pulses in the Bismuth fibre broaden more than in the SF57 fibre

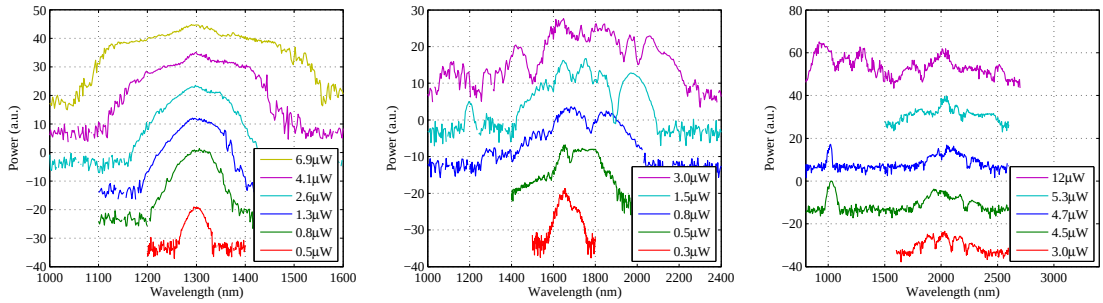

(a) 1300 nm (b) 1650 nm (c) 2000 nm

Figure 8.7.1: Experiments of spectral broadening in a 2 centimetres length of SF57 fiber (Fig. 6.4.4a) pumped at different wavelengths

in the normal dispersion regime and near the ZDW due to higher nonlinearity and lower dispersion in the Bismuth fibre than the SF57 fibre. In the anomalous dispersion regime, the amount of spectral broadening can not be determined using the experimental setup available due to the operation wavelength range and sensitivity of the detector.

Secondly, the soliton-related processes in SF57 fibre contribute more significantly to broadening processes than the one in Bismuth fibre. This is concluded from the degree of asymmetry in the spectral density around the pump wavelength in SF57 fibre which is caused by soliton fission and red shifting processes. Also SF57 fibre has smaller soliton order then Bismuth fibre at same pump wavelengths based on their nonlinearity and dispersion values, which result in higher energy but fewer solitons as indicated by the right sidebands (see Fig. 8.7.1b). One more evidence for more intensive soliton related processes in SF57 can be obtained by comparing the left-most side bands in spectra of pump wavelength longer than 1700 nm. The location of these sidebands is seen to be essentially independent of the pump wavelength. There are called Cherenkov radiation (dispersive waves) which couples to solitons on the long wavelength part of the spectrum [159, 160]. At similar power levels, spectra of the SF57 fibre shows more significant Cherenkov radiation sidebands than one of

the Bismuth fibre, which confirms that more intensive soliton related processes in the SF57 fibre.

Finally, the asymmetry in the spectra also indicates the bandwidth of FWM/MI gain in Bismuth fibre is wider than SF57 fibre. As the solitons split from the main pulse (fission), they constantly shift towards the long wavelength side of the spectrum. During the process, if FWM/MI phase is matched, corresponding Stokes and anti-Stokes side bands will be generated. Since the low and flat dispersion of Bismuth fibre, the FWM/MI gain of the Bismuth fibre is much wider than the one of SF57 fibre and almost covers the whole spectral range leads to more balanced spectra around the pump wavelength in the Bismuth fibre than SF57 fibre.

In comparison to the dispersion properties of the Bismuth fiber, the dispersion profile of the SF57 fiber leads to more intensive soliton related dynamics. Apart from that, the Bismuth fibre generates SC more efficiently in terms of power and bandwidth than the SF57 fibre. This is the result of the combination of low dispersion and high nonlinearity. For the purpose of generating large bandwidth SC, both fibres are capable of achieving the target when enough pumping power is giving. But the SC spectra generated in the Bismuth fibre is more even than the SF57 fibre due to the low and flat dispersion of the Bismuth fibre. It can be concluded that, to further improve the smoothness and suppress soliton-related dynamics as well as MI for maintaining coherence of the spectra, it is better to design dispersion to be low, flat and keep the values in the normal dispersion regime as well for future work.

8.8 Summary

In this chapter, SC generation in soft glass MOFs is demonstrated experimentally with spectra spanning one octave from 1 to at least 2.5 μm for both fabricated bismuth and SF57 fibres.

The experiments started with characterising the femtosecond laser source which shows 10% power fluctuation in average for wavelengths from 1.3 to 1.8 μm. This

information and the information of the spectrum of pump pulses become important references for the simulations in Chapter 7 and the pulse broadening experiments.

The short pulse broadening experiment with SMF-28 fibre shows results matching closely with simulations for all power levels. Good agreement between experimental results and simulations validates the simulation program used in this work, which enable us to work towards developing MOFs for mid-IR SC generation.

In the main experiment part, the details on how the test fibre was aligned are described. This work shows that coupling conditions cannot be guaranteed for wavelengths longer than 1700 nm, and this information is used later when the spectral outputs of the bismuth fibre are discussed.

Pulse broadening in Bismuth fibre for different pumping wavelengths and power levels were presented and discussed. For most pump wavelengths, the Bismuth fibre can generate SC extends an octave. The experimental results match the key features from the prediction in large scale, which means, despite the multimodeness, the fibre is capable of generating spectral output as simulated.

Another sets of experiments based on SF57 fibre was performed. The SF57 fibre has similar structure but different dispersion and nonlinearity profiles. It is used for comparison to the Bismuth fibre. The SC generation in the SF57 fibre was compared in three different prospects, including bandwidth, soliton-related dynamics and FWM/MI gain, from which the direction of improvement fibre design for future work is derived, which is a high nonlinearity and low flat dispersion, but the dispersion profile of the fibre should remain in the normal dispersion regime to avoid soliton-related dynamics and MI.

Chapter 9

Summary of Part I

In the first part of the thesis, the advantages of soft glass materials and microstructured optical fibres are combined for new frequency light generation and explore the potential of applying soft-glass microstructured optical fibres for constructing a femtosecond fibre optical parametric oscillator with nearly transform limited outputs and a highly coherent broadband supercontinuum generation source in the mid-IR. The background theory of this part of work is based on the scalar nonlinear pulse propagation model which is derived using the weak guidance approximation.

The work begins with a literature review on the development of FOPA/FOPO and SC generation. For these two areas (FOPO and SC generation), the existing work has shown that microstructured optical fibre's ability of tailoring dispersion enables FOPOs and SC sources to be constructed with higher efficiencies with respect to pump power, pulse duration, wavelength span and fiber length.

The use of soft glass in SC generation also demonstrated that using highly nonlinear material as the base material of the fiber is a straightforward and efficient way to increase the overall fiber nonlinearity, thus enhances the efficiency of SC generation (generation of broad SC spectrum with low power and short length of fiber). Soft glass is also a good candidature for mid-IR applications due to its good transmission property in that wavelength region.

Soft glass fibres have not been used for making FOPOs before. But the success

of applying soft glass to SC generations indicates its strong potential for FOPOs, especially when it is combined with MOFs. Also the development of soft glass MOFs for SC generation was mainly focused on spectral span. The potential of enhancing the coherence of the SC spectra has not been fully explored. Therefore, after reviewing the literature, a concept of design and optimise structures of soft glass MOFs for these two aspects of nonlinear application was formed.

Design fiber structures for dispersion and nonlinearity control, especially over a large wavelength span, is a challenging task. Previous studies have only achieved it to a certain level with a simplified system such as optimising zero dispersion wavelengths and slope of dispersion at pump wavelengths. Most of the optimisation in the previous studies did not take account the optimisation of nonlinearity either. The reason of doing so is because the complicated relations between nonlinear processes and fiber properties. The dispersion and nonlinearity profiles of a fiber are entangled together, and one profile cannot be changed without altering the other. Furthermore, the material dispersion also limits the degree of freedom of optimisation.

To bypass these difficulties in fiber design, we employed genetic algorithms to help design the fibers. The GA can be employed without simplification of the physical model and it optimises a system in a statistic manner. The GA was applied to optimising fibers for parametric processes. Unlike previous studies, a complete dispersion profile was using in the model. Nonlinearity, phase matching and walk-off between signal and pump were all considered to optimise the overall efficiency of the parametric process. After the designing step, numerical simulations were performed. The numerical simulation also involved a novel procedure. A beam propagation model used for simulating SC generation was used instead of coupled equations that were conventionally used for FWM. In this way, not only FWM processes were simulated, but also other important nonlinear processes such as Raman and cascaded effects were also included in the model to estimate the process more accurately. The output of this part of the work has indicated an impressive result. A femtosecond

pulse pumped FOPO capable of providing approximately 43% peak power conversion with only little pulse quality degradation (TBP ≈ 0.43) was theoretically constructed with only 3 mm of fiber. Such a system can also provide tunability from the near- to mid-IR due to both design and the property of the soft glass.

The success of using GA for optimising FWM gave confidence in optimising SC generation with large bandwidth and high coherence. However, the same GA model cannot be directly applied to SC generation due to the fact that a SC generation is much more complicated than a FWM process and there is no analytic expression in any sort to express the efficiency of a SC generation. To avoid including the pulse propagation model into the GA, a simplified model was developed. The simplified model sacrifices time to map out the relation between different orders of dispersion and nonlinear profiles to the SC bandwidth and coherence. Then a GA was applied to the simplified model. This approach was called a hybrid GA approach. The accuracy of this optimisation approach depends on the complexity of the simplified model. However, numerical results showed that even taking the first order approximations for both dispersion and nonlinearity profiles, the outcome was still good for this work. The simplified model suggested that to obtain broadband coherent SC output, a flat and zero dispersion across a large wavelength region is required. The GA generated a structure with corresponding properties: a nonlinearity value around 175 $W^{-1}km^{-1}$ and a relatively flat dispersion profile from 2 to 3 μm with a maximum variation of 2.5 $ps/km/nm$ around zerp. The SC generation simulation in such fiber showed a transmission window limited spectrum with complete coherence in only a few centimetres.

In next part, fabrication of the fiber designed for SC generation was attempted. Extrusion fabrication method was applied to fabricate the fiber preform. After a few attempts with different die designs and different types of glass, a close structure to the design was fabricated in Bismuth glass with limited distortion.

Numerical modelling was once again applied to the fabricated fiber to analyse the influence of distortion to the dispersion and nonlinearity profile as well as SC gen-

eration. The analysis -indicates that although the structural distortion was minor, the change in the dispersion profile is not negligible. The variation in the dispersion profile increased from 2.5 $ps/km/nm$ to 16 $ps/km/nm$ for which the SC coherence cannot be maintained.

SC experimental work followed. The capability to accurately measure the SC spectrum was firstly confirmed with 1 m of SMF-28 fiber despite of experimental drawbacks such as laser power fluctuations. The low dispersion and multimodeness of the fiber cause difficulties in measuring the dispersion profile directly. An alternative approach was then taken. SC spectra of the fiber output were measured for multiple wavelengths. Through comparing the measured SC spectra with numerical predictions, it can be concluded that the fabricated fiber has reasonable close dispersion and nonlinearity profiles as predicted in the detectable range. Apart from that, broad SC spectra can be easily obtained in this fiber for a large pump wavelength region and variety pump power level.

The theories and calculations in this part of the thesis are based on weak guidance approximation (see Chapter 2). However, in MOFs, especially soft-glass based MOFs, high index contrast and sub-wavelength features are commonly exist. The weak guidance approximation used in the current pulse propagation model starts to break down. As the development of novel waveguides requires more and more of these features, a full vectorial nonlinear pulse propagation model is needed for accurate prediction and better understanding of the nonlinear processes in these high-index-contrast sub-wavelength-scale (HS) waveguides. In the second part of the thesis, a VNPP model is used to study the pulse propagation in HS waveguides.

Part II

Kerr and polarisation effects in the full vectorial model

Chapter 10

Background of Part II

In the first part of the thesis, fibre optical parametric oscillators (FOPOs) and supercontinuum (SC) generation have been studied for fibre design using theories based on a scalar pulse propagation model (see Chapter 2), which assumes:

1. The dielectric constant ϵ is independent of the spatial coordinates (the waveguide has a homogenous cross-section),

2. A weak guidance approximation is applied to the guided mode fields (the guided fields are transverse),

3. A slowly varying approximation is applied to the guided modes.

These theories work well with large core and low index contrast waveguides. However, with the development of highly nonlinear optical waveguides, high index contrast and sub-wavelength features (features smaller than the wavelength of the light propagating in these waveguides) start to appear. These waveguides, including silicon, chalcogenide and soft glass optical waveguides, have formed the base for three highly active field of studies; silicon photonics [161–164], chalcogenide photonics [165, 166], and soft glass microstructured photonic devices. The high index contrast and sub-wavelength scale features of these waveguides indicate that the weak guidance approximation based scalar model is no longer suitable [167]. Significant

differences in nonlinear coefficients were discovered in Ref.[167] including a factor of 2 difference in Kerr nonlinearity with sub-wavelength scale high-index-contrast nano-wires. For accurate predictions of FOPO and SC generation but also other nonlinear phenomena in these waveguides, a vectorial nonlinear pulse propagation model, which does not based on the weak guidance approximate, is needed.

Over the past few years, work on the development of vectorial nonlinear pulse propagation models were performed by many groups (for details, see Ref. [167] and the references within). Among them, a full vectorial nonlinear pulse propagation model (VNPP) was developed [167], which derived directly from Maxwell's equations without making the assumptions that the scalar model used. Based on this new model, significant differences in pulse propagation behaviours were discovered between this model and the scalar model, especially for high-index-contrast sub-wavelength-scale (HS) waveguides. That includes (refer to Section 10.1) new linear interactions between different modes, new definitions for nonlinear coefficients and new high order nonlinear terms (Eq. 10.1.19). Later, following this work, further development on the VNPP model, including vectorial Raman effects, were performed [168, 169]. With the VNPP model, we now cannot only predict the nonlinear pulse propagation more accurately, but also study new nonlinear phenomena in HS waveguides and the influence of these new phenomena to classic nonlinear processes such as FWM parametric processes and SC generation.

In the second part of the thesis, the study is focused on Kerr nonlinearity and novel nonlinear polarisation behaviours within the full vectorial framework.

10.1 The theory of the full vectorial nonlinear pulse propagation model

Before the detailed differences between the VNPP and the scalar models are discussed, the theory of the VNPP model is reviewed first. The VNPP model uses

Maxwell's equations as the starting points. The Maxwell's equation in the Fourier domain can be expressed as

$$\nabla \times \tilde{\mathbf{E}}(\mathbf{r},\omega) = i\mu_0\omega\tilde{\mathbf{H}}(\mathbf{r},\omega), \tag{10.1.1}$$

$$\nabla \times \tilde{\mathbf{H}}(\mathbf{r},\omega) = -i\epsilon_0\omega(\mathbf{r},\omega)\tilde{\mathbf{E}}(\mathbf{r},\omega) - i\omega\tilde{\mathbf{P}}(\mathbf{r},\omega), \tag{10.1.2}$$

where $\mathbf{E}$ is $\mathbf{H}$ are the electric and magnetic field vectors, respectively, $\mathbf{P}$ is the induced electric polarisation $\mathbf{r}$ is spacial coordinates, ω is angular frequency, μ_0 and ϵ_0 are the permeability and permittivity in vacuum, respectively, $\tilde{}$means that the fields are in the Fourier domain.

Firstly, a function $\mathbf{F}_C$ is defined as

$$\mathbf{F}_C = \tilde{\mathbf{E}}_0 \times \tilde{\mathbf{H}}^* + \tilde{\mathbf{E}}^* \times \tilde{\mathbf{H}}_0, \tag{10.1.3}$$

where $\tilde{\mathbf{E}}_0$ and $\tilde{\mathbf{H}}_0$ are the fields of an unperturbed system which represents a pulse with a narrow bandwidth (a single frequency at ω_0). For this unperturbed system, dispersion, loss and nonlinearity terms are zero. The fields $\tilde{\mathbf{E}}^*$ and $\tilde{\mathbf{H}}^*$ are belong to a perturbed system which represents a broadband pulse whose spectrum centred at ω_0. For this perturbed system, dispersion, loss and nonlinearity terms are nonzero. The symbol $*$ represents complex conjugates.

Using the reciprocal theorem [84], following relation between perturbed and unperturbed systems can be obtained,

$$\frac{\partial}{\partial z}\int \mathbf{F}_C \cdot \hat{z} dA = \int \nabla \cdot \mathbf{F}_C dA, \tag{10.1.4}$$

in which $\nabla \cdot \mathbf{F}_C$ can be calculated using Eqs.10.1.1 & 10.1.2, as

$$\nabla\cdot\mathbf{F}_C = -i\mu_0(\omega-\omega_0)\tilde{\mathbf{H}}^*\cdot\tilde{\mathbf{H}}_0 - i\epsilon_0\left[\omega n^2(\mathbf{r},\omega) - \omega_0 n^2(\mathbf{r},\omega_0)\right]\tilde{\mathbf{E}}^*\cdot\tilde{\mathbf{E}}_0 + i\omega_0\tilde{\mathbf{E}}_0\cdot\tilde{\mathbf{P}}^*_{\mathrm{NL}}(\mathbf{r},\omega). \tag{10.1.5}$$

Next, the fields $\tilde{\mathbf{E}}$ and $\tilde{\mathbf{H}}$ are expanded according to the orthonormal basis of the forward propagation modes of the unperturbed system [167]:

$$\tilde{\mathbf{E}}(\mathbf{r},\omega) = \sum_{\mu} \tilde{a}'_{\mu}(z,\omega)\frac{\mathbf{e}_{\mu}(x,y,\omega_0)}{\sqrt{N_{\mu}}}e^{i\beta_{\mu}z}, \tag{10.1.6}$$

$$\tilde{\mathbf{H}}(\mathbf{r},\omega) = \sum_{\mu} \tilde{a}'_{\mu}(z,\omega)\frac{\mathbf{h}_{\mu}(x,y,\omega_0)}{\sqrt{N_{\mu}}}e^{i\beta_{\mu}z}, \tag{10.1.7}$$

$$N_{\mu} = \frac{1}{2}\left|\int \mathbf{e}_{\mu}(x,y,\omega)\times\mathbf{h}^{*}_{\mu}(x,y,\omega)\cdot\hat{z}dA\right|, \tag{10.1.8}$$

where $\mathbf{e}_{\mu}$ and $\mathbf{h}_{\mu}$ are the basis modal sets of the forward propagating electric and magnetic fields, respectively, β_{μ} are the propagation constants, a'_{μ} are the amplitude coefficients and N_{μ} are the normalisation factor.

The fields of unperturbed system $\tilde{\mathbf{E}}_0$ and $\tilde{\mathbf{H}}_0$ can be considered as a special mode (mode ν) of the Eqs. 10.1.9 & 10.1.10, i.e.,

$$\tilde{\mathbf{E}}_0(\mathbf{r},\omega_0) = \frac{\mathbf{e}_{\nu}(x,y,\omega_0)}{\sqrt{N_{\nu}}}e^{i\beta_{\nu}z}, \tag{10.1.9}$$

$$\tilde{\mathbf{H}}_0(\mathbf{r},\omega_0) = \frac{\mathbf{h}_{\nu}(x,y,\omega_0)}{\sqrt{N_{\nu}}}e^{i\beta_{\nu}z}. \tag{10.1.10}$$

Using the orthogonality condition

$$\int \mathbf{e}_{\mu}(x,y,\omega)\times\mathbf{h}^{*}_{\nu}(x,y,\omega)\cdot\hat{(z)}dA = N_{\mu}\delta_{\mu\nu}, \tag{10.1.11}$$

Eq. 10.1.4 can lead to

$$\frac{\partial}{\partial z}\tilde{a}'_{\nu}(z,\omega) = i\sum_{n=1}^{\infty}\frac{(\Delta\omega)^2}{n!}\beta^{(n)}_{\nu}\tilde{a}'_{\nu} + i\sum_{\mu\neq\nu}\sum_{n}\frac{(\Delta\omega)^n}{n!}\beta^{(n)}_{\nu\mu}\tilde{a}'_{\mu} - \frac{i\omega e^{-i\beta_{\nu}z}}{4\sqrt{N_{\nu}}}\int \mathbf{e}^{*}_{\nu}\cdot\tilde{\mathbf{P}}'_{\mathrm{NL}}(\mathbf{r},\omega)dA, \tag{10.1.12}$$

where $\Delta\omega = \omega - \omega_0$, $\beta^{(n)}_{\nu}$ and $\beta^{(n)}_{\nu\mu}$ are coefficients of Taylor series expansion around ω_0, and

$$\beta^{(n)}_{\nu} = \frac{\partial^n}{\partial\omega^n}\beta^{(1)}_{\nu}, \quad \beta^{(1)}_{\nu} = \frac{1}{4N_{\nu}}\int\left[\mu_0|\mathbf{h}_{\nu}|^2 + \epsilon_0\frac{\partial}{\partial\omega}(\omega n^2)|_{\omega=\omega_0}|\mathbf{e}_{\nu}|^2\right]dA, \tag{10.1.13}$$

$$\beta^{(n)}_{\nu\mu} = \frac{\partial^n}{\partial\omega^n}\beta^{(1)}_{\mu\nu}, \quad \beta^{(1)}_{\nu\mu} = \frac{e^{i(\beta_{\mu}-\beta_{\nu})z}}{4\sqrt{N_{\mu}N_{\nu}}}\int\left[\mu_0\mathbf{h}_{\mu}\cdot\mathbf{h}^{*}_{\nu} + \epsilon_0\frac{\partial}{\partial\omega}(\omega n^2)|_{\omega=\omega_0}\mathbf{e}_{\mu}\cdot\mathbf{e}^{*}_{\nu}\right]dA. \tag{10.1.14}$$

To convert Eq. 10.1.12 to the time domain, one can multiply $e^{-i(\omega-\omega_0)t}$ on both sides of Eq. 10.1.12 and take the inverse Fourier transforms. After defining the following relations,

$$a'_\nu(z,t) = \frac{1}{2}\left[a_\nu(z,t)e^{-i\omega_0 t} + c.c.\right], \tag{10.1.15}$$

$$P'_{\mathrm{NL}}(z,t) = \frac{1}{2}\left[P_{\mathrm{NL}}(z,t)e^{-i\omega_0 t} + c.c.\right], \tag{10.1.16}$$

where *c.c.* represents complex conjugates, the time domain version of Eq. 10.1.12 can be obtained:

$$\begin{aligned}\frac{\partial}{\partial z}a_\nu(z,t) =& i\sum_{n=1}^{\infty}\frac{i}{n!}\frac{\partial^n}{\partial t^n}\beta_\nu^{(n)}a_\nu + i\sum_{\mu\neq\nu}\sum_n\frac{i}{n!}\frac{\partial^n}{\partial t^n}\beta_{\nu\mu}^{(n)}a_\mu \\ &- \frac{i\omega e^{-i\beta_\nu z}}{4\sqrt{N_\nu}}\left(1+\frac{1}{\omega_0}\frac{\partial}{\partial t}\right)\int \mathbf{e}_\nu^*\cdot\mathbf{P}_{\mathrm{NL}}(\mathbf{r},t)dA,\end{aligned} \tag{10.1.17}$$

and

$$\mathbf{P}_{\mathrm{NL}} \approx \frac{3}{4}\epsilon_0\chi^{(3)}|\mathbf{E}(\mathbf{r},t)\mathbf{E}(\mathbf{r},t)\mathbf{E}^*(\mathbf{r},t), \tag{10.1.18}$$

where $\chi^{(3)}$ is the third order susceptibility which considered as the lowest order nonlinear terms for waveguides with isotropic materials, and it is assumed to be independent of frequency, i.e. $\dfrac{\partial}{\partial\omega}\chi^{(3)} = 0$.

The third order susceptibility is a fourth rank tensor. There are only 21 elements in $\chi^{(3)}$ tensor that are nonzero. Through expanding the term $\mathbf{e}_\nu^*\cdot\mathbf{P}_{\mathrm{NL}}$ in Eq.10.1.17 for these nonzero $\chi^{(3)}$ terms, a full vectorial nonlinear Schrödinger equation (VNSE) can be obtained

$$\begin{aligned}&\frac{\partial}{\partial z}a_\nu(z,t) + \sum_{n=1}^{\infty}\frac{(i)^{n-1}}{n!}\beta_\nu^{(n)}\frac{\partial^n}{\partial t^n}a_\nu + i\sum_{\mu\neq\nu}\sum_n\frac{i}{n!}\frac{\partial^n}{\partial t^n}\beta_{\nu\mu}^{(n)}a_\mu = \\ &\quad i\sum_{\mu\neq\nu}(\gamma_\nu|a_\nu|^2 + \gamma_{\mu\nu}|a_\mu|^2)a_\nu + i\sum_{\mu\neq\nu}\gamma'_{\mu\nu}a_\mu^2a_\nu^*e^{-2i(\beta_\nu-\beta_\mu)z} \\ &\quad + i\sum_{\mu\neq\nu}\gamma_{\mu\nu}^{(1)}a_\mu^*a_\nu^2e^{-i(\beta_\mu-\beta_\nu)z} + i\sum_{\mu\neq\nu}\left(\gamma_{\mu\nu}^{(2)}a_\mu|a_\nu|^2 + \gamma_{\mu\nu}^{(3)}a_\mu|a_\mu|^2\right)e^{i(\beta_\mu-\beta_\nu)z} \\ &\quad + \sum_{\mu\neq\nu}\text{other higher order terms},\end{aligned} \tag{10.1.19}$$

in which

$$\gamma_\nu = (\frac{k}{4})(\frac{\varepsilon_0}{\mu_0})\frac{1}{3N_\nu^2}\int n^2(x,y)n_2(x,y)[2\left|\mathbf{e}_\nu\right|^4 + \left|\mathbf{e}_\nu^2\right|^2]dA, \tag{10.1.20}$$

$$\gamma_{\mu\nu} = (\frac{k}{4})(\frac{\varepsilon_0}{\mu_0})\frac{2}{3N_\nu N_\mu}\int n^2(x,y)n_2(x,y)\left[\left|\mathbf{e}_\nu.\mathbf{e}_\mu^*\right|^2 + \left|\mathbf{e}_\nu.\mathbf{e}_\mu\right|^2 + \left|\mathbf{e}_\nu\right|^2\left|\mathbf{e}_\mu\right|^2\right]dA, \tag{10.1.21}$$

$$\gamma'_{\mu\nu} = (\frac{k}{4})(\frac{\varepsilon_0}{\mu_0})\frac{1}{3\sqrt{N_\nu^2 N_\mu^2}}\int n^2(x,y)n_2(x,y)\left[2(\mathbf{e}_\mu.\mathbf{e}_\nu^*)^2 + (\mathbf{e}_\mu)^2(\mathbf{e}_\nu^*)^2\right]dA, \tag{10.1.22}$$

$$\gamma^{(1)}_{\mu\nu} = (\frac{k}{4})(\frac{\varepsilon_0}{\mu_0})\frac{1}{3\sqrt{N_\nu^3 N_\mu}}\int n^2(x,y)n_2(x,y)\left[2\left|\mathbf{e}_\nu\right|^2(\mathbf{e}_\mu^*.\mathbf{e}_\nu) + (\mathbf{e}_\nu)^2(\mathbf{e}_\mu^*.\mathbf{e}_\nu^*)\right]dA, \tag{10.1.23}$$

$$\gamma^{(2)}_{\mu\nu} = (\frac{k}{4})(\frac{\varepsilon_0}{\mu_0})\frac{2}{3\sqrt{N_\nu^3 N_\mu}}\int n^2(x,y)n_2(x,y)\left[2\left|\mathbf{e}_\nu\right|^2(\mathbf{e}_\mu.\mathbf{e}_\nu^*) + (\mathbf{e}_\nu^*)^2(\mathbf{e}_\mu.\mathbf{e}_\nu)\right]dA, \tag{10.1.24}$$

$$\gamma^{(3)}_{\mu\nu} = (\frac{k}{4})(\frac{\varepsilon_0}{\mu_0})\frac{1}{3\sqrt{N_\mu^3 N_\nu}}\int n^2(x,y)n_2(x,y)\left[2\left|\mathbf{e}_\mu\right|^2(\mathbf{e}_\mu.\mathbf{e}_\nu^*) + (\mathbf{e}_\mu)^2(\mathbf{e}_\mu^*.\mathbf{e}_\nu^*)\right]dA. \tag{10.1.25}$$

In these equations $k = \dfrac{\omega_0}{c}$ is the propagation constant in vacuum, c is the speed of light in vacuum, γ_ν, $\gamma_{\mu\nu}$, $\gamma'_{\mu\nu}$, $\gamma^{(1)}_{\mu\nu}$, $\gamma^{(2)}_{\mu\nu}$ and $\gamma^{(3)}_{\mu\nu}$ are the effective nonlinear coefficients representing self phase modulation (SPM) (γ_ν and γ_μ), cross phase modulation (XPM) ($\gamma_{\mu\nu}$), coherent coupling between different modes ($\gamma'_{\mu\nu}$, $\gamma^{(1)}_{\mu\nu}$, $\gamma^{(2)}_{\mu\nu}$ and $\gamma^{(3)}_{\mu\nu}$) respectively. And we have $\gamma_{\nu\mu} = \gamma_{\mu\nu} = \gamma_c$ and $\gamma'_{\nu\mu} = \gamma'_{\mu\nu} = \gamma'_c$.

Equation 10.1.19 is a general form of a vectorial nonlinear Schrödinger equation (VNSE) that describes SPM, XPM, FWM and other linear and nonlinear coupling of different co-propagating modes at one frequency. VNSE with Raman effects and multi-frequency components is also developed from another work by Tran and Biancalana [169]. But in this thesis, only single frequency is considered and Raman effects are ignored, therefore Eqs. 10.1.19 are used.

10.2 Discussion

Unlike the scalar model, the VNPP model uses the orthogonality condition Eq.10.1.11 instead of $\int \mathbf{e}_\nu \cdot \mathbf{e}_\mu^* dA = 0$ (or $\mathbf{e}_1 \cdot \mathbf{e}_2 = 0$ for two polarisations), which indicates that the electromagnetic fields of the propagating modes are not transverse in the VNPP model. In fact, there can be strong non-transverse field components for modes of sub-wavelength scale waveguides. To demonstrate this point, the mode fields are calculated with wavelength at 1550 nm for a range of step-index fibres with different core diameters. Fig. 10.2.1 shows the E_z (the longitudinal component of the field $\mathbf{E}$) of the fundamental modes of two fibres made of Bismuth glass ($n = 1.98$, $n_2 = 5.95 \times 10^{-19}$ m/W) core surrounded by air cladding. The fibre in Fig. 10.2.1(a) has a core diameter of 2 μm and fibre in Fig. 10.2.1(b) has a core diameter of 0.5 μm. As the figure shown, both fibre modes consist E_z components which maximises on the edge of the core. The maximum amplitude of the E_z component of the field for 0.5 μm core fibre is a few times larger than that of the 2 μm core fibre.

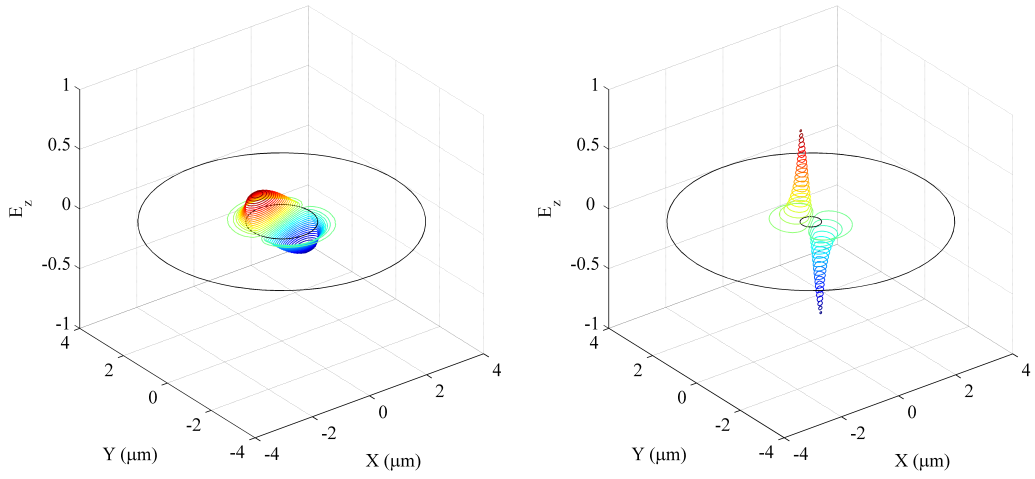

(a) (b)

Figure 10.2.1: The E_z component for the fields at 1.55 μm for fibre with different core diameters. (a) 2 μm core diameter, (b) 0.5 μm core diameter.

To study the strength of the E_z fields with respect to the total field $\mathbf{E}$, a parameter call "Transversality" T can be defined as [167],

$$T = 1 - \frac{\int |E_z^2| dA}{\int |\mathbf{E}^2| dA}. \tag{10.2.1}$$

When the non-transverse field is zero, $T = 1$, otherwise $T < 1$. Transversality T is plotted as a function of core diameter in Fig.10.2.2. Similar results as in Ref. [167] were observed, but here in this work, the operational wavelength is selected to be 1550 nm order to guide the experimental work in Chapter 11. It can be found that for core sizes larger than the wavelength of the field, the transversality approaches 100%, as well as for core diameters much smaller than the wavelength ($\lesssim$0.4 μm) where the fields are mostly out side of the core. In both cases, T approaching 1, the physics is rather different. For small core sizes, is guided field behaves similar to free space propagation while for large core sizes, the field is well confined. There is a core diameter region (around 0.6 μm) for which the transversality decreases dramatically. For fibres with these core diameters, the longitudinal components of the field E_z can be larger than 60% of the total field.

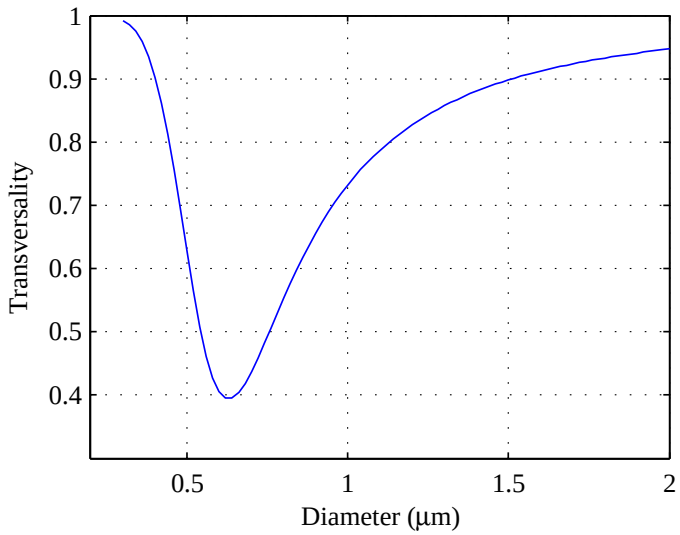

Figure 10.2.2: The transversality T of fundamental modes for different core diameters at wavelength of 1550 nm.

The existence of strong non-transverse component of the electromagnetic fields is the key to the VNPP model. Due to its existence, significant differences are also been observed in nonlinear coefficients between VNPP and scalar models, which includes the definitions of the coefficients and the structural dependence of the coefficients where both of them lead to novel nonlinear polarisation behaviours.

10.3 Summary

In this chapter, following Part I of the thesis, it is pointed out that the weak guidance based nonlinear pulse propagation model is no longer suitable for predicting nonlinear processes in HS waveguides. A VNPP model should be used to describe pulse propagation in these waveguides. The review of the VNPP model shows that

1. the derivation of VNPP model does not invoke the assumptions that are used by the scalar model,

2. the guided modes of the guides, especially HS waveguides, have strong longitudinal field components,

3. the VNPP indicates novel nonlinear polarisation behaviours.

In the following chapters, the Kerr nonlinearity is studied using the VNPP model and the experimental confirmation of VNPP model's prediction of the Kerr nonlinear coefficients in HS waveguides is showed. After that, the nonlinear interactions between polarisation models are studies within the VNPP model.

Chapter 11

Kerr nonlinearity with the VNPP model

11.1 Background

In Chapter 10, we reviewed a VNPP model which shown that in high-index-contrast sub-wavelength-scale (HS) waveguides, strong longitudinal field components are existing in the guided modes. For some cases, such as the 0.6 μm core fibre discussed in Section 10.2, the longitudinal components can be as large as 60% of the total field (Fig. 10.2.2). This large component of the field is having significant impact to the value of Kerr nonlinearity of the waveguide. In this chapter, we are going to focus on studying VNPP model's prediction of Kerr nonlinearity and confirm its prediction through experiments.

11.2 Numerical predictions of Kerr nonlinearity

When considering only the Kerr nonlinearity, the major difference between the scalar and VNPP modes is in the definition of nonlinear coefficients γ in Eq. 2.1.14 and γ_ν in Eq. 10.1.19. Using a finite element method both scalar and VNPP versions of γ's can be modelled.

The modelling of the nonlinear coefficients is preformed with a type of Bismuth glass suspended core fiber whose structure is shown in Fig. 11.2.1. In this structure, a small fiber core is suspended in air through three equally separated struts. The struts are thin and long relative to the fiber core, they have negligible effects to the light guidance of the core. This type of structure is the simplest implementation of an optical nano-wire in fibre, which has the most typical features of a HS waveguide. The example shown in Fig. 11.2.1 has a core diameter (530 nm, the diameter of an enclosed circle) only approximately 1/3 of the operational wavelength (1550 nm). The index contrast (Δn) of this fibre reaches 0.98 which is approximately 160 times higher than a SMF-28 fibre.

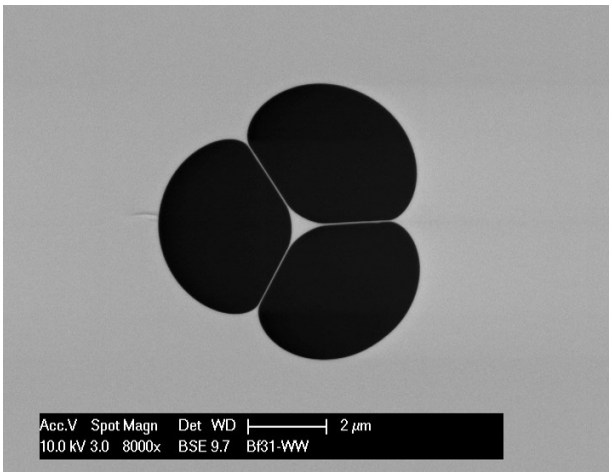

Figure 11.2.1: An example of the cross section of a Bismuth suspended-core fiber with core diameter (the diameter of an enclosed circle) of 530 nm.

We took the SEM image (Fig.11.2.1) and scale it to simulate structures with different core diameters. The nonlinear coefficients of these suspended core fibers are predicted using a finite element method and both vectorial and scalar definitions of γ were used in the calculation. Fig.11.2.2 shows the plot of γs of the two definitions (Eq. 2.1.15 & 10.1.20) at 1552 nm as functions of fiber core diameter (diameter of enclosed circle).

These calculations based on the VNPP model indicate that significant deviations

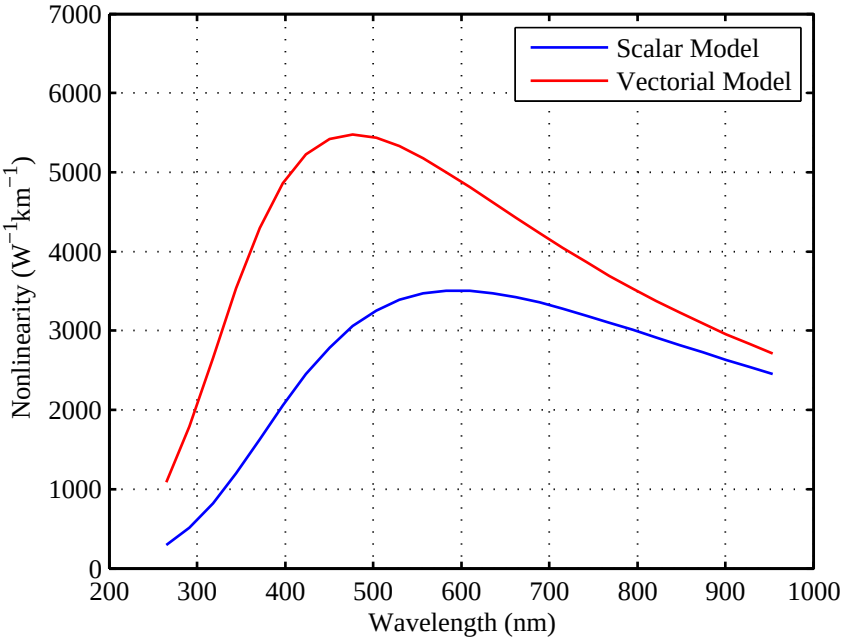

Figure 11.2.2: Predictions of γ at 1552 nm with scalar and vectorial modes for a range of core diameters.

should exist in the nonlinear coefficients from those predicted by the scalar theory (a factor of 1.8 difference is predicted at core diameter of 480 nm).

11.3 The experiments

The measurement is built based on the theory shown in Appendix A.3. According to the theory, to calculate the nonlinear coefficient, two experiments are need to measure two variables. The first one is the ratio between nonlinear phase (ϕ_{SPM}) and input power (P_{avg}). The second one is the fiber loss (α). To confirm the theory, a couple of measurements have to be performed fibers with a range of core diameters.

The experimental setup is shown in fig.11.3.1. Two CW lasers with small wavelength a separation ($0.4 \sim 0.8$ nm) are set to same power through polarisation controllers (PC) and co-polarised using a inline fiber polariser (Pol.) which is then amplified through an Erbium Doped Fiber Amplifier (EDFA). The amplified light

is launched into the fiber under test (FUT) using free space optics and then send to the optical spectrum analyser (OSA).

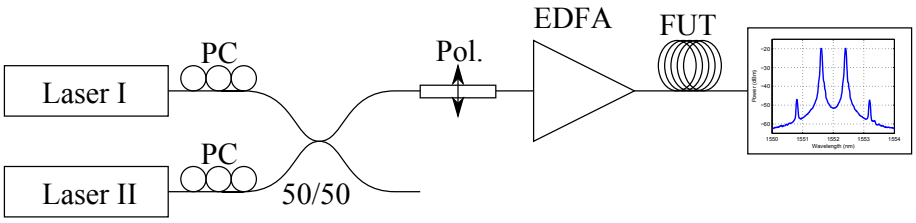

Figure 11.3.1: Schematics of the experimental setup for nonlinear measurement.

Four sets of fibers were tested for multiple times to obtain average measurement values of nonlinear coefficients. The four sets of fibers had core diameters of 450, 507, 530 and 554 nm.

In each measurement, we first increased the pumping power until side peaks started to appear. Then we gradually increased pumping power and measured the increase of the ratio between power in the pump and side bands using the peak values read from the OSA. Fig.11.3.2 shows an example of the output spectrum of the 530 nm core fiber. The central two peaks are the pumps and the outer pair of peaks are generated through nonlinear interactions. The pump power coupled into the fibre core was ranging from 20 to 60 mW.

The ratios of the power between pump and sideband peaks were converted to nonlinear phase shift using Eq.A.3.19. According to Eq.A.3.20, the nonlinear coefficient is the ratio of nonlinear phase shift (ϕ_{SPM}) and twice the product of input power (P_{avg}) and effective length (L_{eff}). The plot of ϕ_{SPM} versus P_{avg} is shown in Fig.11.3.3. By applying a linear fit to the plot, the averaged ratio between ϕ_{SPM} and P_{avg} can be extracted from the slope of the fitted line. The input power is the power launched into the fiber, which is the product of measured power (just before the input into the FUT) and a coupling efficiency. The coupling efficiency can be obtained from a cut-back loss measurement, which will be explained in the following paragraphs. In this case, the slope of the linear fitting line is $3.40 \pm 0.08\ rad/W$.

To calculate effective length, loss of the fibre must be measured. A cut-back

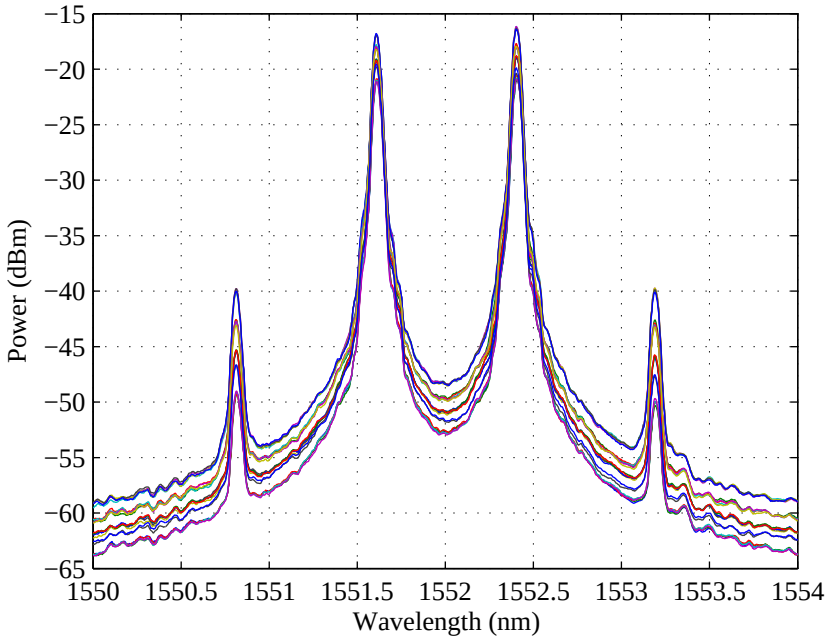

Figure 11.3.2: Spectra of the output of the FUT.

method can be used to perform this task. To start, the FUT was carefully aligned to a probe beam and a CW light at 1552 nm were launched into the fibre. Once the FUT was aligned, the input end the fiber was kept untouched during the whole testing process. The power at the output of the fiber was measured using a power meteor and the fiber was cut from the output end. The lengths of the fibre pieces that had been cut off were measured and recorded. This process was repeated until there was enough points for a linear fit in a logarithmic scale. As shown in Fig.11.3.4, the linear fit of output power in dBm versus fiber length in m ($P_{\text{out}} = aL + b$) give a slope (a) in dB/m which is the loss of the fiber. The intercept of the linear fitted line on the power axis (b) is the power coupled into the fibre. When it is compare to the launching power, the coupling efficiency can be calculated.

The calculated loss of this fiber was 13.2 ± 0.2 dB/m. The fiber used in the nonlinear measurement was 1.037 m which corresponding to effective length of 0.315 ± 0.006 m. Using Eq.A.3.20, the nonlinear coefficient then can be calculated, which is $5400 \pm 230\ W^{-1}km^{-1}$.

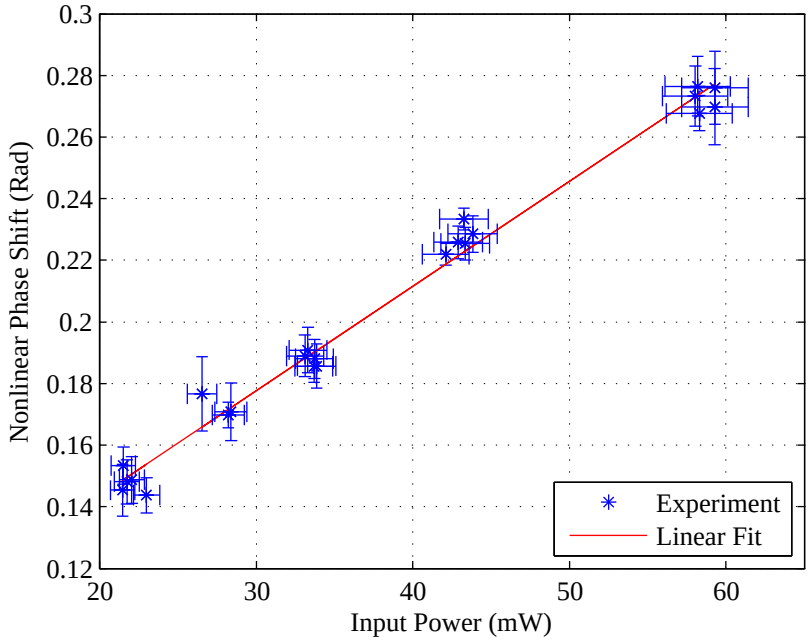

Figure 11.3.3: Nonlinear phase shift versus input power of the FUT with a core diameter of 530 nm. The two centre peaks are the two pumps, the two outer side peaks are generated through nonlinear effects. The input power of the pump is ranging from 20 to 60 mW from bottom to top curves.

Same experiments were also preformed on fibers with core diameters of 450, 507 and 554 nm. The measured nonlinear coefficients of these fiber are 5200 ± 620, 5480 ± 300 and 5170 ± 460 $W^{-1}km^{-1}$. Together with the measurement of fiber with core diameter of 530 nm, the experimental data were plotted on top of the theoretical predictions as shown in Fig.11.3.5. The experimental results match the theoretical predictions of the VNPP model within the range of measurement errors.

It it important to notice that the accuracy of the measured loss is important for the whole nonlinear measurement. There are two major causes of inaccuracy in loss measurement. Firstly, due to the small core size and high core-cladding index contrast, the fibres are multimode and there was a significant amount of power coupled into the cladding region of the fibres in the experiments. These part of the

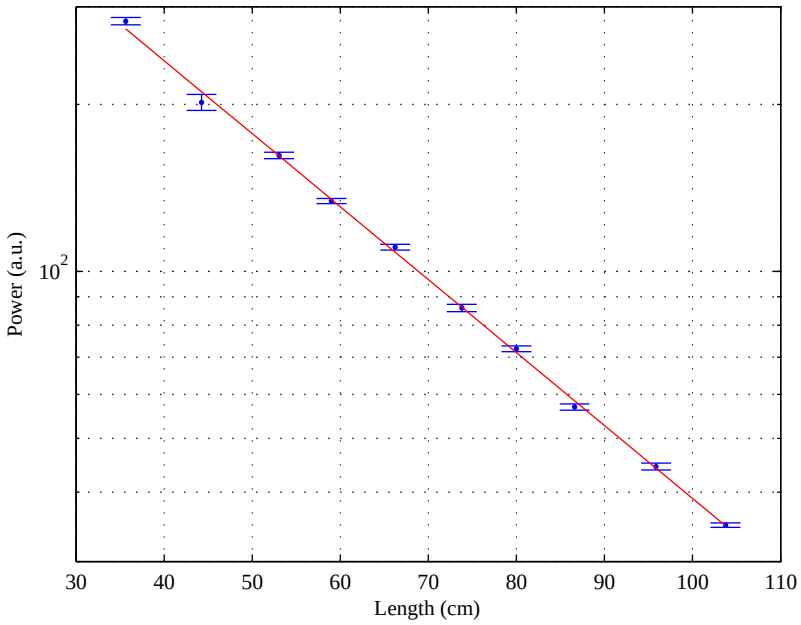

Figure 11.3.4: The power change along the FUT (530 nm core diameter) as a function of fibre length.

light must be removed before the output power was measured. In our work, we used a deflocculated graphite fluid to coat the fiber which effectively removed all cladding light and high-order modes (which is much more lossy than the fundamental mode).

Secondly, as the fibre core size decreases, the loss of the fibre increases exponentially [170], which also indicates that small fluctuation in the core diameter can lead to significant fluctuation in fibre loss. Fig. 11.3.6a shows the fibre loss as a function of fibre core diameter. As one can see, not only the average loss value increases as the core diameter becomes smaller, the error in the loss measurement also increases, especially for the fibre with core diameter of 450 nm. Further study revealed that for the 450 nm core fibre, the loss fluctuates periodically along the fibre. We continuously cut several 1-m-long pieces of fiber and measured the loss of each pieces. The loss along the 450 nm core fibre is shown in Fig. 11.3.6b. As one can see from the figure, the loss fluctuates along the fibre with a period of approximately 6 m. We suspect that this fluctuation could come from the variation of core diameter along

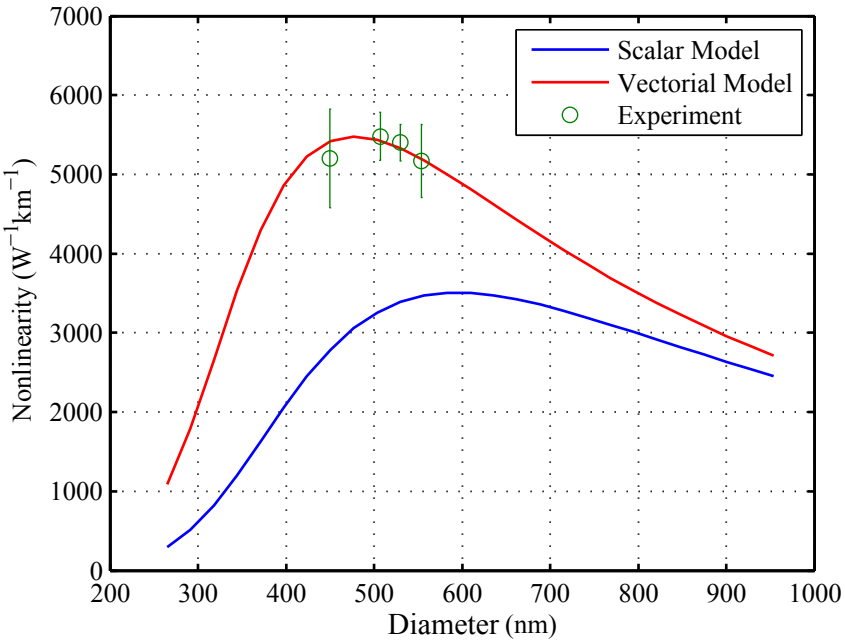

Figure 11.3.5: Comparison between measured values of γ with those of vectorial and scalar predictions.

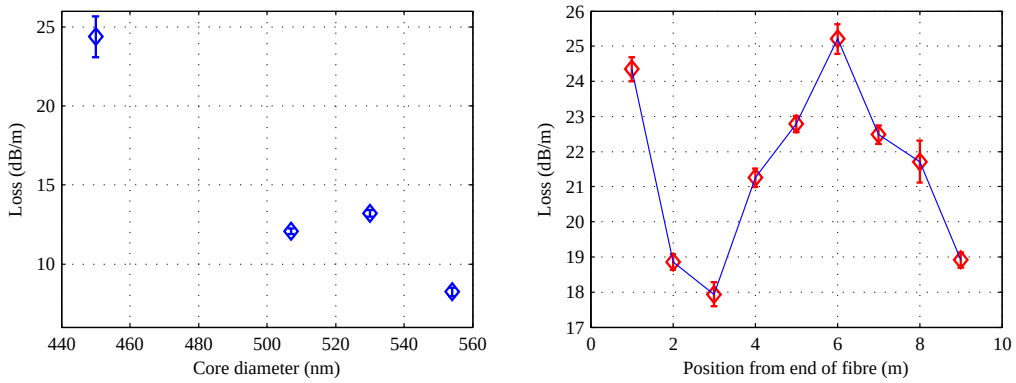

(a) (b)

Figure 11.3.6: (a) Fibre loss as a function of fibre core diameter. (b) The fluctuation of fibre loss along the 450 nm core fibre

the fibre caused by the feedback delay of fibre drawing tower's diameter control system.

11.4 summary

The VNPP model predicts the Kerr nonlinearity for SPM in HS waveguides can be significantly larger than the predictions by the scalar model. In our example, the VNPP predicted Kerr nonlinearity of a Bismuth suspended-core fibre with core diameter of 460 nm is 1.8 times of that of the scalar model.

Using a CW SPM method, we managed to measure the nonlinear coefficients of the four Bismuth suspended-core fibres with core diameters from 450 to 554 nm. Through comparison of the measured data to both VNPP and scalar models, an excellent agreement has been observed between the experimental results and the predictions of the VNPP model. It confirmed the validity of the γ expression of the VNPP model, which also indicates the validity of the VNPP model itself. In the next chapter, we are going to study the nonlinear interactions between different polarisation modes with the VNPP model and the new Kerr nonlinearity definition.

Chapter 12

Nonlinear interactions between two polarisation modes

12.1 Background

The Kerr nonlinear interaction between two polarisations of propagating modes, referred as nonlinear polarisation (NLP) in this thesis, leads to host of physical effects significant from both fundamental and application point of views. It has been studied extensively over the last 30 years [171–183].

Different aspects of the interaction has been investigated. Stolen et al., used the induced nonlinear phase difference between the two polarisations to discriminate high and low power pulses [171]. In the context of counter-propagating waves, NLP has been shown to lead to polarisation domain wall solitons [178–180, 184], which is described as a kink soliton representing a polarisation switching between different domains with orthogonal polarisation states. NLP can also lead to polarisation attraction [179, 181–183, 185, 186] where the state of the polarisation of a signal is attracted towards that of a pump beam. For twisted birefringent optical fibers, NLP related polarisation instability (PL) [172, 173, 175] and polarisation domain wall solitons [180] have been reported. NLP also induces MI which results in

dark-soliton-like pulse-train generation [176, 177]. Large-signal enhanced frequency conversion [187], cross-polarisation modulation for WDM signals [180] have also been reported and attributed to NLP. The stability behaviour of NLP has also been studied in anisotropic crystals [188].

The nonlinear interaction of the two polarisations can also be studied in the context of nonlinear coherent coupling or nonlinear directional coupling (NDC) in which the amplitudes of two or more electric fields, either the two polarisations of a propagating mode of a waveguide or different modes of different waveguides, couple to each other through linear and nonlinear effects [189–191]. The topic of nonlinear directional coupling has been extensively studied over the last 30 years. NDC is a good candidate for ultrafast all-optical switching, e.g. soliton switching [192–196] and all-optical logic gates [197–199]. The interaction of ultrafast beams, with different frequencies and polarisations, in anisotropic media has also been studied and the conditions for polarisation stability have been identified [193, 200].

Previous NLP work used nonlinear models based on the weak guidance approximation and hence these models were only suitable for low-index-contrast and large-dimension waveguides. With the development of VNPP, it is now possible to explore NLP in HS waveguides more accurately. In 2010, pioneer work on the polarisation effects with VNPP model was presented by Danial and Agrawal [201]. In this work, a model was developed to describe the polarisation of the light propagating inside a waveguide and demonstrated the self-polarisation rotation of the light as a function of power. In this work, the waveguide under consideration was highly birefringent, therefore, the authors neglected the term which is responsible for coherent coupling (refer to the theory section of this chapter). Here, a vectorial NLP model is developed with the coherent coupling term included. To explore novel polarisation behaviours, the steady state solutions of the vectorial NLP model are studied. Based on the newly discovered polarisation behaviours, applications such as optical logic gates and optical switches are purposed.

12.2 Structurally induced anisotropic nonlinearity

NLP can be described by two coupled nonlinear Schrödinger equations Eqs. 10.1.19. To proceed looking for the new nonlinear behaviours, Eqs. 10.1.19 is firstly simplified to a form similar to the scalar model. Eqs. 12.2.1 is simplified equations.

$$\frac{\partial a_\nu}{\partial z}+\sum_{n=1}^{\infty}\frac{i^{n-1}}{n!}\beta_\nu^{(n)}\frac{\partial^n a_\nu}{\partial t^n}=i\left(\gamma_\nu\left|a_\nu\right|^2+\gamma_c\left|a_\mu\right|^2\right)a_\nu+i\gamma_c' a_{nu}^* a_\mu^2\exp(-2iz\Delta\beta), \quad (12.2.1)$$

where $\Delta\beta=\beta_\nu-\beta_\mu$. Comparing to Eqs. 10.1.19, Eqs. 12.2.1 ignores the coupled dispersion term $i\sum_{\mu\neq\nu}\sum_n\frac{i}{n!}\frac{\partial^n}{\partial t^n}\beta_{\nu\mu}^{(n)}a_\mu$ and nonlinear terms related to nonlinear coefficients $\gamma_{\mu\nu}^{(1)}$, $\gamma_{\mu\nu}^{(2)}$ and $\gamma_{\mu\nu}^{(3)}$, which are relatively small [167]. These ignored may also have significant influences on NLP, but they are beyond the scope of this thesis.

When comparing Eqs. 12.2.1 to the scalar model [5], it can be found that in the scalar model,

$$\gamma_\nu=\gamma_\mu=\gamma,\quad \gamma_c=\frac{2}{3}\gamma,\quad \gamma_c'=\frac{1}{3}\gamma, \quad (12.2.2)$$

where γ is defined as $\dfrac{2\pi n_2}{\lambda A_{\text{eff}}}$. The relations in Eq.12.2.2 are obtained under the weak guidance approximation which also assumes that the effective mode areas of the two polarisation modes are equal [5].

Using the VNPP model, it can be found that in general

$$\gamma_\nu\neq\gamma_\mu\neq 3\gamma_c\neq 3/2\gamma_c'. \quad (12.2.3)$$

The inequality indicates that even with isotropic materials, anisotropic Kerr nonlinear effects can take place. As an example, Fig.12.2.1&12.2.2 show the γ coefficients of a range of elliptical waveguides made of chalcogenide glass ($n=2.8$, $n_2=1.1\times10^{-17}$ m^2/W at 1550 nm) surrounded by air. The "xAxis" and "yAxis" represent the two axes of the ellipse.

The γ values of the two polarisation fields along the major and minor axes of the ellipse are not equal in general except the ones on the diagonal line where the

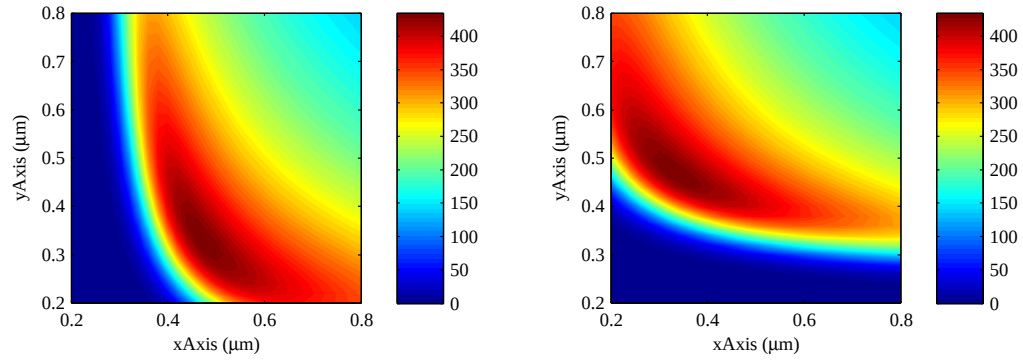

Figure 12.2.1: γ values for x-polarised field (left) and y-polarised field (right) of the elliptical waveguides with different dimensions.

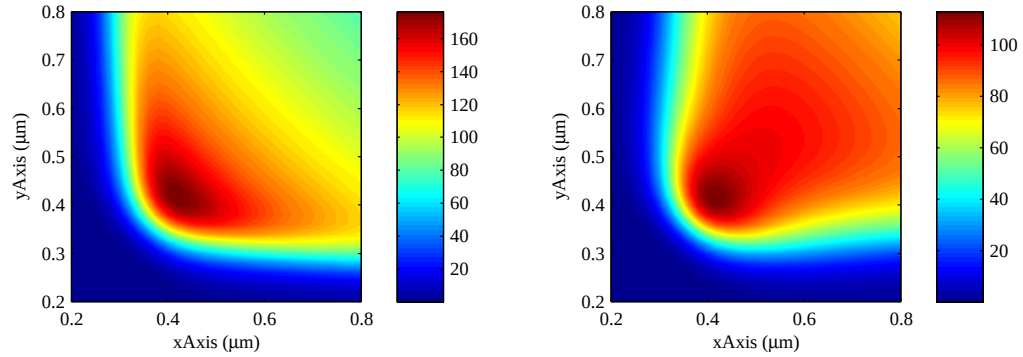

Figure 12.2.2: γ_c and γ_c' of the elliptical waveguides with different dimensions.

ellipses become circles. This phenomena is similar to the γ values in waveguides with anisotropic in which the anisotropy is due to the anisotropy of $\chi^{(3)}$ tensor, but here, the difference in γ is originated from the differences in the field distribution of the two polarisation modes. As a consequence, these waveguides will show anisotropic nonlinear properties even though they are made of isotropic material, which we refer to as structurally induced anisotropic nonlinearity (SIAN).

Besides the SIAN, the highest γ values within the plots are not corresponding to circular waveguides. Elliptical shaped waveguides have higher values of γ than circular shaped waveguides.

The SIAN indicates that even same amount of power are launched into the

two axes of these elliptical waveguides, unequal amount of nonlinear phase will be accumulated for the two polarisation modes along the two principle axes. This phenomenon indicates nonlinear polarisation behaviours of the propagating fields. Furthermore, γ_c and γ_c' also responsible for the interplay between the two polarisation modes. The inequality Eq.12.2.3 provides many new degrees of freedom with respect to the scalar model and shall provide novel nonlinear polarisation behaviours in HS waveguides.

In next section, the NLP is studied in the VNPP framework and the focus is the exploration of new degrees of freedom provided by the inequality Eq.12.2.3 on the steady state solutions of Eqs. 12.2.1. To start, continuous waves are considered.

12.3 New expression of coupled wave equations for continuous waves

To study the nonlinear polarisation behaviours with in VNPP model, continues waves are firstly considered in lossless waveguides so that dispersion and loss of the waveguides can be ignored. Then the coupled VNSE is rewritten in the form of power and phase of the light in the two polarisations to help focusing on studying the polarisation behaviours of the CW fields. After that, the steady state solutions of the equations are found, from which one can finally identify and study different regimes of different polarisation behaviours.

When dispersion and loss of a waveguide is not considered, Eqs. 12.2.1 can be rewritten in the form of field power and phase of the two polarisation modes , which is a move convenient way for study field polarisation. By defining $a_\nu = \sqrt{P_\nu}e^{i\phi_\nu}$,

where P_ν is the power of the field a_ν with phase ϕ_ν, Eqs. 12.2.1 can be rewritten as,

$$\frac{\partial}{\partial z}P_\nu = 2\gamma\prime_c P_\nu P_\mu \sin[2(\phi_\nu - \phi_\mu + \Delta\beta z)] \tag{12.3.1}$$

$$\frac{\partial}{\partial z}P_\mu = -2\gamma\prime_c P_\nu P_\mu \sin[2(\phi_\nu - \phi_\mu + \Delta\beta z)] \tag{12.3.2}$$

$$\frac{\partial}{\partial z}\phi_\nu = \gamma_\nu P_\nu + \gamma_c P_\mu + \gamma\prime_c P_\mu \cos[2(\phi_\nu - \phi_\mu + \Delta\beta z)] \tag{12.3.3}$$

$$\frac{\partial}{\partial z}\phi_\mu = \gamma_\mu P_\mu + \gamma_c P_\nu + \gamma\prime_c P_\nu \cos[2(\phi_\nu - \phi_\mu + \Delta\beta z)]. \tag{12.3.4}$$

From Eqs. 12.3.4, one can notice that when no loss is considered, the total power of the polarisation modes remains constant ($\frac{\partial}{\partial z}(P_\nu + P_\mu) = 0$). Now, if following dimensionless variables (Eqs.12.3.5) are defined,

$$v = \frac{P_1}{P_0}, \quad \theta = 2\Delta\phi, \quad \Delta\phi = \phi_1 - \phi_2 + z\Delta\beta, \quad \tau = 2\gamma\prime_c P_0 z,$$
$$a = -\frac{\Delta\beta}{\gamma\prime_c P_0} - \frac{\gamma_c - \gamma_2}{\gamma\prime_c}, \quad b = \frac{\gamma_1 + \gamma_2 - 2\gamma_c}{2\gamma\prime_c}, \tag{12.3.5}$$

the form Eqs.12.3.4 can be simplified to,

$$\dot{v} \equiv \frac{dv}{d\tau} = v(1-v)\sin\theta,$$
$$\dot{\theta} \equiv \frac{d\theta}{d\tau} = -a + 2bv + (1-2v)\cos\theta. \tag{12.3.6}$$

Initial values $\theta_0 = \theta(0)$, $v_0 = v(0)$ with $0 < v_0 < 1$ are chosen, where τ is regarded as a "time" variable, and for physical reason, one must have $0 \leqslant v(\tau) \leqslant 1$ for all $\tau > 0$ since v is the ratio of power in polarisation state 1 to the total power.

12.3.1 Steady state solutions

One way to study nonlinear polarisation behaviour is to study the steady state solutions (SSSs) of Eqs. 12.3.6 (i.e., $\dot{v} = 0$ and $\dot{\theta} = 0$). In this way, regimes of

different polarisation behaviours can be identified. There are four classes of SSSs:

$$\cos\theta = 1, \quad v = \frac{a-1}{2(b-1)}, \quad (b \neq 1), \tag{12.3.7}$$

$$\cos\theta = -1, \quad v = \frac{a+1}{2(b+1)}, \quad (b \neq -1), \tag{12.3.8}$$

$$\cos\theta = a, \qquad v = 0, \qquad (|a| \leqslant 1), \tag{12.3.9}$$

$$\cos\theta = -a + 2b, \qquad v = 1, \qquad (|a - 2b| \leqslant 1). \tag{12.3.10}$$

The SSSs Eqs. 12.3.9&12.3.10 correspond to light coupled into only one principle axis. The SSSs Eqs. 12.3.7&12.3.8 restricts the possible values of a, b. For SSS Eqs. 12.3.7, the initial conditions (v_0 and θ_0, also referred as fixed points since the solutions are steady) only exist between $a = 1$ and $a = 2b - 1$, labelled as the red and green regions in Fig.12.3.1a. For SSS 12.3.8, the fixed points only exist between $a = -1$ and $a = 2b + 1$, labelled as the yellow and orange regions in Fig.12.3.1b.

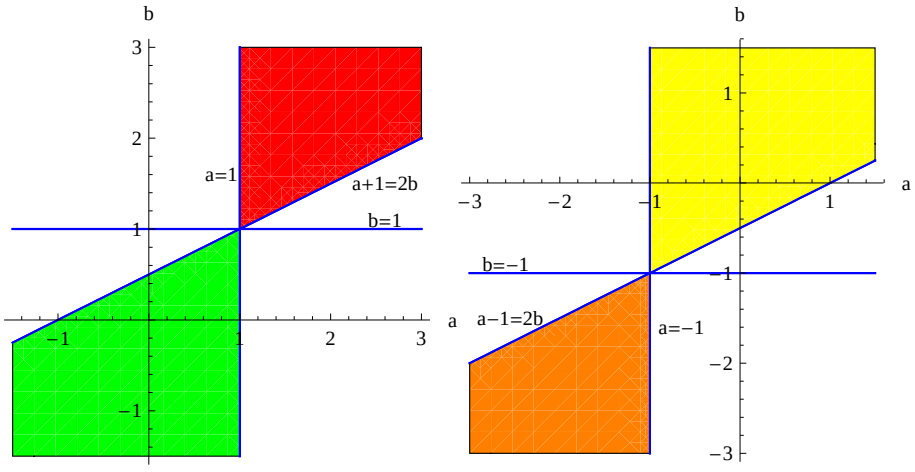

Figure 12.3.1: The stable and unstable regions for parameter a,b in SSSs 12.3.7 (a) and 12.3.8. (a) red region for unstable fixed points and green region for stable ones. (b) orange region for unstable fixed points and yellow region for stable ones.

Interestingly, numerical simulations indicate that some SSSs are very sensitive to the initial conditions and behave unstably to the smallest numerical fluctuations in

the calculations and exhibit periodic behaviours. A stability analysis on Eqs. 12.3.6 was done incorporate with Dr. Max A. Lohe at University of Adelaide (see Appendix A.4). The results show that are unstable and the fixed points in the green and yellow regions in Fig. 12.3.1 are stable but the fixed points in the red and orange regions are unstable.

12.3.2 Periodic behaviours

Further study on the SSSs by Dr. Lohe revealed a constant of the motion $\Gamma = -av + bv^2 + v(1-v)\cos\theta$ exists in Eqs. 12.3.6. It follows Eqs. 12.3.6 that $\dot{\Gamma} = 0$. The conserved quantity Γ enables us to perform one integration of Eqs. 12.3.6. One can have

$$\cos\theta = \frac{\Gamma + av - bv^2}{v(1-v)}, \tag{12.3.11}$$

hence one can rewrite $\dot{v}$ in Eqs. 12.3.6 as

$$\dot{v}^2 = v^2(1-v)^2 - (\Gamma + av - bv^2)^2 \equiv Q(v), \tag{12.3.12}$$

in which Q is a fourth degree polynomial, provided $b^2 \neq 1$. It should be noted that $Q(v)$ can be completely determined by parameter a&b and the initial conditions v_0 and θ_0 since Γ is a constant of motion. Eq. 12.3.12 can be integrated to find $v(\tau)$ as an elliptic integral of the first kind, which is a periodic function, and hence v is a periodic function of τ, specifically one have

$$\frac{dv}{\sqrt{Q(v)}} = \pm d\tau. \tag{12.3.13}$$

Denoting the minimum and maximum values of v over one period by $v_{\min}$ and $v_{\max}$, with $0 < v_{\min} \leqslant v_{\max} < 1$, then $v_{\min}$ and $v_{\max}$ occur when $\dot{v} = 0$, which are two roots of Q. By integrating Eqs. 12.3.13 over half period from τ_0 to τ_1 where τ_0 is given by $v(\tau_0) = v_{\min}$ and τ_1 is given by $v(\tau_1) = v_{\max}$, then

$$\int_{v_{\min}}^{v_{\max}} \frac{ds}{\sqrt{Q(s)}} = \tau_1 - \tau_0 = \frac{T}{2} \tag{12.3.14}$$

where v is an increasing function in this interval so only positive sign is chosen and T is a complete period. This integral may be evaluated explicitly in terms of a complete elliptic integral of the first kind. The precise formulas depend on the relative location of the roots of Q.

Based on Dr. Lohe's work, calculations of the periods are performed based on elliptical waveguides mentioned early in Section 12.2. As an example, an elliptical waveguide with two axes equal to 640 and 620 nm is considered. The parameter b of this waveguide is calculated and $b = 2.39$. Considering the SSS case Eqs. 12.3.7, the input power is set such that the initial condition close to a unstable fixed point. A random power 843.8 W is picked, with $P_1(0) = 50.5\ W$ and $P_2(0) = 793.3\ W$ determined by the condition Eq.12.3.7, such that the parameter $a = 1.19$ satisfies $1 \leqslant a \leqslant 2b + 1$.

Now considering, $P_1(0)$ is perturbed by amount of ΔP but the initial phase remains the same ($\theta_0 = 0$). Due to this perturbation, the relations in Eqs. 12.3.7 are no longer satisfied. As a result, the power (v) and phase (θ) are no longer steady. Instead, they vary periodically as they propagate. Their period T can be plotted as a function of ΔP in Fig.12.3.2. At $\Delta P = 0$, the initial condition is at a steady state, hence T is infinite.

The insets in Fig.12.3.2 show P_1, P_2 and $\cos\Delta\phi$ as functions of z with $\Delta P = 100\ W$, where the periodicity of the power (v) and phase ($\cos\Delta\phi$) are evident. For $\cos\Delta\phi = \pm 1$, the polarisation state of the fields are linear with an angle to one of the principle axes, which is parallel to P_2, equal to $\pm\arctan\frac{P_1}{P_2}$. Every time when $\cos\Delta\phi$ switch from 1 to -1 or vice versa, the polarisation state of the field switch from negative to positive angles which lead to a overall flipping angle of $2\arctan\frac{P_1}{P_2}$ which in this case is approximately 20^o.

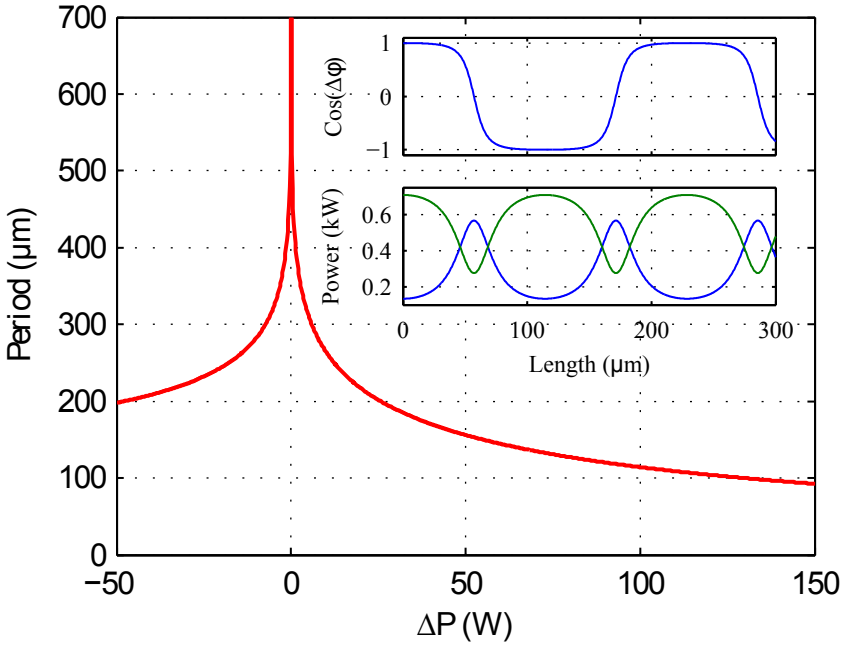

Figure 12.3.2: The period T as a function of the perturbation power ΔP of the input around an unstable fixed point. The insets show the oscillations in power (left) and the cosine of phase (right) corresponding to $\Delta P = 50$ W.

12.3.3 Application – optical logic gates

A direct application of this behaviour is the construction of an optical logic gate. In order to construct such a logic gate, a waveguide that can lead to fast transitions between polarisation states than the example in Fig.12.3.2 is preferred. A fast transition can be represented as a steep slope at $\cos\Delta\phi = 0$. Searching through different elliptical structures, a waveguide with two axes equal to 640 nm and 760 nm are chosen. The period T of this elliptical waveguide is plotted in Figure 12.3.3 as a function of the perturbation power ΔP. In this case, $P_1 = 1538 + \Delta P\ W$, $P_2 = 549\ W$.

The insets show the powers P_1, P_2 (left) and $\cos\Delta\phi$ (right) as a functions of the propagation length for $\Delta P = -1W$ (red circle). The power in the two polarisations also changes periodically but with this structure, the polarisation transition is more

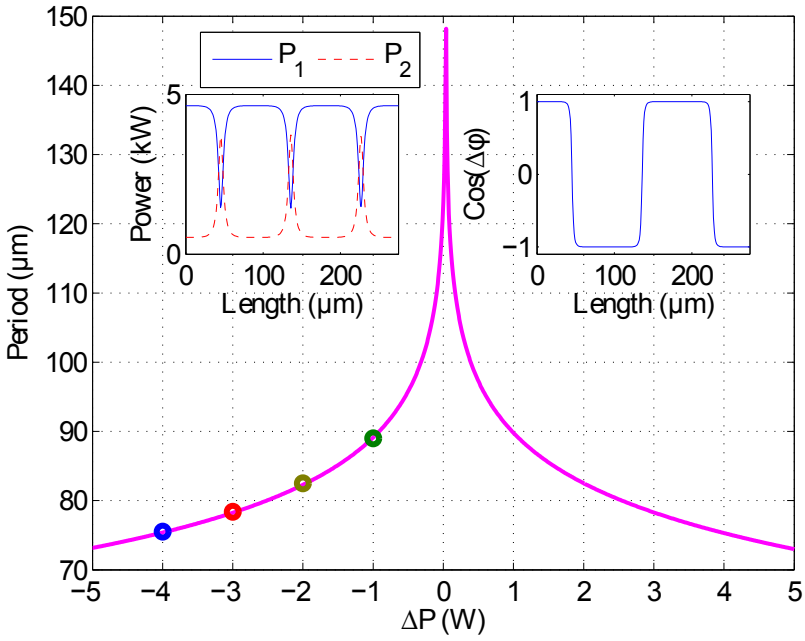

Figure 12.3.3: The period T as a function of the perturbation power ΔP for the "logic-gate" waveguide. The insets show the oscillations in power (left) and the cosine of phase (right) corresponding to $\Delta P = -1$ W. Circles are corresponding to four examples considered in Fig. 12.3.4 with ΔP =-4 (Blue), -3 (Red), -2 (Yellow) and -1 (Green)

quicker than the previous example (Fig. 12.3.2).

Now considering a train of four pulses with ΔP equal to -1 (Green), -2 (Yellow), -3 (Red) and -4 W (Blue) (Fig. 12.3.4 top, their corresponding periods are labelled using the same colours in Fig. 12.3.3) that propagates in the waveguide for 620 μm. The values of $\cos\Delta\phi$ of the pulses as functions of propagation length are calculated and shown in the bottom figure of Fig. 12.3.4. We consider $\Delta P = -5W$ as the power of the clock pulses (background), and denote $1W$ and $2W$ as binary 1 and 0, respectively, and $\cos\Delta\phi = 1$ and $\cos\Delta\phi = -1$ as binary 1 and 0, respectively. Then the first 3 pulses correspond to binary input pairs (0, 0), (1, 0) or (0, 1) and (1, 1), respectively. The $\cos\Delta\phi$ of the pulses at the output of the waveguide (Fig. 12.3.5 Bottom) corresponds to the result of an XOR operation denoted by the truth table

in Fig. 12.3.5.

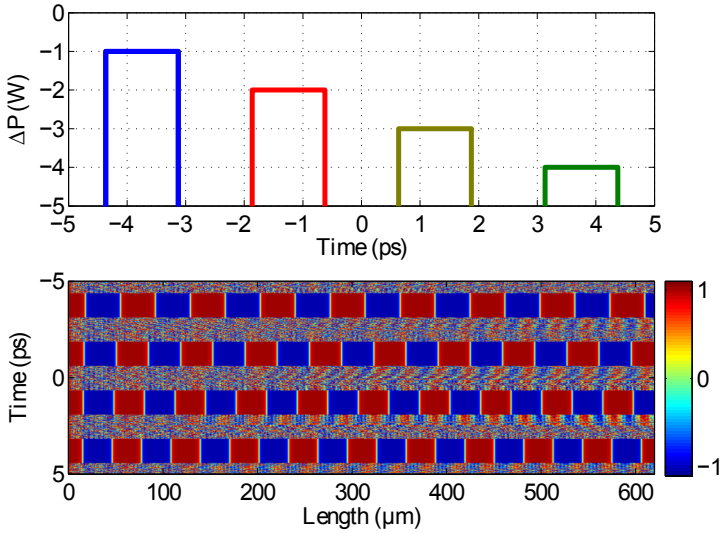

Figure 12.3.4: (Top) A train of pulses corresponding to ΔP = -4 (Blue), -3 (Red), -2 (Yellow) and -1 W (Green), whose periods T are labelled as circles in the same colours in Fig. 12.3.3. The four pulses represents binary XOR operations $0 \oplus 0$, $1 \oplus 0$ or $0 \oplus 1$, $1 \oplus 1$ and 1 when there is only one input. (Bottom) The $\cos \Delta\phi$ of the four pulses in the top figure as a function of propagation length. The Y axis is corresponding to the X axis in the top figure.

The proposed application is theoretical. The lack of dispersion and loss, the high power requirement (1538 W) make the application less practical. However, this application indicates the potential of switching high power signals using signals with orders of magnitude lower power.

12.4 Nonlinear polarisation in asymmetric waveguides

From the parameter a in Eqs. 12.3.5, one can find that the power is related to the value of $\Delta\beta$ through the term $\dfrac{\Delta\beta}{\gamma' {}_c P_0}$. For the elliptical waveguides shown in Chapter

Input 1	0	0	1	1
Input 2	0	1	0	1
Output	0	1	1	0

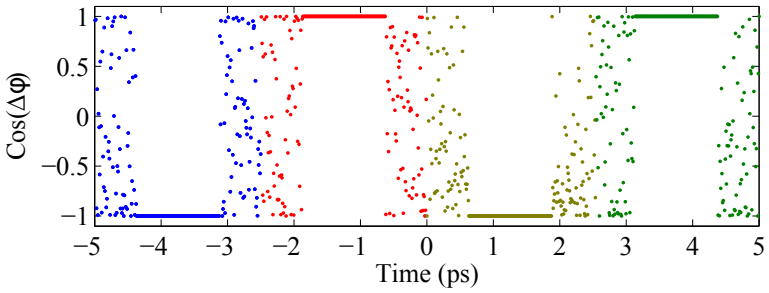

Figure 12.3.5: (Top) The truth table of an XOR operation. (Bottom) The $\cos\Delta\phi$ of the pulses in Fig. 12.3.4 at the output of the waveguide. When $\cos\Delta\phi = -1$ and $\cos\Delta\phi = 1$ are considered as binary 0 and 1, the $\cos\Delta\phi$ of pulses are corresponding to an XOR operation.

10, the values of $\Delta\beta$ is in the order of $10^5 \sim 10^6\ m^{-1}$ for most of the structures. If $\Delta\beta$ can be reduced by a few orders of magnitude or to zero, the power requirement can be also reduced. However, with elliptical waveguide design, $\Delta\beta \to 0$ only exists when the structure close to a circle. In this case, the structurally induced anisotropic nonlinearity (e.g. $\gamma_\nu - \gamma_\mu$) also becomes small. As a result, the polarisation flipping effects become rather difficult to observe. However, if the structure of the waveguide is not symmetric, it is possible to find a structure where nonlinear coefficients of different polarisations are different but the linear birefringence is zero. Hence, rib-waveguides are studied.

12.4.1 Rib-waveguides

Rib-waveguide design has been used in optical waveguide areas for many years. A rib-waveguide has only one-fold symmetry, which cause the electric fields po-

larised along the two principle axes have rather difference distribution patterns (see Fig.12.4.1). This leads to different nonlinear coefficients for the two polarisation modes. Furthermore, with the "rib" design, it is possible to achieve low $\Delta\beta$ at certain wavelengths [202].

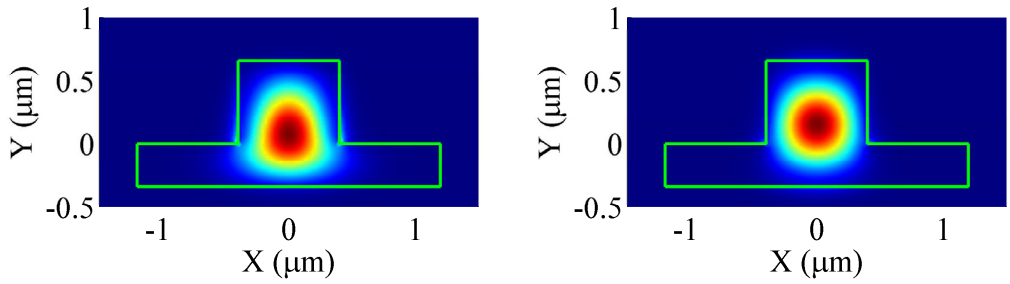

Figure 12.4.1: Mode profiles of the fundamental modes in horizontal (left) and vertical (right) polarisations.

Fig. 12.4.2 shows the birefringence calculated as a function of the rib width and depth for rib waveguides based on a chalcogenide glass surrounded by air. Values for which $\Delta\beta = 0$ are indicated by the white contour.

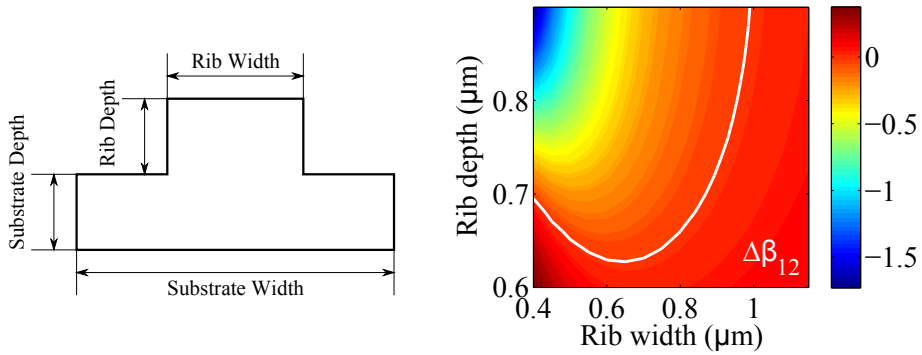

Figure 12.4.2: Contour plot of $\Delta\beta$ in m^{-1} for a range of rib waveguide parameters.

Now one can investigate unstable nonlinear polarisation for the cases where $\Delta\beta \approx 0$. For these cases, as it is clear from Eqs. 12.3.5, a can be rewritten as a' where

$$a = -\frac{\gamma_c - \gamma_2}{\gamma_c'} \equiv a'. \tag{12.4.1}$$

T is period of $v(\tau)$ and $\theta(\tau)$ in dimensionless "times" τ, hence, from here on, it is denoted as T_τ. T_τ is a function of a, b, v_0 and θ_0. Since P_0 is no longer presented in a, P_0 has no effects on T_τ any more. However, since $\tau = 2\gamma\prime_c P_0 z$, then one can show that the period in z is $T_z = T_\tau/(2\gamma'_c P_0)$.

When investigating the values of v, θ at the output $z = L$ of the waveguide, certain the rib waveguide dimensions can be chosen such that $\Delta\beta$ is almost zero, a is almost independent of P_0, then $P_1(z), P_2(z), \cos\Delta\phi(z)$ and T_z are scalable through P_0.

As an example, considering light that is initially linearly polarised ($\theta_0 = 0$), with equal power into the two polarisations ($v_0 = 1/2$). a rib-waveguide with a rib width of 990 nm, a rib height of 900 nm, a substrate width of 2400 nm and a substrate height of 340 nm. We find, in units of $(\mathrm{W.m})^{-1}$: $\gamma_1 = 81.6, \gamma_2 = 82.2, \gamma_c = 49.6, \gamma'_c = 24.7$, with numerical values for $\Delta\beta = 3.8 \times 10^{-4}\ m^{-1}$ consistent with $\Delta\beta \approx 0$. With 1 mW input power and a $L = 1$ m long of such waveguide, the nonlinear phase difference ($(\gamma_\nu - \gamma_\mu)P_0 L$) is more than 200 times larger than the linear contribution ($\Delta\beta L$). With these γ values we have $a = 1.320, b = 1.308$, and so $1 < a < 2b - 1$ is satisfied, and therefore unstable fixed points exist (Fig.12.3.1a). Fig. 12.4.3(left) shows $\cos\Delta\phi$ as a function of z at $P_0 = 1$ W, where $\cos\Delta\phi$ displays flipping between ± 1 with a period $2T_z = 0.94$ m. Similar behaviour is also observed when $\cos\Delta\phi$ plot as a function of input power P_0 too.

12.4.2 Application – optical switches

The flipping properties of $\cos\Delta\phi$, considered as a function of either P_0 or the waveguide length L, enable us to construct in principle a power limiting optical device. Considering a L metre long rib waveguide with the structural parameters of the previous example, a linear polariser is put after the waveguide with its polarisation aligned in parallel to the polarisation of the input beam (45% to the horizontal axis

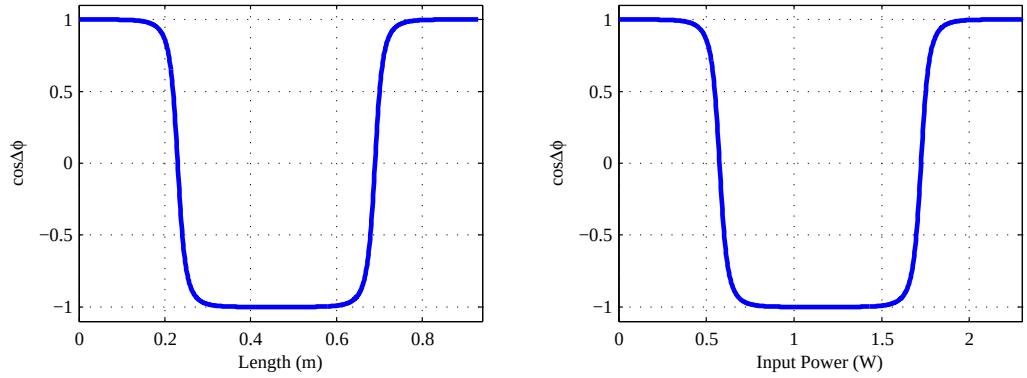

Figure 12.4.3: $\cos\Delta\phi$ as a function of propagation length (left), $\cos\Delta\phi$ as a function of input power (right).

of the waveguide, hence $v = 0.5$). The power after the polariser is be calculated as

$$\begin{aligned} P_{\text{out}}(P_0) &= (\sqrt{P_\nu}e^{i\phi_\nu} + \sqrt{P_\mu}e^{i\phi_\mu})(\sqrt{P_\nu}e^{i\phi_\nu} + \sqrt{P_\mu}e^{i\phi_\mu})^* \\ &= \frac{1}{2}P_0 + \frac{1}{2}P_0 + \frac{1}{2}\sqrt{P_\nu}\sqrt{P_\mu}e^{i\phi_\nu}e^{-i\phi_\mu} + \frac{1}{2}\sqrt{P_\nu}\sqrt{P_\mu}e^{-i\phi_\nu}e^{i\phi_\mu} \\ &= \frac{1}{2}P_0 + \frac{1}{2}\sqrt{vP_0}\sqrt{(1-v)P_0}\cdot 2\cos(\phi_\nu - \phi_\mu) \\ &= \frac{1}{2}P_0 + P_0\sqrt{v(1-v)}\cos\frac{\theta}{2}. \end{aligned} \tag{12.4.2}$$

If $L = L_1 = 0.4$ m is chosen, the response of the output power $P_{\text{out}}^{(1)}$ to the input power P_0 is shown in Fig. 12.4.4a (blue). It responses linearly to P_0 for $P_0 \leqslant 0.3$ W, but falls to zero in the range $0.9 - 1.4$ W due to the periodic change of the polarisation of the light.

To extend the range over which the output power is limited, we attach a similar waveguide and polariser but with waveguide length $L_2 = 2L_1 = 0.8$ m, with an output P_{out}^2 as shown in Fig. 12.4.4a (green); this plot is a compressed copy of the plot for P_{out}^1, as follows from the scaling properties of T_z with respect to P_0 and L. The total output of the device as a function of P_0 is given by $P_{\text{out}}^2(P_{\text{out}}^1(P_0))$, which is shown in Fig. 12.4.4b. The output is linear for $P_0 \leqslant 0.15$ W, but is limited to values $\leqslant 0.2$ W for all input powers $P_0 \leqslant 1.7$ W. The maximum power operation range can be adjusted by varying the lengths and hence periods of the connected

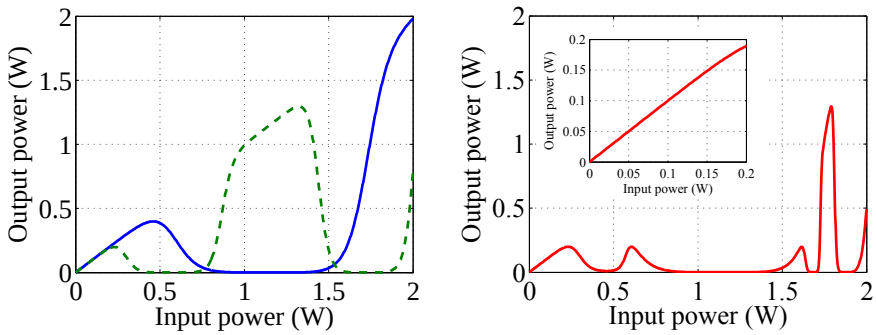

(a) (b)

Figure 12.4.4: (a) Output versus input power for combinations of waveguides and polarisers, (blue) L = 0.4 m, (green dotted) L = 0.8 m. (b) Total output versus input power after connecting two waveguides and polarisers together.

waveguides, and also by adding further stages.

Although this model is time independent, it can still be applied to pulsed systems if dispersion has an negligible effect on the pulse. Some examples of optical power switching are shown here with pulses using the same configuration as the one of Fig. 12.4.4b. Assuming there is no dispersion, Figs. 12.4.5a&b demonstrate power switching of an 1 ns pulse with 2 W peak power and a train of 200 ps pulses with peak powers ranging from 0.1 to 1.6 W, respectively. Comparing the peak power within a pulse (Fig. 12.4.5a) or the peak power of each pulse (Fig. 12.4.5b) with the curve in Fig. 12.4.4b, the output power of all pulses follow the curve in Fig. 12.4.4b regardless of pulse durations, which indicates there is no latency in the switching mechanism (since it is based on Kerr nonlinear processes). Any input pulse power below 1.7 W is under control of the switch. Pulses with peak power lower than 0.2 W pass the switch without being affected and pulses with peak power greater than 0.2 W are cut off to 0.2 W maximum (Fig. 12.4.5b).

The assumption of no dispersion is critical for this switch to work. However, there is a certain margin of dispersion that this switch can tolerate. The margin depends on the dispersion value and pulse duration. Since, for most cases, dispersion

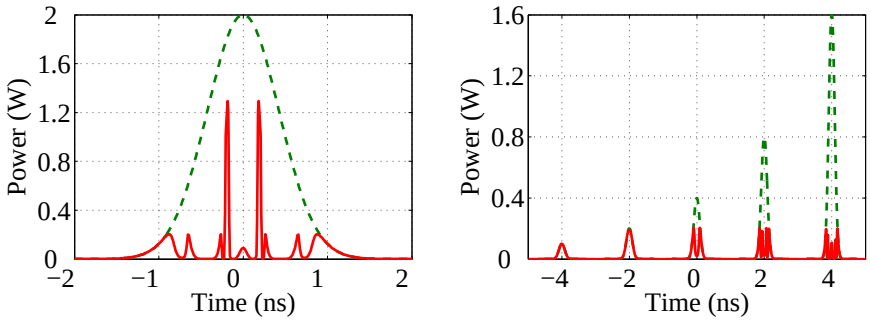

(a) (b)

Figure 12.4.5: Power switching with pulses using nonlinear polarisation bistability, input power under 0.2 W remains unchanged and power larger than 0.2 W is cut off to 0.2 W maximum. (a) Single pulse input (green dashed) and output (red solid) of the switch. (b) A train of pulses with duration of 200 ps and peak power of 0.1, 0.2, 0.4, 0.8 and 1.6 W from left to right showing the inputs (green dashed) and their corresponding outputs (red solid).

values are tied to β values with the condition $\Delta\beta \approx 0$, dispersion can be avoided by through using long pulses with narrow line-widths with respect to dispersion. For example, assuming this switch has β_2 around 100 $ps/nm/km$ for two polarisation modes, pulses with 100 ns duration would experience negligible influence due to dispersion in simulations.

12.5 Summary

In this chapter, a set of equations were derived based on the VNPP model to describe of the polarisation of behaviours of pulses propagating in high-index-contrast sub-wavelength-scale waveguides for continues waves.

The SIAN and the inequality equation Eq. 12.2.3 lead to new regimes of stable and unstable SSSs that have never been seem before. Within the regime of unstable SSSs and linear polarised inputs, periodic behaviours in both power and phase of the

guided modes were discovered. These periodic behaviours in power and phase result in periodic changes in polarisation states. The period of these changes is a function of parameter a b and initial conditions including input powers in each polarisation and the phase difference between them.

Since the periodic behaviours happen around unstable SSSs, they are very sensitive to the initial conditions. Using this property, an application as an optical logic gate is purposed. Three input beams are launched into a waveguide two logic inputs and one clock. After certain length of propagation, the outputs of the waveguide behave like a XOR logic gate. The key of this application is that the light propagating inside the waveguides (gates) switches its polarisation between two states quickly according to small changes in the input power.

There is one drawback, in practice, of using the periodic behaviour for applications. That is the high power requirement. It is related to the linear birefringence $\Delta\beta$. To reduce $\Delta\beta$ but without reduce structural-induced anisotropic nonlinear effects of the waveguides, nonlinear polarisation behaviours in asymmetric waveguides such as rib-waveguides were studied.

In rib-waveguides, it is possible to obtain $\Delta\beta = 0$ for the two polarisation modes. However, the asymmetry of the waveguides produces significant anisotropic nonlinearity to obtain periodic polarisation behaviours. Using rib-waveguides, the required power were reduced from kilowatts level, with elliptical waveguides, to sub-watts level. But the drawback of reducing the operation power is the extension of length of the period. However, by increasing the power, the period can be reduced again.

An application of an optical switch is purpose using combinations of rib-waveguides. Using this optical switch, a linear output-to-input power response can be obtained within a range of input powers, in the example, the range is 0 to 0.2 W. For input powers higher than the up limit of this range (0.2 W) but lower than a power level many times higher than this limit (1.7 W in this example), the output powers are limited to the up limit (0.2 W). The principle behind this application is similar to the first example, the period of the change of polarisation is a function of the input

power. But in this example, the input power was varied continuously instead of discretely and the propagation length was also varied to change the ratio between the input power and the period.

The work in this chapter not only demonstrated new polarisation behaviours and new applications, the discovery of the novel polarisation behaviours also opens the new possibilities to reassess the state-of-art theories of nonlinear processes such as FWM and SC generation studied in Part I using the VNPP model. Based on the results in this chapter, the influences of polarisation interactions on FWM and SC generation in HS waveguides are possible to be significant.

Chapter 13

Summary of Part II

In this part of the thesis, a new developed VNPP model was introduced to accurately describe nonlinear effects in waveguides with high index contrast and sub-wavelength scale features. The key elements of the VNPP model was separated into two aspects. Firstly, significant z-components of the electromagnetic field exist in the guided modes inside these waveguides. Secondly, the orthogonality property of the fields can no longer be expressed in the traditional form $\mathbf{e}_\mu \cdot \mathbf{e}_\mu$ which leads to different expressions of the nonlinear coefficients referred as structurally induced anisotropic nonlinearity (SIAN). The VNPP model predicts significant differences in the values of these nonlinear coefficients as well novel polarisation behaviours of the light propagating in these waveguides.

To confirm the VNPP model, experiments were performed and nonlinear coefficients of fibers with a range of core diameters are measured and compared to both VNPP and the conventional models. The measurement used a CW SPM method. With this method, two CW beams with small wavelength separation and equal peak power were launched into the FUT. The wavelength separation of the two CW beams were so small such that the dispersion between the two wavelengths could be ignored. Through measuring the ratio between peak powers of pump and new generated wavelengths, nonlinear coefficient were calculated and plotted as a function of fiber core diameter. The experimental plot matched with the prediction of VNPP

model thus proved the validity of the nonlinear coefficient definitions of the VNPP model which leads to the indication of the validity of the VNPP model itself.

Once the VNPP model was experimentally confirmed, the model was further analysed in the content of NLP. A simplified version of VNPP model which assumes CW operations without loss was rewrote in dimensionless forms of the power and phase of the polarisation modes. Through study its steady state solutions, significantly differences were found between the VNPP and standard model. Further studying the SSSs, new parameter regions are found where the SSSs were unstable and the polarisation of the modes around these solutions exhibit period behaviours. These results can greatly impact the applications based on NLP. An optical XOR logic gate was proposed to demonstrate the potential of this effect and shown great sensitivity of modulating the polarisation of a high power beam through a beam with orders of magnitude lower power.

The analysis of the dimensionless VNPP model also revealed that the power requirement for observing NLP was closely related to the value of linear birefringence. However, in normal symmetric waveguide structure, reducing linear birefringence lead to reducing of its nonlinear counterpart at a higher rate. Fortunately, from the origin of SIAN, the differences in the field distribution of different polarisation modes, NLP is possible to be observed at low power levels in asymmetric waveguides where linear birefringence is zero or near zero.

Based this hypothesis, nonlinear coefficients and propagation constants were calculated for a range of rib waveguides. For certain rib structures, it is possible to have different nonlinear coefficients and zero linear birefringence. Such structural discovery right away brought down the required power from kW-level to mW-level and a corresponding conceptual application of an optical switch was proposed.

The VNPP model opens the dome of the new era of NLP in high index contrast and subwavelength scale waveguides. The potential of this area is waiting to be explored. At moment, the model only describes continues waves. The effects of dispersion and short pulse waves are potential important in terms of practice. Also

with the increasing needs of developing on chip optical nonlinear devices which fit well in the regime of VNPP model, real life applications including on chip parametric oscillators and SC generations will be significantly influenced by the results of the study of VNPP model.

Chapter 14

Conclusion and future work

14.1 Conclusion

The aim of this thesis is to explore the potential of using soft-glass microstructured optical fibres (MOFs) for nonlinear applications and advance the application of full vectorial nonlinear pulse propagation models for nonlinear device development. In this thesis, two distinct aspects of nonlinear processes in novel optical waveguides have been studied. Aspect (1) is the exploration of the potential of using soft-glass microstructure optical fibres (MOFs) for nonlinear applications as platforms for new frequency light generation in both near- and mid-infrared wavelength regimes. A femtosecond fibre optical parametric oscillator (FOPO) was designed as a narrow band tunable light source, and in contrary, a supercontinuum (SC) source was designed as a broadband light source. Both works were preformed using a conventional nonlinear pulse propagation model that was based on the weak guidance approximation. Aspect (2) is the development of a full vectorial pulse propagation model (VNPP) for studying Kerr nonlinear effects and nonlinear interactions between polarisation modes in high-index-contrast sub-wavelength-scale (HS) waveguides which include soft-glass MOFs. The results from aspect (1) and aspect (2) showed promising potential of using soft glass MOFs for future nonlinear applications.

In the first part of the thesis, a genetic algorithm (GA) based fibre structure designing approach was applied to design fibres for (1) a femtosecond FOPO which can be pumped using a telecomm-band pump source at 1560 nm and generate nearly transform limited output around 880 nm with only 3 mm of fibre and a high pump power conversion efficiency of 43%, and (2) a SC source in mid-IR with a flat and near-zero dispersion from $2 \sim 3$ μm that can generate a glass-transmission-window limited broadband continuum with high coherence. Soft glasses were used for both fibres. Soft glasses provide MOFs a few orders of magnitude higher nonlinearity than silica glass as well as good transmission in mid-infrared which beyond the capability of silica glass. Soft glass had not been used for FOPOs before. In this work, soft glass was used for the first time as the fibre material for a FOPO.

The designed soft-glass MOFs was successfully fabricated after a few trials. According to calculations based on the SEM image of the MOFs, a flat and near-zero dispersion profile in the mid-infrared was achieved in the fabricated MOF. Due to fabrication distortion, the dispersion profile of the fabricated fibre was deviated from the design. But the fabricated fibre still showed three zero dispersion wavelengths (ZDWs) at 1.7, 2.7, 3.5 μm with a relative small variation in the dispersion value, 16 $ps/km/nm$ around zero, within the region of the 3 ZDWs. Simulations and experiments of short pulse broadening were performed with the fabricated fibres. The results showed extensive broad SC spectra and when the simulation was compared to the experimental results, qualitative agreements were observed which indicates that with a good structure designing algorithm, such as a genetic algorithm, soft-glass MOFs are a good platform for nonlinear applications especially for those require high compactness and operating in the mid-infrared wavelength regime.

In the second part of the thesis, Kerr nonlinearity and nonlinear polarisation interactions were studied within a VNPP model. The VNPP model predicts that in HS waveguides, larger non-transverse field components exist in guided modes. These non-transverse field components are the sources of new types of interactions between different modes which do not show in the scalar model. The VNPP model also

predicts significant higher Kerr nonlinearity in HS waveguides than the prediction of the scalar model.

To validate the VNPP model, an experiment was set up to measure the nonlinear coefficient in a suspended core fibre which is a typical example of a HS waveguide. A range of suspended core fibres with core diameters around 500 nm were fabricated using Bismuth glass. A CW SPM method was used to measure the nonlinear coefficients. The measured data were compared to both VNPP and the scalar model and good agreements were observed between experiment and VNPP model's prediction which indicated that the VNPP model itself is accurate.

The study of VNPP model based nonlinear polarisation interaction revealed that HS waveguides are capable of showing anisotropic nonlinear behaviours even when the materials of the waveguides are isotropic. This discovery opened the possibilities of observing novel nonlinear polarisation behaviours in HS waveguides which is crucial element polarisation dependent or sensitive nonlinear processes such as FWM and SC generation in HS waveguides.

14.2 Future work

For future work, the following elements may be considered. First of all, the direct measurement of fibre dispersion profiles, measurements of the pulse spectra to at least 4 μm and measurements of the coherence of the SC spectra are the most important works need to be done next. Dispersion measurement can be challenging due to the multimode nature and the low dispersion value of the fibres. However, by effectively removing the high order modes such as banding the fibres and splice the fibres to standard single mode fibres to increase dispersion slope and dispersion value, the dispersion of the fibres are likely to be measured. To measure the extended spectra of the pulses requires a different detector. The low repetition rate the pump laser used in this work limited the detector's ability to detect the signals. A different pump source may be considered for future work. Coherence measurement

also requires a new detection system.

The constructions of FOPOs using the fabricated fibres are also of interest for future work. The SC measurement made in this work indicated the existence of FWM parametric processes in the fabricated fibres. With an external cavity, the FWM processes in the fibres are likely to be enhanced and tune the fibres into tunable FOPOs.

For future work, the fabrication accuracy of the designed fibre is needed to be refined. In this work, approximately 10% average distortion were observed in the structure. Because of this distortion, simulations showed that the coherence of the SC generation in the fabricated fibres are reduced. The key to improve the fabrication accuracy is to find the best temperature for the preform extrusion process.

For fibre design, the fitness function in the GA for optimising the FOPO was based on the small signal gain of degenerate FWM which assumes the signal power is much lower than the pump and the pump has a narrow band and does not deplete. However, in practice, when femtosecond pump pulses were considered, the pump line width is around 50 nm at 20 dB below the peak. Also, as the power in the signal pulse increases, the gain at signal wavelength and the FWM phase mismatch change with power. In the future work, these aspects can also be considered as part of the fitness function.

In the work of designing fibre for coherent broadband SC generation, a hybrid GA approach was used. The quality of the final fibre design highly depends on the simplified model used in the hybrid GA. In this work, only the first order dispersion and nonlinearity are considered in the simplified model. Although the outcome of the GA reached our design target, the design can still be improved. In wavelength regimes where the material dispersion dominates the overall fibre dispersion, high order dispersion terms are needed to be considered into fitness function to counter the effects these terms bring into the pulse broadening process, especially the effects on coherence degradation.

The initial fibre structure used in GA can be simplified, which was performed before fabrication. However, in general it is better to simplify the initial structure before running GA. From the experience of this work, we know that the outer ring of the initial structure is unnecessary, and the inner-most ring of holes can be set to the same size. To modify these features for future fibre design work can significantly improve GA's efficiency since we reduce GA's free parameters from 6 to 4.

For the future work of the second part of the thesis, the exploration of the effects of high-order dispersion, loss and Raman effects on the polarisation including those steady state solutions are important for moving the theory towards practice. Developing a general full vectorial nonlinear Schrödinger equation will be the next following step. When this is done, the current state-of-art nonlinear applications including FOPOs and SC generation sources can be reassessed. It is likely there will be new opportunities for soft-glass MOFs to perform in the nonlinear area.

On the experimental side, works with regard to the nonlinear polarisation, such as an optical polarisation switch, can be demonstrated. Especially the power switch purposed in Chapter 12, it does not require a stable pump laser as long as the polarisation of the light can be guaranteed. Although the fibre fabrication required for this work is challenging due to the need of zero birefringence, the device is still likely to be demonstrated with a tunable laser source.

Appendix A

Appendices

A.1 Nonlinear response function

The nonlinear response function $R(t)$ in the general nonlinear Schrödinger equation Eq. 2.1.17 is an important feature for describing Raman effects. An accurate form of nonlinear response function is needed especially when the pump has a short pulse duration (sub-picosecond to femtosecond). This is because that certain nonlinear processes such as Raman effects are retarded in time, and the delays are at order of 10s of femtosecond, which are significant for short pulses. The nonlinear response function is responsible for both spontaneous and stimulated Raman scattering as well as Raman solitons.

The nonlinear response function can be expressed in the form [5]

$$R(t) = (1 - f_R)\delta(t) + f_R h_R(t), \tag{A.1.1}$$

where f_R is the Raman fraction and $h_R(t)$ is Raman response function. The first term represents instantaneous nonlinear effects and the second term represents delayed effects. Previously, in silica glass, f_R is estimated by using the peak value of the Raman gain [5]. However, this is not accurate for glasses with multiple peaks in Raman gain. In this work, the Raman fraction f_R is calculated through an integration over the Raman gain spectrum. According to Ref.[203], the complex nonlinear

refractive index can be expressed as

$$N_2(\Omega) = f_R N_2(0)\tilde{h}_R(\Omega) \tag{A.1.2}$$

where $\Omega = \omega - \omega_0$, $N_2(0) = n_2(\omega_0)$. The imaginary part of the nonlinear refractive index $N_2(\Omega)$ can be expressed in terms of Raman gain [203],

$$Im(N_2(\Omega)) = \frac{\lambda_0 g(\Omega)}{4\pi} \tag{A.1.3}$$

using the Kramers-Kronig relations, we can obtain the real part of $N_2(\Omega)$ and express $N_2(\Omega)$ as

$$N_2(\Omega) = (\frac{\lambda_0}{4\pi}\frac{1}{\pi}\mathcal{P}\int_{-\infty}^{\infty} d\Omega\prime \frac{g(\Omega)}{\Omega\prime - \Omega}) + i(\frac{g(\Omega)\lambda_0}{4\pi}) \tag{A.1.4}$$

where $\mathcal{P}$ is the Cauchy principle value. Taking the inverse Fourier transform on Eq. (A.1.2) and then integrate over t on both side, and recall $\int_0^\infty h_R(t)dt = 1$, therefore one can obtain

$$h_R(t) = \frac{\mathcal{F}^{-1}(N_2(\Omega))}{\int_0^\infty \mathcal{F}^{-1}(N_2(\Omega))dt}, \tag{A.1.5}$$

$$f_R = \frac{\int_0^\infty \mathcal{F}^{-1}(N_2(\Omega))dt}{N_2(0)}. \tag{A.1.6}$$

Notice the symmetry of the real part and the antisymmetry of the imaginary part of N_2, the outcome of the integral f_R is real.

In this thesis, a type of tellurite glass ($70TeO_2 - 10Na_2O - 20ZnF_2$) [145] is used in fibre design. Its Raman response function and Raman fraction are calculated using the approach presented here. The Raman gain spectrum of the tellurite glass as shown in Fig. 1.1.1. The Raman fraction f_R is calculated to be 0.064 for this composition of glass. Although this value is about 3 times smaller than that of silica glass (0.18), the fact that the nonlinear refractive index n_2 of this tellurite glass ($5.9 \times 10^{-19} m^2/W$) is much higher than silica glass ($2.36 \times 10^{-20} m^2/W$) [204] results in much higher Raman response ($\gamma f_R h_R(t)$) for tellurite glass than silica glass.

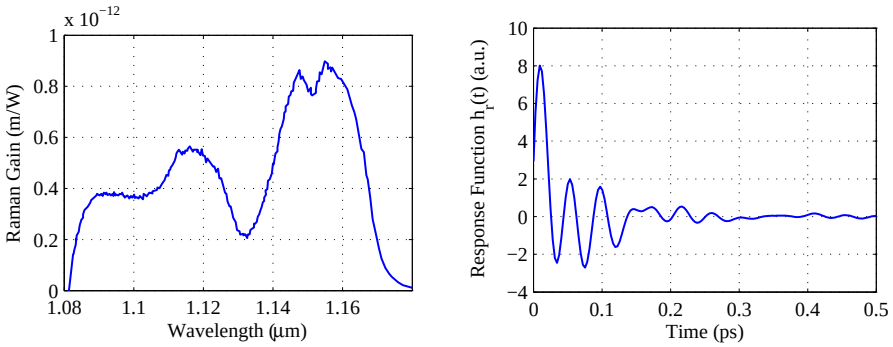

Figure 1.1.1: Raman gain spectrum of $70TeO_2 - 10Na_2O - 20ZnF_2$ glass, pumped at 1060nm [145] (left) and calculated Raman response function using the maximum Raman gain at 1155nm (right)

A.2 M^2 measurement

M^2 is a quantity that is commonly used to describe the degree of variation of an actual beam from an ideal Gaussian beam at the same wavelength. An ideal TEM00 mode has M^2 equal to 1. Any actual beam will have M^2 greater than 1.

M^2 can be measured indirectly by measuring the divergence of the beam. Focusing a collimated beam and measuring its width change across the minimum, the width data along the propagating direction will then form a quadratic curve from which M^2 is calculated. This method also requires a beam width calculation based on the second-moment definition. The second moment of the beam intensity profile I(x,y) can be described by Eq. A.2.1

$$\sigma_n^2 = \frac{\int_{-\infty}^{\infty}(n-n_0)^2 I(x,y)dxdy}{\int_{-\infty}^{\infty} I(x,y)dxdy} \tag{A.2.1}$$

where $n = x$ or y. The second-moment-based beam width is defined as $W_n = 2\sigma_n$. With this definition, the beam width W_n follows the following rule during propagation in free space.

$$W_n^2(z) = W_{0n}^2 + M_n^4 \left(\frac{\lambda}{\pi W_{0n}}\right)^2 (z - z_{0n})^2 \tag{A.2.2}$$

where λ is wavelength. M^2 can be extracted by fitting the polynomial Eq. A.2.2 to the experiment data.

The measurement setup is the same as the one shown in Fig.8.2.1. The only change is instead of project the image of the fiber output on the camera directly, the image plane was set approximately 30 cm away from the output lens (Thorlabs 355390-C). The measurement was performed at 1750 nm. The focal length of the lens is approximate 2.8 mm which results in an image with approximately 0.64 cm in diameter. During the measurement, the camera was moving along the beam from 12 cm in front of the image plane to 12 cm behind. The beam profiles were taken for every 2 cm.

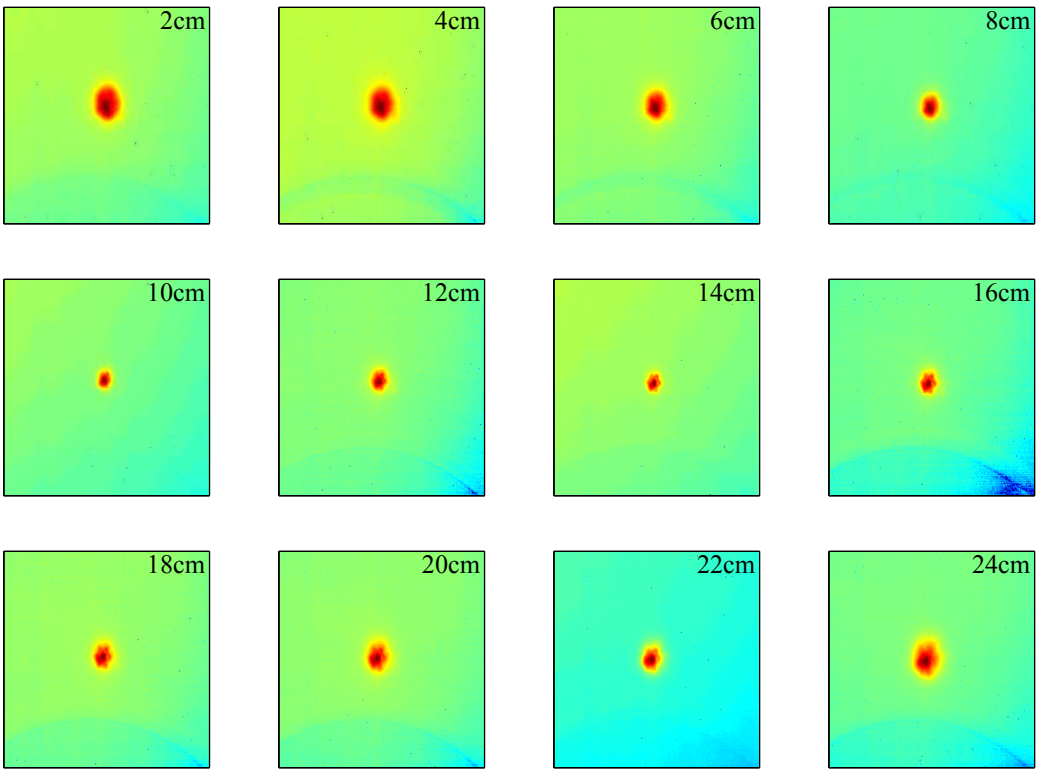

Figure 1.2.1: Beam profiles of the fiber output along the propagation direction.

Fig. 1.2.1 shows the recorded beam profiles taken during the experiment. In these plots blue represents minimum values and red represents maximum values. As one can see that all images show significant noise which comes from the background light detected by the camera. The second-moment definition can be applied to arbitrary

beams but under the influences of the noise it is difficult to determine the beam width. To remove the background noise additional data process is required before M^2 can be calculated.

We first sample the four corners of each image (Fig. 1.2.2a) and then use the data to interpolate the background noise (Fig. 1.2.2b). Once the DC component of the noise is removed (Fig. 1.2.2c), a Fourier transform is applied to the image (Fig. 1.2.2d). In the Fourier space, we manually set a threshold of 1% of the maximum intensity and remove any data below that threshold, which removes all high frequency components (Fig. 1.2.2e). At last we inverse transform the image back to the spacial domain to obtain refined images (Fig. 1.2.2f).

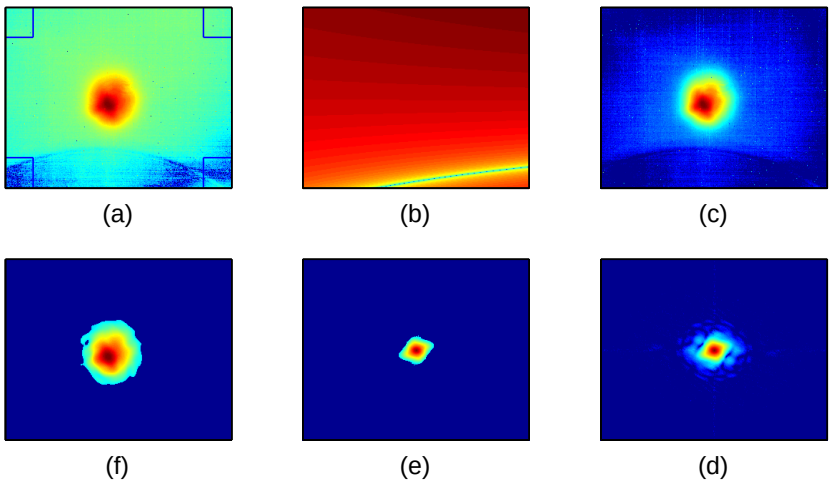

Figure 1.2.2: Image processing process of the recorded beam profiles. (a) Original image. (b) Interpolated mean noise background. (c) Image with removed noise. (d) Fourier transform of the image in (c). (e) Background noise and high frequency components are removed in frequency domain. (f) Processed image transformed back to spacial domain.

Fig. 1.2.3 shows the processed images in the same order as in Fig. 1.2.1. Applying the second-moment calculation to these new images and fitting the beam width with quadratic function, M^2 values can be extracted.

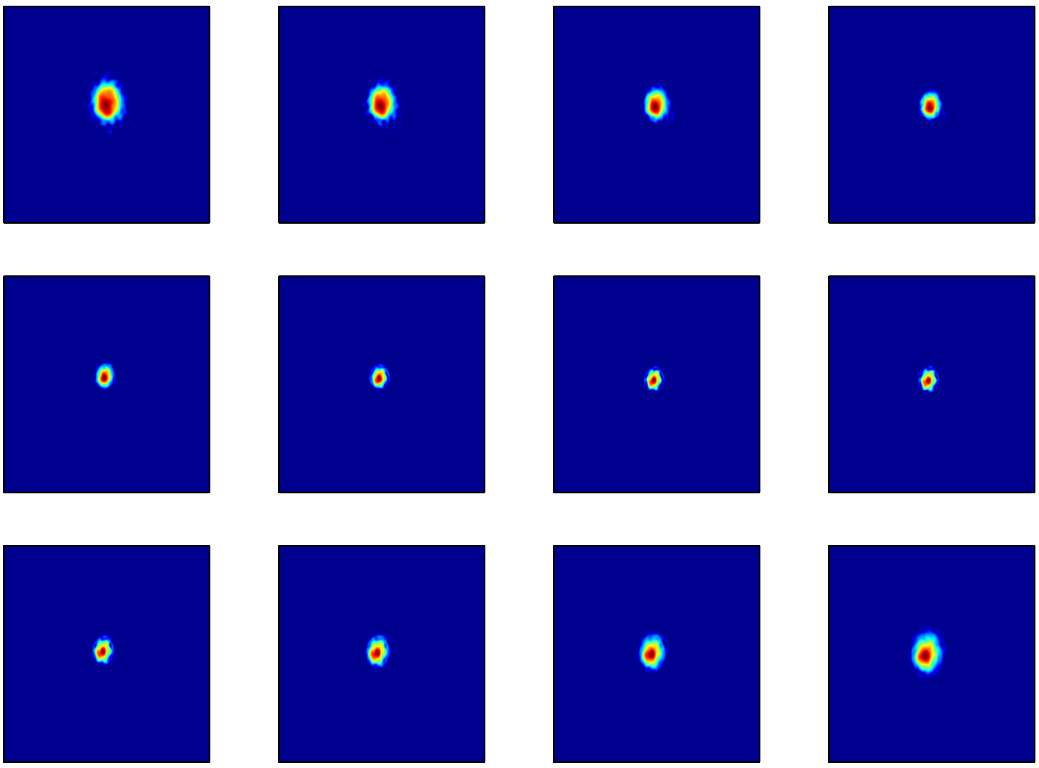

Figure 1.2.3: Processed beam profiles of the fiber output along the propagation direction.

Fitting the beam width in x and y directions separately with quadratic functions, we get M^2 for x and y: $M_x^2 = 15.1 \pm 0.2$ and $M_y^2 = 13.8 \pm 0.2$. The M^2 values indicate that the fibre is highly multimode and it matches our prediction in Chapter 7 which shows 49 core modes supported in the fibre.

A.3 Theory of Kerr nonlinearity measurement

The nonlinearity of a fiber can be measured using continuous-wave (CW) self-phase modulation (SPM) method [205]. In this method, two CW lasers are co-polarised and launched in the fiber under test (FUT). Due to nonlinearity of the FUT, sidebands can be generated and they increases as pump power increases. Through measuring the intensity relation between pumps and sidebands, nonlinear phase can

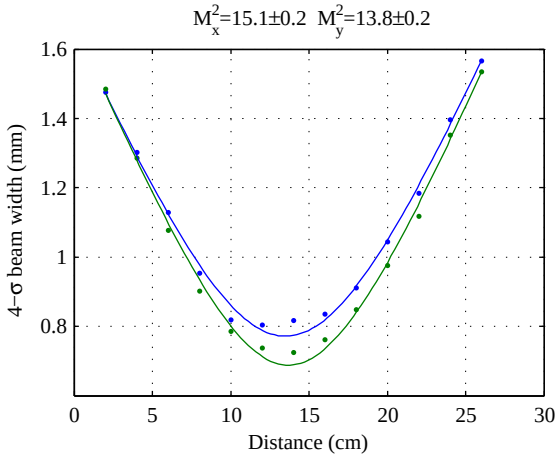

Figure 1.2.4: Polynomial fits of the 4-σ beam width in x and y direction versus propagation distance.

be derived as well as the nonlinear coefficient.

The measurement based on two key assumptions.

1. the wavelength separation is small ($< 1nm$) that it allow us to ignore the dispersion,

2. only SPM is considered during the propagation.

Based on these two assumptions, the nonlinear process in the FUT can be described using the Eq. A.3.1.

$$\frac{\partial}{\partial z}a(z,t) + \frac{\alpha}{2}a(z,t) = i\gamma_\nu \left|a(z,t)\right|^2 a(z,t). \tag{A.3.1}$$

If we define a normalised amplitude U as

$$a(z,t) = \sqrt{P_0}e^{-\alpha z/2}U(z,t), \tag{A.3.2}$$

where P_0 is peak power and the exponential term count for loss, we can obtain

$$\frac{\partial U}{\partial z} = i\gamma P_0 e^{-\alpha z}\left|U\right|^2 U. \tag{A.3.3}$$

Note that in this definition, U is normalised to its peak and therefore $U|_{t=0} = 1$. This equation has a solution

$$U(L,T) = U(0,T)e^{i|U(0,T)|^2\phi_{SPM}}, \tag{A.3.4}$$

$$\phi_{SPM} = \gamma P_0 L_{\text{eff}}. \tag{A.3.5}$$

where L_{eff} is a effective length when the fiber is lossy. The effective length is a length at which the nonlinear phase of a pulse accumulated in a lossless fibre is equivalent to the nonlinear phase of the same pulse accumulated in a lossy fibre. Mathematically we have

$$P_0 L_{\text{eff}} = \int_{l=0}^{L} P_0 e^{-\alpha l} dl, \tag{A.3.6}$$

which lead to,

$$L_{\text{eff}} = \frac{1 - e^{-\alpha L}}{\alpha}. \tag{A.3.7}$$

The key to obtain the nonlinear coefficient γ is to calculate ϕ_{SPM}. When two CW laser with different frequencies are presented, $U(0,T) = Ae^{i\omega_1 T} + Be^{i\omega_2 T}$. Insert $U(0,T)$ into Eq. A.3.4, the dual frequency solution can be written as

$$U(L,T) = \left(Ae^{i\omega_1 T} + Be^{i\omega_2 T}\right) e^{i\left|Ae^{i\omega_1 T} + Be^{i\omega_2 T}\right|^2 \phi_{\text{SPM}}}. \tag{A.3.8}$$

If ω_0 is defined as the middle frequency between ω_1 and ω_2 with equal separation of $\Delta\omega$, then one can write $\omega_1 = \omega_0 - \Delta\omega$ and $\omega_2 = \omega_0 + \Delta\omega$. Eq.A.3.8 can be simplified to

$$U(L,T) = e^{i(A^2+B^2)\phi_{\text{SPM}}} \cdot e^{2iAB\cos(2T\Delta\omega)\phi_{\text{SPM}}} \cdot e^{-iT(\Delta\omega-\omega_0)} \cdot (A + Be^{2iT\Delta\omega}), \tag{A.3.9}$$

among which the second exponential term can be expressed in terms of Bessel functions of the first kind using Jacobi-Anger expansion [206],

$$e^{2iAB\cos(2T\Delta\omega)\phi_{\text{SPM}}} = \sum_{n=-\infty}^{\infty} i^n J_n(2AB \cdot \phi_{\text{SPM}}) e^{2inT\Delta\omega}. \tag{A.3.10}$$

Substituting Eq.A.3.10 into Eq.A.3.9 and expanding it according to different frequencies, one can get the coefficients in front of $e^{iT(\omega_0-\Delta\omega)}$, $e^{iT(\omega_0+\Delta\omega)}$, $e^{iT(\omega_0-3\Delta\omega)}$ and $e^{iT(\omega_0+3\Delta\omega)}$ as shown in Eqs. A.3.11∼A.3.14, which are corresponding to the field amplitudes of two pumps and the first pair of side bands next to the pumps

respectively.

$$C_{\omega_1} = [AJ_0(2AB \cdot \phi_{\text{SPM}}) + iBJ_1(2AB \cdot \phi_{\text{SPM}})]e^{i(A^2+B^2)\phi_{\text{SPM}}} \quad \text{(A.3.11)}$$

$$C_{\omega_2} = [BJ_0(2AB \cdot \phi_{\text{SPM}}) + iAJ_1(2AB \cdot \phi_{\text{SPM}})]e^{i(A^2+B^2)\phi_{\text{SPM}}} \quad \text{(A.3.12)}$$

$$C_{\omega_1-2\Delta\omega} = [iAJ_1(2AB \cdot \phi_{\text{SPM}}) - BJ_2(2AB \cdot \phi_{\text{SPM}})]e^{i(A^2+B^2)\phi_{\text{SPM}}} \quad \text{(A.3.13)}$$

$$C_{\omega_2+2\Delta\omega} = [iBJ_1(2AB \cdot \phi_{\text{SPM}}) - AJ_2(2AB \cdot \phi_{\text{SPM}})]e^{i(A^2+B^2)\phi_{\text{SPM}}} \quad \text{(A.3.14)}$$

From these coefficients, the power of the field at these frequencies can also be obtained

$$I_{\omega_1} = A^2J_0^2(2AB \cdot \phi_{\text{SPM}}) + B^2J_1^2(2AB \cdot \phi_{\text{SPM}}), \quad \text{(A.3.15)}$$

$$I_{\omega_2} = B^2J_0^2(2AB \cdot \phi_{\text{SPM}}) + A^2J_1^2(2AB \cdot \phi_{\text{SPM}}), \quad \text{(A.3.16)}$$

$$I_{\omega_1-2\Delta\omega} = A^2J_1^2(2AB \cdot \phi_{\text{SPM}}) + B^2J_2^2(2AB \cdot \phi_{\text{SPM}}), \quad \text{(A.3.17)}$$

$$I_{\omega_2+2\Delta\omega} = B^2J_1^2(2AB \cdot \phi_{\text{SPM}}) + A^2J_2^2(2AB \cdot \phi_{\text{SPM}}). \quad \text{(A.3.18)}$$

If equal mount of power are using for the two pump lasers, and recall U is normalised to its peak. Therefore, at $T = 0$, we have $U = A + B = 2A = 1$, $A = B = \frac{1}{2}$. The ratio of pump and side band power can be expressed as

$$r = \frac{I_{\omega_1}}{I_{\omega_1-2\Delta\omega}} = \frac{J_0^2\left(\frac{\phi_{\text{SPM}}}{2}\right) + J_1^2\left(\frac{\phi_{\text{SPM}}}{2}\right)}{J_1^2\left(\frac{\phi_{\text{SPM}}}{2}\right) + J_2^2\left(\frac{\phi_{\text{SPM}}}{2}\right)} \quad \text{(A.3.19)}$$

from which ϕ_{SPM} can be solved numerically. Once ϕ_{SPM} is known, γ can be calculated through Eq.A.3.5, i.e.

$$\gamma = \frac{\phi_{\text{SPM}}}{P_0L_{\text{eff}}} = \frac{\phi_{\text{SPM}}}{2P_{\text{avg}}L_{\text{eff}}}, \quad \text{(A.3.20)}$$

where P_{avg} is the average power measured in experiment, and $P_0 = 2P_{\text{avg}}$.

A.4 Stability analysis of the VNPP model

A stability analysis of SSSs Eqs. 12.3.7&12.3.8 can be performed by applying a small perturbation about the SSS Eq. 12.3.7. Set

$$v = \frac{a-1}{2(b-1)} + \epsilon, \quad \theta = 2n\pi + \eta, n = 0, 1, \cdots \quad \text{(A.4.1)}$$

then Eqs. 12.3.6 reduce to

$$\begin{aligned}\dot{\epsilon} &= 2(b-1)\eta + O(\epsilon^2),\\ \dot{\eta} &= -\frac{(a-1)(a+1-2b)}{4(b-1)^2}\epsilon + O(\eta\epsilon) + O(\epsilon^3) + O(\eta^3)\end{aligned} \tag{A.4.2}$$

Stability is therefore determined by the equation $\dot{x} = Ax$ where $x = \begin{pmatrix}\epsilon\\ \eta\end{pmatrix}$ and

$$A = \begin{pmatrix} 0 & 2(b-1)\\ -\dfrac{(a-1)(a+1-2b)}{4(b-1)^2} & 0\end{pmatrix}. \tag{A.4.3}$$

The eigenvalues of A are

$$\pm\sqrt{\frac{(a-1)(a+1-2b)}{a(b-1)}}. \tag{A.4.4}$$

If these eigenvalues are real then these fixed points are unstable saddle points, otherwise these eigenvalues are imaginary and the fixed points are stable. In this case, the fixed points in the red region of Fig.12.3.1a are unstable, the ones in the green region are stable. Similar analysis can also be applied to SSS 12.3.8 which reveals that the fixed points in the orange region of Fig.12.3.1b are unstable and the ones in yellow region are stable.

The stable fixed points mean that even with fluctuations, the solutions are still confined and remain relative steady. On the contrary, for the unstable fixed points, even the smallest fluctuations can dramatically alter the polarisation behaviour of the fields. Some preliminary numerical results show that the polarisation states of unstable SSSs actually behave periodically as the fields propagate.

With the scalar model, one has $\gamma_1 = \gamma_2 = \gamma$ $\gamma_c = 2/3\gamma$ and $\gamma_c' = 1/3\gamma$. These relations lead to constant $b = 1$ and $a = -\dfrac{3}{4}\dfrac{\Delta\beta}{\gamma P_0} + \dfrac{1}{2}$. For two initial conditions ($\cos\theta = 1$ and $\cos\theta = -1$), following results can be obtained:

1. To have SSSs with linear input polarisations ($\cos\theta = 1$), b cannot be equal to 1, which means all the parameter space for both stable and unstable SSSs with this type of initial conditions.

2. To have SSSs with circular/elliptical polarisations ($\cos\theta = -1$), $b = 1$ lead to

$$v = \frac{P_1}{P_0} = \frac{a+1}{2(b+1)} = -\frac{3\Delta\beta}{4\gamma P_0} + \frac{1}{2}, \tag{A.4.5}$$

$$P_2 - P_1 = \frac{3}{2}\frac{\Delta\beta}{\gamma}. \tag{A.4.6}$$

On the contrary, with the VNPP model, the parameter space for achieving SSSs has been greatly expanded. Furthermore, for both linearly and circularly/elliptically polarised inputs, stable and unstable SSSs regions are found.

Bibliography

[1] S. Kumar, *Impact of Nonlinearities on Fiber Optic Communications* (Springer, 2011), 1st ed.

[2] G. P. Agrawal, *Applications of nonlinear fiber optics* (Academic Press, 2008).

[3] D. Woods and T. J. Naughton, "Optical computing," Applied Mathematics and Computation **215**, 1417–1430 (2009).

[4] J. L. O'Brien, "Optical quantum computing," Science **318**, 1567–1570 (2007).

[5] G. Agrawal, *Nonlinear Fiber Optics* (Academic Press, 2001), 3rd ed.

[6] P. M. Morse and H. Feshbach, *Methods of Theoretical Physics, Part II* (Mcgraw-Hill College, 1953), 1st ed.

[7] K. Blow and D. Wood, "Theoretical description of transient stimulated raman scattering in optical fibers," Quantum Electronics, IEEE Journal of **25**, 2665–2673 (1989).

[8] N. Karasawa, S. Nakamura, N. Nakagawa, M. Shibata, R. Morita, H. Shigekawa, and M. Yamashita, "Comparison between theory and experiment of nonlinear propagation for a-few-cycle and ultrabroadband optical pulses in a fused-silica fiber," IEEE JOURNAL OF QUANTUM ELECTRONICS **37**, 398–404 (2001).

[9] J. Hansryd, P. A. Andrekson, M. Westlund, J. Li, and P. O. Hedekvist, "Fiber-based optical parametric amplifiers and their applications," IEEE Journal of Selected Topics in Quantum Electronics **8**, 506–520 (2002).

[10] M. Fiorentino, P. L. Voss, J. E. Sharping, and P. Kumar, "All-fiber photon-pair source for quantum communications," IEEE Photonics Technology Letters **14**, 983–985 (2002).

[11] S. Kaasalainen, T. Lindroos, and J. Hyyppa, "Toward hyperspectral lidar: Measurement of spectral backscatter intensity with a supercontinuum laser source," IEEE GEOSCIENCE AND REMOTE SENSING LETTERS **4**, 211–215 (2007).

[12] C. Colley, J. Hebden, D. Delpy, A. Cambrey, R. Brown, E. Zibik, W. Ng, L. Wilson, and J. Cockburn, "Mid-infrared optical coherence tomography," REVIEW OF SCIENTIFIC INSTRUMENTS **78** (2007).

[13] J. Hult, R. S. Watt, and C. F. Kaminski, "High bandwidth absorption spectroscopy with a dispersed supercontinuum source," OPTICS EXPRESS **15**, 11385–11395 (2007).

[14] K. Shi, P. Li, and Z. Liu, "Broadband coherent anti-Stokes raman scattering spectroscopy in supercontinuum optical trap," APPLIED PHYSICS LETTERS **90** (2007).

[15] H. Kano and H.-o. Hamaguchi, "Coherent raman imaging of human living cells using a supercontinuum light source," JAPANESE JOURNAL OF APPLIED PHYSICS PART 1-REGULAR PAPERS BRIEF COMMUNICATIONS & REVIEW PAPERS **46**, 6875–6877 (2007).

[16] D. Pestov, X. Wang, G. Ariunbold, R. Murawski, V. Sautenkov, A. Dogariu, A. Sokolov, and M. Scully, "Single-shot detection of bacterial endospores via coherent raman spectroscopy," PROCEEDINGS OF THE NATIONAL

ACADEMY OF SCIENCES OF THE UNITED STATES OF **105**, 422–427 (2008).

[17] S. Diddams, D. Jones, J. Ye, S. Cundiff, J. Hall, J. Ranka, R. Windeler, R. Holzwarth, T. Udem, and T. Hnsch, "Direct link between microwave and optical frequencies with a 300 THz femtosecond laser comb," Physical Review Letters **84**, 5102–5105 (2000).

[18] D. J. Jones, "Carrier-Envelope phase control of femtosecond Mode-Locked lasers and direct optical frequency synthesis," Science **288**, 635–639 (2000).

[19] R. H. Stolen, "Phase-matched three-wave mixing in silica fiber optical waveguides," Applied Physics Letters **24**, 308 (1974).

[20] K. O. Hill, B. S. Kawasaki, Y. Fujii, and D. C. Johnson, "Efficient sequence-frequency generation in a parametric fiber-optic oscillator," Applied Physics Letters **36**, 888 (1980).

[21] M. Ohashi, "Phase-matched light amplification by three-wave mixing process in a birefringent fiber due to externally applied stress," Applied Physics Letters **41**, 1111 (1982).

[22] S. Trillo and S. Wabnitz, "Parametric and raman amplification in birefringent fibers," Journal of the Optical Society of America B **9**, 1061–1082 (1992).

[23] M. E. Marhic, N. Kagi, T. Chiang, and L. G. Kazovsky, "Broadband fiber optical parametric amplifiers," Optics Letters **21**, 573–575 (1996).

[24] K. Inoue, "Polarization independent wavelength conversion using fiber four-wave mixing with two orthogonal pump lights of different frequencies," Journal of Lightwave Technology **12**, 1916–1920 (1994).

[25] S. Radic and C. J. McKinstrie, "Two-pump fiber parametric amplifiers," Optical Fiber Technology **9**, 7–23 (2003).

[26] K. Washio, K. Inoue, and S. Kishida, "Efficient large-frequency-shifted three-wave mixing in low dispersion wavelength region in single-mode optical fibre," Electronics Letters **16**, 658–660 (1980).

[27] C. T. Chang, "Minimum dispersion in a single-mode step-index optical fiber," Applied Optics **18**, 2516–2522 (1979).

[28] M. Yu, C. J. McKinstrie, and G. P. Agrawal, "Modulational instabilities in dispersion-flattened fibers," Physical Review E **52**, 1072 (1995).

[29] G. A. Nowak, Y. Kao, T. J. Xia, M. N. Islam, and D. Nolan, "Low-power high-efficiency wavelength conversion based on modulational instability in high-nonlinearity fiber," Optics Letters **23**, 936–938 (1998).

[30] T. Tanemura, C. S. Goh, K. Kikuchi, and S. Y. Set, "Highly efficient arbitrary wavelength conversion within entire c-band based on nondegenerate fiber four-wave mixing," IEEE Photonics Technology Letters **16**, 551–553 (2004).

[31] K. K. Wong, M. E. Marhic, K. Uesaka, and L. G. Kazovsky, "Polarization-independent two-pump fiber optical parametric amplifier," IEEE Photonics Technology Letters **14**, 911–913 (2002).

[32] J. Lu, L. Chen, Z. Dong, Z. Cao, and S. Wen, "Polarization insensitive wavelength conversion based on orthogonal pump Four-Wave mixing for polarization multiplexing signal in High-Nonlinear fiber," Journal of Lightwave Technology **27**, 5767–5774 (2009).

[33] M. Nakazawa, K. Suzuki, and H. A. Haus, "Modulational instability oscillation in nonlinear dispersive ring cavity," Physical Review A **38**, 5193 (1988).

[34] J. E. Rothenberg, "Visible fibre modulational instability parametric oscillator," Electronics Letters **28**, 479–480 (1992).

[35] R. Leonhardt and J. D. Harvey, "Characteristics of a visible modulation instability fiber laser," IEEE Journal of Quantum Electronics **30**, 1463–1468 (1994).

[36] D. K. Serkland and P. Kumar, "Tunable fiber-optic parametric oscillator," Optics Letters **24**, 92–94 (1999).

[37] S. Saito, M. Kishi, and M. Tsuchiya, "Dispersion-flattened-fibre optical parametric oscillator for wideband wavelength-tunable ps pulse generation," Electronics Letters **39**, 86– 88 (2003).

[38] M. E. Marhic, K. K. Wong, L. G. Kazovsky, and T. Tsai, "Continuous-wave fiber optical parametric oscillator," Optics Letters **27**, 1439–1441 (2002).

[39] S. Coen, M. Haelterman, P. Emplit, L. Delage, L. M. Simohamed, and F. Reynaud, "Experimental investigation of the dynamics of a stabilized nonlinear fiber ring resonator," Journal of the Optical Society of America B **15**, 2283–2293 (1998).

[40] S. Coen, M. Haelterman, P. Emplit, L. Delage, L. M. Simohamed, and F. Reynaud, "Bistable switching induced by modulational instability in a normally dispersive all-fibre ring cavity," Journal of Optics B: Quantum and Semiclassical Optics **1**, 36–42 (1999).

[41] J. E. Sharping, M. Fiorentino, A. Coker, P. Kumar, and R. S. Windeler, "Four-wave mixing in microstructure fiber," Optics Letters **26**, 1048–1050 (2001).

[42] K. S. Abedin, J. T. Gopinath, E. P. Ippen, C. E. Kerbage, R. S. Windeler, and B. J. Eggleton, "Highly nondegenerate femtosecond four-wave mixing in tapered microstructure fiber," Applied Physics Letters **81**, 1384 (2002).

[43] A. Y. H. Chen, G. K. L. Wong, S. G. Murdoch, R. Leonhardt, J. D. Harvey, J. C. Knight, W. J. Wadsworth, and P. S. J. Russell, "Widely tunable optical

parametric generation in a photonic crystal fiber," Optics Letters **30**, 762–764 (2005).

[44] T. V. Andersen, K. M. Hilligsoe, C. K. Nielsen, J. Thgersen, K. P. Hansen, S. R. Keiding, and J. J. Larsen, "Continuous-wave wavelength conversion in a photonic crystal fiber with two zero-dispersion wavelengths," pp. 4113–4122 (2004).

[45] J. E. Sharping, M. Fiorentino, P. Kumar, and R. S. Windeler, "Optical parametric oscillator based on four-wave mixing in microstructure fiber," Optics Letters **27**, 1675–1677 (2002).

[46] J. D. Harvey, R. Leonhardt, S. Coen, G. K. L. Wong, J. Knight, W. J. Wadsworth, and P. St.J. Russell, "Scalar modulation instability in the normal dispersion regime by use of a photonic crystal fiber," Optics Letters **28**, 2225–2227 (2003).

[47] Y. Deng, Q. Lin, F. Lu, G. P. Agrawal, and W. H. Knox, "Broadly tunable femtosecond parametric oscillator using a photonic crystal fiber," Optics Letters **30**, 1234–1236 (2005).

[48] J. E. Sharping, M. A. Foster, A. L. Gaeta, J. Lasri, O. Lyngnes, and K. Vogel, "Octave-spanning, high-power microstructure-fiber-based optical parametric oscillators," Opt. Express **15**, 1474–1479 (2007).

[49] C. J. S. de Matos, J. R. Taylor, and K. P. Hansen, "Continuous-wave, totally fiber integrated optical parametric oscillatorusing holey fiber," Optics Letters **29**, 983–985 (2004).

[50] T. M. Monro and H. Ebendorff-Heidepriem, "Progress in microstructured optical fibers," Annual Review of Materials Research **36**, 467–495 (2006).

[51] J. H. V. Price, "Non-silica microstructured optical fibers for mid-IR supercontinuum generation from 2 m - 5 m," in "Proceedings of SPIE," (San Jose, CA, USA, 2006), pp. 61020A–61020A–15.

[52] J. Sharping, "Microstructure fiber based optical parametric oscillators," Lightwave Technology, Journal of **26**, 2184–2191 (2008).

[53] R. R. Alfano and S. L. Shapiro, "Emission in the region 4000 to 7000 å via Four-Photon coupling in glass," Physical Review Letters **24**, 584 (1970).

[54] R. R. Alfano and S. L. Shapiro, "Observation of Self-Phase modulation and Small-Scale filaments in crystals and glasses," Physical Review Letters **24**, 592 (1970).

[55] J. M. Dudley, G. Genty, and S. Coen, "Supercontinuum generation in photonic crystal fiber," Reviews of Modern Physics **78**, 1135–1184 (2006).

[56] C. Lin and R. H. Stolen, "New nanosecond continuum for excited-state spectroscopy," Applied Physics Letters **28**, 216 (1976).

[57] A. Hasegawa, "Transmission of stationary nonlinear optical pulses in dispersive dielectric fibers. i. anomalous dispersion," Applied Physics Letters **23**, 142 (1973).

[58] L. F. Mollenauer, R. H. Stolen, and J. P. Gordon, "Experimental observation of picosecond pulse narrowing and solitons in optical fibers," Physical Review Letters **45**, 1095 (1980).

[59] J. Satsuma and N. Yajima, "B. initial value problems of One-Dimensional Self-Modulation of nonlinear waves in dispersive media," Progress of Theoretical Physics Supplement **55**, 284–306 (1974).

[60] R. H. Stolen, L. F. Mollenauer, and W. J. Tomlinson, "Observation of pulse

restoration at the soliton period in optical fibers," Optics Letters **8**, 186–188 (1983).

[61] L. F. Mollenauer, R. H. Stolen, J. P. Gordon, and W. J. Tomlinson, "Extreme picosecond pulse narrowing by means of soliton effect in single-mode optical fibers," Optics Letters **8**, 289–291 (1983).

[62] J. P. Gordon, "Theory of the soliton self-frequency shift," Optics Letters **11**, 662–664 (1986).

[63] F. M. Mitschke and L. F. Mollenauer, "Discovery of the soliton self-frequency shift," Optics Letters **11**, 659–661 (1986).

[64] P. K. A. Wai, C. R. Menyuk, Y. C. Lee, and H. H. Chen, "Nonlinear pulse propagation in the neighborhood of the zero-dispersion wavelength of monomode optical fibers," Optics Letters **11**, 464–466 (1986).

[65] Y. Kodama and A. Hasegawa, "Nonlinear pulse propagation in a monomode dielectric guide," IEEE Journal of Quantum Electronics **23**, 510– 524 (1987).

[66] E. A. Golovchenko, E. M. Dianov, A. M. Prokhorov, and V. N. Serkin, "Decay of optical solitons," JETP Lett **42**, 87–91 (1985).

[67] P. Beaud, W. Hodel, B. Zysset, and H. Weber, "Ultrashort pulse propagation, pulse breakup, and fundamental soliton formation in a single-mode optical fiber," IEEE Journal of Quantum Electronics **23**, 1938– 1946 (1987).

[68] J. Schtz, W. Hodel, and H. Weber, "Nonlinear pulse distortion at the zero dispersion wavelength of an optical fibre," Optics Communications **95**, 357–365 (1993).

[69] A. S. Gouveia-Neto, M. E. Faldon, and J. R. Taylor, "Solitons in the region of the minimum group-velocity dispersion of single-mode optical fibers," Optics Letters **13**, 770–772 (1988).

[70] M. N. Islam, G. Sucha, I. Bar-Joseph, M. Wegener, J. P. Gordon, and D. S. Chemla, "Broad bandwidths from frequency-shifting solitons in fibers," Optics Letters **14**, 370–372 (1989).

[71] M. N. Islam, G. Sucha, I. Bar-Joseph, M. Wegener, J. P. Gordon, and D. S. Chemla, "Femtosecond distributed soliton spectrum in fibers," Journal of the Optical Society of America B **6**, 1149–1158 (1989).

[72] M. Nakazawa, K. Suzuki, H. Kubota, and H. A. Haus, "High-order solitons and the modulational instability," Physical Review A **39**, 5768 (1989).

[73] E. M. Dianov, A. Y. Karasik, P. V. Mamyshev, A. M. Prokhorov, V. N. Serkin, M. F. Stel'Makh, and A. A. Fomichev, "Stimulated-Raman conversion of multisoliton pulses in quartz optical fibers," Soviet Journal of Experimental and Theoretical Physics Letters **41**, 294 (1985).

[74] K. Tai, A. Hasegawa, and N. Bekki, "Fission of optical solitons induced by stimulated raman effect," Optics Letters **13**, 392–394 (1988).

[75] Y. Silberberg, "Solitons and two-photon absorption," Optics Letters **15**, 1005–1007 (1990).

[76] T. Morioka, K. Mori, and M. Saruwatari, "More than 100-wavelength-channel picosecond optical pulse generation from single laser source using supercontinuum in optical fibres," Electronics Letters **29**, 862–864 (1993).

[77] T. Morioka, S. Kawanishi, K. Mori, and M. Saruwatari, "Nearly penalty-free, <4 ps supercontinuum gbit/s pulse generation over 1535-1560 nm," Electronics Letters **30**, 790–791 (1994).

[78] M. Nakazawa, K. Tamura, H. Kubota, and E. Yoshida, "Coherence degradation in the process of supercontinuum generation in an optical fiber," Optical Fiber Technology **4**, 215–223 (1998).

[79] H. Kubota, K. R. Tamura, and M. Nakazawa, "Analyses of coherence-maintained ultrashort optical pulse trains and supercontinuum generation in the presence of soliton-amplified spontaneous-emission interaction," Journal of the Optical Society of America B **16**, 2223–2232 (1999).

[80] G. A. Nowak, J. Kim, and M. N. Islam, "Stable supercontinuum generation in short lengths of conventional Dispersion-Shifted fiber," Applied Optics **38**, 7364–7369 (1999).

[81] T. M. Monro, D. J. Richardson, N. G. Broderick, and P. J. Bennett, "Holey optical fibers: an efficient modal model," Journal of Lightwave Technology **17**, 1093–1102 (1999).

[82] A. Ferrando, E. Silvestre, J. J. Miret, and P. Andrs, "Nearly zero ultraflattened dispersion in photonic crystal fibers," Optics Letters **25**, 790–792 (2000).

[83] D. Marcuse, *Theory of Dielectric Optical Waveguides* (Academic Pr, 1991), 2nd ed.

[84] A. Snyder and J. Love, *Optical Waveguide Theory* (Springer, 2010), 2nd ed.

[85] J. C. Knight, J. Arriaga, T. A. Birks, A. Ortigosa-Blanch, W. J. Wadsworth, and P. S. Russell, "Anomalous dispersion in photonic crystal fiber," IEEE Photonics Technology Letters **12**, 807–809 (2000).

[86] J. K. Ranka, R. S. Windeler, and A. J. Stentz, "Optical properties of high-delta air silica microstructure optical fibers," Optics Letters **25**, 796–798 (2000).

[87] J. K. Ranka, R. S. Windeler, and A. J. Stentz, "Visible continuum generation in air-silica microstructure optical fibers with anomalous dispersion at 800 nm," OPTICS LETTERS **25**, 25–27 (2000).

[88] L. Provino, J. M. Dudley, H. Maillotte, N. Grossard, R. S. Windeler, and

B. J. Eggleton, "Compact broadband continuum source based on microchip laser pumped microstructured fibre," Electronics Letters **37**, 558–560 (2001).

[89] S. Coen, A. H. L. Chau, R. Leonhardt, J. D. Harvey, J. C. Knight, W. J. Wadsworth, and P. S. J. Russell, "White-light supercontinuum generation with 60-ps pump pulses in a photonic crystal fiber," Optics Letters **26**, 1356–1358 (2001).

[90] A. V. Husakou and J. Herrmann, "Supercontinuum generation of Higher-Order solitons by fission in photonic crystal fibers," Physical Review Letters **87**, 203901 (2001).

[91] X. Liu, C. Xu, W. H. Knox, J. K. Chandalia, B. J. Eggleton, S. G. Kosinski, and R. S. Windeler, "Soliton self-frequency shift in a short tapered air-silica microstructure fiber," Optics Letters **26**, 358–360 (2001).

[92] B. R. Washburn, S. E. Ralph, P. A. Lacourt, J. M. Dudley, W. T. Rhodes, R. S. Windeler, and S. Coen, "Tunable near-infrared femtosecond soliton generation in photonic crystal fibres," Electronics Letters **37**, 1510–1512 (2001).

[93] S. Coen, A. H. L. Chau, R. Leonhardt, J. D. Harvey, J. C. Knight, W. J. Wadsworth, and P. S. J. Russell, "Supercontinuum generation by stimulated raman scattering and parametric four-wave mixing in photonic crystal fibers," Journal of the Optical Society of America B **19**, 753–764 (2002).

[94] J. M. Dudley, L. Provino, N. Grossard, H. Maillotte, R. S. Windeler, B. J. Eggleton, and S. Coen, "Supercontinuum generation in air-silica microstructured fibers with nanosecond and femtosecond pulse pumping," Journal of the Optical Society of America B **19**, 765–771 (2002).

[95] B. Washburn, S. Ralph, and R. Windeler, "Ultrashort pulse propagation in air-silica microstructure fiber," Opt. Express **10**, 575–580 (2002).

[96] G. Genty, M. Lehtonen, H. Ludvigsen, J. Broeng, and M. Kaivola, "Spectral broadening of femtosecond pulses into continuum radiation in microstructured fibers," Opt. Express **10**, 1083–1098 (2002).

[97] A. Apolonski, B. Povazay, A. Unterhuber, W. Drexler, W. J. Wadsworth, J. C. Knight, and P. S. J. Russell, "Spectral shaping of supercontinuum in a cobweb photonic-crystal fiber with sub-20-fs pulses," Journal of the Optical Society of America B **19**, 2165–2170 (2002).

[98] A. B. Fedotov, A. N. Naumov, A. M. Zheltikov, I. Bugar, J. Chorvat, D. Chorvat, A. P. Tarasevitch, and D. von der Linde, "Frequency-tunable supercontinuum generation in photonic-crystal fibers by femtosecond pulses of an optical parametric amplifier," Journal of the Optical Society of America B **19**, 2156–2164 (2002).

[99] A. V. Husakou and J. Herrmann, "Supercontinuum generation, four-wave mixing, and fission of higher-order solitons in photonic-crystal fibers," Journal of the Optical Society of America B **19**, 2171–2182 (2002).

[100] T. Udem, J. Reichert, R. Holzwarth, and T. W. Hnsch, "Accurate measurement of large optical frequency differences with a mode-locked laser," Optics Letters **24**, 881–883 (1999).

[101] V. R. Kumar, A. George, W. Reeves, J. Knight, P. Russell, F. Omenetto, and A. Taylor, "Extruded soft glass photonic crystal fiber for ultrabroad supercontinuum generation," Opt. Express **10**, 1520–1525 (2002).

[102] H. Hundertmark, D. Kracht, D. Wandt, C. Fallnich, V. V. R. K. Kumar, A. George, J. Knight, and P. Russell, "Supercontinuum generation with 200 pJ laser pulses in an extruded SF6 fiber at 1560 nm," Opt. Express **11**, 3196–3201 (2003).

[103] J. Y. Leong, P. Petropoulos, S. Asimakis, H. Ebendorff-Heidepriem, R. C. Moore, K. Frampton, V. Finazzi, X. Feng, J. H. Price, T. M. Monro, and D. J. Richardson, "A lead silicate holey fiber with $\gamma = 1820\ w^{-1}km^{-1}$ at 1550 nm," (Optical Society of America, 2005), Technical Digest (CD), p. PDP22.

[104] H. Hundertmark, S. Rammler, T. Wilken, R. Holzwarth, T. W. Hänsch, and P. S. Russell, "Octave-spanning supercontinuum generated in SF6-glass PCF by a 1060 nm mode-locked fibre laser delivering 20 pJ per pulse," Opt. Express **17**, 1919–1924 (2009).

[105] J. S. Sanghera, I. D. Aggarwal, L. E. Busse, P. C. Pureza, V. Q. Nguyen, F. H. Kung, L. B. Shaw, and F. Chenard, "Chalcogenide optical fibers target mid-IR applications." Laser Focus World **41**, 83–87 (2005).

[106] F. G. Omenetto, N. A. Wolchover, M. R. Wehner, M. Ross, A. Efimov, A. J. Taylor, V. V. R. K. Kumar, A. K. George, J. C. Knight, N. Y. Joly, and P. S. J. Russell, "Spectrally smooth supercontinuum from 350 nm to 3 μm in sub-centimeter lengths of soft-glass photonic crystal fibers," Opt. Express **14**, 4928–4934 (2006).

[107] C. Xia, M. Kumar, O. R. Kulkarni, M. N. Islam, F. L. Terry, and M. J. Freeman, "Mid-infrared supercontinuum generation to 4.5 μm in ZBLAN fluoride fibers by nanosecond diode pumping," Optics Letters **31**, 2553–2555 (2006).

[108] P. Domachuk, N. A. Wolchover, M. Cronin-Golomb, A. Wang, A. K. George, C. M. B. Cordeiro, J. C. Knight, and F. G. Omenetto, "Over 4000 nm bandwidth of mid-IR supercontinuum generation in sub-centimeter segments of highly nonlinear tellurite PCFs," Opt. Express **16**, 7161–7168 (2008).

[109] G. Qin, X. Yan, C. Kito, M. Liao, C. Chaudhari, T. Suzuki, and Y. Ohishi, "Ultrabroadband supercontinuum generation from ultraviolet to 6.28 μm in a fluoride fiber," Applied Physics Letters **95**, 161103 (2009).

[110] M. Bellini and T. W. Hnsch, "Phase-locked white-light continuum pulses: toward a universal optical frequency-comb synthesizer," Optics Letters **25**, 1049–1051 (2000).

[111] X. Gu, M. Kimmel, A. P. Shreenath, R. Trebino, J. M. Dudley, S. Coen, and R. S. Windeler, "Experimental studies of the coherence of microstructure-fiber supercontinuum," OPTICS EXPRESS **11**, 2697–2703 (2003).

[112] J. Nicholson and M. Yan, "Cross-coherence measurements of supercontinua generated in highly-nonlinear, dispersion shifted fiber at 1550 nm," Opt. Express **12**, 679–688 (2004).

[113] C. Gross, T. Best, D. van Oosten, and I. Bloch, "Coherent and incoherent spectral broadening in a photonic crystal fiber," OPTICS LETTERS **32**, 1767–1769 (2007).

[114] R. Holzwarth, T. Udem, T. W. Hansch, J. C. Knight, W. J. Wadsworth, and P. S. J. Russell, "Optical frequency synthesizer for precision spectroscopy," PHYSICAL REVIEW LETTERS **85**, 2264–2267 (2000).

[115] L. Hollberg, C. W. Oates, E. A. Curtis, E. N. Ivanov, S. A. Diddams, T. Udem, H. G. Robinson, J. C. Bergquist, R. J. Rafac, W. M. Itano, R. E. Drullinger, and D. J. Wineland, "Optical frequency standards and measurements," IEEE Journal of Quantum Electronics **37**, 1502–1513 (2001).

[116] B. Washburn and N. Newbury, "Phase, timing, and amplitude noise on supercontinua generated in microstructure fiber," Opt. Express **12**, 2166–2175 (2004).

[117] J. M. Dudley and S. Coen, "Coherence properties of supercontinuum spectra generated in photonic crystal and tapered optical fibers," Optics Letters **27**, 1180–1182 (2002).

[118] J. Dudley and S. Coen, "Numerical simulations and coherence properties of supercontinuum generation in photonic crystal and tapered optical fibers," Selected Topics in Quantum Electronics, IEEE Journal of **8**, 651–659 (2002).

[119] J. W. Nicholson, A. D. Yablon, M. F. Yan, P. Wisk, R. Bise, D. J. Trevor, J. Alonzo, T. Stockert, J. Fleming, E. Monberg, F. Dimarcello, and J. Fini, "Coherence of supercontinua generated by ultrashort pulses compressed in optical fibers," Optics Letters **33**, 2038–2040 (2008).

[120] J. Nicholson, M. Yan, A. Yablon, P. Wisk, J. Fleming, F. DiMarcello, and E. Monberg, "A high coherence supercontinuum source at 1550 nm," (2003), pp. 511–512.

[121] N. Nishizawa and J. Takayanagi, "Octave spanning high-quality supercontinuum generation in all-fiber system," JOURNAL OF THE OPTICAL SOCIETY OF AMERICA B-OPTICAL PHYSICS **24**, 1786–1792 (2007).

[122] L. E. Hooper, P. J. Mosley, A. C. Muir, W. J. Wadsworth, and J. C. Knight, "Coherent supercontinuum generation in photonic crystal fiber with all-normal group velocity dispersion," Opt. Express **19**, 4902–4907 (2011).

[123] T. Torounidis and P. Andrekson, "Broadband Single-Pumped Fiber-Optic parametric amplifiers," Photonics Technology Letters, IEEE **19**, 650–652 (2007).

[124] K. Garay-Palmett, A. B. U'Ren, R. Rangel-Rojo, R. Evans, and S. Camacho-Lopez, "Ultrabroadband photon pair preparation by spontaneous four-wave mixing in a dispersion-engineered optical fiber," Physical Review A (Atomic, Molecular, and Optical Physics) **78**, 043827–13 (2008).

[125] H. Chen, H. Wang, M. N. Slipchenko, Y. Jung, Y. Shi, J. Zhu, K. K. Buhman, and J. Cheng, "A multimodal platform for nonlinear optical microscopy and microspectroscopy," Opt. Express **17**, 1282–1290 (2009).

[126] K. Kieu, B. G. Saar, G. R. Holtom, X. S. Xie, and F. W. Wise, "High-power picosecond fiber source for coherent raman microscopy," Optics Letters **34**, 2051–2053 (2009).

[127] A. F. Pegoraro, A. Ridsdale, D. J. Moffatt, J. P. Pezacki, B. K. Thomas, L. Fu, L. Dong, M. E. Fermann, and A. Stolow, "All-fiber CARS microscopy of live cells," Opt. Express **17**, 20700–20706 (2009).

[128] J. A. Nelder and R. Mead, "A simplex method for function minimization," The Computer Journal **7**, 308 –313 (1965).

[129] H. Schwefel, *Evolution and Optimum Seeking* (Wiley-Interscience, 1995), Har/Dis ed.

[130] J. Neumann, "Zur theorie der gesellschaftsspiele," Mathematische Annalen **100**, 295–320 (1928).

[131] H. P. Williams, *Model Solving in Mathematical Programming* (John Wiley & Sons, 1993).

[132] E. Silvestre, T. Pinheiro-Ortega, P. Andrés, J. J. Miret, and A. Ortigosa-Blanch, "Analytical evaluation of chromatic dispersion in photonic crystal fibers," Optics Letters **30**, 453–455 (2005).

[133] J. Holland, *Adaptation in natural and artificial systems* (University of Michigan Press, 1975).

[134] S. Kirkpatrick, D. Jr., and M. P. Vecchi, "Optimization by simmulated annealing," science **220**, 671–680 (1983).

[135] K. E. Parsopoulos and M. N. Vrahatis, "Recent approaches to global optimization problems through particle swarm optimization," Natural computing **1**, 235–306 (2002).

[136] M. Dorigo and L. M. Gambardella, "Ant colony system: A cooperative learning approach to the traveling salesman problem," Evolutionary Computation, IEEE Transactions on **1**, 53–56 (1997).

[137] T. Bäck and H. P. Schwefel, "An overview of evolutionary algorithms for parameter optimization," Evolutionary computation **1**, 1–23 (1993).

[138] F. Poletti, V. Finazzi, T. M. Monro, N. G. R. Broderick, V. Tse, and D. J. Richardson, "Inverse design and fabrication tolerances of ultra-flattened dispersion holey fibers," OPTICS EXPRESS **13**, 3728–3736 (2005).

[139] L. Davis, *Handbook Of Genetic Algorithms* (Thomson Publishing Group, 1991), 1st ed.

[140] "IEEE standard for floating-point arithmetic," (2008).

[141] E. Kerrinckx, L. Bigot, M. Douay, and Y. Quiquempois, "Photonic crystal fiber design by means of a genetic algorithm," Opt. Express **12**, 1990–1995 (2004).

[142] J. Harvey, S. Murdoch, S. Coen, R. Leonhardt, D. Mechin, and G. Wong, "Parametric processes in microstructured and highly nonlinear optical fibres," OPTICAL AND QUANTUM ELECTRONICS **39**, 1103–1114 (2007).

[143] M. E. Marhic, K. K. Wong, and L. G. Kazovsky, "Wide-band tuning of the gain spectra of one-pump fiber optical parametric amplifiers," IEEE Journal of Selected Topics in Quantum Electronics **10**, 1133– 1141 (2004).

[144] J. Tukey, "An introduction to the calculations of numerical spectrum analysis," Spectral Analysis of Time Series pp. 25—46 (1967).

[145] M. D. O'Donnell, K. Richardson, R. Stolen, A. B. Seddon, D. Furniss, V. K. Tikhomirov, C. Rivero, M. Ramme, R. Stegeman, G. Stegeman, M. Couzi, and T. Cardinal, "Tellurite and fluorotellurite glasses for fiberoptic raman

amplifiers: Glass characterization, optical properties, raman gain, preliminary fiberization, and fiber characterization," Journal of the American Ceramic Society **90**, 1448–1457 (2007).

[146] J. Y. Y. Leong, P. Petropoulos, J. H. V. Price, H. Ebendorff-Heidepriem, S. Asimakis, R. C. Moore, K. E. Frampton, V. Finazzi, X. Feng, T. M. Monro, and D. J. Richardson, "High-nonlinearity dispersion-shifted lead-silicate holey fibers for efficient 1-mu m pumped supercontinuum generation," JOURNAL OF LIGHTWAVE TECHNOLOGY **24**, 183–190 (2006).

[147] J. J. Miret, E. Silvestre, and P. Andrés, "Octave-spanning ultraflat supercontinuum with soft-glass photonic crystal fibers," Opt. Express **17**, 9197–9203 (2009).

[148] Z. Zhu and T. Brown, "Effect of frequency chirping on supercontinuum generation in photonic crystal fibers," Opt. Express **12**, 689–694 (2004).

[149] D. Lorenc, D. Velic, A. N. Markevitch, and R. J. Levis, "Adaptive ferntosecond pulse shaping to control supercontinuum generation in a microstructure fiber," pp. 288–292 (2007).

[150] J. C. Travers, S. V. Popov, and J. R. Taylor, "Extended blue supercontinuum generation in cascaded holey fibers," Optics Letters **30**, 3132–3134 (2005).

[151] A. Ferrando, E. Silvestre, P. Andres, J. Miret, and M. Andres, "Designing the properties of dispersion-flattened photonic crystal fibers," Opt. Express **9**, 687–697 (2001).

[152] E. Silvestre, T. Pinheiro-Ortega, P. Andrés, J. J. Miret, and A. Coves, "Differential toolbox to shape dispersion behavior in photonic crystal fibers," Optics Letters **31**, 1190–1192 (2006).

[153] H. Ebendorff-Heidepriem and T. M. Monro, "Extrusion of complex preforms for microstructured optical fibers," Opt. Express **15**, 15086–15092 (2007).

[154] W. Q. Zhang, V. S. Afshar, H. Ebendorff-Heidepriem, and T. M. Monro, "Record nonlinearity in optical fibre," Electronics Letters **44**, 1453–1455 (2008).

[155] M. Sheik-Bahae, A. Said, T. Wei, D. Hagan, and E. Van Stryland, "Sensitive measurement of optical nonlinearities using a single beam," Quantum Electronics, IEEE Journal of **26**, 760–769 (1990).

[156] F. Poletti and P. Horak, "Description of ultrashort pulse propagation in multimode optical fibers," Journal of the Optical Society of America B **25**, 1645–1654 (2008).

[157] F. Poletti and P. Horak, "Dynamics of femtosecond supercontinuum generation in multimode fibers," Opt. Express **17**, 6134–6147 (2009).

[158] A. W. Snyder, "Coupled-Mode theory for optical fibers," Journal of the Optical Society of America **62**, 1267–1277 (1972).

[159] N. Akhmediev and M. Karlsson, "Cherenkov radiation emitted by solitons in optical fibers," Physical Review A **51**, 2602 (1995).

[160] H. Liu, Y. Dai, C. Xu, J. Wu, K. Xu, Y. Li, X. Hong, and J. Lin, "Dynamics of cherenkov radiation trapped by a soliton in photonic-crystal fibers," Optics Letters **35**, 4042–4044 (2010).

[161] V. R. Almeida, Q. Xu, C. A. Barrios, and M. Lipson, "Guiding and confining light in void nanostructure," Optics Letters **29**, 1209 (2004).

[162] O. Boyraz, P. Koonath, V. Raghunathan, and B. Jalali, "All optical switching and continuum generation in silicon waveguides," Opt. Express **12**, 4094 (2004).

[163] M. A. Foster, A. C. Turner, R. Salem, M. Lipson, and A. L. Gaeta, "Broad-band continuous-wave parametric wavelength conversion in silicon nanowaveguides," OPTICS EXPRESS **15**, 12949–12958 (2007).

[164] C. Koos, P. Vorreau, T. Vallaitis, P. Dumon, W. Bogaerts, R. Baets, B. Esembeson, I. Biaggio, T. Michinobu, F. Diederich, W. Freude, and J. Leuthold, "All-Optical High-Speed signal processing with Silicon-Organic hybrid slot waveguides," nature photonics **3**, 216 (2009).

[165] M. Pelusi, F. Luan, T. D. Vo, M. R. E. Lamont, S. J. Madden, D. A. Bulla, D. Choi, B. Luther-Davis, and B. J. Eggleton, "Photonic-Chip-Based Radio-Frequency spectrum analyser with terahertz bandwidth," nature photonics **3**, 139 (2009).

[166] B. J. Eggleton, B. Luther-Davies, and K. Richardson, "Chalcogenide photonics," nature photonics **5**, 141–148 (2011).

[167] S. Afshar V. and T. M. Monro, "A full vectorial model for pulse propagation in emerging waveguides with subwavelength structures part i: Kerr nonlinearity," Opt. Express **17**, 2298–2318 (2009).

[168] M. D. Turner, T. M. Monro, and S. Afshar V., "A full vectorial model for pulse propagation in emerging waveguides with subwavelength structures part II: stimulated raman scattering," Opt. Express **17**, 11565–11581 (2009).

[169] T. X. Tran and F. Biancalana, "An accurate envelope equation for lightpropagation in photonic nanowires: newnonlinear effects," Opt. Express **17**, 17934–17949 (2009).

[170] H. Ebendorff-Heidepriem, S. C. Warren-Smith, and T. M. Monro, "Suspended nanowires: fabrication, design and characterization of fibers with nanoscale cores," Opt. Express **17**, 2646–2657 (2009).

[171] R. H. Stolen, J. Botineau, and A. Ashkin, "Intensity discrimination of optical pulses with birefringent fibers," Optics Letters **7**, 512–514 (1982).

[172] F. Matera and S. Wabnitz, "Nonlinear polarization evolution and instability in a twisted birefringent fiber," Opt. Lett. **11**, 467–469 (1986).

[173] H. G. Winful, "Polarization instabilities in birefringent nonlinear media: application to fiber-optic devices," Opt. Lett. **11**, 33–35 (1986).

[174] C. Menyuk, "Nonlinear pulse propagation in birefringent optical fibers," Quantum Electronics, IEEE Journal of **23**, 174 – 176 (1987).

[175] S. F. Feldman, D. A. Weinberger, and H. G. Winful, "Polarization instability in a twisted birefringent optical fiber," J. Opt. Soc. Am. B **10**, 1191–1201 (1993).

[176] G. Millot, E. Seve, and S. Wabnitz, "Polarization symmetry breaking and pulse train generation from the modulation of light waves," Phys. Rev. Lett. **79**, 661–664 (1997).

[177] G. Millot, E. Seve, S. Wabnitz, and M. Haelterman, "Dark-soliton-like pulse-train generation from induced modulational polarization instability in a birefringent fiber," Opt. Lett. **23**, 511–513 (1998).

[178] S. Pitois, G. Millot, and S. Wabnitz, "Polarization domain wall solitons with counterpropagating laser beams," Phys. Rev. Lett. **81**, 1409–1412 (1998).

[179] S. Pitois, G. Millot, and S. Wabnitz, "Nonlinear polarization dynamics of counterpropagating waves in an isotropic optical fiber: theory and experiments," Journal of the Optical Society of America B **18**, 432–443 (2001).

[180] S. Wabnitz, "Polarization domain wall solitons in elliptically birefringent optical fibers," PIERS ONLINE **5**, 621–624 (2009).

[181] V. V. Kozlov and S. Wabnitz, "Theoretical study of polarization attraction in high-birefringence and spun fibers," Opt. Lett. **35**, 3949–3951 (2010).

[182] J. Fatome, S. Pitois, P. Morin, and G. Millot, "Observation of light-by-light polarization control and stabilization in optical fibre for telecommunication applications," Opt. Express **18**, 15311–15317 (2010).

[183] V. V. Kozlov, J. Nuo, and S. Wabnitz, "Theory of lossless polarization attraction in telecommunication fibers," J. Opt. Soc. Am. B **28**, 100–108 (2011).

[184] V. E. Zakharov and A. V. Mikhailov, "Polarization domains in nonlinear optics," JETP Lett. **45**, 349–352 (1987).

[185] S. Pitois, A. Picozzi, G. Millot, H. R. Jauslin, and M. Haelterman, "Polarization and modal attractors in conservative counterpropagating four-wave interaction," Europhysics Letters **70**, 88–94 (2005).

[186] S. Pitois, J. Fatome, and G. Millot, "Polarization attraction using counterpropagating waves in optical fiber at telecommunication wavelengths," Opt. Express **16**, 6646–6651 (2008).

[187] E. Seve, G. Millot, S. Trillo, and S. Wabnitz, "Large-signal enhanced frequency conversion in birefringent optical fibers: theory and experiments," J. Opt. Soc. Am. B **15**, 2537–2551 (1998).

[188] G. Gregori and S. Wabnitz, "New exact solutions and bifurcations in the spatial distribution of polarization in third-order nonlinear optical interactions," Phys. Rev. Lett. **56**, 600–603 (1986).

[189] S. M. Jensen, "The nonlinear coherent coupler," IEEE Journal of Quantum Electronics **18**, 1580–1583 (1982).

[190] C. M. de Sterke and J. E. Sipe, "Polarization instability in a waveguide geometry," Opt. Lett. **16**, 202–204 (1991).

[191] Y. Wang and W. Wang, "Nonlinear optical pulse coupling dynamics," J. Lightwave Technol. **24**, 2458 (2006).

[192] Y. S. Kivshar, "Switching dynamics of solitons in fiber directional couplers," Opt. Lett. **18**, 7–9 (1993).

[193] D. C. Hutchings, J. S. Aitchison, and J. M. Arnold, "Nonlinear refractive coupling and vector solitons in anisotropic cubic media," J. Opt. Soc. Am. B **14**, 869–879 (1997).

[194] H. S. Eisenberg, Y. Silberberg, R. Morandotti, A. R. Boyd, and J. S. Aitchison, "Discrete spatial optical solitons in waveguide arrays," Phys. Rev. Lett. **81**, 3383–3386 (1998).

[195] U. Peschel, R. Morandotti, J. M. Arnold, J. S. Aitchison, H. S. Eisenberg, Y. Silberberg, T. Pertsch, and F. Lederer, "Optical discrete solitons in waveguide arrays. 2. dynamic properties," J. Opt. Soc. Am. B **19**, 2637–2644 (2002).

[196] K. R. Khan, T. X. Wu, D. N. Christodoulides, and G. I. Stegeman, "Soliton switching and multi-frequency generation in a nonlinear photonic crystal fiber coupler," Opt. Express **16**, 9417–9428 (2008).

[197] C. C. Yang, "All-optical ultrafast logic gates that use asymmetric nonlinear directional couplers," Opt. Lett. **16**, 1641–1643 (1991).

[198] T. Fujisawa and M. Koshiba, "All-optical logic gates based on nonlinear slot-waveguide couplers," J. Opt. Soc. Am. B **23**, 684–691 (2006).

[199] W. Fraga, J. Menezes, M. d. Silva, C. Sobrinho, and A. Sombra, "All optical logic gates based on an asymmetric nonlinear directional coupler," Optics Communications **262**, 32 – 37 (2006).

[200] D. C. Hutchings and B. S. Wherrett, "Theory of the anisotropy of ultrafast

nonlinear refraction in zinc-blende semiconductors," Phys. Rev. B **52**, 8150–8159 (1995).

[201] B. Daniel and G. Agrawal, "Vectorial nonlinear propagation in silicon nanowire waveguides: polarization effects," Journal of the Optical Society of America B **27**, 956–965 (2010).

[202] S. P. Chan, C. E. Png, S. T. Lim, G. T. Reed, and V. M. Passaro, "Single-mode and polarization-independent silicon-on-insulator waveguides with small cross section," Journal of Lightwave Technology **23**, 2103– 2111 (2005).

[203] R. H. Stolen, J. P. Gordon, W. J. Tomlinson, and H. A. Haus, "Raman response function of silica-core fibers," Journal of the Optical Society of America B **6**, 1159–1166 (1989).

[204] K. S. Kim, R. H. Stolen, W. A. Reed, and K. W. Quoi, "Measurement of the nonlinear index of silica-core and dispersion-shifted fibers," Optics Letters **19**, 257–259 (1994).

[205] A. Boskovic, S. Chernikov, J. Taylor, L. GrunerNielsen, and O. Levring, "Direct continuous-wave measurement of n(2) in various types of telecommunication fiber at 1.55 mu m," OPTICS LETTERS **21**, 1966–1968 (1996).

[206] A. A. Cuyt, V. Petersen, B. Verdonk, H. Waadeland, and W. B. Jones, *Handbook of Continued Fractions for Special Functions* (Springer, 2008), 1st ed.